HAL
open science

A study of multi-standard radio transmitters for GSM/WCDMA/LTE base stations

Sandeep Kowlgi Srinivasan

To cite this version:

Sandeep Kowlgi Srinivasan. A study of multi-standard radio transmitters for GSM/WCDMA/LTE base stations. Networking and Internet Architecture [cs.NI]. Télécom ParisTech, 2013. English. NNT : 2013ENST0018 . tel-01180009

HAL Id: tel-01180009

https://pastel.hal.science/tel-01180009

Submitted on 23 Jul 2015

HAL is a multi-disciplinary open access archive for the deposit and dissemination of scientific research documents, whether they are published or not. The documents may come from teaching and research institutions in France or abroad, or from public or private research centers.

L'archive ouverte pluridisciplinaire **HAL**, est destinée au dépôt et à la diffusion de documents scientifiques de niveau recherche, publiés ou non, émanant des établissements d'enseignement et de recherche français ou étrangers, des laboratoires publics ou privés.

ParisTech
INSTITUT DES SCIENCES ET TECHNOLOGIES
PARIS INSTITUTE OF TECHNOLOGY

TELECOM ParisTech

2013-ENST-0018

EDITE - ED 130

Doctorat ParisTech

THÈSE

pour obtenir le grade de docteur délivré par

TELECOM ParisTech

Spécialité « Communications et Électronique »

présentée et soutenue publiquement par

Sandeep KOWLGI SRINIVASAN

le 11 Avril 2013

A Study Of Multi-Standard Radio Transmitters For GSM/WCDMA/LTE Base Stations

Directeur de thèse : **Patrick LOUMEAU**
Co-encadrement de la thèse : **Corinne BERLAND**

Jury

Mme Nathalie ROLLAND, Professeur, IEMN, Université de Lille	(rapporteur)
M. Yann DEVAL, Professeur, Laboratoire IMS, Université de Bordeaux	(rapporteur)
M. Amara AMARA, Professeur, ISEP, Paris	(examinateur)
M. Patrice GAMAND, Directeur HDR, NXP Semiconductors, Caen	(examinateur)
M. Dominique MORCHE, Ingénieur au CEA LETI, MINATEC, Grenoble	(examinateur)
M. Tim RIDGERS, Ingénieur, NXP Semiconductors, Caen	(examinateur)

TELECOM ParisTech
école de l'Institut Mines-Télécom - membre de ParisTech
46 rue Barrault 75013 Paris - (+33) 1 45 81 77 77 - www.telecom-paristech.fr

THÈSE

A Study Of Multi-Standard Radio Transmitters For GSM/WCDMA/LTE Base Stations

Sandeep KOWLGI SRINIVASAN

Supervisors:

Prof. Patrick LOUMEAU

Prof. Corinne BERLAND

Tim RIDGERS

April 11, 2013

Acknowledgements

This work has been the result of a great many discussions during the past few years with experts both in the academia and the industry. To have the opportunity to be in both worlds at the same time, I am very fortunate.

It is with pleasure that I acknowledge the help and support of the many people whose contribution has been invaluable throughout my Ph.D. program. To begin, I would like to thank my supervisors Prof. Corinne Berland, Timothy Ridgers and Prof. Patrick Loumeau for their their guidance and support. Prof. Berland has been generous in her encouragement and for her timely feedback. Her energy and her liveliness have been inspirational. I am grateful to her for her support through this entire period. I am thankful also to Mr. Ridgers for his critical feedback and the many detailed discussions we had during the initial phases of the thesis. His perspicaciousness in technical analysis and depth and breadth of knowledge in the field influence all those who work with him. I would also like to thank Prof. Loumeau for his support and for ensuring that my academic interests were met.

I feel a deep sense of appreciation and gratitude towards Dr.(HDR) Patrice Gamand, the General Manager of the RF Innovation Centre (ICRF) at NXP Semiconductors, France for his unwavering support and encouragement during my program. His personable, approachable nature, his measured involvement in the technical activities of his group and his ability to solve issues amicably are lessons that I will keep for the rest of my professional career. His interest and involvement has been instrumental in my establishing interactions with several groups company wide.

There are numerous members at NXP that deserve mention. Discussions with senior scientists such as Aykut Erdem, Laurent Gambus, Paul Mattheijssen and Robin Wesson provided a wealth of knowledge and inspiration. Thought provoking discussions with Aykut were key to my appreciation of system level concepts and issues in the cellular domain. I also benefited from some of his measurements and his help in the RF lab, in validating certain aspects of my work. I had the fortune of also working closely with Paul Mattheijssen and Robin Wesson on many aspects related to the system design and the framework in developing the performance budget. I have gained much from their experience in this field, their inputs and their reviews of my work, for all of which I am grateful. The many technical discussions with Laurent Gambus during the design of the Analog Quadrature Modulator (AQM) and his work on the LO Polyphase filter, were invaluable inputs. During the design of the attenuator network, I benefited from critical inputs and the original works of Dr. Jos Bergervoet, Prof. Domine Leenaerts and Hassan Gul, which were invaluable in the design of the gain stage for the multi-mode AQM. I remain thankful to all of these people for their support and involvement in my work, despite unforgiving deadlines and commitments.

I also thank Dr. Ian Gresham of NXP Semiconductors, USA, who was kind enough to host me in his group in Billerica. It was a pleasure to have worked with his group, particularly Dr. Kathir Krishnamurthy and Mohsin Asif.

My involvement in the Par4CR project allowed me to work in the groups of Prof. Arthur Roermund and Prof. Peter Baltus at the Technical University of Eindhoven. The summer months on campus were refreshing, especially in the company of Asst. Prof. Rob Mestrom, Dr. Olga Zyldareva and several others.

My interactions with Prof. Georg Fischer of the University of Erlangen-Nuremberg, based on his work at Bell Labs R&D and later Alcatel Lucent provided valuable perspectives of the Base-Station Original Equipment Manufacturers (OEMs) and were useful in identifying the system-level bottlenecks.

I would like to acknowledge the financial support of the Association Nationale de la Recherche et de la Technologie (ANRT) under the CIFRE convention and also NXP Semiconductors, where I was employed, for making this program possible.

For my time at NXP, I would like to also acknowledge the support and contributions of Prof. Philippe Descamps, Guy Le Moal, Dr. Olivier Aymard, Thomas Francois, Philippe Barre, Dr. Vincent Fresnaud (presently with Integrated Device Technology, IDT), John Hug (presently with Analog Devices), Gwendal le Padellec, Dr. Olivier Tesson, Dr. Patrick Jean, Dr. Philippe Meunier and many others with whom I have interacted. Marie-José Moreno our team assistant brought the whole group together with her cheerfulness and an inexplicable source of energy. She has been a marvel at ensuring that all of our administrative needs are met without hassle.

The years would not have passed without the friendship and lighter moments with my NXP colleagues, Vincent Regnauld, Dr. Sebastien Darfeuille and Dr. Laure Rolland Du Roscoat. The ice-hockey matches, the many visits to the Normandy beaches, the odd games of 'Pétanque', the many get-together's, the French Open at Roland Garros, the drives along the country side and much more, are all unforgettable memories. I cannot thank Vincent enough for he has been of immense help and support all the way. I am also fortunate to have had the company of Dr. Mathieu Perin, Dr. Fatima Ghanem, Dr. Guillaume Monnerie, Dr. Manohiaina Ranaivoniarivo, Dr. Bilal Elkassir, Dr Sidina Wane and Francois Moreau, during my years at NXP.

My dear parents Srinivasan Kowlgi and Jahnavi Srinivasan, my grandmother Mrs. Janakibai Sira deserve all of my gratitude for their belief in me, their support and all the encouragement they have provided me through these years. The values they instilled and the lessons they imparted remain guiding principles for my life. The many week-end discussions about issues of the world with my dear brother Sunil, were stimulating reminders of a world outside the Ph.D; a reminder of challenges to be overcome, lessons to be learnt and the simple pleasures to be gained along the way. I would also like to thank the rest of my family for their support and understanding all along.

Lastly and most of all, my dear wife Chithrupa. You have stood by my side with unfaltering support. I cannot thank you enough for your sacrifices, your kindness through our highs and your patience and support through lows. I am glad to have you with me for the rest of my life. I conclude this chapter by dedicating this thesis to my family.

Abstract

Contemporary telecommunication Base-Stations for GSM/EDGE, WCDMA/HSPA and LTE are increasingly complex and energy intensive. The complexity and inefficiency manifest as bottlenecks in network performance and increased power consumption, both of which need to be addressed. Simultaneously, with the growing strength of hardware-agnostic, software- or data-centric systems, the need for reconfigurable or universal solutions is becoming evident. The favoured solution is a truly multi-standard transmitter or single Radio Access Network (single-RAN), that also benefits from advanced antenna technologies, improved signal processing and the latest power amplifier technologies. Such solutions are more economical in their power consumption besides having a smaller footprint. Subsequently, by operating multiple standards simultaneously, cellular network deployment and efficient resource-management are markedly improved.

Modern base station transmitters are often multi-standard, in that they can support different air-interface standards or modes. However, this is achieved not through concurrent operation of the different standards or 'modes', but by means of reconfiguration, which leads to increased costs of equipment, maintenance and also occasional unavailability of network resources.

We envision a practical, fully multi-mode transmitter capable of simultaneously supporting GSM/EDGE, WCDMA/HSPA and LTE carriers. In order to identify the feasibility of multi-mode transmission, this work attempts to analyze the system design of such a RF chain, to a first-order of approximation. The concurrent operation of multiple access technologies on a unified/converged-radio platform is analysed in this work, to result in several stringent requirements on the performance of the multi-mode RF-transmitter. Our contribution includes the analysis of the critical 3GPP-specified performance metrics, including Error-Vector-Magnitude and Adjacent/Alternate Channel Leakage Ratio, in order to perform the translation from system-level specifications to block-level requirements. Our approach of analyzing block-level contributions to the various signal-distortion mechanisms, is based directly on the 3GPP modulation-quality and spectral-leakage metrics. Amongst other benefits, this facilitates deriving more accurate individual block-level performance requirements. First-order approximations of transmitter impairments of each of the blocks in a typical transmission chain are considered for this analysis. To serve a parallel objective of improving transmitter performance, an insightful heuristic method using cost functions to enhance the budgeting of transmitter performance parameters is also suggested. The issue of high Peak-to-Average-Power-Ratio (PAPR) for multi-mode signals is also analysed through simulations and incorporated into the dimensioning of the chain.

This work brings forth some system-level issues and also highlights challenges in the operation of multi-standard Base-Stations. Some of these include multi-mode signal crest-factor reduction, carrier-to-carrier interference mitigation, per-carrier power-control, etc. The evolution of 3GPP standards towards multi-mode operation is in the nascent stage. To contribute to this effort, our work revisits the architecture of the traditional macro-cell Base-Station transmitter in order to analyse and define performance requirements for a multi-standard cellular radio platform. Our system analysis and design also identifies a potential bottleneck in the proposed multi-mode chain, for which analysis is presented. Consequently

and lastly, we propose the conceptual design of a variable-gain Analog Quadrature Modulator that bypasses the bottleneck, highlighting scope for future development and validation of this work.

Index Terms - *ACLR, Base-Station, budgeting, Cellular, EDGE, EVM, GSM, LTE, Mixer, Modulator, multi-carrier, multi-standard, non-linearity, transmitter, transmitter impairments, VGA, WCDMA/HSPA.*

Abbreviations

3GPP	3rd Generation Partnership Project
ACLR	Adjacent Channel Leakage Ratio
AM	Amplitude Modulation
ARCEP	Autorité de Régulation des Communications Électroniques
AQM	Analog Quadrature Modulator
ARP	Antenna Reference Point
ASIC	Application Specific IC
BCCH	Broadcast Control Channel
BC	Band Category
BS Tx/Rx	Base Station Transmitter / Receiver
BStn	Base Station
BW	Bandwidth
CCDF	Complementary Cumulative Distribution function
CFR	Crest Factor Reduction
CPE	Common Phase Error
cm	common mode
CM	Current Mirror
CMD	Cross Modulation
DAC	Digital to Analog Converter
DFT	Discrete Fourier Transform
DL	Down-Link
DPD	Digital Pre-Distortion
DR	Dynamic Range
DSP	Digital Signal Processing
DUC	Digital Up-Conversion
ETSI	European Telecommunications Standards Institute
E-UTRA	Evolved- Universal Terrestrial Radio Access
EVM	Error Vector Magnitude
FDD	Frequency Division Duplexing
FET	Field Effect Transistor
FFT	Fast Fourier Transform
FIR	Finite Impulse Response
GSM	Global System for Mobile
HSPA	High Speed Packet Access

IBO	Input Back-off
ICI	Inter-Carrier Interference
IF	Intermediate Frequency
IMDn	Intermodulation Distortion products of order 'n'
IMT	International Mobile Telecommunications
***IP*2/*IP*3**	Intercept Point order 2 / order 3
IQ	In-Phase and Quadrature
LO	Local Oscillator
LPF	Low-Pass Filter
LTE	Long Term Evolution
MC	Multi-Carrier
MCPA	Multi-Carrier Power Amplifier
MOD	Baseband Modulator
MOS	Metal Oxide Semiconductor Field Effect Transistor
NCO	Numeric Complex Oscillator
NF	Noise Figure
OFDM	Orthogonal Frequency Division Multiplexing
OFDD	Orthogonal Frequency Division De-multiplexed
OIP3	3rd Order Output Intercept Point
OOB	Out of Band
ORFS	Output RF Spectrum
PA	Power Amplifier
PAPR	Peak to Average Power Ratio
PDF	Probability Density Function
PM	Phase Modulation
PPF	Poly Phase Filter
PSD	Power Spectral Density
QoS	Quality of Service
RAN	Radio Access Network
RAT	Radio Access Technology
RBW	Resolution Bandwidth
RF	Radio Frequency
RPE	Random Phase Error
Rx	Receive / Receiver
SEM	Spectral/Spurious Emissions Mask
TDD	Time Division Duplexing
Tx	Transmit / Transmitter / Transmission
UE	User Equipment
UL	Uplink
UMTS	Universal Mobile Telecommunications Systems
UTRA	Universal Terrestrial Radio Access
VGA	Variable Gain Amplifier / Attenuator
WCDMA	Wideband Code Division Multiple Access

Contents

1 Introduction (en français) 1
1.1 Motivation . . . 1
1.2 Méthodologie . . . 3
1.3 Contributions . . . 13

2 Introduction 15
2.1 Motivation . . . 15
2.2 Methodology . . . 17
2.3 Contributions of this work . . . 27

3 Background 29
3.1 Identifying a Use-Case Scenario . . . 29
3.2 Spectrum Availability and Constraints . . . 30
3.3 Architectural and Topological Considerations . . . 32
3.4 Co-existence Issues . . . 39

4 Transmitter - System Level Analysis 45
4.1 Architecture of a contemporary Base Station radio transmitter . . . 45
4.2 Synthesizing Link-Level Performance Requirements from System-Level Requirements . . . 47
4.3 Spectrum Emissions Requirements . . . 64
4.4 Summary . . . 83

5 Multi-Mode Transmitter Performance Budgeting 87
5.1 Cascade Analysis for Cumulative Errors . . . 87
5.2 Other Errors . . . 97
5.3 Power Control Issues in a Multi-mode Transmitter . . . 101
5.4 Multi-mode AQM with Mode-specific Gain Control . . . 104
5.5 Summary . . . 105

6 The Design of a Multi-Mode Variable Gain AQM 109
6.1 NXP-QUBiC4X Technology . . . 113
6.2 AQM Input Stage . . . 115
6.3 Mixers . . . 141

6.4 Quadrature LO Generation 161
6.5 Common Base Output Stage 172
6.6 Simulation results 180
6.7 Time domain waveforms 181
6.8 S-parameter simulation results 182
6.9 Parametric sweeps 183
6.10 Monte Carlo simulations 187
6.11 Summary 191

Conclusion **193**

A The Simplified Concept of Pre-Distortion **203**
A.1 Basics of Pre-Distortion 203

B Basic Polynomial Non-linearity Mechanisms **205**
B.1 Intermodulation Distortion 205
B.2 Composite Triple Beat 206
B.3 Cross Modulation 209
B.4 Intermodulation Enhancement 209

C Multi-mode DAC Dynamic Range Requirements **213**

D Derivations from Chapter 6 **217**
D.1 Derivation RF voltage visible at the IF node of the Mixers 217
D.2 Input Impedance of the Common-Emitter Stage with Series-Series/Shunt-Shunt Feedback 219

Bibliography **231**

List of Figures

1.1 Typique contemporain station de base carte de l'émetteur-récepteur 6
1.2 Bilan de puissance dans une station de base UMTS 2/2/2 7
1.3 Hiérarchie du système des Stations de Base 9
1.4 Consommation mondiale d'énergie des systèmes de communication mobile . . 10
1.5 Répartition de la consommation d'énergie dans l'émetteur-récepteur radio pour les différente variantes de la Station de Base 12
1.6 Méthodologie de l'analyse 13

2.1 Traditional Base Station sub-system supporting 2G and 3G/4G 16
2.2 Typical contemporary Base Station transceiver card 20
2.3 Power budget in a 2/2/2 UMTS base station 21
2.4 Base Station system hierarchy 23
2.5 Global Energy Consumption of Mobile Communications 24
2.6 A breakdown of power consumption in the radio transceiver for different Base Station variants 25
2.7 Methodology of Analysis 26

3.1 A brief summary of the typical transmitter architectures 34
3.2 Multi Carrier GSM/EDGE TDMA/FDD & TDMA/FDMA 39
3.3 LTE Resource-Block on a time and frequency scale 40
3.4 Base Station with Operator Shared-carrier and Dedicated-carrier RAN sharing for LTE/WCDMA and GSM/EDGE 43

4.1 Illustration of the DAC interpolation (with LPF) and subsequent relaxation of the Anti-Aliasing Filter requirements 46
4.2 Error Vector Magnitude for one symbol on the constellation diagram 49
4.3 Transmitter impairments that contribute to the EVM 51
4.4 Error Vector Magnitude due to IQ DC Offsets 53
4.5 Error Vector Magnitude due to IQ Gain and Phase imbalances 55
4.6 Simulated impact of IQ Gain and Phase imbalances on the EVM of LTE, WCDMA, EDGE 57
4.7 Error Vector Magnitude due to Phase Noise 58
4.8 Effect of Phase Noise in multi-carrier OFDM 59

4.9 Simulated impact of composite Phase Error on the EVM of LTE, WCDMA, EDGE . . . 60
4.10 Error Vector Magnitude due to non-linearity . . . 61
4.11 Simulated EVM due to Non-linearity on LTE, WCDMA, EDGE . . . 63
4.12 3GPP ORFS spectral mask for GSM/EDGE . . . 66
4.13 Phase Noise, Random noise and IMD contribution to the Adjacent and Alternate Channel Leakage power . . . 67
4.14 Simulated bandwidth spreading for 3rd order coefficient of non-linearity polynomial . . . 69
4.15 Correction factors obtained from measurements of GMSK modulated carriers subjected to non-linearity . . . 70
4.16 Six-carrier GMSK IMD products . . . 71
4.17 Four-carrier WCDMA IMD products . . . 74
4.18 Degradation of Rx sensitivity by Tx noise leakage into Rx frequency band . . . 77
4.19 Degradation of Rx sensitivity as varying levels of duplexer rejection and Tx noise . . . 78
4.20 Simulated CCDF of the PAPR for multi-carrier transmission . . . 80
4.21 ACLR degradation for six EDGE carriers, at the output of each block along the transmit chain, with $P_o = 49.0$ dBm . . . 84

5.1 Block-wise distribution of EVM . . . 92
5.2 Actual block-wise percentage EVM for IP3 and Noise . . . 94
5.3 Percentile block-wise impairments in a multi-mode BStn transmitter . . . 95
5.4 Class A amplifier stage linearity versus static power relationship . . . 96
5.5 Block-level actual and percentage EVM contributions across a multi-mode BStn transmitter . . . 98
5.6 Piecewise linear approximation of the Phase noise mask for the calculation of integrated phase noise and jitter . . . 100
5.7 Block diagram of Power (Gain) control in legacy Base Stations . . . 103
5.8 The (DAC) bottleneck in the Multi-mode Gain-control scheme . . . 104
5.9 The issue of dynamic range requirements for the DAC from multi-mode signal transmission . . . 105
5.10 The proposed multi-mode transmitter gain control scheme with separate gain control paths . . . 108

6.1 Frequency translation to the upper sideband by the Analog Quadrature Modulator . . . 109
6.2 Block diagram of the Analog Quadrature Modulator . . . 114
6.3 The interfacing between the DAC and the AQM . . . 115
6.4 Level shifting the common-mode output voltage from the DAC to the AQM input . . . 116
6.5 Output stage of the 16-bit DAC1627D1G25 Digital to Analog Converter . . . 117
6.6 Unloaded and Loaded Full-Scale voltage swing at the output of the DAC . . . 117
6.7 Input stage of the AQM for the In-phase path . . . 118

6.8 Feedback compensation of common-mode drift at the input of the AQM . . . 119
6.9 Phase and amplitude of the comparator gain, versus frequency 120
6.10 Phase and amplitude of the feedback loop gain between the pMOS and the comparator, versus frequency 121
6.11 Schematic of the feedback Op-amp comparator 122
6.12 Circuit for the analysis of the input resistance looking into node Y_a,(Y_b) . . . 122
6.13 Input stage with the linear-in-dB analog Gain-control stage using exponentially-sized resistor string 128
6.14 A single cell of the Gain (Attenuation) stage, showing the comparator and the resistor string 133
6.15 Tap voltages $V_{s,i}$ of the V_{control} resistor string 134
6.16 Variation of the Collector-Base junction capacitance C_{bc} with respect to V_{BC} 137
6.17 Simplified schematic showing critical nodes for DC-to-IF bandwidth analysis 139
6.18 Dividing the C_{be} capacitance to calculate equivalent capacitance at the internal node Ⓑ 140
6.19 Simplified operating principle of the Passive Current-Driven Mixer 141
6.20 Mixer nMOSFET switch ON resistance R_{ON} for different values of V_{GS} and V_{DS} 143
6.21 Impedance at the output of the Mixer looking back towards the source 144
6.22 Time varying conductance of the switches and its Thevenin equivalent circuit 145
6.23 Mixing function of the double-balanced mixer 148
6.24 Cross-sectional block diagram of the Isolated nMOS transistor showing the isolating Deep-Trench and the isolated Bulk 149
6.25 Small-signal representation of the Common-Base amplifier showing the output balun and the bias network. 152
6.26 Current division at the output of the attenuation stage impacting the overall current gain 154
6.27 Flicker noise during 'ON' overlap in the current-commutating switches 156
6.28 White noise transfer in the current-commutating switches 158
6.29 Single-phase illustration of a PPF cell 162
6.30 A single stage or Four-phase PPF network showing the positive and negative sequences 163
6.31 Simulated Image Rejection Ratio (dB) as a function of IQ phase and amplitude mismatch 166
6.32 Degradation of IRR due to process variations and mismatch 167
6.33 Illustration of the variation in zero-crossing due to finite rise-time 168
6.34 Illustration of the LO chain including the PPF network and the LO buffer-amplifiers 170
6.35 Concept of the voltage doubler showing the clamp 171
6.36 Circuit schematic of the voltage doubler 171
6.37 Voltage swing on the Gate and Source terminals of a switch in the passive Mixer 172
6.38 Common Base Output Stage and RF transformer at mid to high frequencies . 173
6.39 Network to calculate output current noise of the Common Base stage 175
6.40 Mixing and output buffer stages of the AQM 178
6.41 Lateral transformer RF characteristics 179

6.42 Differential voltage swing at the input of the I and Q pins of the AQM 181
6.43 Attenuator differential output voltage swing and Mixer differential input current 182
6.44 Variation of attenuator cell currents with control voltage 183
6.45 Variation of Mixer input common-mode voltage and switch V_{GS}, with respect to the control voltage $V_{control}$ 184
6.46 Mixer output current and quadrature LO voltage signals 185
6.47 Mixer input and output current waveforms 186
6.48 RF output voltage and current across the output impedance-matching resistor 187
6.49 S11 at the IF input port and LO port of the AQM and S22 at the RF output port 188
6.50 IF stage output power showing IF bandwidth 189
6.51 Output frequency sweep showing 1 dB RF bandwidth 189
6.52 OIP3, power gain, voltage gain, current gain and IIP3 for 50 MHz and 70 MHz input-tone frequencies 190
6.53 OIP3, power gain, voltage gain, current gain and IIP3 for 200 MHz and 220 MHz input-tone frequencies 190
6.54 OIP3, power gain, voltage gain, current gain and IIP3 for 350 MHz and 370 MHz input-tone frequencies 191
6.55 Accuracy and range of the power gain with respect to the control voltage ($F_{IF} = 200$ MHz) 192
6.56 Output NSD, single-tone output power and calculated dynamic range, with respect to the control voltage ($F_{IF} = 200$ MHz) 193
6.57 Output NSD, single-tone output power and calculated dynamic range, with respect to the DAC output current ($F_{IF} = 200$ MHz) 194
6.58 Output NSD, single-tone output power and calculated dynamic range, with respect to LO power sweep ($F_{IF} = 200$ MHz) 194
6.59 Output NSD, single-tone output power and calculated dynamic range, with respect to LO power sweep ($F_{IF} = 100$ MHz) 195
6.60 Output noise versus frequency for a DAC output current of 20 mApp, LO power = 0 dBm, $F_{IF} = 200$ MHz 195
6.61 Output noise versus frequency for a DAC output current of 5 mApp, LO power = 0 dBm, $F_{IF} = 200$ MHz 196
6.62 Output noise versus frequency for a DAC output current of 5 mApp, LO power = 0 dBm, $F_{IF} = 200$ MHz and control voltage = 0.0V, 2.0V and 4.5V 196
6.63 OIP3, power gain, voltage gain, current gain and IIP3 at 100 MHz, 120 MHz input tone frequencies, at control voltage = 0.0V, with respect to temperature 197
6.64 Power gain simulated at 0.0V control voltage, with respect to temperature. . 197
6.65 Distributions of performance parameters over 100 Monte-Carlo runs 198

B.1 IMD and CTB products from 3-tone input subject to 3rd order non-linearity 206
B.2 Non-linearity products from a six carrier input to 3rd order polynomial non-linearity 208
B.3 Cross Modulation (CMD) between GSM/EDGE and WCDMA carriers 210
B.4 Measured non-linear products from a Base Station RF small-signal chain . . . 211

List of Tables

1.1 Rendement de la station de base de la Figure 2.3 8

2.1 System-level efficiency for the Base Station of Figure 2.3 22

3.1 Paired bands in E-UTRA, UTRA and GSM/EDGE 30
3.2 A brief summary of typical transmitter architectures 33
3.3 Operator Downlink Spectrum Allocation for E-GSM900, France, 2008 41
3.4 Operator Downlink Spectrum Allocation for E-GSM1800, France, 2008 41

4.1 Comparison of Downlink R.M.S. EVM requirements for LTE, UMTS and GSM 50
4.2 Comparison of ACLR / ORFS values 73
4.3 Phase noise for frequency offsets < 10MHz 75
4.4 Simulated PAPR values for Downlink signals 81
4.5 RF parameters for Simultaneous Multi-Mode Tx derived from analysing EVM contributions 84

5.1 Integrated-Phase-noise and Jitter Calculation 102
5.2 Transmitter Performance Budgeting for six EDGE carriers 106

6.1 Summary of AQM performance requirements 110
6.2 AQM electrical performance requirements 111
6.3 Simulated design values for the passives of the 3-stage PPF 165
6.4 AQM primary noise contributions 177

C.1 Multi-mode DAC dynamic range requirements 213

Chapter 1

Introduction (en français)

1.1 Motivation

Dans les systèmes de télécommunication d'aujourd'hui, faire face aux besoins croissants d'information de l'utilisateur nécessite que les sous-systèmes du réseau soient améliorés périodiquement pour offrir de nouveaux services ainsi qu'une augmentation de la couverture du réseau et de leurs capacités. La demande des abonnés pour un débit plus élevé provient de l'utilisation d'applications telles que le streaming vidéo , la diffusion vidéo en ligne-jeux, les réseaux sociaux et la voix sur IP,sur des dispositifs tels que les téléphones intelligents et les tablettes.

Dans le cadre des améliorations afin d'optimiser le fonctionnement du réseau, les opérateurs télécom ont incorporés des degrés supplémentaires de multiplexage dans les anciennes normes, tels que le Multi-Carrier-GSM/EDGE (MC-GSM) et Multi -Carrier UMTS-WCDMA/HSPA (MC-WCDMA), pour leurs sous-systèmes station de base (BStn) . Ces nouvelles méthodes de multipexages des données utilisateurs permettent la distribution de ces données en de multiples canaux (ou supports) ce qui résulte d'un débit plus élevé. Parallèlement, les nouvelles technologies multi-porteuses/multi-canaux déployées dans les interfaces airs des nouveaux standards, tel que le LTE OFDM (Long Term Evolution), sont rapidement adoptées, dans le cadre de la 3.9G ≫ et au-delà des systèmes.

Envisagé dès le début des activités de normalisation de la 3G (version 99), le schéma de déploiement multi-porteuses (maintenant étendu aux systèmes 2G), a été proposé avec l'intention de satisfaire les besoins en mobilité et également les besoins de couverture réseau et de capacité. Les déploiements des réseaux multi-porteuses répond essentiellement au besoin d'augmentation de la capacité [1], et également à l'amélioration des services: couverture réseaux et management de la mobilité. L'adoption de ces techniques permet ainsi l'amélioration de la qualité de service (QoS) pour l'utilisateur final et permet d'alléger les contraintes au niveau du réseau. Cependant, il reste des défis implicites qui restent à traiter, au delà du niveau réseau, concernant la mobilité, l'inter-opérabilité, etc.

Les émetteurs des stations de base actuellement déployées (Figure 2.1) sont souvent multi-

[1] L'augmentation du nombre de porteuses d'une station de base augmente la capacité de la cellule en fonction du facteur de réutilisation des fréquences. Ceci va dans le sens d'une réduction des installations

standards, en ce qu'ils peuvent supporter différentes normes. Jusqu'à récemment, ceci était réalisé de deux manières: par la reconfiguration du matériel soit lors de l'installation du site (avec une reconfiguration en usine) ou bien par logiciels pour régler à distance la performance tandis que la station de base est en fonctionnement (définie par logiciel ou 'run-time reconfiguration' à distance). Ces deux méthodes nécessitent un certain degré d'intervention explicite qui est souvent coûteux, en s'ajoutant aux coûts de fonctionnement et de maintenance ('OpEx.') de la station de base . Tout matériel radio permettant la transmission et la réception simultanée des supports précités serait en mesure de fonctionner de manière quasi indépendante, nécessitant peu ou pas d'intervention autre que pour l'entretien.

Les nombreuses variantes des stations de base actuellement en service sont très fragmentés [1] dans les besoins qu'elles servent. Elles diffèrent selon les paramètres suivants:

- les types de porteuses cellulaires ou *modes* pris en charge
- le nombre de porteuses ou de canaux pris en charge
- les largeurs de bande et les fréquences de fonctionnement pris en charge
- les niveaux de puissance de sortie pris en charge, etc.

La convergence vers une solution d'émetteurs multi-porteuses et multi-technologies, qui répondent à plusieurs de ces aspects dans une seule solution, apporterait plusieurs avantages à l'opérateur. Ici, nous définissons un "¡émetteur convergent"¿ comme étant capable de transmettre *simultanément* plusieurs porteuses cellulaires différentes avec une seule plate-forme matérielle. Ceci permet donc une séparation de la problématique de l'interface air et la réalisation de l'implémentation matérielle, ce qui apparaît actuellement une demande fondamentale. Du point de vue matériel, passer de plusieurs cartes d'émetteurs-récepteurs spécifiques par porteuse à la réalisation d'une carte unifiée pour toutes les interfaces aériennes impliquerait un coût réduit du CapEx[2] pour les opérateurs, en plus d'une diminution des frais liés à l'immobiliers. L'efficacité énergétique serait potentiellement améliorée (réduction de l' OpEx [3]) en réduisant ou en réutilisant les blocs périphériques tels que les blocs d'alimentation (PSU), de refroidissement / ventilateurs etc. Les avantages au niveau du réseau suivent également. Avec une radio multi-standard, l'opérateur est en mesure de se concentrer sur d'autres goulets d'étranglement dans le système, tels que le réseau 'back-haul'. la gestion du site cellulaire, la mobilité de l'utilisateur, la transfert ('handover'), etc.

Les macro stations de base sont généralement classées en trois catégories [2] dans l'ordre croissant d'efficacité, basée sur le regroupement des unités de radio et de l'interface avec le matériel de traitement de bande de base de la station de base.

- Stations de base classiques
- Remote-Radio-Head stations de base

[2] Dépenses en capital.
[3] dépenses opérationnelles

- Active-Antenne-Réseau stations de base

Ces évolutions portent non seulement sur l'amélioration de l'efficacité du matériel, mais aussi sur la modification de l'architecture et le regroupement / partage des différentes fonctions sur une station de base. Au centre de toutes ces catégories, se trouve l'amplificateur de puissance dont la gestion détermine le rendement de la station de base. Les modules amplificateur de puissance multi-canaux (MCPA), capables de supporter une transmission simultanée multi-mode, sont en passe de devenir la norme dans les station de base contemporaines. L'amélioration de l'efficacité de ces modules MCPA leur permettra d'être placé à proximité de l'antenne, ce qui ainsi pourrait éliminer la nécessité d'un dispositif de combinaison de puissance éliminant alors les pertes associées. Cette avancée de la "Remote-Radio-Head" (RRH) [4] pour les stations de bases classiques résulte dans une diminution les pertes des câbles-RF de raccordement à l'unité d'antenne. Un intégration plus poussée des des modules amplificateurs et des transmetteurs, avec des solutions avancées pour les antennes, permettrait une solution consistant en une unité radio unique qui peut être dupliquée pour réaliser une réseau de traitement radio systolique connu sous le nom d' Antenne Réseau Active (AAA). Ces solutions sont étudiée pour l'évolution des futures stations de base. Dans ce travail, cependant, nous nous concentrons sur l'évolution de la RRH actuelle parce que les normes, à notre avis, n'ont pas encore suffisamment évoluée pour soutenir des solutions AAA.

1.2 Méthodologie

1.2.1 Objectifs et définition de la problématique

Un émetteur multi-mode offre plusieurs avantages au niveau du réseau par l'intermédiaire d'un contrôle transparent et souple entre les différents modes ou interfaces aériennes [5] entre autres choses, le tout à la lumière d'une expérience utilisateur améliorée. Les autres avantages pour l'opérateur comprennent [3]:-

1. la réduction des dépenses d'investissement par le remplacement de plusieurs unités avec du matériel tout-en-un, la réutilisation d'infrastructures de site existant pour le déploiement de nouveaux réseaux .

2. la réduction des dépenses d'exploitation au travers d'un effort de reconfiguration réduit , une réduction des coûts énergétiques et installation plus aisée lors de l'utilisation RRH/AAA .

3. l' utilisation flexible du spectre disponible via le déploiement de marqueterie de nouvelles technologies par exemple LTE et LTE-A.

[4] permet la réduction des pertes de puissance du signal RF dans les câbles servant de connexion entre l'amplificateur de puissance et le connecteur d'antenne.Ces pertes s'évaluent environ à 50% de la puissance ou 3 dB (macro-cellule, y compris alimentation, cavalier et connecteurs). Avec le RRH, l'amplificateur de puissance (à savoir, l'émetteur-récepteur) se rapproche de l'antenne, de sorte que les pertes du câble sont essentiellement limitées à la seule perte de connecteur. Cela facilite également l'utilisation d'antennes actives pour lesquelles les mécanismes d'inclinaison électriques bruyantes d'antennes passives sont évités.

[5] Cela permet une meilleure gestion de la capacité par répartition de la charge et sans doute facilite les transferts en raison de une meilleure coordination des interférences.

4. l'évolutivité des réseaux en rendant la technologie indépendante de l'opération.

Le découplage du *mode* de fonctionnement du matériel permet à ces avantages à être facilement étendu également aux "¡OEM" (Original Equipment Manufacturers) et aux opérateurs qui peuvent par conséquent se concentrer sur la gestion et l'entretien d'autres goulets d'étranglement dans le système de réseau, au lieu de la RAN (Radio Access Network). Cependant, il y a d'autres défis en fonctionnement, telles que la charge accrue sur la performance du traitement numérique du signal et de la bande de base,[6] unités qui seront abordés dans les chapitres suivants.

Avec l'évolution des normes 3GPP vers un fonctionnement multi-standard et multi-support, nous revisitons l'architecture de l'émetteur traditionnel de la station de base macro-cellulaire en envisageant une solution matérielle unique. Les futures RAN (Radio Access Network) mis en œuvre sont susceptibles d'être basés sur des stations de base capables de supporter la plupart ou toutes les technologies d'interface aérienne en place en même temps que les technologies entrantes (LTE/4G), le tout dans une unité de radio unique. Il s'agit d'un écart important par rapport aux implémentations existantes de l'unité de radio. Ceci permet de capitaliser sur la base et l'infrastructure des 2G (GSM/EDGE), systèmes matures mais saturés, ainsi que sur la base du système 3G (WCDMA/HSPA).Cette étude de cas sera abordée dans les premiers chapitres de cette thèse, où nous présentons également une brève introduction aux scénarios existants. Avec l'augmentation des contributions à l' empreinte carbone globale du sous-système RAN [4], des solutions écologiques permettant l'amélioration du rendement énergétiques sont sollicitées. Le but est donc d'avoir une meilleure efficacité énergétique pour la plate-forme unifiée. Afin d'identifier la faisabilité de la transmission multi-mode, ce rapport présente les discussions et les délibérations sur la base des approximations de premier ordre pour la conception de système d'une telle chaîne RF.

Le fonctionnement simultané de plusieurs normes sur les résultats matérielles partagées dans plusieurs exigences strictes sur la performance de la multi-mode RF-émetteur. L'analyse de quelques paramètres ou indicateurs en particulier (par exemple, Erreur-Vector-Magnitude ou EVM , Alternate/Adjacent Channel Leakage Ratio ou ACLR et les émissions spectrales masque ou SEM), tels que définis par les normes, permet aux concepteurs de systèmes de traduire les exigences au niveau du système en des spécifications de performance de niveau de bloc. En analysant les contributions des distortions des différentes fonctions électroniques sur la qualité de modulation (EVM) et les remontées spectrales (par exemple ACLR), il est possible de définir les exigences de performance chaque sous circuit individuellement (comme le bruit de phase, l' IP3, le déséquilibre du modulateur I/Q, du facteur de bruit, etc.). Dans cette analyse, nous proposons également méthodologie pour une meilleure répartition des performances entre les différents blocs analogiques de la chaîne. Ces analyses sont basées sur des

[6] Par exemple, l'ordre de grandeur de l'effort de calcul pour la réduction de PAPR des signaux 5 MHz LTE est de l'ordre de centaines de plusieurs MOps./sec et varie en fonction de la technologie de l'interface air. Avec un DSP FPGA fonctionnant à 4,0 GMAC/mW, ces opérations impliquent une consommation d'énergie de dizaines de milli-watts pour juste cette réduction de PAPR réduction. La réduction su PAPR pour les applications multi-modes avec une pré distortion numérique (DPD) sont susceptibles de nécessiter encore plus de capacité de calcul, exigeant alors un budget de puissance plus élevée pour le coeur du DSP. La dissipations de puissance pour les périphériques ne sont pas inclus dans ce calcul et seront à considérer avec, en plus, plusieurs calculs supplémentaires concernant le traitement du signal.

contributions de premier ordre (distorsions non-linéaires, le bruit de phase, les déséquilibres IQ, le bruit additif, etc.) de chaque bloc dans une chaîne classique de transmission.

Les réseaux peuvent être rendus plus efficaces:

1. avec du matériel radio plus efficace
2. en améliorant la gestion de la charge et de traitement en bande de base
3. en réalisant des améliorations au niveau du réseau pour soutenir les évolutions des stations de base
4. en concentrant ou compactant les réseaux cellulaires

En outre, l'efficacité de la radio devra être étroitement associée à des évolutions du niveau réseau et du niveau du système. Nous observons qu'il y a aussi des problèmes de mise en œuvre au niveau du système qui doivent évoluer avec la radio pour devenir multi-standard: nous citerons ici la réduction du facteur de crête, l'atténuation des interférences entre porteuses, le contrôle de la puissance des porteuses. Bien que les questions de niveau de réseau sont au-delà de la portée de ce travail, nous présentons quelques-uns des problèmes pour un souci d'exhaustivité.

1.2.2 L'Efficacité énergétique

Dans le contexte des systèmes de radio optimisés en termes de rendement, l'objectif principal de ce travail est d'identifier les spécifications de performances pour une chaîne d'émetteur qui est capable d'effectuer plusieurs transmissions multi-standards simultanément, footnote label Dossier d:optimisedpowerefficiency Les paramètres de l'efficacité énergétique seront définis avec plus de précision à un stade ultérieur tout en améliorant la répartitions des spécifications des performances entre les différents blocs qui constituent un émetteur. L'illustration de la Figure 2.2 montre les différents composants d'une carte radio.

Considérons le bilan de puissance d'une macro-cellule 6 émetteur-récepteur à 6 porteuses (2/2/2 [7] UMTS WCDMA)-BStn [5] présentée sur la Figure 2.3, avec 20 W de puissance de sortie par porteuse.

La consommation d'énergie de la station de base peut varier jusqu'à un facteur deux, en fonction des conditions de chargement et les mécanismes de gestion dynamique de la puissance (par exemple transmission discontinue ou de DTX, WCDMA et LTE), incorporés dans les différentes technologies d'accès cellulaire. Les mécanismes de contrôle de la puissance de la porteuse jouent un rôle important dans la détermination des caractéristiques de performance et sont brièvement abordées dans ce travail. Fait intéressant, l'efficacité de la MCPA est optimisée pour les périodes de charge élevée lorsque le débit de la cellule doit être à son plus haut, offrant des rendements aussi élevés que 40%, pouvant diminuer jusqu'à 10% pour 10% de charge.

Bien que l'exemple cité ci dessus n'est pas récent, les chiffres sont encore représentatifs d'un grand nombre de stations de base qui sont actuellement opérationnelles. Le tableau 2.1 résume brièvement l'efficacité énergétique de la station de base et montre que l'amélioration

[7] 3-secteurs avec 2 porteuses par secteur, Alcatel-Lucent, 2006

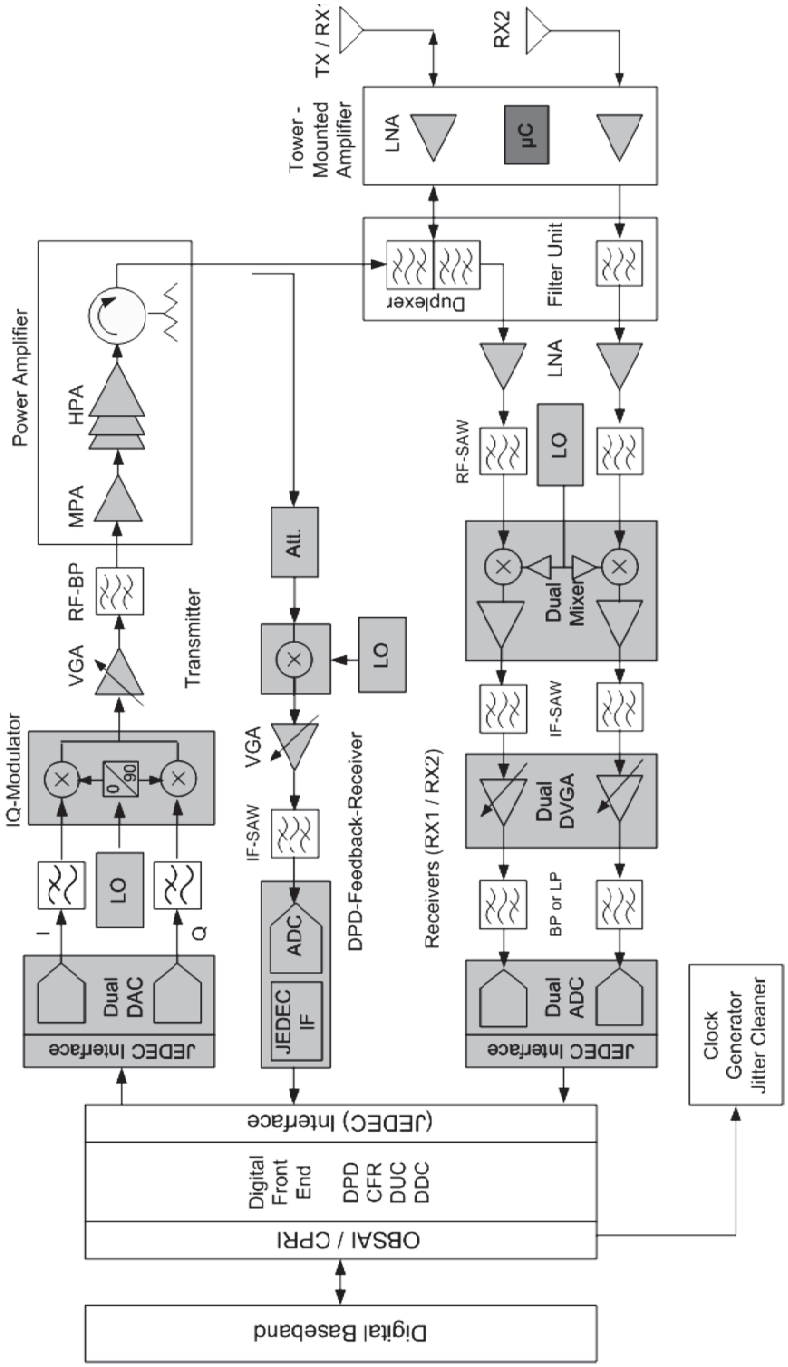

Figure 1.1: Schéma de principe d'une station de base typique contemporain carte d'émetteur-récepteur (*Permission: NXP Semiconductors*)

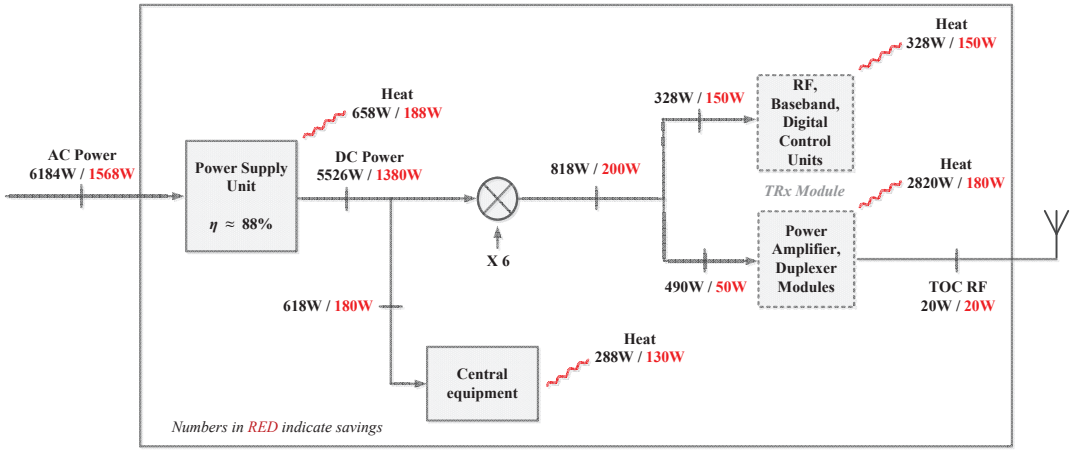

Figure 1.2: Bilan de puissance dans une station de base UMTS 2/2/2. Les chiffres en rouge indiquent des améliorations sur les valeurs précédentes, indiquées en noir, à la suite des innovations en matière d'architecture et de design.

du rendement de l'amplificateur de puissance (PA) se traduit par des améliorations marginales sur le rendement global du RAN. Une des principales raisons à cela est que toute puissance qui n'est pas convertie en énergie rayonnée est considérée comme un gaspillage. Ce raisonnement s'applique en particulier à l'équipement périphérique et le traitement en bande de base qui constituent une grande partie du bilan de puissance derrière l'émetteur (Tx), qui n'est pas directement convertie en énergie RF. Quand la puissance de sortie de la station de base est augmentée, le budget de puissance du module PA devient plus important que celui du traitement en bande de base et l'amélioration du rendement de ce module amène une amélioration de l'efficacité globale de la station de base. Cependant, les progrès récents dans les solutions à réseau d'antennes (AAA) qui nécessitent des modules amplificateurs à faible puissance de sortie, a reporté la problématique de rendement sur la partie numérique et la partie petit signal [8] du module RF.

Il existe plusieurs modèles complexes décrivant la consommation d'énergie des stations de base, (voir [4, 6]). Cependant, nous n'approfondirons pas le sujet dans ce travail. Si nous exprimons le rendement de la station de base comme étant simplement le rapport de la puissance RF transmise à la puissance d'alimentation secteur, l'inefficacité frappant la station de base est facilement perceptible, en raison de la faible fraction de puissance effectivement transmise par l'interface air. Si l'on se réfère au tableau 2.1 nous observons que l'efficacité globale de la station de base n'est que marginalement améliorée malgré une nette amélioration du rendement de l'amplificateur de puissance. Des améliorations importantes seraient possibles si l'architecture de la station de base elle-même était revue et améliorée.

[8] Il s'agit de la partie de la chaîne de l'émetteur-récepteur analogique/RF qui se trouve entre le CAN/CNA et le module amplificateur de puissance/amplificateur faible bruit.

Table 1.1: Rendement de la station de base de la Figure 2.3

Dissipation de chaleur	
Base Station	$6184W - (6 * 20W) - 330W = 5734W$
PA RF Path	$(490W - 20W) * 6 = 2820W$
Rendement	
Rendement utile du module PA	$20W/490W = 4\%$
Rendement global	$(6 * 20W)/6184W = 1.9\%$
Rendement amélioré	$(6 * 20W)/1568W = 7\%$

C'est l'objet des méthodologies RRH [9] et AAA mentionnées plus tôt.

Le sous-système station de base est qu'un composant du réseau complet de communication sans fils, comme illustré à la Figure 2.4. Il ya plusieurs goulets d'étranglement au niveau des divers sous-systèmes dans le scénario présenté. Par exemple, les antennes actuelles avec leur diagramme de rayonnement peu directifs et non optimisés conduisent à un gaspillage considérable d'énergie. Cette question est abordée dans les systèmes AAA où la directivité et la puissance du faisceaux d'antennes sont contrôlés de manière adaptative en utilisant des éléments de phase cohérente, afin d'obtenir les diagrammes de rayonnement spécifiques à l'utilisateur ou à une région.

Au vue de la figure 2.5, il est évident que les stations de base (en particulier les macro-cellules) sont responsables de plus de 90% de la consommation d'énergie dans les RAN, principalement en raison de leur faible rendement, phénomène exacerbé par leurs déploiements en grand nombre. L'impact des technologies de l'information et des communications sur l'empreinte carbone humaine a été le sujet de plusieurs travaux récents (voir [7, 8]). Pour cette raison, le sujet de ce travail est limitée à l'analyse de la partie émission radio (TX) de la station de base.

Comme indiqué précédemment (voir la section **??**), il y a plusieurs endroits où des améliorations en matière de rendement du RAN peuvent être explorées, simultanément avec l'amélioration du réseau lui-même. Certains procédés comprennent:

- **BStn RAN matériel**
  - Des amplificateur de puissance Multi-Band, Multi-Canaux avec l'utilisation d'algorithmes avancés de traitement du signal (pré-distorsion, réduction du facteur crête ou crest-factor-reduction)
  - Un haut degré de coordination entre la radio analogique et le traitement numérique du signal
  - **Une chaine de transmission RF petit signal à forte dynamique et multi-standard**

[9] Dans la RRH en particulier, d'importantes économies d'énergie sont obtenues en plaçant le module radio refroidi par air directement sur le mât, ce qui élimine la perte (-3 dB) du câble d'alimentation RF. La puissance délivrée l'amplificateur de puissance est réduite de moitié, ce qui élimine le besoin de ventilateurs de refroidissement puissants et également le besoin de climatisation pour le rack.

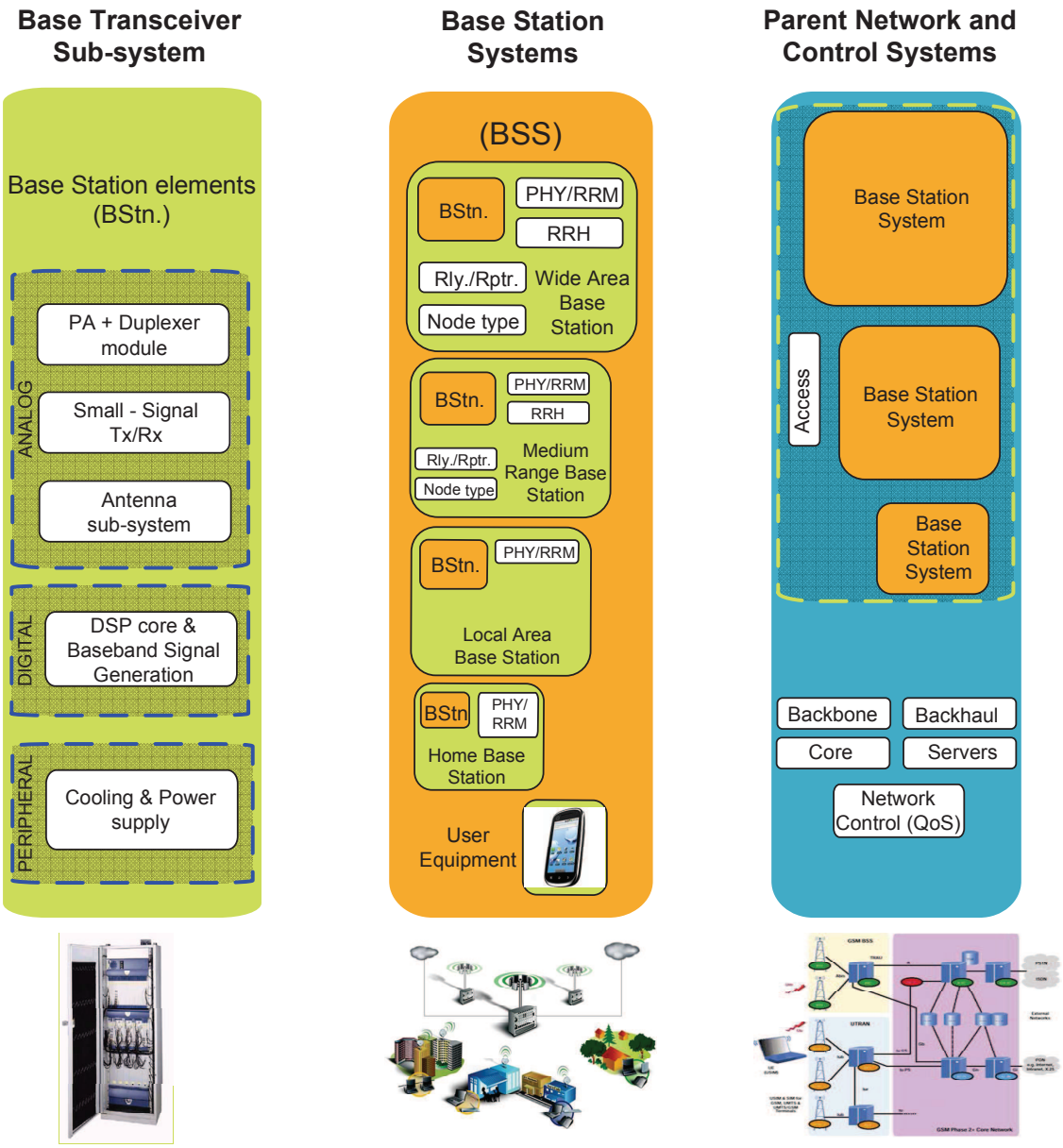

Figure 1.3: Hiérarchie du système des Stations de Base.

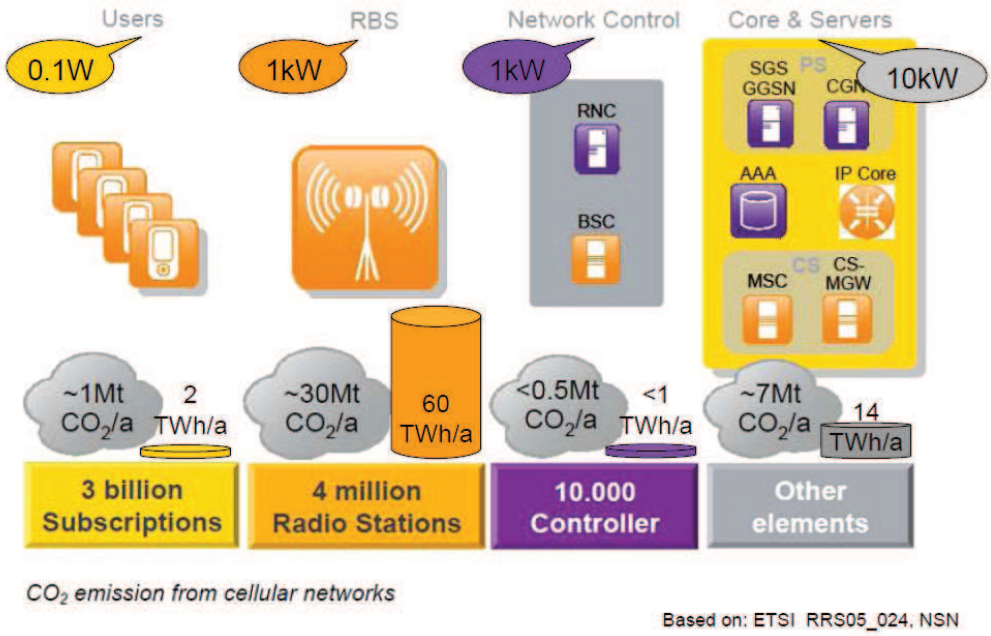

Figure 1.4: Consommation mondiale d'énergie des systèmes de communication mobile

- Des ASIC fonctionnant à fréquence élevées, consommant une faible puissance pour réduire la consommation d'énergie en bande de base
- Un système d'antennes adaptatif (actif et reconfigurable)

- **Optimisation de la cellule**
  - Un compactage de la taille de la cellule, avec une meilleure coordination entre les cellules
  - Une gestion coopérative des interférences entre les cellules, avec le partage des ressources
  - L'utilisation de spectre revu, ce qui implique la co-implantation de sites cellulaires

- **Adaptation dynamique de la charge**
  - La gestion automatique de la reconfiguration du réseau: SON (Self-Organising-Network)
  - Le déploiement de réseaux hétérogènes (i.e., Macro-cellules , Femto-cellules et Pico-cellules)
  - l'adaptation dynamique de puissance d'alimentation de l'amplificateur de puissance en fonction de la charge

Plusieurs de ces caractéristiques commencent à être prises en charge par les nouvelles normes d'accès, permettant un potentiel considérable pour la réduction de la consommation d'énergie. Alors que la plupart des optimisations au niveau du réseau adressent également la problématique du rendement, celles-ci portent principalement sur les goulets d'étranglement au niveau des performances qui apparaissent avec l'augmentation des débits.

D'un point de vue purement électronique, le potentiel important de réduction de la puissance est vu dans le domaine des amplificateurs de puissance pour les macro-cellules. C'est également le cas pour les émetteurs-récepteurs et circuits en bande de base pour les applications de pico-et femto-cellules, [10] qui sont de plus en plus utilisées et implantées.

Bien que ce travail est dédié aux macro-cellules, les méthodes développées pour l'analyse sont tout aussi pertinentes pour les variantes les plus compactes. Toutefois, l'amélioration de la performance au niveau composant pour un rendement plus élevé n'a que peu d'impact sur le rendement global de la station de base (voir la figure 2.1), indiquant la nécessité d'innovations au niveau de l'architecture. Parmi les autres méthodes pour l'amélioration du rendement, nous trouvons les faisceaux multi-antennes, MIMO , une meilleure sectorisation de l'antenne [9] et les technologies d'amplificateurs de puissance avec un meilleur rendement, tels que l'amplificateur commuté (Switched Power Amplifier Mode ou SMPA), le Doherty à N voies couplé avec une pré-distorsion adaptative (DPD), la technique du suivi d'envelope ou Envelope Tracking(ET) etc. Ceux-ci sont progressivement intégrées pour améliorer l'efficacité au niveau du bloc ciblant une performance de niveau système amélioré. La future station de base bénéficiera certainement de ces fonctionnalités pour fournir des services nouveaux et améliorés tout en fonctionnant de manière économique et écologique. Pour des contraintes de temps, ce travail a une portée limitée au seul émetteur de la radio.

Dans ce travail, nous limitons notre attention seulement à la radio et en particulier, l'émetteur dans la configuration FDD. La puissance consommée par chaque sous circuit de cette partie radio peut être analysée. Le graphique de la figure 2.6 résume les contributions en pourcentage des divers composants des différentes variantes des stations de base: macro, micro, pico, femto et RRH.

Parmi les différents sous-blocs de radio, l'amplificateur de puissance est le plus gourmand en énergie. Les solutions actuelles et futures pour l'amplification de puissance sont non linéaires et doivent être soutenues par des mécanismes de pré-distorsion qui modifient les caractéristiques du signal de telle sorte que le signal résultant de l'amplificateur non linéaires soit dans le respect des contraintes des émissions parasites et de distorsion. Pour que les mécanismes de pré-distorsion fonctionnent correctement, il est impératif que la partie de la chaîne d'émission qui se trouve entre la sortie de bande de base et l'entrée de l'amplificateur de puissance soit à la fois linéaire et une importante plage de dynamique, notamment lorsque les mécanismes de commande de puissance sont prises en compte, ce que nous verrons ultérieurement. Nous revisitons l'architecture de cette partie de la chaîne afin d'identifier les compromis de conception qui peuvent être mieux optimisées en éliminant les divers points bloquants au niveau performance.

[10] Les Pico- et femto-cellules sont des variantes compactes des stations de base qui couvrent en terme de portée des zones beaucoup plus petites, comme un étage de bureaux ou une maison.

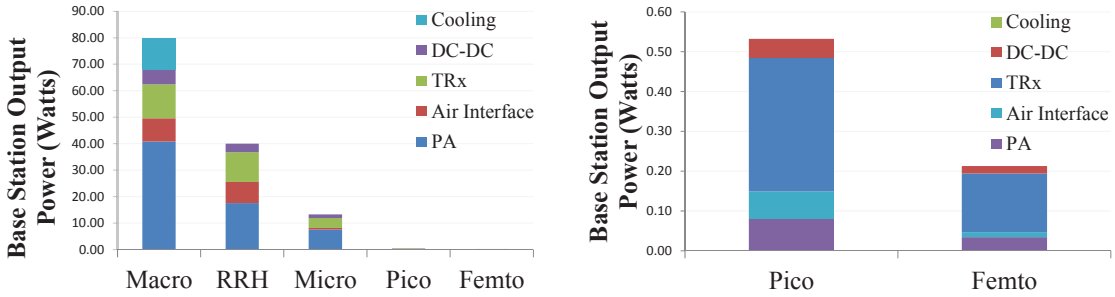

Figure 1.5: Répartition de la consommation d'énergie dans l'émetteur-récepteur radio pour les différentes variantes de Station de Base (*Permission: EARTH FP7-IP Project, 2010*)

1.2.3 Organisation de la thèse

La thèse est structurée de la manière suivante. Pour imaginer un émetteur multi-mode et multi-bande pour un proche avenir, nous commençons par analyser si un tel scénario est possible ou, en paraphrasant, en identifiant un *scénario utilisateur*. Les scénarios Multi-mode, multi-bandes n'existent pas aujourd'hui et ils dépendent directement de la configuration implémentée par les opérateurs, de l'allocation des fréquences et de l'optimisation du réseau, dont certains sont au-delà de la portée de ce travail bien qu'ils aient un impact significatif sur l'analyse du système. Dans le chapitre 3 nous décrivons un scénario d'utilisation d'un tel système multi-standard convergent, tout en montrant ses impacts au niveau du réseau. Une fois que les contraintes au niveau de l'écosystème [11] [10] de ce cas d'utilisation sont établis, les spécifications de performance de l'émetteur 3GPP - SEM, EVM, ACLR, contrôle de puissance, co-existence etc., correspondant aux différents modes peuvent alors être identifiés et rassemblés dans un cahier des charges unique pour l'émetteur multi-standard.

Dans les chapitres suivants, nous soulignons certains des défis techniques dans le cadre de la mise en œuvre d'un front-end RF pour un tel émetteur convergent multi-mode ou de technologie d'accès multi-Radio (Multi-RAT) pour la Liaison-Descendante (DL). L'exploitation d'un émetteur unique implique des exigences de performance très strictes durcissant le bilan de puissance. Dans le chapitre 4 nous nous occupons de l'analyse des besoins de performance et de traduire les spécifications du niveau système, rassemblées dans les spécifications matérielles, au niveau des composants pour la chaîne de transmission. Les hypothèses prises pour ce travail sont indiquées. Le chapitre 5 porte sur l'analyse de l'architecture et du bilan de la budgétisation des performances issues de nos spécifications. Ici, nous développons des mécanismes de répartition des performances basées sur les spécifications du système et proposons également des méthodes pour intégrer les fonctions d'objectif dans le processus. Ce travail n'inclut pas d'analyse détaillée du module amplificateur de puissance, ce bloc étant le plus consommant d'énergie dans l'émetteur, plusieurs hypothèses raisonnables seront faites

[11] Co-existence, géographique, topologique (TDD/FDD), etc.

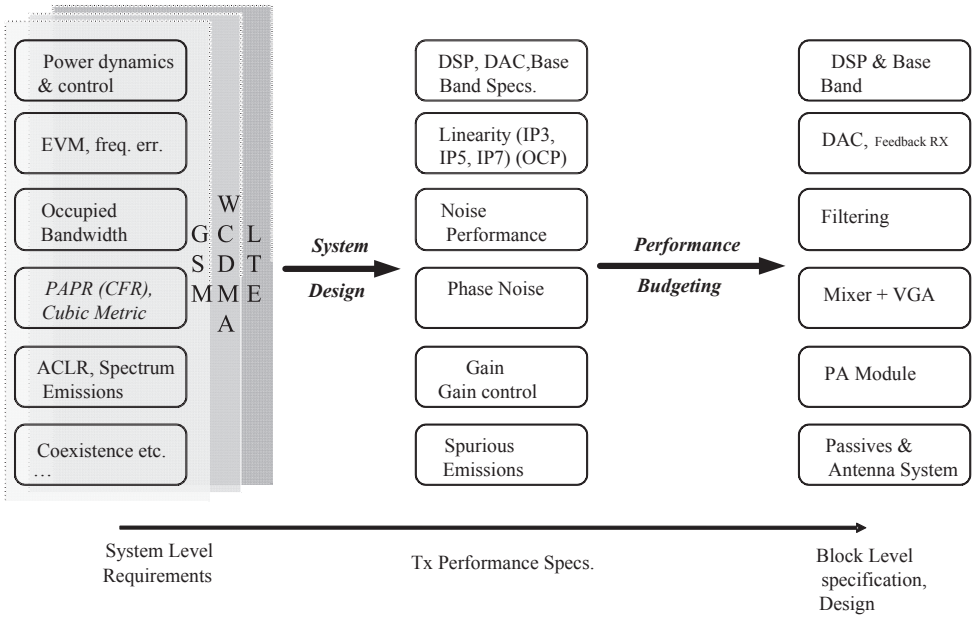

Figure 1.6: Méthodologie de l'analyse

pour analyser sa contribution sur les performances de la chaîne d'émission complète. Comme nous le voyons sur la figure 2.6, la question commune parmi les variantes des stations de base reste la performance de l'émetteur-récepteur (à l'exclusion de l'amplificateur de puissance) et des composants en bande de base, ce qui rend l'analyse du seul module émetteur-récepteur pertinent.

Dans le chapitre 5 la question cruciale du contrôle de puissance dans la transmission multi-standard simultanée est mis en avant en soulignant la limitation de la plage dynamique du convertisseur numérique-analogique (CAN). Dans le chapitre 6, nous nous occupons de la conception su modulateur analogique en quadrature multi-mode avec contrôle dynamique de la puissance, comme une solution possible pour la question du contrôle de puissance dans une transmission multi-standard. Plusieurs aspects de la conception sont discutés, avec la mise en évidence des compromis de performance et des contributeurs qui ont un impact au niveau du système. Les résultats de simulation de la conception en SiGe BiCMOS sont également présentés. Le chapitre finale 6.11 résume les conclusions et conclut en établissant le cadre pour la poursuite des travaux.

1.3 Contributions

Bien qu'il y ait eu récemment des efforts importantes réalisés dans les domaines mis en évidence précédemment (voir la section 2.2.2), peu de travaux ont portés sur l'analyse et la prise en compte des défis liés à la transmission simultanée de porteuses multi-mode

dans les stations de base. Les contributions de cette thèse sont divisés en trois parties. Dans la première partie, nous présentons une analyse étape par étape de la traduction des spécifications 3GPP, dans les critères de performance pour une macro-cellule multi-mode Tx. L'accent est mis sur la linéarité (avec un point de recul ou Input-Back-Off (IBO) raisonnable), le bruit de phase, le plancher de bruit large bande et les effets de déséquilibre IQ . La deuxième partie de l'ouvrage traite de la budgétisation des performances où les critères issus de la partie précédente sont répartis entre les différents sous-circuits Tx. Dans la troisième partie, nous résumons notre analyse du point bloquant de la plage de dynamique de l'émetteur multi-mode et nous présentons comme solution possible à ce problème la conception du modulateur analogique en quadrature (AQM) à gain variable, en technologie SiGe BiCMOS.

Les publications suivantes ont pu être réalisées dans le contexte de ce travail:

Conferences

[11]: **S. Kowlgi** and C. Berland, "Linearity considerations for multi-standard cellular Base-Station transmitters," in Proceedings of the 41st IEEE European Microwave Conference (EuMC), Manchester, October 2011, pp. 226-229.

[12]: **S. Kowlgi**, P. Mattheijssen, B. Corinne, and T. Ridgers, "EVM considerations for convergent multi-standard cellular Base-Station transmitters," in Proceedings of the 22nd IEEE Personal Indoor Mobile Radio Communications Conference (PIMRC), Toronto, September 2011.

Articles and Letters

[13]: S. Kowlgi, P. Mattheijssen, C. Berland and T. Ridgers, "System level considerations for convergent GSM/EDGE/WCDMA/LTE multi-standard Base-Station RF transmitters," IEEE Circuits and Systems Magazine. *In preparation.*

[14]: S. Kowlgi, L. Gambus, T. Ridgers, and C. Berland, "Design of a DC-300MHz Passive Current-driven Quadrature Modulator with 24dB attenuation range with ± 0.5 dB accuracy, 1.5 dB power gain and > 24 dBm IIP3, in SiGe BiCMOS," Electronic Letters. *In preparation.*

Invited Presentations and Internal Technical reports

[10]: **S. Kowlgi**, "Multi-mode GSM/WCDMA/LTE Base Station Transmitter: System level requirements analysis," PANAMA Project, Tech. Rep., June 2010.

[15]: **S. Kowlgi**, "System level considerations for Multi-mode Base-Station transmitter design", PAR4CR Project, Presentation, Technical University of Eindhoven, Eindhoven, July 2010 and April 2011.

Chapter 2

Introduction

2.1 Motivation

In today's telecommunication systems, coping with growing informational needs from the user requires network subsystems to be periodically ameliorated to provide new services alongside improved network coverage and capacity. The increasing subscriber demand for higher throughput stems from data intensive user-applications such as video streaming, video broadcasting, online-gaming, social networking and voice-over-IP among others, via devices like smart-phones and tablets.

As part of the enhancements to optimize network operation, telecom operators have been incorporating additional degrees of multiplexing in relatively older standards, such as Multi-Carrier-GSM/EDGE (MC-GSM) and Multi-Carrier UMTS-WCDMA/HSPA (MC-WCDMA), into their Base Station (BStn) subsystems. These relatively new multiplexing methods allow user data to be distributed into multiple channels (or Carriers) resulting in a higher throughput for the user. Alongside, new multi-carrier/multi-channel technologies such as the OFDM based LTE (Long Term Evolution) air-interface standard are being quickly adopted, as part of the 3.9G 'and beyond' systems.

Envisioned from the start of the 3G (release 99) standardization activities, the multi-carrier deployment scheme (now extended also to 2G systems), was proposed with an intention to satisfy not only mobility but also coverage and capacity management requirements. Most multi-carrier deployments address network capacity[1] augmentations, although some also cater service-improvement needs. This caters to enhanced coverage and mobility-management schemes. Adopting such techniques improves the Quality of Service (QoS) for the end-user and even alleviates some of the network level issues. However, there are implicit implementation challenges besides the network level issues of handover, mobility, inter-operability etc., that remain to be addressed.

Contemporary BStn transmitters (Figure 2.1) are often multi-standard, in that they can support different air-interface standards. Until recently, this was being achieved in two ways: through reconfiguration of the hardware either during installation of the cell-site (factory

[1] Increasing the number of carriers in a BStn increases cell capacity depends on the frequency re-use factor and results in an overall reduction in the number of installations.

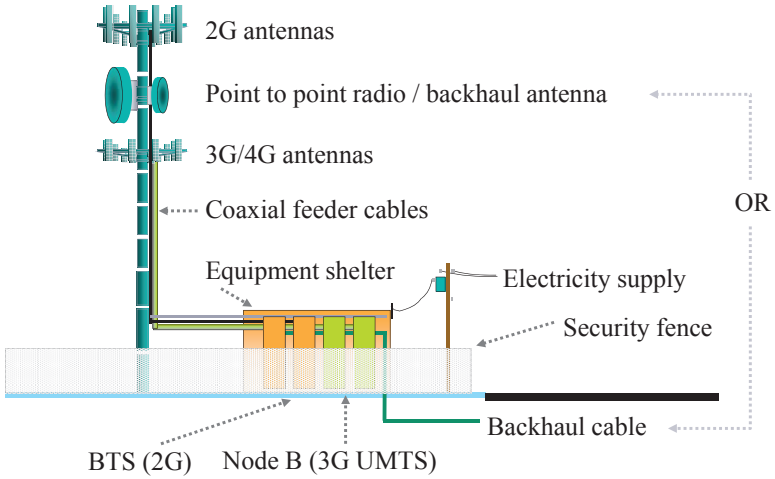

Figure 2.1: Traditional Base Station sub-system supporting 2G and 3G/4G (*Courtesy: NXP Semiconductors*)

reconfiguration), by using software to remotely adjust its performance while the BStn is in operation (software defined or run-time remote reconfiguration). Both these methods require some degree of explicit intervention which is often expensive, adding to the maintenance/operational costs (Opex.) of the BStn. Any radio hardware that fully supports simultaneous transmission and reception of the aforementioned carriers would be able to operate almost independently, requiring little or no intervention other than for maintenance.

The numerous variants of BStns currently in operation are highly fragmented [1] in the needs they serve. They differ with respect to

- the types of cellular carriers or *modes* supported
- the number of carriers or channels supported
- the bandwidths and operational frequencies supported
- carrier output power levels supported, etc.

Operating convergent multi-carrier, multi-technology transmitters that align several of these aspects into a single solution, would bring several benefits to the operator. Here, we establish a 'convergent' transmitter as that which is capable of *simultaneously* transmitting varied and multiple cellular carriers on a single hardware platform. This is in effect a decoupling of the air-interface Standard from the hardware-implementation which is emerging as a prominent requirement. From this hardware perspective, shrinking from several carrier specific transceiver cards to a unified card for all air-interfaces would imply a lowered cost of ownership CapEX[2] besides deflated real-estate related costs. Power efficiency is po-

[2]Capital Expenditure

tentially improved (reduced OpEX[3]) by reducing or reusing the peripheral blocks such as the power supply units (PUS), cooling/fans etc. Network level benefits also follow. With a multi-standard radio, the operator is able to focus on other bottlenecks in the system, such as the network back-haul. Cell-site management, user mobility, hand-overs etc. are also made efficient.

Macro BStns are typically arranged into three categories [2] in increasing order of efficiency, based on grouping of the radio units and the interfacing to the Baseband processing hardware of the BStn.

- Classic Base Stations
- Remote-Radio-Head Base Stations
- Active-Antenna-Array Base Stations

These evolutions focus not only on improving unit hardware efficiency, but also changing the architecture and grouping/sharing of the various functions on a BStn. Central to all of these categories, is the Power-Amplifier and how it is manipulated that determines how efficient the BStn is. Multi-Channel Power Amplifier (MCPA) modules, which are capable of supporting simultaneous multi-mode transmission, are fast becoming the standard in contemporary BStns. Improving efficiencies of the MCPA modules allow them to be placed close to the antenna, thereby potentially eliminating the need for the power combiner and the losses associated with it. This aligns with the now established Remote-Radio-Head (RH)[4] evolution moving forward from classic BStns where the RF-cable losses previously connecting the PA to the Antenna unit, are consequently diminished. Further integration of PA modules and transceivers allow them to be tightly integrated together with advanced antenna solutions resulting in a single radio unit that can be reproduced to create a systolic radio-processing-array known as the Active-Antenna-Array (AA). Such solutions are quickly gaining favour as the future evolution of BStns. In this work however, we focus on the current RH evolution because the standards, in our opinion, have not yet fully evolved to support AA solutions.

2.2 Methodology

2.2.1 Objectives and Problem Definition

A multi-mode transmitter offers several network level benefits via seamless and flexible control between the different modes or air-interfaces [5] among other things, all in the light of an improved user experience. Other Operator benefits include [3]:

[3] Operational Expenditure

[4] RH reduces the loss in signal power at RF, in the combiners and the feeder-cable between power amplifier and antenna connector. Typically feeder-cable losses amount to around 50% or 3dB (macro-cell, including feeder, jumper and connectors). With RH the power amplifier (i.e. the transceiver) moves closer to the antenna, so that cable loss is essentially restricted to only the connector loss. This also facilitates active antennas whereby the noisy electrical tilt mechanisms of passive antennas are avoided.

[5] This allows better capacity management via improved load distribution and arguably easier hand-offs owing to better interference coordination.

1. Reduced Cape by replacing multiple units with all-in-one hardware, reusing existing site infrastructure for new network deployment.

2. Reduced Opec due to smaller footprints, reduced reconfiguration effort, reduced energy costs, easy installation when using RRH/AAA.

3. Flexible use of available spectrum via inlay deployment of new technologies e.g LTE and LTE-A.

4. Future-proofing networks by making operation technology-agnostic.

Decoupling the *mode* from the hardware allows these benefits to be easily extended also to OEMS (Original Equipment Manufacturers) and Operators who can consequently focus on the management and servicing of other bottlenecks in the network system, instead of the RAN (Radio Access Network). Simultaneously however, there are also challenges in operation, such as the increased burden on the performance of the digital signal processing and baseband[6] units that will be touched upon in the following chapters.

With the 3GPP standards evolving towards multi-standard, multi-carrier operation, we revisit the architecture of the traditional Macro-cell BStn transmitter, envisioning one such single-hardware solution. Future RAN (Radio Access Network) implementations are likely to be based on BStns capable of supporting most or all of the incumbent air-interface technologies concurrently with incoming technologies (LTE/4G), all within a single radio unit. This is a significant departure from existing radio unit implementations. It allows capitalizing on the existing subscriber base and infrastructure of the mature but saturating 2G (GSM/EDGE) systems and also the growing 3G (WCDMA/HSPA) systems worldwide. The case for this will be elaborated in the first few chapters of this thesis, where we also present a brief introduction to the existing scenario(s). With increasing contributions to the global human carbon footprint from the RAN subsystem [4], energy-efficiency enhanced eco-friendly solutions are solicited. The goal is therefore to have improved power efficiency for the unified platform. In order to identify the feasibility of multi-mode transmission, this report presents discussions and deliberations based on first-order approximations for system design of such an RF chain.

The concurrent operation of multiple standards on shared hardware results in several stringent requirements on the performance of the multi-mode RF-transmitter. The analysis of a few parameters or metrics in particular (e.g. Error-Vector-Magnitude or EVM, Adjacent/Alternate Channel Leakage Ratio or ACLR and Spectral Emissions Mask or SEM), as set by the standards, allows system designers to translate system level requirements into block level performance specifications. By analyzing the block level contributions to distortions in the modulation quality (EVM) and spectral leakage (e.g. ACLR), it is possible to derive individual block level performance requirements (e.g. phase noise, IP3, IQ imbalance, noise

[6]For example, the approximate computation effort for PAPR reduction for 5MHz LTE signals is of the order of hundreds of several Mops./s and varies with the air-interface technology. With typical DSP FUGA rated at roughly 4.0GMACs/mW, this implies a power consumption of tens of millie-Watts for PAPR-reduction alone. Multi-mode PAPR reduction together with PA Digital Pre-Distortion (DPD) are likely to be more computation intensive, demanding a higher power budget for the DSP core. Power dissipations for peripheral devices is not included in this calculation and will be in addition to several other signal manipulation computations.

factor etc.). In this analysis, we also suggest a mechanism for better performance budgeting among the various analog blocks in the chain. These analyses are based on first-order contributions (non-linear distortions, phase noise, IQ imbalances, additive noise etc.) from each block in a typical transmission chain.

Networks can be made more efficient by

1. Making radio hardware efficient
2. Improving load management and baseband processing
3. Making backhaul and network-level enhancements to support BStn evolutions
4. Concentrating or compacting cell networks

Furthermore, radio efficiency will need to be tightly coupled with network-level and system-level evolutions. We observe that there are also system-level implementation issues that need to evolve with the radio, among them, crest factor reduction, carrier-to-carrier interference mitigation, per-carrier power control etc., which arise or become complicated with multi-standard operation. While network-level issues are beyond the scope of this work, we introduce some of the aforementioned link-level issues for the sake of completeness.

2.2.2 Energy Efficiency

In the context of energy efficient radio systems, the primary focus of this work is to identify the performance specifications for a transmitter chain that is capable of simultaneous multi-standard transmission (i.e., multi-Radio Access Technology(RAT) systems), while also improving the distribution of performance specifications among the various blocks that constitute a transmitter. The illustration in Figure 2.2 shows the various components in a radio-card.

Consider the following power budget for a typical macro-cell 6-carrier transceiver (2/2/2 [7]) UMTS-WCDMA BStn [5] shown in Figure 2.3, with 20W output power per carrier.

The power consumption of the BStn can vary by as much as a factor of two, depending on loading conditions and the dynamic power handling mechanisms (e.g. Discontinuous-Transmission or DTx, in WCDMA and LTE), incorporated into the various cellular access technologies. The carrier power control mechanisms play a significant role in determining the performance specifications and are briefly touched upon in this work. Interestingly, the efficiency of the MCPA is optimised for high load periods when the throughput of the cell needs to be at its highest, providing efficiencies as high as 40%, reducing to as low as 10% for 10% loading.

Although the illustrated example is not recent, the numbers are still representative of a vast number of BStns that are currently operational. The Table 2.1 briefly summarises the efficiency of the BStn and shows that improving only the efficiency of the Power Amplifier (PA) results in marginal improvements to the overall RAN efficiency. A major reason for this is that any power that is not translated into radiated energy is considered wasteful. This reasoning applies particularly to the peripheral equipment and the baseband processing

[7] 3-sectors with 2 carriers per sector, Alcatel Lucent, 2006

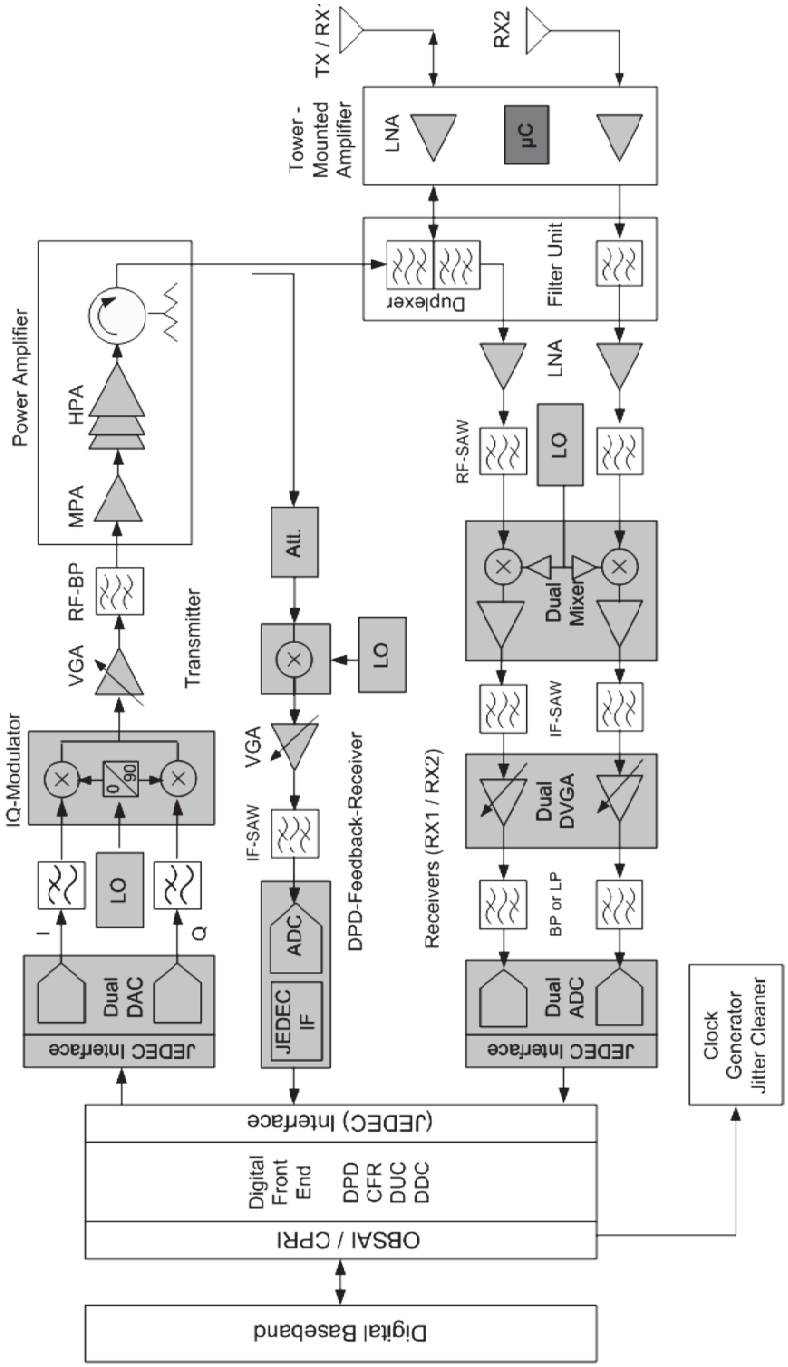

Figure 2.2: Block diagram of a typical contemporary Base Station transceiver card (*Courtesy: NXP Semiconductors*)

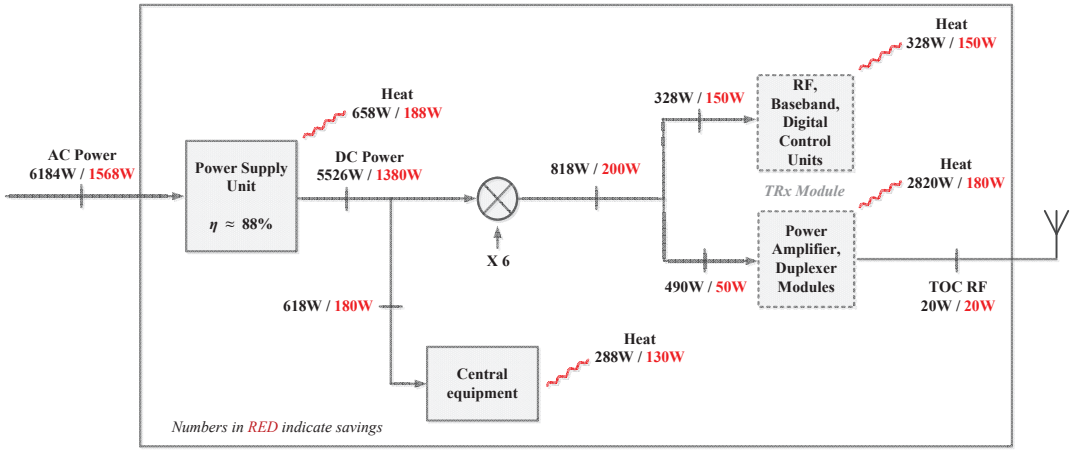

Figure 2.3: Power budget in a 2/2/2 UMTS base station. Numbers in red indicate improvements on the previous values, indicated in black, following innovations in architecture and design.

which constitute a bulk of the power budget behind the transmitter (Tx), which is not directly converted into RF power. As the output power of the BStn is increased, the power budget of the PA module outweighs that of the baseband processing, improving the overall efficiency of the BStn. However, recent advances in systolic antenna-array (Active Antenna Array or AA) solutions which require low output-power PA modules, has brought the focus back to the efficiency and performance of the digital and small-signal[8] RF module.

There exist several complex power models describing the power consumption of the BStn power, (see [4, 6]). However, we do not delve into the topic in this work. If we express the efficiency of the BStn simply as a ratio of the transmitted RF power to the AC Mains power, the stark inefficiency of BStns is readily noticeable, owing to the fraction of the power is transmitted into the air. Referring to Table 2.1 we observe that the overall efficiency of the BStn is only marginally improved despite marked improvements in PA efficiency. Significant improvements would be possible if the architecture of the BStn itself is revisited and revised. This is the subject of the RH [9] and AA methodologies mentioned earlier.

The BStn sub-system forms one component of the entire wireless-communications network setup as illustrated in Figure 2.4. There are several performance bottlenecks in various sub-systems in the scenario illustrated. For instance, contemporary antennas with their highly spread and non-optimized emission patterns lead to a significant wastage of energy. This

[8] Refers to the part of the Analog/RF Transceiver chain that lies between the DAC/ADC and the PA/LNA module.

[9] In the RH in particular, a significant power savings is achieved by placing the lighter, air-cooled radio-module directly on the mast, eliminating the lossy (-3dB) RF feeder cable. The power delivered by the PA is halved, eliminating the need for power hungry cooling fans and also air-conditioning for the rack.

Table 2.1: System-level efficiency for the Base Station of Figure 2.3

Heat Dissipation	
Base Station	$6184W - (6 * 20W) - 330W = 5734W$
PA RF Path	$(490W - 20W) * 6 = 2820W$
Efficiency	
Usable efficiency of PA Module	$20W/490W = 4\%$
Overall efficiency	$(6 * 20W)/6184W = 1.9\%$
Improved efficiency	$(6 * 20W)/1568W = 7\%$

issue is addressed in AA systems where directionality and strength of antenna-patterns are adaptively controlled by using phase-coherent elements, in order to achieve user or area-specific beam patterns.

From Figure 2.5 it is evident that BStns (particularly macro-cells) are responsible for more than 90% of the energy consumption in RANs, primarily due to their poor efficiency, exacerbated by their large deployment numbers. The impact of Information and Communication Technologies on the human carbon footprint has been the topic of several recent works (see [7,8]). For this reason, the scope of the work is limited to analysis of only the BStn radio (Tx) sub-system.

As previously indicated (see Section 2.2.2), there are several fronts where improvements in RAN efficiency can be explored, simultaneously with improvements in the Network itself. Some methods include,

- **BStn RAN hardware**
  - Multi-Band, Multi-Channel Power Amplifier and enhanced signal-processing (pre-distortion, crest-factor-reduction)
  - High degree of coordination between Analog radio and Digital processing
  - **Multi-standard, high dynamic-range small-signal RF chain**
  - Low-power, high-speed ASICs for reduced Baseband power consumption
  - Adaptive (active and reconfigurable) Antenna systems
- **Cell optimisation**
  - Compacting Cell-size with better inter-cell coordination
  - Cooperative interference mitigation with resource-sharing
  - Use of re-farmed spectrum, implying co-location of cell-sites
- **Dynamic adaptation to load**
  - SON (Self-Organising-Network) management for reconfiguration
  - Heterogeneous Network deployment (i.e., Macro-cells for overlay and Pico,Femto-cells for inlay)

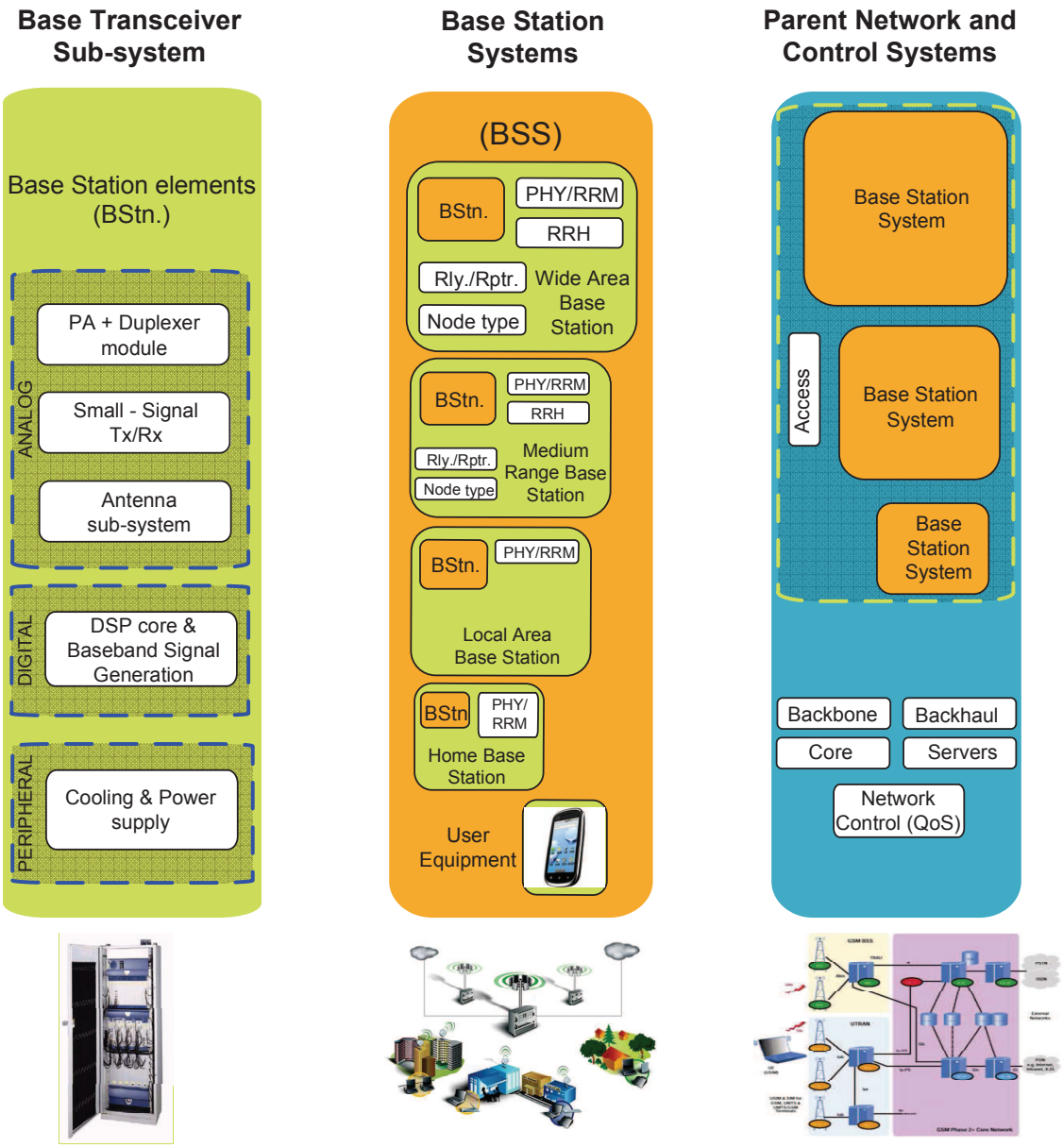

Figure 2.4: Base Station system hierarchy.

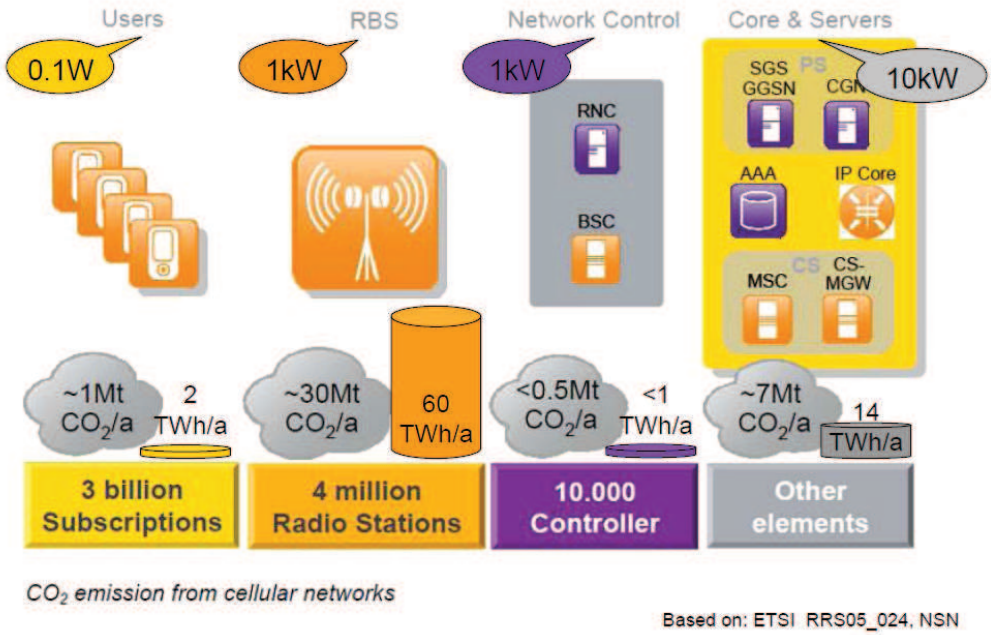

Figure 2.5: Global Energy Consumption of Mobile Communications

– Power Amplifier power supply adaptation to dynamic loading

Several of these features are beginning to be supported by the newer access standards, allowing considerable potential for reduced energy consumption. While most of the optimisations at network level also cater to power efficiency, they primarily address the performance bottlenecks that arise from the increasing processing required for higher data rates.

From a purely electrical standpoint, significant potential for power reduction is seen in the area of PAs for macro-cells. This is also the case for the transceivers and baseband circuits in pico- and femto-cell applications,[10] which are becoming more prominent.

While this work is dedicated to macro-cells, methodologies developed for analysis are equally relevant to the more compact variants. However, improving only component level performance for higher electrical efficiency has little impact on the overall efficiency of the BStn (see Figure 2.1), prompting the need for architectural innovation. Among other methods to improve efficiency are multi-antenna beam forming, MIMO, higher antenna-sectorisation [9], and more efficient PA technologies, such as, Switched Mode Power Amplifier (SMPA), N-way Doherty PA coupled with adaptive-Digital-Pre-Distortion (DPD), Envelope Tracking (ET), etc. These are being gradually incorporated to improve block-level efficiency targeting an enhanced system-level performance. The future BStn will likely take advantage of such features

[10] Pico- and femto-cells are progressively compact variants of BStns that cater to much smaller areas such as an office floor or a house.

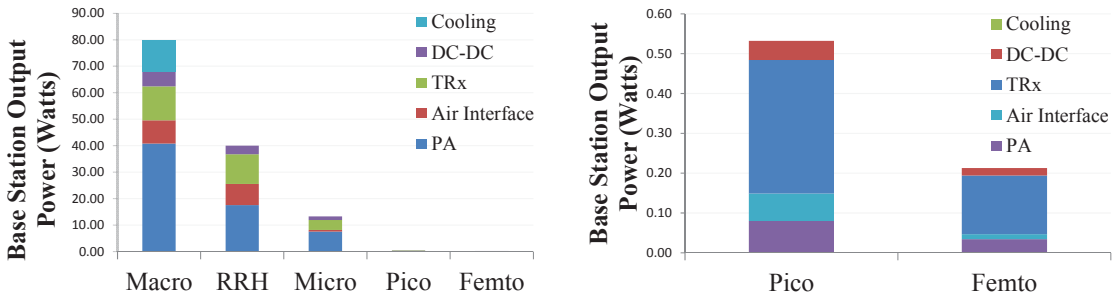

Figure 2.6: A breakdown of power consumption in the radio transceiver for different Base Station variants (*Courtesy: EARTH FP7-IP Project, 2010*)

to provide new and improved services while still being economical and ecological to operate. For constraints of time, this work is limited in scope to only the transmitter of the radio.

In this work, we limit our focus to only the radio and in particular, the transmitter in the FDD configuration. Accordingly, the power in the radio can be further sub-divided depending on the functions of the various blocks in the chain. The chart in Figure 2.6 summarises the percentage contributions of the various components in macro, micro, pico, femto and RH BStn variants.

Among the various radio sub-blocks, the PA is the most power hungry. Contemporary and future PA solutions, both, are non-linear and need to be supported by pre-distortion mechanisms which modify the characteristics of the signal such that the resulting signal from the non-linear PAs is in adherence to leakage, spurious emissions and signal distortion specifications. In order for pre-distortion mechanisms to function correctly, the part of the transmitter chain that lies between the Baseband output and the PA input needs to be both linear and have a challengingly high dynamic range, particularly when power control mechanisms are considered, as we will see later. We revisit the architecture of this part of the chain in order to identify design tradeoffs that can be better optimised, alongside any eliminable performance bottlenecks.

2.2.3 Organization of the Thesis

The thesis is structured in the following manner. Envisioning a multi-mode, multi-band transmitter for the near future, we begin by rationalizing whether such a scenario is possible or, paraphrasing, by identifying a *Use-Case* scenario. Multi-mode, multi-band scenarios do not exist today and they depend significantly on the operator settings, spectrum settings and network optimizations, some of which are beyond the scope of this work, but have a significant impact on the system analysis. In Chapter 3 we outline a potential Use-Case scenario for such a convergent multi-standard system, simultaneously highlighting relevant

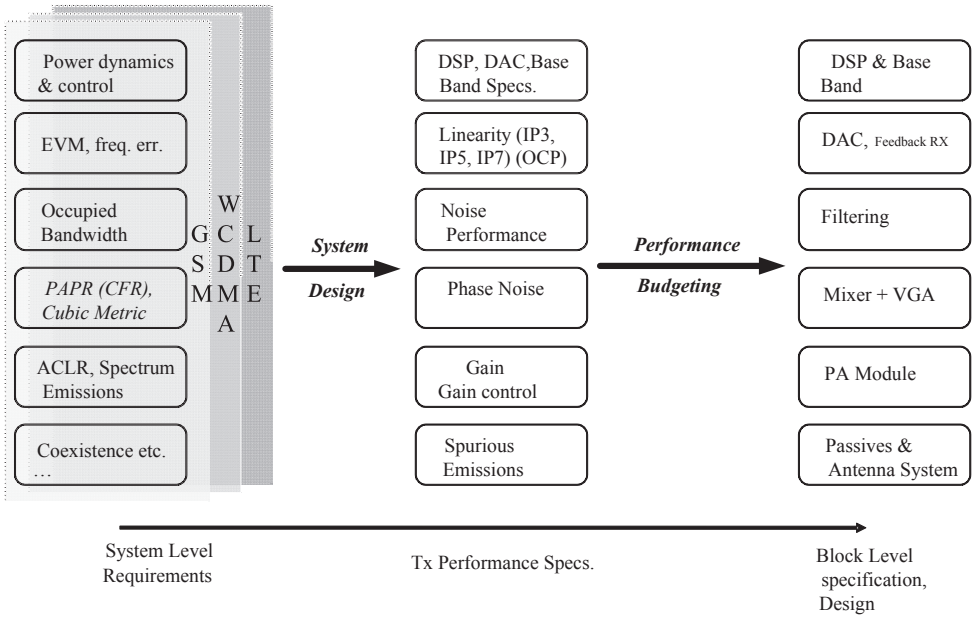

Figure 2.7: Methodology of Analysis

network-level issues. Once the ecosystemic constraints[11] [10] of the Use-Case are established, the 3GPP transmitter performance specifications - SEM, EVM, ACLR, Power control, Co-existence etc., corresponding to the different modes are identified and collated into a single performance specification for the multi-standard Tx.

In the subsequent chapters we highlight some of the technical challenges within the scope of implementing an RF front-end for such a convergent multi-mode or multi-Radio-Access-Technology (Multi-RAT) transmitter for the Downlink (DL). Operating a single-hardware Tx entails very stringent performance requirements, stressing the power budget. In Chapter 4 we deal with the analysis of performance requirements, translating the collated system-level specifications into component-level hardware specifications for the transmission chain. Assumptions, where relevant, are indicated accordingly. Chapter 5 deals with an architectural analysis or a link performance budgeting based on our derived specifications. Here we develop mechanisms for performance budgeting based on system specifications and also suggest methods to incorporate goal functions into the process. This work excludes a detailed analysis of the Power Amplifier module, but, because the PA is by far the most power hungry block in the transmit chain, several reasonable assumptions will be made to analyse its contribution to the performance of the entire transmit chain. As is evident from Figure 2.6, the common issue among the variants remains the performance of the transceiver (excluding the PA) and base-band components, making analysis of only the transceiver module pertinent.

In Chapter 5 the critical issue of power control in simultaneous multi-standard trans-

[11] Co-existence, geographical, topological (TDD/FDD), etc.

mission is brought into focus by highlighting the dynamic range limitation of the DAC. In Chapter 6, we deal with the design of multi-mode Analog-Quadrature-Modulator with dynamic power control, as a possible solution for the highlighted issue. Several design aspects are discussed, including the highlighting of performance tradeoffs and critical contributors that have a system-level impact. Simulation results of the conceptual design in SiGe BiCMOS are also presented. The final Chapter 6.11 summarizes the findings and concludes by establishing the scope for further work.

2.3 Contributions of this work

While there been significant efforts made in areas highlighted earlier (see Section 2.2.2), until recently, not many have analysed and addressed the challenges associated with the simultaneous transmission of multi-mode carriers in BStns. The contributions of this thesis are divided into three parts. In the first part, we present a step-by-step analysis of the translation of the 3GPP specifications, into performance criteria for a macro-cell multi-mode Tx. Focus is given to linearity (at reasonable Input Back-Off or IBO), phase noise, broadband noise floor and IQ imbalance effects. The second part of the work discusses the performance budgeting whereby criteria derived from the previous part are distributed among the various Tx sub-circuits. In the third part, we summarise our analysis of a dynamic-range bottleneck owed to a multi-mode power-control issue and consequently, present the circuit design of a variable gain Analog Quadrature Modulator (AQM) in SiGe BiCMOS, as a plausible solution.

Based on the work so far, the following material has resulted :-

Conferences

[11]: **S. Kowlgi** and C. Berland, "Linearity considerations for multi-standard cellular Base-Station transmitters," in Proceedings of the 41st IEEE European Microwave Conference (EuMC), Manchester, October 2011, pp. 226-229.

[12]: **S. Kowlgi**, P. Mattheijssen, B. Corinne, and T. Ridgers, "EVM considerations for convergent multi-standard cellular Base-Station transmitters," in Proceedings of the 22nd IEEE Personal Indoor Mobile Radio Communications Conference (PIMRC), Toronto, September 2011.

Articles and Letters

[13]: S. Kowlgi, P. Mattheijssen, C. Berland and T. Ridgers, "System level considerations for convergent GSM/EDGE/WCDMA/LTE multi-standard Base-Station RF transmitters," IEEE Circuits and Systems Magazine. *In preparation.*

[14]: S. Kowlgi, L. Gambus, T. Ridgers, and C. Berland, "Design of a DC-300MHz Passive Current-driven Quadrature Modulator with 24dB attenuation range with ±0.5dB accuracy, 1.5dB power gain and > 24dBm IIP3, in SiGe BiCMOS," Electronic Letters. *In preparation.*

Invited Presentations and Internal Technical reports

[10]: **S. Kowlgi**, "Multi-mode GSM/WCDMA/LTE Base Station Transmitter : System level

requirements analysis," PANAMA Project, Tech. Rep., June 2010.
[15]: **S. Kowlgi**, "System level considerations for Multi-mode Base-Station transmitter design", PAR4CR Project, Presentation, Technical University of Eindhoven, Eindhoven, July 2010 and April 2011.

Chapter 3

Background

3.1 Identifying a Use-Case Scenario

Envisioning a unified multi-standard transmitter requires rationalizing whether the need for simultaneously transmitting signals of multiple standards exists and subsequently, if such a situation is feasible. We refer to this as identifying a Use-Case scenario. In the 'layer-cake' evolution of standards, where, over the years, new air-interface-technologies have been regularly added to existing networks, the possibility of the co-existence of several standards has always been incorporated. These scenarios, while not in existence today, will depend significantly on the operator's overall deployment strategy where network and sub-system performance settings define constraints on the transmitter operation. For example, an operator such as Vodafone or T-mobile may choose to share its LTE BStn with other operators. With this, the maximum number of carriers and the signal bandwidth that need to be supported could increase, placing significantly tougher requirements on the hardware beyond a certain limit. This highlights one such limiting scenario. There is also a significant dependence on the spectral requirements of each air-interface or standard and the co-existence between them. We will establish them in Chapter 4. Collectively, all of these aspects come to define the eco-system of the multi-standard transmitter.

Once multi-standard co-existence, geographical and topological (TDD/FDD etc.) constraints in a use-case scenario are established, the individual requirements for each air interface of the different modes can be identified. 3GPP documents use terms such as Spectral Emissions Mask (SEM), Error Vector Magnitude (EVM), Adjacent Channel Leakage Ratio (ACLR), Dynamic Range and Power Control, Co-existence criteria etc., to specify the maximum permissible distortion in a transmitter.

While designing and operating a transceiver to support individual access technologies has its own set of challenges, operating more than one technology on the same hardware is understandably more complex. Issues arise at both system (e.g. inter-operability, interference, resource sharing) and hardware or block-levels (e.g. composite signal PAPR, power levels, frequency offsets, non-linearity). For this reason, it is necessary to understand how the system specifications for each standard impact the performance requirements of the unified transmitter. Particularly, attention has to be given to co-existence and compatibility between the different technologies, while maintaining efficiency for all systems.

E-UTRA Band	UTRA Band	GSM Band	Uplink (UL) BS receive UE transmit	Downlink (DL) BS transmit UE receive	Band category
1	I	-	1920 MHz – 1980 MHz	2110 MHz – 2170 MHz	1
2	II	PCS 1900	1850 MHz – 1910 MHz	1930 MHz – 1990 MHz	2
3	III	DCS 1800	1710 MHz – 1785 MHz	1805 MHz – 1880 MHz	2
4	IV	-	1710 MHz – 1755 MHz	2110 MHz – 2155 MHz	1
5	V	GSM 850	824 MHz – 849 MHz	869 MHz – 894MHz	2
6	VI	-	830 MHz – 840 MHz	875 MHz – 885 MHz	1
7	VII	-	2500 MHz – 2570 MHz	2620 MHz – 2690 MHz	1
8	VIII	E-GSM	880 MHz – 915 MHz	925 MHz – 960 MHz	2
9	IX	-	1749.9 MHz – 1784.9 MHz	1844.9 MHz – 1879.9 MHz	1
10	X	-	1710 MHz – 1770 MHz	2110 MHz – 2170 MHz	1
11	XI	-	1427.9 MHz – 1447.9 MHz	1475.9 MHz – 1495.9 MHz	1
12	XII	-	698 MHz – 716 MHz	728 MHz – 746 MHz	1
13	XIII	-	777 MHz – 787 MHz	746 MHz – 756 MHz	1
14	XIV	-	788 MHz – 798 MHz	758 MHz – 768 MHz	1
…					
17	-	-	704 MHz – 716 MHz	734 MHz – 746 MHz	1 *
18	-	-	815 MHz – 830 MHz	860 MHz – 875 MHz	1 *
19	XIX	-	830 MHz – 845 MHz	875 MHz – 890 MHz	1
20	XX		832 MHz – 862 MHz	791 MHz – 821 MHz	1
21	XXI		1447.9 MHz – 1462.9 MHz	1495.9 MHz – 1510.9 MHz	1
* NOTE: The band is for E-UTRA only.					

Table 3.1: Paired bands in E-UTRA, UTRA and GSM/EDGE [16]

3.2 Spectrum Availability and Constraints

For multi-mode operation, the choice of frequency of operation is an important deliberation for hardware design, more so from a network system management point-of-view. From a spectrum bandwidth and geographical standpoint there exist only a few bands which can allow the co-existence of GSM/EDGE, WCDMA/HSPA and LTE.

The Table 3.1 gives an indication of the FDD frequency bands available for different standards, with Band Category 2, and Multi Standard Radio Bands 2/II, 3/III, 5/IV and 8/VIII referring to those currently amenable to multi-mode operation. In order to simplify the problem at hand, the focus of this work shall be limited European (ETSI) FDD bands while not being oblivious to limitations posed by respective bands in other geographies (e.g. in North America). Within Europe, there exist two bands EGSM900 / UTRA-VIII (925 – 960MHz) and the DCS1800 / UTRA-III (1805 – 1880MHz), which can support GSM, UMTS, and LTE. A typical telecommunication network license in most countries is issued for one or more standards.

A growing trend is to re-use or 're-farm' spectrum or bands currently allocated to one technology such as GSM/EDGE, to deploy more spectrally efficient technologies such as WCDMA/HSPA and LTE/LTE-A. This is because lower frequencies allow better propagation

conditions, especially when large coverage distances and depth i.e. availability of services indoors, or coverage area, are key. This takes advantage of the existing infrastructure and high penetration of GSM/EDGE technologies while significantly reducing the network deployment costs. Network planning and performance management issues still remain to be tackled but the discussion of these issues is beyond the scope of this work. Some part of the benefit from lower frequency operation, however, is lost, since antenna gains tend to get smaller at lower frequencies. To maintain the antenna gain at lower frequency would require a physically larger antenna which is not always feasible at base station sites and in small terminals. As a side note, only by around 2015 will the Digital Dividend band ($470 - 862$MHz) be fully available, providing bandwidths similar to existing bands (≈ 100MHz for FDD and TDD). It is however unlikely to be globally harmonized.

Contrarily, for more congested or high density urban scenarios, known as 'hot spots', higher frequencies become interesting. This is because they are less than the lower bands, they offer larger bandwidths and consequently greater potential for higher data-rates. This would make the DCS1800 / UTRA-III an ideal candidate for throughput evolution. However, being closer to the popular 2100MHz UMTS band, it would offer only a minor cost benefit to shift, providing an obvious tradeoff. Returning to spectrum re-farming, the GSM specific 900MHz and 1800MHz spectrums in Europe have been re-farmed over the last few years to also support WCDMA networks [17, 18]. There are already several Base Station products that support this development, although most of them need to be factory reconfigured when switching bands. Software reconfiguration is still a growing trend. Interestingly, all of the LTE (E-UTRA) bands are common with the UTRA bands, implying that LTE and WCDMA can be deployed together, however, with the caveat that not all WCDMA (UTRA) bands support full bandwidth (20MHz) operation of LTE, being limited either by the spectrum availability or the bandwidth allocated to the operator (which typically varies from band to band and is different for each country). This would also apply to the GSM (GERAN) bands that also can support LTE [19, 20].

From the above table, it can be seen that the IMT-2000 band earmarked for WCDMA operations, UMTS-I ($2110 - 2170$MHz), which is also the most prevalent WCDMA band in Europe, can simultaneously support three full LTE bands (20MHz). This band does not currently support GSM/EDGE networks and is therefore a difficult choice for simultaneous multi-mode transmission. Despite this, multi-mode schemes can be extended to this band for WCDMA/LTE coexistence.

Higher frequency bands such as the $2570 - 2620$MHz band earmarked for deployment of LTE based networks appear to be the primary choice for European operators. These bands are already available in most parts of Northern Europe and Central Europe. However, the global choice of band for LTE operation is yet relatively unclear with several operators preferring to deploy LTE in bands with existing infrastructure as deployment costs are significantly reduces. Furthermore, at such high frequencies, enhanced data rates can be better supported as opposed to enhanced coverage distances. In 2010, there were over 51 network commitments in 24 countries worldwide, representing a significant shift towards these frequencies. However, each with their own frequency of operation, with the EU mainly adhering to 2.6GHz for LTE or planning for the digital dividend ($790 - 862$MHz) [21]. American operators preferred using 700MHz, in Japan, the 800MHz, 1.5GHz or 1.7GHz spectrum depending on operator, with

China committing to TD-LTE by 2012 and Australian operators choosing 2.6GHz (urban) and 700MHz (rural). A list of deployment and frequencies for each operator is available in [22]. To our knowledge, a few operators have even chosen to deploy LTE in GSM bands, e.g. SmarTone-Vodafone - EGSM900 in Hong Kong, Bouygues-Telecom - the DCS1800 band in western France.

In summary, we notice that in Europe four primary bands exist, E-UTRA Band- 1, 3, 7 and 8, each with their set of advantages and disadvantages. However it is also clear that there in no clear consensus, at the time of writing this work, on which band will be central to the evolution of multi-standard transmitters.

3.3 Architectural and Topological Considerations

3.3.1 Architectures

The Table 3.2 briefly summarises the pros and cons of the primary transmitter architectures.

Polar architectures (typically limited to the User-Equipment or UE) have until recently mostly supported modulated signals of lower bandwidth (e.g. GSM/EDGE) [23,24] although more broadband solutions have appeared in research recently [25–27], limited to lower power levels. The bandwidth expansion associated with accurately converting the Cartesian $(I(t) + j.Q(t))$ baseband signal to Polar form $(R(t)\angle\theta(t)$, with $R(t) = \sqrt{I(t)^2 + Q(t)^2}$ and $\theta(t) = \arctan x(t),)$ requires several[1] frequency terms, increasing the bandwidth of operation [28] to typically, greater than 5 times signal bandwidth, depending on the accuracy required [29] [2]. The RF chain on BStns is still largely Cartesian based although hybrid architectures such as Envelope-Tracking (ET) are being increasingly adopted for future implementations, facilitating better control of the PA power efficiency. Most of the analysis in this document is therefore limited to Cartesian (Zero/Low/High-IF) transmitter architectures.

Until recently, most BStns exploited the superheterodyne architecture for up-conversion of the baseband signal. More recent BStns however, use either the direct up-conversion or the two-step up-conversion in the Tx for the flexibility and economy they afford. Referring to the Tx architecture of Figure 2.2, the feedback Rx or the observation Rx typically involves an IF down-conversion, with image rejection achieved in the baseband. This is done so as to minimise additional contributions from the feedback path and to sense only the Tx distortions.

Direct up-conversion (Zero-IF) and Low/High-IF Cartesian architectures are prevalent and preferred for Base station transmitters. The Figure 3.1 illustrates the block diagrams of the various two-step or low/high-IF up-conversion in comparison to the superheterodyne architecture. Among other reasons related to baseband processing and fewer parts, Zero-IF also brings with it limitations in DC offset correction and has so far seen greater acceptance in mobile equipment [30] than in BStns. Furthermore, in Low/High-IF architectures, with the feed-through LO signal and the unwanted RF sideband falling out-of-band, some benefit

[1] If $x = \frac{Q(t)}{I(t)}$, then the Taylor series expansion of the Polar argument, $\theta = \arctan x$, is given by, $\sum_{n=0}^{\infty} \frac{(-1)^n}{(2n+1)} x^{2n+1}$, which is a non-linear function yielding numerous terms for the phase modulated spectrum of the original signal.

[2] Bandwidth expansion is also different for phase and amplitude envelopes of the signal

Table 3.2: A brief summary of typical transmitter architectures

Architecture	Disadvantages	Advantages
Superheterodyne	• Higher cost, bulky due to additional components, requires high Q analog filters • Difficult to integrate, mainly due to the high Q passives required • Several issues at receiver including higher NF and power dissipation • Inflexible with analog filters being tailored to one specific standard or bandwidth • Higher power consumption due to extra stages in analog chain	• Superior sensitivity • Superior selectivity
Direct Conversion	• LO leakage, LO pulling, LO self-mixing • DC offset • $1/f$ noise issue	• Lower cost due to fewer components • Consequently, more easily integrated • Lesser power consumption (fewer components and NCO can be Off) • Greater flexibility, with simpler frequency plan for multi-mode operation • No Image-signal problem
Two-Step Up-conversion	• Issue of unwanted Image-signal • LO leakage is a function of the 'IF' frequency • NCO in the DAC consumes more power (similar for higher DAC clock rates which depend on 'IF', with NCO Off)	• DC offset cancellation is simple (done in the DAC or Baseband) • $1/f$ noise issue overcome if signal has no component at DC • Lower cost due to relatively fewer analog parts • Consequently, more easily integrated

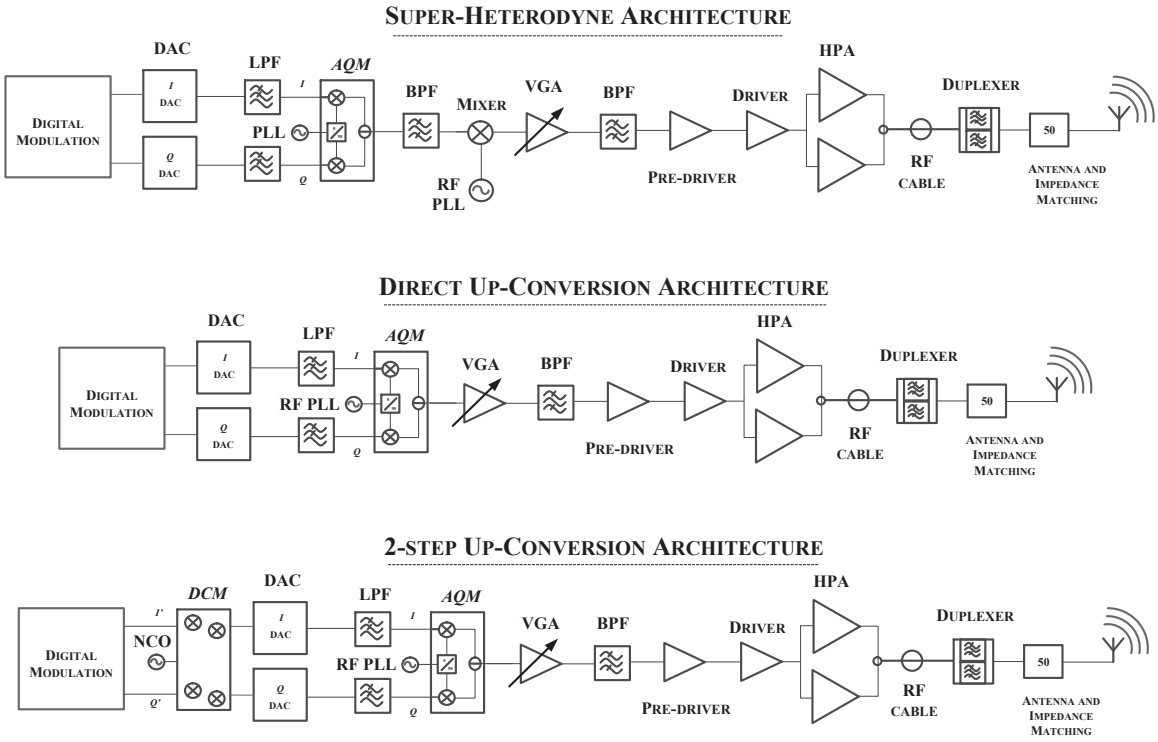

Figure 3.1: A brief summary of the typical transmitter architectures

in the rejection can be gained from the Duplexer isolation and also the various compensation mechanisms available in contemporary DACs. Injection-locking or LO-pulling is another issue in Zero-IF architectures where the VCO locks to an external stimulus. A noisy LO signal results if the amplified LO feed-through, reflections and/or leaked signals from the antenna are insufficiently attenuated[3]. There are also disadvantages to the Low/High-IF, where valuable compensation bandwidth necessary for the DPD, is lost by placing the wanted signal asymmetrically in the pass-band spectrum. The Digital Up-Conversion (DUC) provided by the DAC requires a Numeric Complex Oscillator (NCO), which increases power consumption and phase noise in the DAC. The commonality in both architectures however, is that, carrier aggregation and processing is achieved in the digital domain while the up-conversion to RF for transmission is achieved in the analog domain. The tradeoffs in design and the overall power budget differ significantly and the choice is specific to the deliberations of the individual BStn OEM.

Although it was previously mentioned that first stage of the two-step up-conversion is

[3]Electromagnetic shielding, dual VCO and offset VCO architectures are sometimes used to overcome this issue.

done primarily in the baseband, there nevertheless exist several flavours [30]. The digital I/Q up-conversion is preferred because modern high-speed DACs are quite flexible in the choice of 'IF' frequency and also in the various calibration processes they provide [31–33]. The following equation illustrates the digital I/Q up-conversion operation using the NCO and a complex modulator.

$$\begin{aligned} I_{+,\mathrm{USB}}(t) &= I_{\mathrm{BB}}(t) \cdot \cos(\omega_{\mathrm{NCO}} t) - Q_{\mathrm{BB}}(t) \cdot \sin(\omega_{\mathrm{NCO}} t) \\ Q_{+,\mathrm{USB}}(t) &= I_{\mathrm{BB}}(t) \cdot \sin(\omega_{\mathrm{NCO}} t) + Q_{\mathrm{BB}}(t) \cdot \cos(\omega_{\mathrm{NCO}} t) \end{aligned} \tag{3.1a}$$

$$\begin{aligned} I_{+,\mathrm{LSB}}(t) &= I_{\mathrm{BB}}(t) \cdot \cos(\omega_{\mathrm{NCO}} t) + Q_{\mathrm{BB}}(t) \cdot \sin(\omega_{\mathrm{NCO}} t) \\ Q_{+,\mathrm{LSB}}(t) &= I_{\mathrm{BB}}(t) \cdot \sin(\omega_{\mathrm{NCO}} t) - Q_{\mathrm{BB}}(t) \cdot \cos(\omega_{\mathrm{NCO}} t) \end{aligned} \tag{3.1b}$$

$$\begin{aligned} I_{-,\mathrm{USB}}(t) &= I_{\mathrm{BB}}(t) \cdot \cos(\omega_{\mathrm{NCO}} t) - Q_{\mathrm{BB}}(t) \cdot \sin(\omega_{\mathrm{NCO}} t) \\ Q_{-,\mathrm{USB}}(t) &= -I_{\mathrm{BB}}(t) \cdot \sin(\omega_{\mathrm{NCO}} t) - Q_{\mathrm{BB}}(t) \cdot \cos(\omega_{\mathrm{NCO}} t) \end{aligned} \tag{3.1c}$$

$$\begin{aligned} I_{-,\mathrm{LSB}}(t) &= I_{\mathrm{BB}}(t) \cdot \cos(\omega_{\mathrm{NCO}} t) + Q_{\mathrm{BB}}(t) \cdot \sin(\omega_{\mathrm{NCO}} t) \\ Q_{-,\mathrm{LSB}}(t) &= -I_{\mathrm{BB}}(t) \cdot \sin(\omega_{\mathrm{NCO}} t) + Q_{\mathrm{BB}}(t) \cdot \cos(\omega_{\mathrm{NCO}} t) \end{aligned} \tag{3.1d}$$

where, the subscripts USB and LSB refer to the upper-side-band and lower-side-band respectively. The subscript BB refers to the baseband signal. The + and − refer to the positive and negative sidebands respectively. Depending on which side-band (among the above) is required, the corresponding output of the complex modulator can be selected for transmission.

Returning to the architecture, we have earlier highlighted the importance of the PA in the efficiency of the transceiver. Several PA architectures exist that suggest different strategies of exploitation to improve the efficiency of the non-linear PA [34], among them :

Envelope Elimination and Restoration (EER) This method, initially proposed by [35], is based on the idea that a signal can be split into its amplitude-modulated (AM) and phase-modulated (PM) constituents and belongs to a family of Polar-modulation architectures. These are then processed separately before combining them at the non-linear power amplifier. The PM of the signal is preserved by passing it through limiter which eliminates any AM-PM distortion in the non-linear, PA. The saturated, more efficient PA is driven by the PM signal and the AM of the signal is separately fed through the supply to restore the signal envelope. Eliminating the requirement for linear operation of the PA (since there is no AM in the signal), enables the device to have efficiency that can be maximised for each modulation. This method has met with recent interest despite challenges such as designing an accurate supply voltage, requirements on the conditioning path of the AM signal and associated dynamic range issues.

Envelope Tracking (ET) Here, the benefits of the separated modulated envelope in EER are put to use by driving an already linear PA with a supply voltage that 'tracks' the envelope of the signal in phase. Due to the fact that the supply follows the modulated signal envelope, (greater than) rail-to-rail swing is possible, allowing the linear PA to run under constant compression enabling higher efficiency, over a wide, linear input power range (AM waveforms). The constraints on the bandwidth/speed, linearity and phase coherence of the supply circuit are obvious, although the tracking need not be as accurate as that in the EER technique, owing to the linear PA which operates with a certain margin.

N-way Doherty In this PA configuration, two amplifiers ('Main' and 'Auxiliary') are connected in parallel, driven by the same signal through a power splitter. Their outputs are connected via an impedance transformation transmission-line. Being active devices, they act as generators (sources) sinking current into a common load. This enables either amplifier to modulate the load of the other which sees both the common load and the output transconductance of the other. By controlling the phase relationship between the currents and the values of the load impedances, it is possible to arrive at a constant voltage across the 'Main' amplifier (which is a necessary condition in order) to guarantee its maximum efficiency while its output load is changing owed to the current supplied by the 'Auxiliary'. This configuration has been the mainstay of modern BStns, for its tradeoff between efficiency and linearity. Extensions of the same concept, the N-way Doherty and more recently Digital Doherty (which overcome the narrow-band, impedance sensitive transformation of the power splitter) have been gaining dominance in modern BStns.

LInear amplification using Non-linear Components (LINC) This Chireix[4] Outphasing PA architecture [36] utilises non-linear PAs unlike the Doherty which suffers the limitation of using linear PAs for its output signal. The following equation illustrates the operation of the LINC PA architecture. If an amplitude modulated signal $s(t)$ is applied to a phase modulator, it is possible to break up or create two signals $s_1(t)$ and $s_2(t)$ of equal and constant amplitude such that when they are amplified and combined, an amplified version of the original signal results.

If we assume $s(t)$ to be,

$$s(t) = A(t) \cdot \exp^{j\phi t} \tag{3.2a}$$

then,

$$s_1(t) = A_m(t) \cdot \exp^{j\phi t + \alpha(t)} \; s_2(t) \quad = A_m(t) \cdot \exp^{j\phi t - \alpha(t)} \tag{3.2b}$$

where, $\alpha(t) = \frac{A(t)}{A_m(t)}$. Assuming the gain of the amplification is G_v, then,

$$s(t) = G_v(s_1(t) + s_2(t)) \tag{3.2c}$$

or,

$$s(t) = G_v \cdot A(t) \cdot \exp^{j\phi t} \tag{3.2d}$$

The key developments here being the generation of the two constant amplitude signals that capture the AM information of the original signal as a differential phase shift, and also the combiner that allows load modulation to take place, improving the overall efficiency of the setup. Being of constant amplitude, non-linear amplifiers can be used since the AM information is recovered by the summation. Noticeably, the signals do not modify the PM content of the original signal, implying that the PM information of that signal can also be fully reassembled. The system, like the Doherty, is nevertheless vulnerable to mismatch in

[4]LINC and Chireix are related but also different. The discerning reader is referred to [34] for further discussion on the topic.

the phase and/or gains of the two amplifications paths, leading to distortion of the output signal. The bandwidth expansion in the LINC PA is an additional downside.

Pulse Width Modulation (PWM/SMPA) In this method, also referred to as digital direct-conversion, a Switched-Mode PA (SMPA) is indirectly driven by the output of a digital modulator bearing the baseband information that is up-converted to RF. There are several flavours of this architecture specifying how the SMPA is actually interfaced to the digital baseband information. These include a multi-bit DAC, a $\Sigma\Delta$ converter with an inherently-linear 1-bit DAC and more recently, an RF DAC which combines the functionalities of both a DAC and an up-conversion Mixer [37].

While the Doherty amplifiers remain the mainstay of BStns, the LINC and PWM/SMPA architectures are being increasingly researched for deployment in modern BStns. That being said, most of the previously discussed efficiency enhancement techniques do not address the insufficient linearity of the PA itself and to an extent even degrade the linearity performance. Central to all these methods and PA implementations are 'linearisation' methods that are commonplace in all macro-cell BStns. Several methods have emerged over the years. Among them [38],

- Direct and Indirect Feedback (Cartesian and Polar loops)
- Feed-forward
- Pre-Distortion (previously analogue and recently digital, also neural networks based)
- LINC, EER

To be more accurate LINC and EER/ET are actually classified as efficiency enhancement techniques, as discussed earlier, but are often included here as they allow a higher degree of non-linearity in the PA while having an output that could theoretically reach acceptably low levels of distortion. While Feed-forward schemes were common earlier, the increase in Digital Signal Processing (DSP) capacity has led to Pre-Distortion becoming the linearisation method of choice for a majority of the modern BStns. The scheme involves the application of a signal conditioned with the inverse function of the PA module, at its inputs, so that the resulting output signal is theoretically free from distortion (see Section A). Evidently, there are two aspects in this process, the first of which involves determining the mathematically inverse transfer function of the PA module. The second requires that this process be achieved in real-time as adjusting the input signal to the PA based on much older samples would provide little benefit to the linearity. While the 'hard'-saturation of the PA is not modified, this method helps to extend the linear range of the PA when in 'soft'-saturation. PA's are characterised by amplitude (AM) and phase (PM) responses and an additional dimension, where the PA's output does not have a one-to-one relation with instantaneous input, referred to as 'memory'. Memory effects can be further characterised as 'slow' and 'fast', which are caused by thermal fluctuations, gain ripples and also reactive impedances in the design. PA's

are modeled using Volterra series[5] or simplified versions thereof, i.e., Weiner, Hammerstein, Weiner-Hammerstein combinations and Memory Polynomials.

DPD schemes depend on an 'expansion' which is the inverse of 'compression' observed in PAs as they approach hard saturation. The 'expansion' involves generating larger signals for the given inputs as consequently leads to an increase in the Peak-to-Average-Power-Ratio (PAPR) metric of the amplitude envelope of the Baseband signal. An increasing PAPR adversely impacts circuit design because the deviation from the nominal power increases which manifests in designing with bigger margins. For this reason Crest-Factor-Reduction (CFR) algorithms that limit the PAPR of the signal, are often bundled together with DPD processes. In CFR, the in-channel quality of a signal (EVM) is typically traded-off with the leakage (ACLR, SEM) performance of the wanted signal. The EVM budget allocated to DPD-CFR is often a significant portion of the overall requirement (typically, 3%-5%). CFR and the EVM impact are both critical and therefore incorporated into the performance budgeting. Assumptions made in this work are based on measurement results made available by engineers of NXP Semiconductors, Smithfield, USA.

A significant issue in DPDs today is the limited speed, bandwidth and dynamic range of processing solutions (typically FPGAs or ASICs) that process various parameters in the mathematical models and the correction required to the signal. Pre-characterised Look-Up-Tables (LUT) which speed up the correction are also used, but although dynamic, these are relatively inflexible in that PAs need to be individually characterised under different conditions for this purpose. The accuracy, speed and (baseband) bandwidth of the processing solutions together with the complexity of the modeling determine the maximum correctable bandwidth of the signal. We observe that while the RF chain that up-converts and amplifies the signal to drive the inputs of the PA is relatively wide-band, it is the PA design together with the DPD solutions which limit the RF bandwidth of the transmitter. Pre-distortion and the design aspects of the PA are quite involved and further details deviate from the main scope of this work. For this reason we include a caveat here that a detailed analysis of the PA are not included in this work and only working assumptions are used.

3.3.2 Topology or Access scheme

As far as the topology is concerned, 2G-TDMA/FDD and 3G-FDD systems are relatively ubiquitous and dominant access-technologies in most geographies (excluding China, today). Although GSM/EDGE (TDMA/FDD) is a TDD topology on the UE, the BStn has always been FDD. This is because the GSM/EDGE BStn unlike the UE, continuously transmits and receives signals. For this reason, GSM/EDGE also lends itself to multi-mode operation together with UMTS-FDD and LTE-FDD on an FDD BStn. In order to address the demand for higher data rates, both GSM/EDGE and UMTS-WCDMA/HSPA have incorporated multi-carrier concepts, GSM/EDGE shifts to TDMA/FDMA (see Figure 3.2) adhering to the same analysis. In LTE this is done more explicitly by using allocating individual 'blocks' of time and frequency into a transmission resource structure called Resource-Blocks, to a User.

Some of the analyses in the following sections could also benefit the 3GPP TDD systems

[5]These model both the amplitude and phase non-linearity of the PA and modeling involves determining the Volterra series coefficients which sufficiently predict the PA's non-linearity.

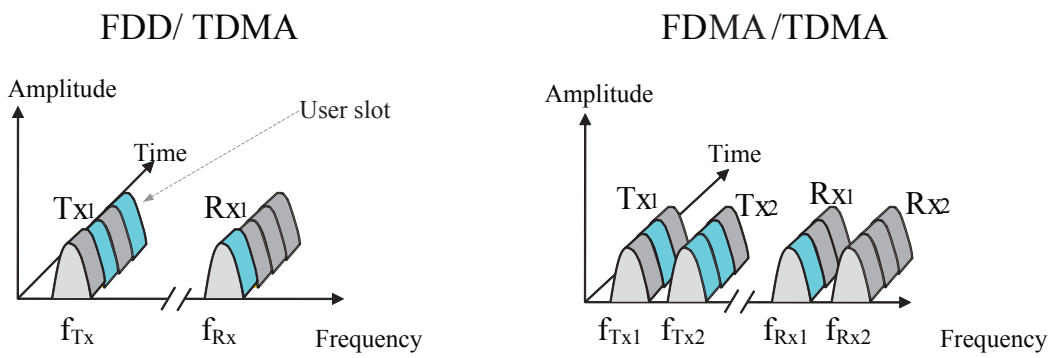

Figure 3.2: Multi Carrier GSM/EDGE TDMA/FDD & TDMA/FDMA

owing to certain similarities between TDD and FDD architectures. However, because of the nature of duplexing in TDD and also the dissimilarity in the sample rates for each of the modes, a multi-mode TDD transmitter could be challenging to implement. Apart from the reduced useable spectrum due to the need for guard-bands between the two topologies, combining FDD and TDD also faces technical challenges relating to the isolation between the two modes, which results in obvious issues of isolation.

A multi-standard transmitter chain can either be implemented as a convergent chain supporting simultaneous transmission or as a fully reconfigurable set of blocks. Reconfiguration is achieved by manually replacing mode specific blocks (e.g. PA module, filters etc.) offline or using software to tune the component performance, during (low traffic conditions of) operation itself. A convergent transmission chain designed based on the most severe performance specifications will likely be over designed for the other modes being simultaneously transmitted. This will be illustrated for the linearity requirements in Chapter 4. Such a methodology could result in large design margins and a relatively lower overall efficiency if attention is not given to proper budgeting. As will be identified in the sections below, a minimum degree of reconfigurability will be beneficial for more optimized performance.

3.4 Co-existence Issues

3.4.1 Available Spectrum

We discussed earlier about the parameters of the network eco-system playing a role in determining the feasibility of multi-mode operation within the particular band, in this case, the coexistence of multi-mode carriers within the same band. One of these parameters is the availability of licensed spectrum to any one network operator. The sequential evolution of telecommunication standards over several years has resulted in the network operators having to deploy new air interface technologies in the presence of existing network infrastructure supporting older standards. Owed to this the newer standards have always incorporated several

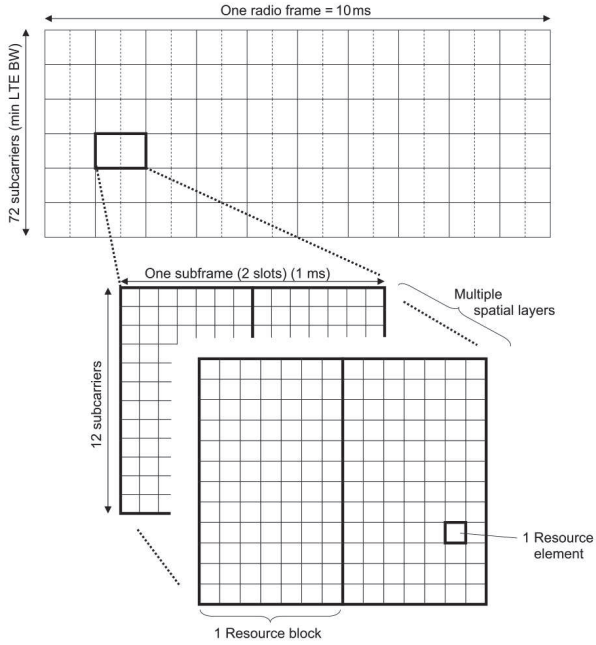

Figure 3.3: LTE Resource-Block on a time and frequency scale. *Source:* [20]

co-existence and backwards-compatibility mechanisms to mitigate interference to each other. This has set the stage for future evolutions, favouring multi-standard (multi-RAT) solutions. Older standards such as the GSM/EDGE are also being revised to be in accordance with the evolved technologies.

The available spectrum within a band is typically divided by regulatory authorities among several operators, who are issued standard specific licenses. The EGSM900 band has a DL bandwidth of 35MHz (960 − 925MHz), distributed roughly equally among operators within a certain geography. The Figures 3.3 and 3.4 [39, 40] illustrate spectrum allocation and the bandwidth allocated to each operator within France. They also indicate the technology specific licenses (for France), with regulatory authorities encouraging operators to provide IMT (WCDMA/HSPA or LTE) services in GSM bands, while retaining existing networks and services. The primary reason for to allow other services to operate in incumbent network bands is the economical operation that lower frequencies provide (3.2).

With each operator being allocated roughly 10MHz of spectrum in the 900MHz band, 20MHz of spectrum in the 1800MHz band and 15MHz of spectrum in the 2100MHz band, knowing that the GSM spectrum is shared by UMTS and given that the variable bandwidth of LTE facilitates its operation even in relatively narrow bandwidths, there exist several possibilities in which carriers of different technologies can be transmitted within these bands.

880-915 MHz / 925-960 MHz[2]

Operator	Frequencies (downlink)	Technology used (optional)	Licence duration, tradability
Bouygues Télécom	Very dense areas: 925.1 – 934.9 MHz Other areas: 925.1 – 934.9 MHz (except the 25 first channels which cannot be used around the military bases) and 945.1 – 949.9 MHz	GSM* (GSM currently deployed)	8 December 1994 – 7 December 2009, not tradable
Orange France	Very dense areas: 935.1 – 947.5 MHz Other areas: 935.1 – 945.1 MHz	GSM or UMTS (GSM currently deployed)	25 March 2006 – 24 March 2021, not tradable
Société Française du Radiotéléphone	Very dense areas: 947.5 – 959.9 MHz Other areas: 949.9 – 959.9 MHz	GSM or UMTS (GSM currently deployed)	25 March 2006 – 24 March 2021, not tradable

[2] – In this band duplex separation is 45 MHz, uplink and downlink bands are equal in size

Table 3.3: Operator Downlink Spectrum Allocation for E-GSM900, France, 2008

1710-1785 MHz / 1805-1880 MHz[3]

Operator	Frequencies (downlink)	Technology used (optional)	Licence duration, tradability
Bouygues Télécom	Very dense areas: 1853.3 – 1879.9 MHz Other areas: 1858.3 – 1879.9 MHz	DCS	8 December 1994 – 7 December 2009, not tradable
Orange France	1808.1 – 1831.9 MHz	DCS	25 March 2006 – 24 March 2021, not tradable
Société Française du Radiotéléphone	1805.1 – 1807.9 MHz and 1832.1 – 1853.1 MHz	DCS	25 March 2006 – 24 March 2021, not tradable

[3] – In this band duplex separation is 95 MHz, uplink and downlink bands are equal in size

Table 3.4: Operator Downlink Spectrum Allocation for E-GSM1800, France, 2008

3.4.2 Frequency Reuse Factor

The frequency reuse factor (FRF) is another parameter which is based on the interference tolerance of the access technology and plays an important role in co-existence scenarios. FRF is defined as the ratio of the occupied spectrum at one cell-site to the total spectrum available to that network operator. The value indicates which transmission channels can be re-used within a set of neighboring cells and limits the number of active carriers at a cell-site. A higher value indicates higher spectral use, therefore more channels per cell-site, resulting in fewer BStn installations. In the case of the GSM/EDGE, the frequency reuse factor (typically improving from $\frac{1}{7}$ to $\frac{1}{3}$ for omni directional base stations, and potentially better for EDGE) is determined at a network performance level based on factors such as the *QoS*, handover performance, inter-operability, interference (C/Ic), cost etc. WCDMA/HSPA base stations sharing the same frequency, having a reuse factor of 1 implying that all cell sites could theoretically share the same channel frequency[6]. As for LTE, the frequency factor could vary roughly between 1 (near cell site) and $\frac{1}{3}$ (near cell limits), depending on the distance from the Base Station, known as a variable frequency-reuse. Given a multi-mode band, knowledge

[6] This is feasible when cells sites use different scrambling codes for transmission

of the frequency reuse factor mechanics allows the RF design engineer dynamic range and bandwidth limitations that arise from operating multiple carriers on a BStn. The issue of dynamic range will be discussed further in the Chapter 4.

3.4.3 Spectrum Reuse or Re-farming

The issue of recovering spectrum from incumbent, but less efficient bands to re-use them for more efficient technologies has been introduced in Section 3.2. Extending WCDMA/HSPA and LTE operation to GSM bands does not imply immediate cessation of GSM services [7] but is actually intended to harmonize the transition from GSM to the more spectrally efficient technologies over a period of time. With advanced power control, cooperation and resource management strategies, UMTS and LTE standards (which are also backwards compatible with GSM/EDGE) are well suited to co-exist with the older technology in the same band. The requirements for the coexistence (coordinated and uncoordinated operation) between UMTS and GSM networks in these bands have partially been covered in their respective 3GPP standards (although not for same band of operation) and to a certain extent also in [41]. Recent releases of the GSM/EDGE standards and their evolutions are also focused on harmonizing performance and coexistence requirements with the newer standards. Because of the inter-carrier distortions, the RF design engineer would need to pay particular attention to the frequency separation between the similar and multi-mode carriers and also to the relative carrier power levels which will depend on network-level settings and hardware limitations. Examples of this are discussed in Chapter 4.

3.4.4 Multi-Operator resource sharing

With base stations offering multi-band solutions (not limited to region specific bands, as is most likely the case) spectrum allocation no longer remains the primary constraint for design. Manufacturers such as Nokia Siemens Networks propose different degree of sharing resources [42] such as

- Roaming-Based-Sharing: an operator can share another operator's RAN indirectly via the core networks controlling the RAN
- RAN-Sharing: operators have dedicated carriers but share network elements up to and including the radio network controller (RNC), or possibly only the base stations
- Site-Sharing: shared equipment room, transmission equipment, power supply, roof top resources such as towers, poles and outdoor wire channels and other auxiliary facilities such as monitoring equipment and air conditioning

Some examples are illustrated in the Figure 3.4 [43].

In such a scenario, there are multiple bands to cover and shared resources to operate. Consequently, spectrum allocation no longer becomes a limitation for hardware design. While

[7] in fact GSM is expected/predicted to last at least until 2020

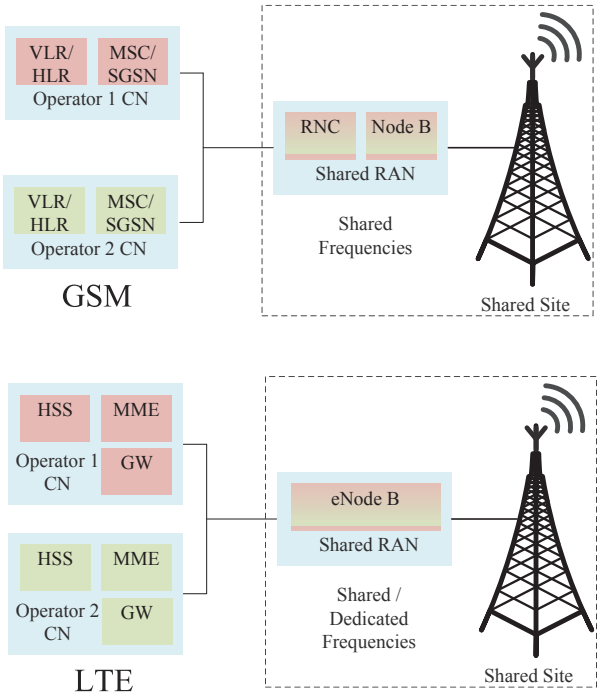

Figure 3.4: Base Station with Operator Shared-carrier and Dedicated-carrier RAN sharing for LTE/WCDMA and GSM/EDGE (Based on http://www.telecom-cloud.net/

Roaming-Based-Sharing seems a significant challenge to implement[8], RAN-sharing and Site-Sharing already being implemented. Implementation then becomes dependent on the economics of operation and performance potential of the components by design. By increasing the number of carriers, several issues arise. Among them block level implementation issues such as inter-modulation, cross-modulation, broadband noise etc. are prominent and we will discuss these in the subsequent chapters. We highlight a critical limitation for design, the composite Peak-to-Average-Power-Ratio (PAPR) of the combination of simultaneously transmitted carriers which defines the dynamic range of the signal, which will be discussed in Section 4.3.9. While the peak PAPR is not of significant importance, it is the PAPR which occurs with a probability of greater than a threshold of 0.0001% (or a probability of 0.000001) known as the 'level of confidence' probability that poses a problem. This level of

[8]One of the issues in implementing this flavour of sharing is that with nomadic carriers moving between agnostically between BStns, it becomes quite an issue to optimise the throughput metrics (or loosely, the SINR) of a carrier. This is particularly true of WCDMA carriers where interference control mechanisms in the higher layers of the network stack depend on the interference in the cell environment. With a changing cell environment, this could become challenging.

PAPR of a signal is obtained from a plot of the Cumulative Complementary Distributive Function (CCDF) of the PAPR of the transmitted carriers[9] In Chapter 4 we present simulation results on the PAPR of multi-mode transmissions involving different combinations of carriers, performed in ADS and support them by laboratory measurements where possible.

Another plausible challenge that arises from Roaming-Based-Sharing is the issue of having independent power control settings per carrier. In Chapter 5 we present this topic in further detail. This subject is currently open within the 3GPP workgroups, hence we assume that RAN-sharing with independent power control is a foreseeable challenge to design for and thereby, present the system-analysis for a multi-mode transmitter supporting such a feature, by means of a variable-gain Analog-Quadrature-Modulator (AQM) (see Chapter 6).

[9] A caveat here is that the *Level-of-Confidence PAPR* is relevant for design assuming only CFR - Crest Factor Reduction. With the addition of Digital Pre-distortion or DPD, the entire probability distribution curve of the PAR must be considered. We will discuss this further in Chapter 4.

Chapter 4

Transmitter - System Level Analysis

4.1 Architecture of a contemporary Base Station radio transmitter

The architecture of a typical BStn transceiver card was shown in Figure 2.2. Referring to transmitter in the figure, we can see that the modulated carrier aggregate is generated in the Baseband engine (typically composed of ASICs) and converted from the digital to the analogue domain by means of a high-dynamic range multi-bit DAC. The Baseband processing also implements Digital pre-Distortion (DPD) and CFR necessary to improve linearity and relax the dimensioning of the transmission chain. Despite the appellation, the DAC on the transmitter achieves many functions including - interpolation, complex frequency domain up-conversion (see (3.1)) and also the digital to analog conversion. Signal interpolation rates on the DAC are typically $2\times/4\times/8\times$, depending on the choice of IF frequency, the bandwidth of the signal and the quality of the digital to analog conversion clock at different frequencies. The interpolation generates replicas or aliases at multiple frequencies (see Figure 4.1, which are rejected by a reconstruction filter (see Chapter 6, Figure 6.3).

The figure shows consecutive Low-Pass Filters (LPF) being used to select the signal in the first Nyquist zone. If a higher order interpolation image is required, the LPF can be followed by a High-Pass FIR Filter (HPF) (see [44]) and a Band-pass Anti-Aliasing Filter (AAF). The Spurious Free Dynamic Range (SFDR) usually degrades in higher Nyquist zones, so this flexibility is manufacturer specific. The selected signal is then up-converted to the wanted carrier frequency by mixing with a Local Oscillator (LO). The architecture of the Mixer and the LO path that supplies the Mixer with switching signals will be discussed further in Chapter 6. A Variable Gain Amplifier (VGA) amplifies the Mixer output signal and completes what is referred to as the 'low-power' RF chain on the BStn. The VGA is also responsible for compensation of any loss or fluctuations in the gain of the RF chain. This low-power section of the transmitter has significant demands on the performance owing to the fact that the DPD only models the PA transfer function and assumes the contributions of the low-power section to be negligible. Practically however, the section is non-ideal. Consequently, DPD

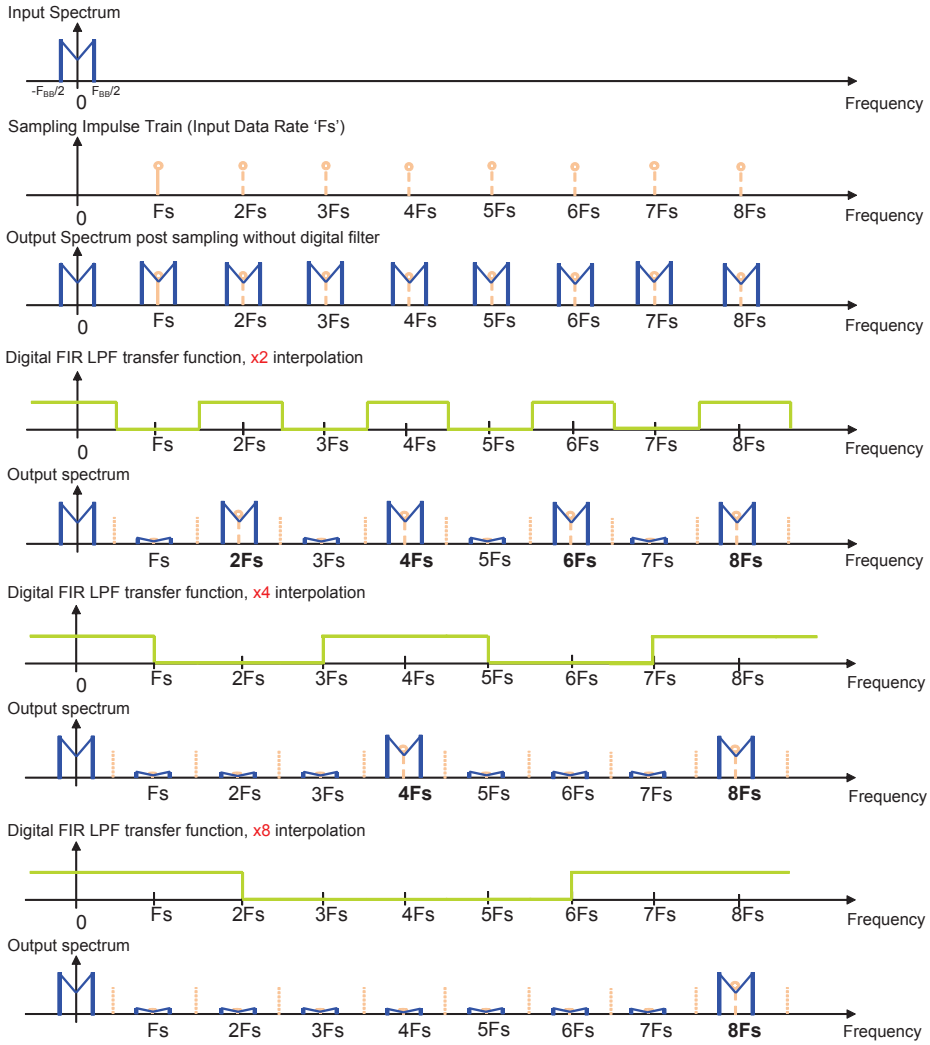

(a) Interpolation with Up-sampling and ideal Low-Pass/Low-Pass/Low-Pass FIR Filter response. Sample-hold Sinc pulse roll-off not indicated.

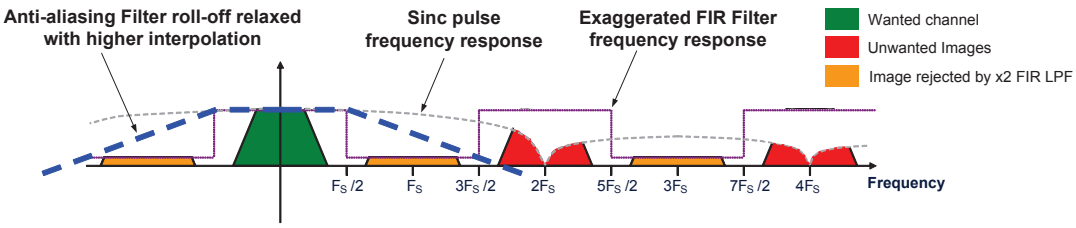

(b) Anti-Aliasing Filter requirement for 2x Interpolation

Figure 4.1: Illustration of the DAC interpolation (with LPF) and subsequent relaxation of the Anti-Aliasing Filter requirements

algorithms also incorporate calibration mechanisms to compensate for non-idealities and is part of a field that is being broadly referred to as 'Dirty-RF' compensation [45, 46].

The VGA output drives a pre-driver amplifier which in turn drives the PA module, typically implemented in multiple stages - a driver amplifier and a high-power amplifier (HPA). Although this multi-stage structure comes with a few penalties, it is not always easy to incorporate all the objectives required of an amplifier, into one single stage. The most efficient operation of the amplifier is when it is close to compression. However this is also a very non-linear region. For this DPD schemes are deployed. The working of DPD is quite complex and its treatment is beyond the scope of this work. A brief treatment of the concept of pre-distortion is available in Appendix A.1.

The PA module is connected by means of a isolator to the duplex filter. The duplex filter connects to the antenna structure and provides isolation between the Tx and Rx frequencies. Any noise or signal that leaks into the Rx path desensitises the receiver. Duplex filter rejection ratios are therefore typically between 50 and 80dB. A coupler is also behind the isolator (not shown here) and the duplex filter, sensing the PA output and providing an attenuated signal (typically -30dB) to the feedback path. The feedback path serves to detect the non-linear output of the PA for purposes of establishing the right coefficients in the DPD algorithms.

Each stage of the transmitter adds to the signal distortion degrading the quality of the signal. The signal quality needs to adhere to specifications set for the transmitter, by the Radio-Access-Network (RAN) work-group 3GPP, in order to guarantee a certain throughput in the network. We discuss some of these details in the following sections.

4.2 Synthesizing Link-Level Performance Requirements from System-Level Requirements

The system-level performance of a transmitter in the physical layer is broadly characterised by the 3GPP Standards using the following metrics:

- Output Power

  Output Power levels

  Output Power Control dynamics and range

- Transmitted signal quality

  Frequency accuracy

  Error Vector Magnitude (EVM) or Modulation accuracy

  Timing alignment, Filtering specifications (if any)

- Output RF Spectrum Emissions (or Spectrum Emissions Mask - SEM)

  Occupied Bandwidth

  Adjacent Channel Leakage power Ratio (ACLR, ORFS)

  In-Band Unwanted Spectral Emissions (including broadband noise floor)

  Out-of-Band Spurious Emissions

Coexistence spectral requirements

- Other special requirements or relaxations

Each of the access technologies has its own set of specifications and these are derived from exhaustive simulations performed by the participants to the RAN work-group (WG4) of 3GPP. For example, the modulation accuracy is set to be that value which results in a degradation of the throughput to 95%. This is calculated as an imperfect EVM induced throughput loss for all users, or, as a capacity reduction for UE's using the corresponding modulation scheme for which the modulation quality is calculated [47], assuming the transmission has sufficient SNR for correct estimation. The throughput loss when stripped down to its bare meaning is the Carrier to Noise, Distortion and Interference ratio (C/NDI) seen by the UE concerned.

Starting from the 3GPP Standards requirements, we can translate the system-level tolerance (EVM, ACLR, SEM etc.) specifications to link-level performance requirements by establishing a relationship between the distortions mechanisms in the transmitter and how they impact these 3GPP metrics. This was what we referred to as the mechanism of system analysis illustrated in Figure 2.7. We begin by analysing the EVM specification.

4.2.1 Output Power

There exist different classes of BStns (Wide-Area, Local-Area and Home), for each of which a maximum power level is specified in keeping with the EIRP (equivalent isotropically radiated power) specified by the regulatory bodies. This output power from a BStn is measured for the total carrier-aggregate, at the antenna connector, also referred to as the Antenna Reference Point (ARP). In Wide-Area BStns, the output power levels are typically a prerogative of the operator due to the varying coverage and throughput optimisations of the network and is not explicitly specified in the standard. For all calculations in this document we refer to 49dBm (80W) of average output power which is common in the industry.

Power control in BStns is necessary to ensure not only minimum interference to other networks but also to guarantee minimum coverage and throughput for users within the network. GSM/EDGE mandates 15 steps of power control levels with a step size of 2dB ±1.5dB at a rate of $\frac{1}{480\text{msec}}$ (see clause 4.2.1 of [48], see Chapter 2 of [49]). WCDMA/HSPA requires a minimum 18dB of dynamic range of power control, in 1.0dB steps with an accuracy of ±0.5dB at a rate of $\frac{1}{1500slots}$sec (see Section 6.4 of [50]). LTE, with its aggressive frequency scheduling which is also variable with distance from Cell, does not specify DL power control for macro cells, but specifies a per carrier dynamic range of 20dB which is assumed constant unless updated by the Reference Signal to the UE in the DL [19]. We observe that these varied requirements become an issue when operating multi-RAT (Radio Access Technology) BStns and we will discuss this further in the next chapter.

4.2.2 Error Vector Magnitude

The Error Vector Magnitude (EVM) is a modulation-quality metric used in the communication standards, that measures the error between the transmitted signal and the ideal signal. This is calculated as the magnitude of the vector difference between the transmitted

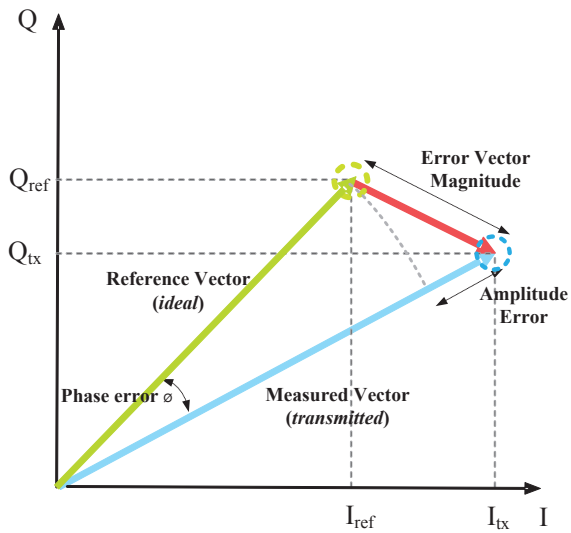

Figure 4.2: Error Vector Magnitude for one symbol on the constellation diagram

and reference vectors, represented on a complex plane, i.e., the constellation diagram. The constellation diagram shows the complex vector at a snapshot in time. In practical measurements, a modulated reference data stream or a vector set $\boldsymbol{r}_k$, where $k = 0, \ldots, N$ symbols, as described by the 3GPP Standards test specifications, is transmitted through the transmit chain. The distorted signal $\boldsymbol{m}_k$ at the output port or antenna connector is then detected, demodulated and quantified on the constellation diagram corresponding to the modulation scheme used in the test vector, against the reference data (see Figure 4.2). The phase of the error vector (not to be confused with phase-error, or the error in phase between the transmitted vector and the ideal) has little analysis value because of the randomness of data and is ignored. The error magnitude $\boldsymbol{e}_k$ is represented as a ratio or percentage of the reference vector magnitude. The result is measured for specified sizes of data-sets (e.g. bursts) and is typically averaged or measured over several such data-sets.

$$\mathrm{EVM}_{R.M.S.} = \sqrt{\frac{\frac{1}{N} \cdot \sum_{k=0}^{N-1} |\boldsymbol{r}_k - \boldsymbol{m}_k|^2}{\frac{1}{N} \cdot \sum_{k=0}^{N-1} |\boldsymbol{r}_k|^2}} = \sqrt{\frac{\frac{1}{N} \cdot \sum_{k=0}^{N-1} |\boldsymbol{e}_k|^2}{\frac{1}{N} \cdot \sum_{k=0}^{N-1} |\boldsymbol{r}_k|^2}} \tag{4.1}$$

4.2.2.1 3GPP System-Level EVM Requirements

Transmitter EVM, being comparable to receiver Bit Error Rate (BER), has a direct impact on the system throughput and is therefore specified by the 3GPP standards that define system performance requirements. The mechanisms of the measurement (time and ensemble[1] averaged) and the individual tolerances for signal distortion (see Table 4.1) differ significantly

[1]EVM is also measured and averaged over combinations of time, frequency and carrier data elements.

Table 4.1: Comparison of Downlink R.M.S. EVM requirements[a] for LTE, UMTS and GSM

Modulation Scheme	LTE	UMTS-WCDMA	GSM/EDGE
QPSK	$\leq 17.5\%$	$\leq 17.5\%$	$\leq 8.0\%$[B]
16-QAM	$\leq 12.5\%$	$\leq 12.5\%$	$\leq$ **5.78**%[C]
64-QAM	$\leq 8.0\%$	-	-

[A] Additional requirements for Peak-EVM (reserved for transitory distortions with a lower probability of occurrence and/or for the highest symbol-distortions) and 95th-percentile-EVM (with a higher tolerance) also need to be satisfied.
[B] 8-PSK also. 7.0% before the combining equipment.
[C] For 16/32 QAM under normal conditions, higher symbol rate. Includes passive combining equipment, and an Origin Offset Suppression (OOS) error of 35 dB (or $10^{-35/20} \times 100\%$). Or, a more demanding requirement of 4.0% and OOS, if excluding combining equipment.

among the standards [19, 48, 50]. In its bare form, the R.M.S. signal power is measured over several symbols of various constellations from the different carriers combined, with the EVM being essentially a ratio of the square root error power and the square root signal power for a given symbol, both being normalized to R.M.S. carrier power.

However, for multi-mode transmission, we would need to know how the requirements compare with each other and how a common EVM can be drawn up. The EVM is measured at a stage where symbols that are detected and demodulated still have most of the error correction mechanisms embedded within them. This is evident when we compare the requirements for the same modulation scheme in GSM/EDGE and WCDMA or LTE. With GSM/EDGE being the older, less efficient standard, has a lower tolerance for errors in the transmitted signal and consequently a tougher (i.e.,lower) EVM requirement. Having established this, we are left with comparing the toughest EVM requirement in GSM/EDGE, WCDMA and LTE. It is possible to determine the reference EVM (R.M.S.) limit for multi-mode by simply referring to the toughest EVM requirement for the modulation scheme that is common among the three standards, in this case, i.e., 16/32−QAM in GSM/EDGE. This is because the 3GPP EVM that is specified by the Standard already incorporates all of the corresponding tolerances for the transmitter.

4.2.2.2 EVM Contributors

Referring to the architecture of Figure 2.2, there are different possible imperfections in the transmit chain that induce signal distortions. These distortions can be analyzed from the distinguishable effect each imperfection produces on the constellation diagram (see Section 4.2.3). When limited to a first-order approximation of distortions, a transmit chain has the following typical types of impairments:

- I/Q path imbalances (quadrature skew, gain, path delay)
- Phase(-noise) and (uncompensated) frequency error
- Non-linearity distortions (AM/AM, AM/PM)
- Carrier leakage (DC offset, port-port isolation)

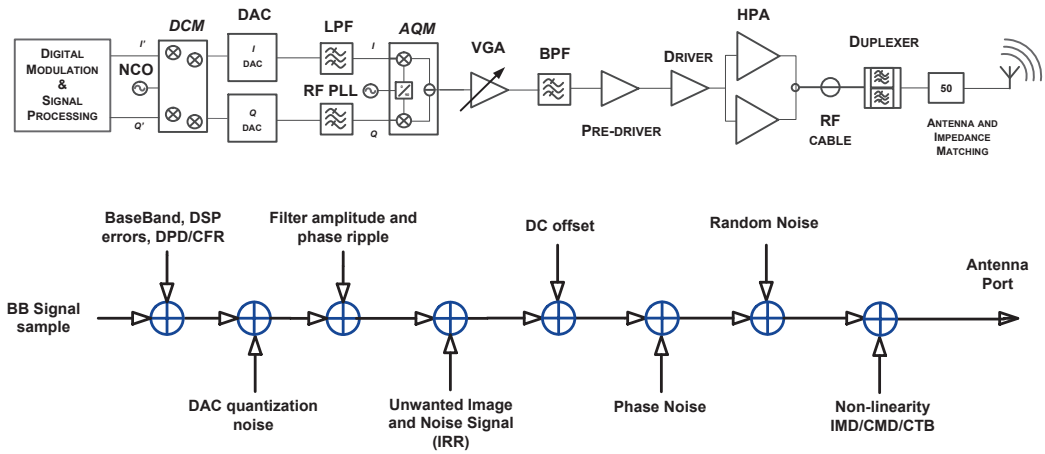

Figure 4.3: Transmitter impairments that contribute to the EVM

- Random broadband noise
- DSP errors (also including quantisation noise, DPD-CFR)

Here we ignore the Spurious and Transient effects. Assuming reasonably that the various imperfections and also that the signals themselves are all sufficiently uncorrelated, the first order approximation of the total R.M.S. error, i.e., $\mathrm{EVM}_{\mathrm{net}}$, can be expressed as the quadratic sum of its principal constituents (also R.M.S.), in the form,

$$\begin{aligned}\mathrm{EVM}_{\mathrm{net}} \approx \Big[& (\mathrm{EVM}_{\mathrm{IQ\ Imbalances}})^2 + (\mathrm{EVM}_{\mathrm{Phase,Frequency\ Err.}})^2 \\ & + (\mathrm{EVM}_{\mathrm{Non\text{-}Linear\ Distortion}})^2 + (\mathrm{EVM}_{\mathrm{Random\ Noise}})^2 \\ & + (\mathrm{EVM}_{\mathrm{DSP,\ Baseband\ Err.}})^2 \Big]^{1/2}\end{aligned} \tag{4.2}$$

where the subscript under the EVMs indicates the type of transmitter imperfection contribution to the error. Also, because they are assumed uncorrelated, the net R.M.S. error can also be directly obtained taking the time and ensemble average of the cumulative error $\mathrm{EVM}_{\mathrm{net}}$.

It is worth pointing out that the method in (4.2) is not so pessimistic, although it would be more accurate to first combine separately, all the amplitude errors and all the phase errors in the transmitter, either by quadratic summation or linear addition (depending on the errors) and then follow it up with translating these distortions to EVM using equations that we will describe in the next sections. The total EVM budget can then be obtained by a simple quadratic sum of the resulting EVMs from the previous step.

4.2.3 Impact of Transmitter Impairments on Error Vector Magnitude

Based on simplified assumptions, several authors including [51–54] have developed useful analytical and semi-analytical expressions relating the magnitude of different transmitter

imperfections (in (4.2)) to a corresponding EVM contribution. This relationship allows us to derive the preliminary performance requirements at link level. It is perhaps worth mentioning that the reference EVM in all access technologies is collected after applying the modulated symbols to a baseband pulse-shaping filter. The pulse-shaping filter is used in the baseband before transmission, to achieve a tradeoff between the in-channel and leakage performance and is therefore qualified separately from transmitter imperfections. In the case of GSM/EDGE, a linearised GMSK pulse (i.e., the main component in a Laurent decomposition of the GMSK modulation, specified by clause 3.5 of [55]) is used. For WCDMA transmissions, a root-raised cosine (RRC) with frequency domain roll-off of $\alpha = 0.22$, specified by clause 6.8.1 of [50] is deployed. In the case of LTE a simple rectangular pulse shape with a time period that is inverse of the sub-carrier spacing, is used in the DownLink (DL). For the sake of simplicity, we do not represent the filter in the calculations as this would complicate the analysis. Including the effect of the baseband filter would involve convolving the modulated symbols with the impulse response of the filter in time domain [56], making the equations tedious. Similar assumptions have been made by the authors of the works cited above, in deriving their respective equations. In all cases, we will discuss the sources of these errors in further detail in the next chapter for performance budgeting. Here we only look at the impact of the errors on the EVM and how the total EVM can be broken down into its constituents.

Relationship between EVM and SNR Any signal that is passed through a transmitter experiences both multiplicative (IQ imbalances, Non-linearity, Phase noise etc.) and additive (broadband noise, DC offset) distortions. If we were to assume that the signal is only corrupted by the noise in the system, assumed AWGN, then (4.1) reduces to

$$\mathrm{EVM}_{R.M.S.} = \sqrt{\frac{\frac{1}{N}\cdot\sum_{k=0}^{N-1}|\boldsymbol{N}_k|^2}{\frac{1}{N}\cdot\sum_{k=0}^{N-1}|\boldsymbol{r}_k|^2}} \tag{4.3}$$

where, $\boldsymbol{N}_k$ is the noise at each symbol instant. If this is integrated over sufficiently large values, we can make the simplification,

$$\begin{aligned}\mathrm{EVM}_{R.M.S.} &= \sqrt{\frac{N_o}{E_s}} \\ &= \sqrt{\frac{1}{SNR}}\end{aligned} \tag{4.4}$$

where, $E_s = \frac{1}{M}\sum_{k=0}^{N-1}|S_m|^2$ is the average symbol (S_m) energy independent of the modulation order M. In [57] it has been shown that the use of preambles or pilot symbols to measure EVM, in all access technologies, validates the simplification that $EVM_{\mathrm{R.M.S.}} = \sqrt{\frac{1}{SNR}}$ (in this case, $\mathrm{EVM}_{\mathrm{Random\ Noise}} = \sqrt{\frac{1}{SNR}}$ due to broadband random noise), in the absence of all other transmitter imperfections. Without the aid of pilot data sequences, the EVM to SNR ratio would be dependent on the modulation order or more broadly, the modulation scheme. Consequently, we would then not be able to relate the distortions to the EVM in

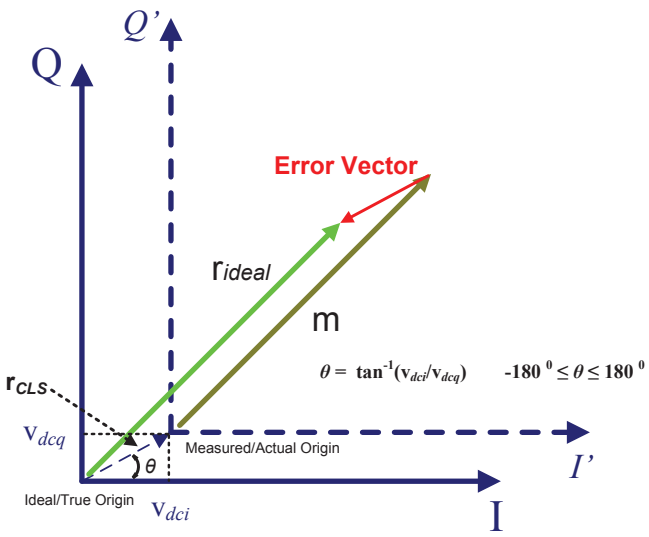

Figure 4.4: Error Vector Magnitude due to IQ DC Offsets

the simplified manner for all modulation schemes, as we do in the following sections. EVM is a metric for all transmitter impairments not just noise, so we make the assumption that the SNR is high enough for the transmitted symbols to be detected correctly and for the EVM to be measured accurately.

As a caveat, here we make working assumptions for a first approximation of the analysis. As a consequence the EVM predicted by these equations is not fully representative of the magnitude of EVM for the given distortions. The EVM analysis mechanisms are developed here with the intention of relating their magnitude to distortion mechanisms but it is to be noted that we are stretching sinusoidal EVM expressions to also understand the degradation of EVM in modulated signals, to enable better budgeting.

4.2.3.1 LO Leakage and Base-band DC Offset

LO leakage occurs as harmonics of the LO signals that appear directly through leakage at the RF port or by LO signals combining with the complex DC imbalances in the transmitter. In the case of the non-OFDM systems (GSM/EDGE, UMTS-WCDMA), the corresponding linear EVM over N symbols has been shown to be

$$\mathrm{EVM_{CLS}} = \left[\frac{\frac{1}{N} \cdot \sum_{k=0}^{N-1} \left(v_{\mathrm{dc,i}}^2 + v_{\mathrm{dc,q}}^2 \right)}{v_{\mathrm{RMS}}^2} \right]^{\frac{1}{2}} \tag{4.5}$$

where, $v_{\mathrm{dc,i}}^2$, $v_{\mathrm{dc,q}}^2$ and v_{rms}^2 denote the DC offsets in the I and Q paths and the R.M.S. voltage of the signal over N symbols. The impact of DC offsets is illustrated in Figure 4.4.

Carrier Leakage Suppression (CLS) is an explicit requirement in GSM transmissions and is technically referred to as Origin Offset Suppression (OOS). The specification for OOS is 35dB in GSM, equivalent to a linear EVM of $10^{\frac{-35}{20}} = 1.78\%$.

For LTE this is somewhat more complex due to the FFT operation (in the receive). For OFDM signals that are directly up-converted from Baseband, the LO mixes with the DC offsets or leaks directly to the RF, resulting in a tone at RF. In LTE, the DC index sub-carrier is usually unused and can be ignored. Furthermore, in LTE, (see clause E.3 of [19]), the Frequency and timing offsets among other impairments, are assumed compensated at the instant of transmitter EVM estimation. We therefore need to make no budget for the EVM due to Frequency Offsets in LTE[2]. However, in the presence of any residual frequency offset known as Carrier Frequency Offset (CFO), the DC offsets when transmitted and later down-converted, will end up having a frequency component. The authors of [58] present the analysis of DC offset in the transmitter depending on how well the measurement equipment compensates for the CFO. If the symbol is represented as

$$x(n) = \frac{1}{\sqrt{N}} \sum_{r=\frac{-N}{2}}^{\frac{N}{2}-1} X_r \exp^{j2\pi nr/N} + \eta_{\mathrm{DC}} \tag{4.6}$$

where $n = 0, 1, \ldots, N-1$, with N being the number of sub-carriers in the OFDM transmission, η_{DC} corresponds to the normalised constant in time DC offset in the transmitter, X_r is the transmitted modulation symbol corresponding to the rth sub-carrier. We use the subscripts r and m to denote the reference and measured sub-carrier indexes respectively. If we assume the channel to be flat, noiseless, for the sake of simplicity and that there are no other impairments in the transmitter or the receiver (but for the frequency offset), the corresponding received signal after CFO compensation and Discrete Fourier Transform (DFT) is

$$Y_m = \frac{1}{\sqrt{N}} \sum_{m=\frac{-N}{2}}^{\frac{N}{2}-1} \left(\frac{1}{\sqrt{N}} . \sum_{r=\frac{-N}{2}}^{\frac{N}{2}-1} X_r \exp^{j2\pi nr/N} + \eta_{\mathrm{DC}} \right) \exp^{-j2\pi nm/N} \tag{4.7}$$

where, $m = -\frac{N}{2}, -\frac{N}{2}+1, \ldots, \frac{N}{2}-1$. If $m = r$, the resulting DC content per symbol is

$$I_m^{\mathrm{DC}} = \eta_{\mathrm{DC}} \sqrt{N} \exp^{j2\pi(m-\Delta_\epsilon)(N-1)/2N} \frac{sinc(m-\Delta_\epsilon)}{sinc((m-\Delta_\epsilon)/N)} \tag{4.8}$$

where $\Delta_\epsilon = (\Delta f_r - \Delta f_m)/T_s$ is the normalised residual error after imperfect CFO compensation between the measured and received clocks and T_s is the OFDM symbol period. Evidently, the transmitter DC offset η_{DC} has a frequency component depending on the residual error of measurement. In LTE, each carrier is modulated with an independent modulation scheme, as indicated by X_r above. The EVM per modulated symbol is then obtained from the SNR

[2]Here we ignore the Doppler frequency shift error between the UE and the BStn because the UE uses the BStn signals as reference.

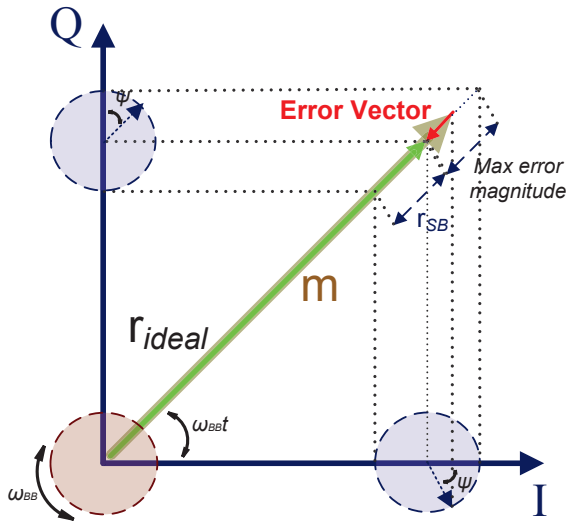

Figure 4.5: Error Vector Magnitude due to IQ Gain and Phase imbalances [52]

as

$$EVM_{\mathrm{CLS},m} = \frac{1}{\sqrt{SNR}} = \left[\frac{\mathbb{E}\left[|Y_m|^2 \frac{\sin^2(\pi\Delta_\epsilon)}{N^2 \sin^2((\pi\Delta_\epsilon)/N)}\right]}{\mathbb{E}\left[|I_m^{\mathrm{DC}}|^2\right]}\right]^{-\frac{1}{2}} \tag{4.9}$$

where $\mathbb{E}[.]$ denotes the expectation. We ignore the distortion from the CFO. We leave it here because in LTE, there are several dimensions of averaging (i.e., w.r.t. time, frequency, data sets) to be made and that would make equations complicated.

4.2.3.2 IQ-path Imbalances

If the phase between the in-phase 'I' and the quadrature 'Q' paths is anything but 90° (i.e., quadrature skew) and/or their ratio of amplitudes is anything but 1 then the constellation diagram is skewed in the manner shown in Figure 4.5. Differences in the timing of signals in the two paths also amounts to phase delay and has a similar effect. Imbalance rejection leads to non-ideal suppression of the other half sideband (image) from the up-conversion. A image signal that falls into a signal of interest (not a concern in Direct up-conversion transmitters) wideband, would cause its quality to degrade [3]. For the sake of simplicity, only imbalances in amplitude ($\epsilon_A = \epsilon/2A_{\mathrm{IQ}}$) and phase ($\Delta\theta = \frac{\Delta\phi}{2}$), are considered here.

For a time domain RF signal (or symbol in the case of OFDM systems) with amplitude

[3] An image signal that falls out-of-band will need to conform to the transmitter spurious specifications limit. For a general case, this is −90dBm/Hz

and phase imbalances, its baseband equivalent (see [54]) is represented as

$$\begin{aligned} x(t) &= \big[(1+\epsilon_A)\cos\Delta\theta x_I(t) + (1+\epsilon_A)\sin\Delta\theta x_Q(t)\big] \\ &\qquad + j\big[(1-\epsilon_A)\cos\Delta\theta x_Q(t) + (1-\epsilon_A)\sin\text{-}\Delta\theta x_I(t)\big] \\ &= (\cos\Delta\theta + j\epsilon_A\sin\Delta\theta)x(t) + (\epsilon_A\cos\Delta\theta - j\sin\Delta\theta)x^\star(t) \\ &= \alpha\cdot x(t) + \beta\cdot x^\star(t) \end{aligned} \tag{4.10}$$

where $x_I(t)$ and $x_Q(t)$ refer to the In-phase and Quadrature components of the baseband symbol respectively, '$\star$' indicates the complex conjugate and

$$\begin{aligned} \alpha &= \cos\Delta\theta + j\epsilon_A\sin\Delta\theta \\ \beta &= \epsilon_A\cos\Delta\theta - j\sin\Delta\theta \end{aligned} \tag{4.11}$$

Consequently, $\text{EVM}_{\text{IQ Imbalances}}$ for non-OFDM systems is given by [51]

$$\begin{aligned} \text{EVM}_{\text{IQ Imbalances}} &= \sqrt{\frac{1}{SNR} + 2\left(1 - \sqrt{\frac{1}{1+IRR}}\right)} \\ \text{EVM}_{\text{IQ Imbalances}} &\approx \sqrt{IRR} \quad \text{, if } SNR >> 1 \text{ and } IRR << 1 \end{aligned} \tag{4.12}$$

where, $IRR = 10^{\frac{IRR_{\text{dB}}}{20}}$ is the Image Rejection Ratio expressed as the linear ratio $\frac{P_{\text{image}}}{P_{\text{wanted}}}$ using the mismatch terms ϵ_A (or[4] ϵ/A_{LO}) and $\Delta\theta$. Refer to Section (see 6.69) for the derivation. In the case of OFDM signals, the authors of [53] suggest an expression for the EVM due to IQ imbalances,

$$\text{EVM}_{\text{IQ Imbalances}} = \sqrt{\frac{\epsilon_A^2 + 2(1-\cos\Delta\theta)}{\frac{X_{m,\max}^2}{\mathbb{E}[|X_m|^2]}}} \tag{4.13}$$

where X_m and $X_{m,\max}$ correspond to the modulation symbol of the subcarrier, and its peak value. The denominator is identical to the Peak-to-Average-Power-Ratio (PAPR) of the modulation scheme. A table comparing PAPR values for complex different modulation schemes given by [59]. With a typical value for the IRR_{dB} is -40dBc, the $\text{EVM}_{\text{IQ Imbalances}} < 1\%$, giving values for ϵ_A and $\Delta\theta$ that correspond to the -40dB contour in Figure 6.31. DPD algorithms and DACs often incorporate correction (by upwards of 20dB, i.e., < -60dB or $< 0.1\%$) of the native IQ imbalance by compensation in the digital domain, relaxing the EVM requirements for the baseband signal and also the AQM. The Figure 4.6 shows the simulated (EVM) impact of transmitter non-linearity in the considered access technologies.

4.2.3.3 Phase Noise and Frequency Error

Phase- and uncompensated frequency-errors when integrated over signal bandwidth, produce a phase rotation ϕ_n (radians) on the symbol $\boldsymbol{r}_k$ as shown in Figure 4.7. This rotation is primarily attributed to the RF PLL and Baseband DSP clocks (apart from AM-PM in the

[4] ϵ_A is normalised with respect to the amplitude A_{LO} of the LO waveform.

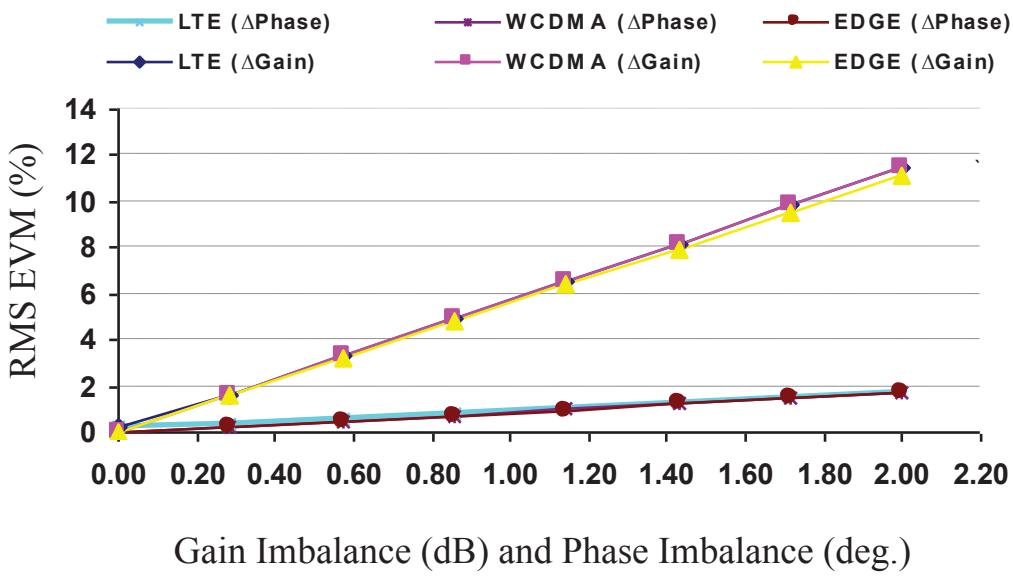

Figure 4.6: Simulated impact of IQ Gain and Phase imbalances on the EVM of LTE (20MHz, Resource Block EVM, 64QAM), WCDMA (1 of 4 carriers, contiguous) and EDGE (1 of 4-carriers, equal spacing) signals at 49dBm average power, in Agilent ADS.

HPA and the filters which contribute lesser). In the case of non-OFDM technologies, the Phase noise (PN) produces a symbol-independent phase rotation on the wanted vector, due to which the EVM varies marginally with the power and configuration of the active carriers. GSM/EDGE carriers being relatively narrow-band and lacking in processing gain are more sensitive to PN at small offsets or the *Close-in* ϕ_n [5]. This requires the ϕ_n to be very small over small offsets ($<$ 100KHz) for GSM/EDGE. Typical loop bandwidths of $\leq$ 30KHz are not uncommon. For offsets from carrier frequency $\Delta f_c > 200KHz$, the GSM PN mask requirement can be related to the modulation spectrum. We will discuss this further in the next chapter on performance budgeting. By assuming a high SNR environment and subsequently a Gaussian distribution for phase error within the PLL bandwidth, the author of [51] suggests a relation between the phase noise and the corresponding EVM ($\text{EVM}_{\text{Phase,Frequency Err.}}$) that can be used for GSM/EDGE and WCDMA analysis.

$$\text{EVM}_{\text{Phase,Frequency Err.}} = \sqrt{\frac{1}{SNR} + 2 - 2 \cdot \exp^{-\phi^2_{n,\text{rms}}/2}} \tag{4.14}$$

which simplifies to (4.15) when using the Taylor series expression for

$$\text{EVM}_{\text{Phase,Frequency Err.}} = \sqrt{\frac{1}{SNR} + \phi^2_{n,\text{rms}}} \tag{4.15}$$

[5] Close-in phase noise refers to that which is integrated from the Carrier frequency up to the bandwidth of the wanted signal

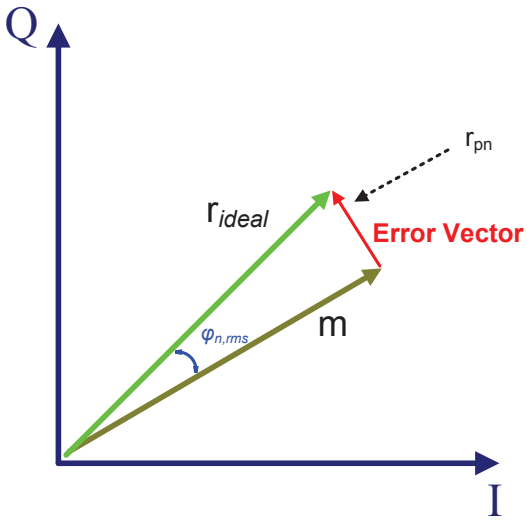

Figure 4.7: Error Vector Magnitude due to Phase Noise

where, $\phi_{n,\text{rms}} = 2\int_{f_{\text{LO}}}^{f_{\text{LO}}+B_{\text{-3dB,PLL}}} \left(10^{\frac{\mathcal{L}_{\phi_n}(f)}{20}} df\right)$ (rad. or alternatively in deg. after dividing by 180°) is the R.M.S. phase noise integrated over the bandwidth $B_{\text{-3dB,PLL}}$ of the PLL, with $L_{\phi_n}(f)$ dBc/Hz being the one sided Power Spectral Density (P.S.D., see [60]) of the oscillator's phase deviation, relative to the carrier. Typical $\phi_{n,\text{rms}}$ values are in the order of $\leq 0.3°$ R.M.S.

OFDM signals however, exhibit a greater sensitivity to phase noise than the single carrier systems. In LTE-OFDM, phase-noise, like most distortion types, combines with the symbol itself to produce a noise-like error [61]. In most of the cases, this error increases with the constellation symbol amplitude. With PN, the degradation of the sub-carrier has a symbol-dependent multiplicative effect that is two-fold (see Figure 4.8) [53, 62] producing a phase rotation that is unequal for the different constellation symbols. This makes LTE the most sensitive to PN distortions, consequently constraining the required PLL loop bandwidth ($B_{\text{-3dB,PLL}}$). The first of the effects is a subcarrier Common-Phase-Error ($\phi_{n_{\text{CPE}}}$) which is largely compensated by observing the average effect on pilot-symbols [54, 63, 64] and the second effect, a Random-Phase-Error (RPE) manifesting as Inter-Carrier-Interference ($\phi_{n_{\text{ICI}}}$). The corresponding EVM degradation depends on the variance of the PN and the ratio of bandwidths ($B_{-\text{3dB,PLL}}/\Delta\text{f}$, where, Δf is the subcarrier spacing of 15KHz or 7.5KHz), with preferably $\phi_{n_{\text{ICI}}} < \phi_{n_{\text{CPE}}}$ [65, 66].

Assuming the presence of only PN, if the transmitted OFDM symbol is assumed as in (4.6), the measured symbol Y_m can be expressed as

$$Y_m = \frac{1}{\sqrt{N}} \sum_{m=\frac{-N}{2}}^{\frac{N}{2}-1} \left[\frac{1}{\sqrt{N}} \cdot \sum_{r=\frac{-N}{2}}^{\frac{N}{2}-1} X_r \exp^{j2\pi nr/N} \exp^{\phi_n(n)} \right] \exp^{-j2\pi nm/N} \tag{4.16}$$

where $\phi_n(n)$(discrete form of the phase domain jitter $\phi_n(t)$) is the integrated phase noise of

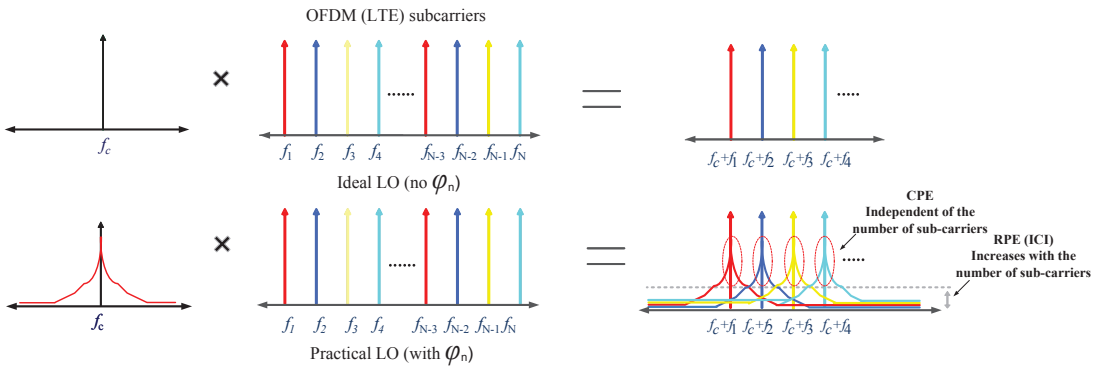

Figure 4.8: Effect of Phase Noise in multi-carrier OFDM

the measurement equipment and the transmitter consolidated into one single specification at the transmitter [67]. With some simple manipulation[6], the above equation simplifies to

$$Y_m = X_m + \underbrace{j \cdot X_m \cdot \frac{1}{N} \sum_{n=-\frac{N}{2}}^{\frac{N}{2}-1} \exp^{\phi_n(n)}}_{\text{CPE}} + \underbrace{\frac{j}{N} \sum_{n=-\frac{N}{2}}^{\frac{N}{2}-1} \exp^{\phi_n(n)} \sum_{r=-\frac{N}{2}, r\neq m}^{\frac{N}{2}-1} X_r \exp^{j2\pi n(r-m)/N}}_{\text{RPE}} \tag{4.17}$$

The second term of the above expression (with $r = m$) refers to the CPE while the last term (with $r \neq m$) refers to the RPE. It is evident that the in the third term, the phase noise has a multiplicative effect such that the errors at any sub-carrier m, are the superimposed disturbances from all other sub-carriers ($\neq m$ and up to the PN bandwidth), multiplied by the symbol on the aggressor carriers. Naturally, for 64QAM symbols, which require a higher SNR for accurate detection, this error is the highest. By assuming PN to be zero-mean Gaussian we can estimate the variance (which is consequently also the Power Spectral Density, PSD,) of ϕ_n, in order to arrive at an expression for EVM as in [62, 67, 68].

$$\text{EVM}_{\text{Phase Err.}} = \frac{\mathbb{E}\left[\left|\overbrace{\frac{j}{N} \sum_{n=-\frac{N}{2}}^{\frac{N}{2}-1} \exp^{\phi_n(n)} \sum_{r=-\frac{N}{2}, r\neq m}^{\frac{N}{2}-1} X_r \exp^{j2\pi n(r-m)/N}}^{\text{RPE}}\right|^2\right]}{\mathbb{E}\left[|Y_m|^2\right]} \tag{4.18}$$

We can consider one aggressor sub-carrier at a time, whose symbol can be set at unit amplitude, i.e. $X_k = 1$ and $X_m = 0\ \forall m \neq k$ and $\mathbb{E}[|X_k|^2] = 1$. If the PN is modeled as a Wiener Process with a Lorentzian PSD then the Expected value of the RPE from subcarrier k has

[6]The expansion of $\exp^{\phi_n}$ is only approximated to the first order to be $\approx 1 + j\phi_n$, with higher powers ignored.

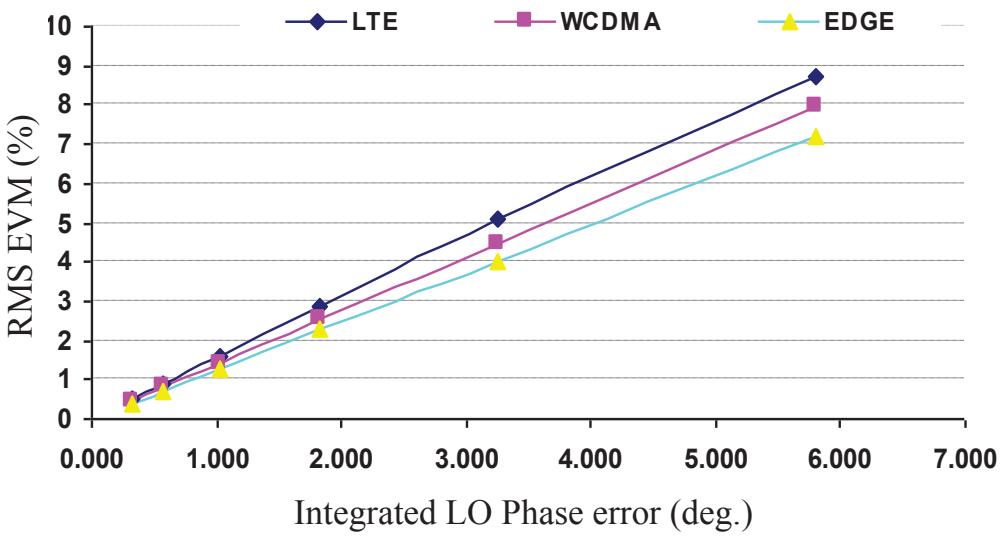

Figure 4.9: Simulated impact of composite Phase Error (Phase noise) on the EVM of LTE (20MHz, Resource Block EVM, 64QAM), WCDMA (1 of 4 contiguous carriers) and EDGE (1 of 4 equally spaced carriers) signals at 49.0dBm average power, in Agilent ADS.

been shown in [66] as a continuous time expression, to be

$$\begin{aligned} \mathbb{E}\left[|\mathrm{RPE}_k|^2\right]_{r\neq m} &= \sigma^2_{\phi_n\ k,m} \\ &\approx 2\cdot\int_{-\infty}^{\infty} 10^{[\mathcal{L}_{\phi_n}(f-[f_r-f_m])]/10} sinc^2(\pi f T)df \end{aligned} \tag{4.19}$$

where $f = n/N$, T is the symbol period, RPE_k is the transmitted RPE at the kth subcarrier and $\sigma^2_{\phi_n\ k,m}$ rad^2 is the noise variance (i.e., second moment of ϕ_n). As mentioned earlier, the disturbance at any carrier is a superimposed set of disturbances from all other carriers. The above expression unfortunately does not yield an easy analytical solution, so we leave it here, for verification through simulation, in future developments of this work. [53] provides a more tractable relationship for EVM due to phase noise. By using this and a piecewise log-linear approximation of $\mathcal{L}_{\phi_n}(f)$ to relate to RPE_k in the above expression allows one to approximate the R.M.S. ϕ_n (typically $\leq 0.3°$ or ≥ 45 dB SNR) and consequently, derive the phase noise mask requirements. Using this approximation, we derive the first approximation of the phase noise mask in the next chapter. The Figure 4.9 shows the simulated (EVM) impact of transmitter non-linearity in the various access technologies.

4.2.3.4 In-Channel Non-linearity Distortion Products

Non-linearities in components produce distortion products which fall within neighbouring channels that may occupied by other carriers. Consequently, for multi-carrier systems including OFDM, non-linearity needs to be budgeted for both in-channel distortion and unwanted

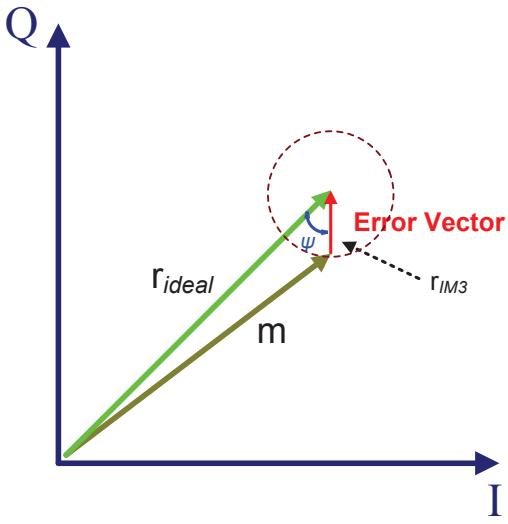

Figure 4.10: Error Vector Magnitude due to non-linearity

leakage (i.e., ACLR, OOB Spectral Emissions masks etc.). For the non-OFDM signals, the distortion products when viewed in time domain, cause a linear deviation of the amplitude of the ideal constellation symbol, as a function of the AM/AM characteristic of the non-linear block. This can simply be represented as

$$\text{EVM}_{\text{Non-Linear Distortion}} = \sqrt{10^{\frac{\text{IMR}_{\text{dBc}}}{20}}} \tag{4.20}$$

where IMR_{dBc}, the Inter-Modulation-Ratio, is the difference between the wanted signal power and the intermodulation distortion signal of any order. This effect is illustrated in Figure 4.10, where ψ is the phase difference between the intermodulation by-product and the desired RF signal. Incidentally, leakage of spurs in-band also has a similar effect on the signal EVM, with $\text{EVM}_{\text{In-band Spurs}} = \sqrt{\frac{1}{\text{SDR}}}$ where SDR is the Signal-to-Distortion Ratio expressed on a linear scale. For simplicity, we also refer to $\text{EVM}_{\text{Non-Linear Distortion}}$ as EVM_{NLD} in this document.

Assumed memoryless, the non-linearity of a block (including the PA) can be expressed as an nth order polynomial function $(a_0, a_1, a_2, a_3, \ldots, a_n)$. Correspondingly, the average EVM over N samples, in terms of the polynomial coefficients (here, only third order non-linearity; see [69]) is given by

$$\begin{aligned} \text{EVM}_{\text{Non-Linear Distortion}} &= \sum_{k=1}^{N} \frac{3}{4}\frac{a_3}{a_1} S_m^2 \\ &\approx \sum_{k=1}^{N} \frac{a_1^2}{IP3} S_m^2 \end{aligned} \tag{4.21}$$

where, $S_m^2 = |X_m|^2 = |X_I + jX_Q|^2$ is the normalised power corresponding to the mth symbol of the constellation and $IP3 = 2a_1^3/3a_3$ is the two-tone test 3rd order Intercept Point at

the output. The PA which forms the single largest contributor to non-linear distortions (see Chapter 5) has also AM/PM in addition to AM/AM characteristics that was assumed above. If memory effects are taken into account, the non-linearity of the PA can be described using a Wiener-Hammerstein (simplified Volterra-series based) model [70], as a cascade of a band-pass filter ($\Delta\theta_1$, b_1), memoryless-polynomial for non-linearity ($a_0, a_1, a_2, a_3, \ldots, a_N$ corresponding to an Nth order polynomial) and a subsequent band-pass filter ($\Delta\theta_2$, b_2). Here, b_i and $\Delta\theta_i$ correspond to the loss or compression and phase-rotation (or phase-shift) of the Linear-Time-Invariant filters of the model. An expression for the corresponding EVM due to non-linear distortion [69] is given as

$$\begin{aligned}\mathrm{EVM}_{\text{Non-Linear Distortion}} = \Bigg(& \frac{\left[X_I - (b_2[a_1 + \frac{a_1^3}{2 \cdot IP3} \cdot b_1^2.S_m^2]b_1 \cdot \sqrt{S_m^2})\cos(\theta - \Delta\theta_1 - \Delta\theta_2)\right]^2}{S_m^2} \\ & + \frac{\left[X_Q - (b_2[a_1 + \frac{a_1^3}{2 \cdot IP3} \cdot b_1^2.S_m^2]b_1 \cdot \sqrt{S_m^2})\cos(\theta - \Delta\theta_1 - \Delta\theta_2)\right]^2}{S_m^2}\Bigg)^{1/2}\end{aligned} \tag{4.22}$$

where $\theta = \arctan(X_Q^2/X_I^2)$.

For OFDM systems, using an alternative baseband polynomial model suggested by [71],

$$y_n = \sum_{k=1}^{K} b_k x_n |x_n|^{k-1} \tag{4.23}$$

where, x_n and y_n correspond to the baseband PA input and output signals, respectively, K is the (integer) polynomial order, and b_k are coefficients of the polynomial. The authors of [53] predict the approximate EVM due to 3rd order non-linear distortions as

$$\mathrm{EVM}_{\text{Non-Linear Distortion}} = \sqrt{\frac{24|c_3|^2\sigma^2}{\frac{X_{m,\max}^2}{\mathbb{E}[|X_m|^2]}}} \tag{4.24}$$

where $c_3 = b_3/b_1$ is the 3rd order coefficient of the polynomial and σ^2 is the variance (Rayleigh distribution) of the input signal x_n (assumed Gaussian distribution). This non-linear distortion manifests as Inter-Carrier-Interference (ICI) for the neighbouring sub-carriers, showing up as state-spreading [61] or a noise-like cloud surrounding a symbol.

Ignoring even-order distortions for transmission bands less than an octave, the odd-order non-linearity products (IM3, IM5 etc.) that fall in-channel distort the signal proportional to the combined magnitude of the in-channel distortion products. This issue is aggravated in the case of 3 or more carriers due to the Composite Triple Beat (CTB, see (B.4)) effect. Another insidious form of odd-order non-linear distortion which occurs at the carrier frequency itself is Cross-Modulation (CMD, see Figure B.3) of the carrier. It is the modulation of wanted signal by the other modulated channels in the band, that is dependent on relative amplitudes of the active carriers (and independent of the carrier frequency separation). Its impact is typically greater on the EVM than on the ACLR of the channel. Given a varying number of modulated signals of dissimilar modes and varying power levels, the analysis of CMD becomes involved[7].

[7]For sinusoidal input signals, the CM/IM3 ratio is approximately 4.0 (6.02 dB).

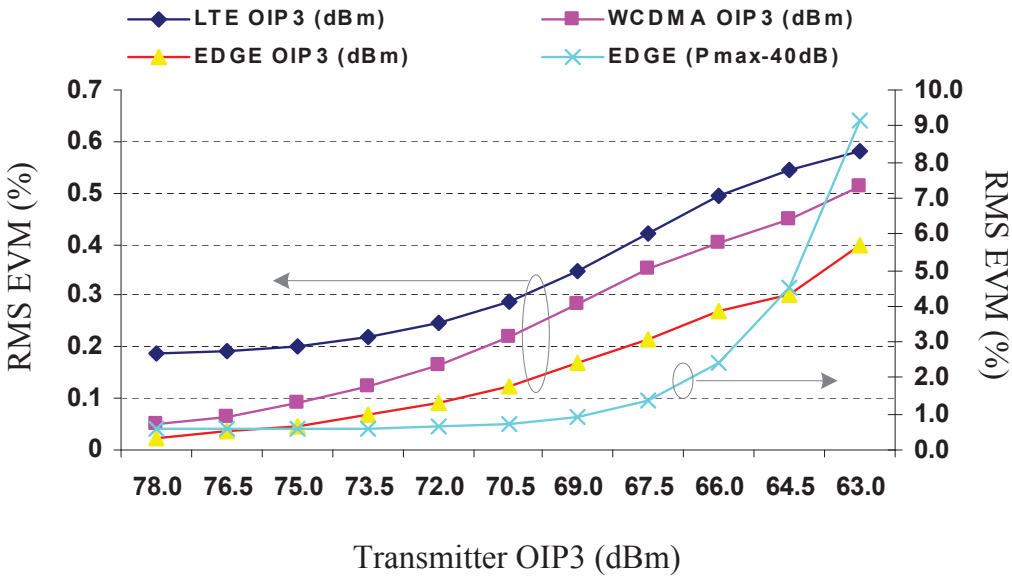

Figure 4.11: Simulated impact of Non-linearity on the EVM of LTE (20MHz, Resource Block EVM, 64QAM), WCDMA (1 of 4 contiguous carriers) and EDGE (1 of 4 equally spaced carriers) signals at 49dBm average power, in Agilent ADS.

In this work, we have not explicitly treated the contribution of CMD and a detailed treatment is suggested for future work. Nevertheless, the effect becomes somewhat clearer if in (4.22), the symbols X_I and X_Q are represented by a combination of symbols of varying amplitudes and the effect is observed over time. $\text{EVM}_{\text{Non-Linear Distortion}}$ is actually less demanding on the linearity of the block than the spectrum leakage specifications (ACLR, SEM etc.), so we deal with other distortion mechanisms such as the (CTB)[8] (CMD is not covered here), in more detail under the leakage specifications, in the next section. The Figure 4.11 shows the simulated (EVM) impact of transmitter non-linearity in the various access technologies. These simulations were made in the presence of low noise, but the effect of noise is visible at high OIP3 levels in Figure 4.11, where the curve becomes flatter as the noise begins to dominate (see Figure 4.13).

4.2.3.5 Other contributions

In the analysis presented in the previous sections, we have ignored the impact of baseband filtering, impedance mismatch, gain fluctuations, complex PA non-linear effects (e.g. memory effects) and other secondary effects such as VCO pulling, LO harmonics, LO amplitude fluctuation, filter group-delay, amplitude droop etc. Furthermore, while the details of DSP

[8]Intermodulation Distortion or IMD refers to non-linear distortion when subject to two-tone excitation, while CTB refers to distortion for greater than two input tones or signals.

or baseband errors[9] and spurious emissions are random and mostly manifest as noise and impact EVM ($\text{EVM}_{\text{DSP, Baseband Err.}}$), a detailed treatment is unfortunately beyond the scope of this work. Nevertheless, the mechanism of weighted contributions (which we will cover in the next chapter) to the total EVM budget (described above) will be valid for these errors also.

Filter amplitude and phase ripple For a filter with an attenuation $\alpha(f)$ and unwrapped phase $\varphi(f)$, the in-band R.M.S attenuation and phase ripple has been shown in [72] to be equal to

$$\Delta\alpha_{\text{rms}} = \frac{1}{B}\int_{f_{\text{lo}}}^{f_{\text{hi}}} \left[\frac{\alpha(f) - \alpha_{\text{rms}}}{\alpha_{\text{rms}}}\right]^2 df \tag{4.25a}$$

$$\Delta\varphi_{\text{rms}} = \frac{1}{B}\int_{f_{\text{lo}}}^{f_{\text{hi}}} \left[\varphi(f) - \varphi_{\text{linear}}\right]^2 df \tag{4.25b}$$

where $B = f_{\text{hi}} - f_{\text{lo}}$ refers to the bandwidth of the filter with corner frequencies f_{hi} and f_{lo}. α_{rms} and φ_{linear} refer to the R.M.S. attenuation and the linear in-band phase shift of the filter, respectively. The corresponding group-delay is given by $t_g = d\varphi/(2\pi df)$. If the EVM can be expressed as a function of its normalised amplitude and phase, as

$$\text{EVM}_{\text{R.M.S.}} = \sqrt{\text{EVM}^2_{\text{mag,R.M.S.}} + \text{EVM}^2_{\text{phase,R.M.S.}}} \tag{4.26}$$

The EVM due to the SAW filter can be expressed as in [72],

$$\text{EVM}_{\text{SAW Filter}} = \sqrt{\Delta\alpha^2_{\text{rms}} + \Delta\varphi^2_{\text{rms}}} \tag{4.27}$$

Typical values for amplitude and phase ripple in the pass-band of the filter are $\leq 0.5\%$ and $\leq 0.5°$ R.M.S, respectively, where the latter is the standard deviation of the phase from ideally linear behavior. In the case of OFDM, this imperfection produces ICI, but there is little need to budget for this EVM since SAW filters are typically designed with slightly larger bandwidths to reduce in-band distortion and also because the multi-carrier OFDM with its low symbol rate and Cyclic Prefix (CP) is quite resilient to these imperfections (see [20]).

4.3 Spectrum Emissions Requirements

Transmitters must preserve the spectrum of all the signals without significant distortion and spurious signal generation within its own spectrum and into neighboring channels alike. This leakage power into neighboring channels defines the local interference which adversely impacts overall system capacity and is therefore specified in the system requirements. In order to guarantee efficient spectrum usage for all operators and also its subscribers, the 3GPP standards body sets in place stringent specifications that limit this leakage into neighbouring channels and neighbouring bands. The spectral power limits of the signal are defined in the 3GPP Standards using terminologies such as Spectral/Spurious Emissions Mask, ACLR

[9] Some of these include imperfect fractional-interpolation, errors due to truncation because of limited digital filter-length, floating-point to fixed-point conversion errors, amplitude-clipping [53], CFR etc.

(for WCDMA/LTE), Output RF Spectrum (ORFS, for GSM/EDGE), Out-of-Band Emissions (OOB) and Co-existence specifications, at various frequencies relative to the either the carrier(s) or the transmission band itself.

Transceiver linearity requirements for the simultaneous transmission of multiple cellular signals are particularly demanding owing to the increasing PAPR (see Section 4.3.9) and the demanding SEMs that are only slightly relaxed [16] for multi-carrier transmissions. In order to identify the feasibility of multi-mode transmission, transmitter non-linearity (OIP3) requirements for future multi-standard, multi-carrier, macro-cell base stations based on first-order approximations are analysed, highlighting the issue of reduced dynamic range.

4.3.1 3GPP Spectrum Mask Requirements

Termed as *in-band* emissions, ACLR and ORFS define the limits for the leakage signal in the channel vicinity as absolute power levels (dBm/Hz, and valid for lower Tx powers) or as power levels relative (i.e., dBc/BW or dBr/RBW, Resolution BandWidth (RBW)) to the wanted-signal power in the channel being considered. It is a single channel transmission metric measured at the outermost signals in a multi-carrier transmission scenario. The measurement bandwidth however varies significantly between the various standards. For example, in the WCDMA [50] and LTE [19] standards, the ACLR is defined to be −45dBc (ACLR1, adjacent channel) or −50dBc (ACLR2, alternate channel). For GSM/EDGE, this is stated differently, as shown in Figure 4.12.

The *out-of-band* emission requirements define the power levels for both wanted, leakage and spurious emissions at various offsets from each signal channel complementary to the ACLR / ORFS / Intermodulation attenuation requirements. In case of overlaps, specific cases are defined. There are also other specifications, for example, as defined in the Co-existence requirements, which guard the receiver sensitivity in the same BStn or transceivers in other neighbouring BStns.

In a multi-mode transmission scenario, the toughest linearity specification comes from the GSM/EDGE standard [48], requiring −70 dBc/RBW (GSM Class 1) or −60 dBc/RBW (GSM Class 2)[10], with exceptions for several specific cases. In both cases, the RBW for both carrier and intermodulation products being 300kHz at offsets larger than 6 MHz, 100 kHz at offsets between 1.8 and 6 MHz, and 30 kHz at offsets below 1.8 MHz. For scenarios not involving GSM/EDGE, the requirements are obtained from the WCDMA [50] and LTE [19] standards, where the ACLR[11] is defined to be 45 dBc (ACLR_1) and 50 dBc (ACLR_2).

4.3.2 Leakage Mechanisms

Contributors to the spectral leakage (Figure 4.13) include (odd-order) Inter-Modulation Distortion (IMD) and Cross-Modulation products, large-frequency-offset phase noise and in-band random noise. The dominant contributors are the IM3 (3rd-order IMD) products that fall into

[10] GSM/EDGE Class 2 is a newer relaxation of the spectral mask, focusing on PA efficiency rather than linearity, with a small penalty on network throughput.

[11] We also need to consider that the Occupied BandWidth (OBW) of a 5MHz LTE signal is greater than a corresponding WCDMA signal by [4.51−3.84]MHz, resulting in a higher ACLR ($ACLR_{\text{LTE}} \approx ACLR_{\text{WCDMA}} +$ (0.9 *to* 1.8)dB) in LTE than WCDMA for a given carrier power [73].

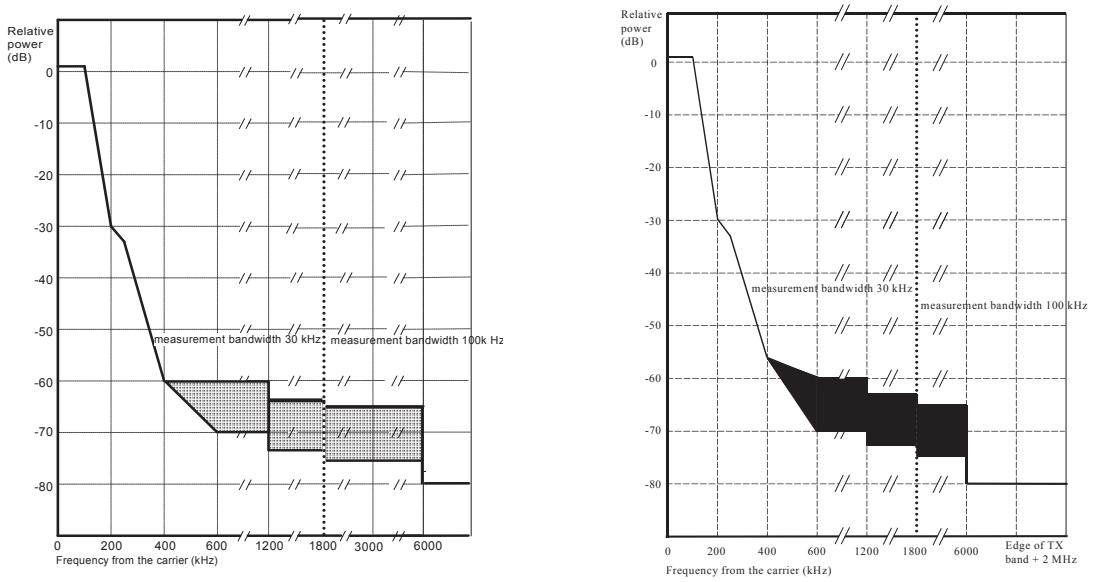

(a) GMSK **(b) 8-PSK, AQPSK, 16-QAM and 32-QAM**

Figure 4.12: Half sideband spectral mask for GSM/EDGE corresponding to (a)GMSK modulation (b) Other supported GSM/EDGE modulation schemes (Source: [50])

the neighboring channels, followed by higher odd-order non-linearity products (IM5, IM7) of the hardware blocks. Higher order IMD terms come into effect only at larger input power levels (closer to saturation). The (phase and amplitude) CMD, which occurs at the signal center frequency itself, depends on the phase and amplitudes of the aggressor signals (envelopes). With several contributors, a power efficient system design requires well proportioned power budgeting between the various agents of the leakage.

Gross non-linearity from cut-off and hard-saturation effects of the active devices, for transmission bandwidths less than an octave can be ignored. Although, in cases where there is feedback in the circuit schematic or other possible second order effects (e.g. LO harmonics causing in-band mixing products) IP2 is sometimes also relevant. CMD however, has a greater impact on the signal EVM although it originates from similar mechanisms that generate IMD. Assuming sufficient Back-Off[12] and ignoring any memory-effects, IM3 is always related to a specific output power level and therefore can be used to predict the stringent linearity requirement of a transmitter at rated power. For a first-order approximation of linearity, the relation ACLR≈IM3 can be used to obtain the overall OIP3 (3rd-order Output referred Intercept Point) requirement at the antenna connector (or ARP, Antenna Reference Point) using the familiar two (n) tone IP3 (n) relation given by

[12]Back-Off indicates setting the operating point and the peak signal swing several dB below the Compression point of the non-linear device.

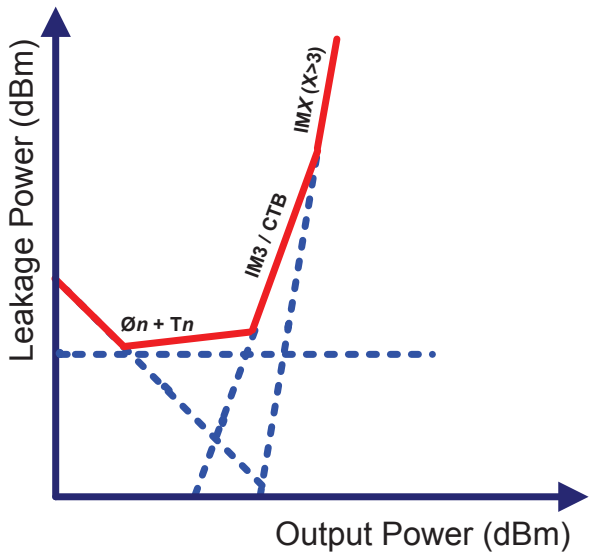

Figure 4.13: Phase Noise (ϕ_n), Random (primarily Thermal) noise (T_n) and IMD (IM of order 'x') contribution to the Adjacent and Alternate Channel Leakage power

$$\mathrm{OIP}n_{\mathrm{dB}} = P_{\mathrm{out}} + \frac{(\mathrm{Interferer}_{\mathrm{out}_{\mathrm{low,high}}} - \mathrm{IM}n_{\mathrm{high,low}})}{(n-1)} \tag{4.28}$$

or,

$$\mathrm{IM3}_{\mathrm{dBc}} = 2(P_{\mathrm{out}} - \mathrm{OIP3}) \tag{4.29}$$

Extending this analysis to modulated signals requires applying a correction factor C_n to the two-tone signal expression for IP3, which we will discuss in the next sections. As defined above, Tx linearity requirements are defined by the GSM standard where the 2-carrier GSM case gives the highest absolute $\mathrm{IM3}_{\mathrm{dB}}$ power level. Although, increasing the number of carriers also generates a relatively high Inter Modulation Ratio ($\mathrm{IMR}_{\mathrm{dBc}}$) which approaches the limits of the 3GPP specifications, assuming the total output power is shared equally between all carriers, given maximum possible frequency separation. This is because, with more than 2 carriers, CTB (Composite Triple Beat) becomes relevant, cumulating IMD products at certain frequency offsets, with the highest IMD levels being closest to the carrier. The concepts of IMD, CMD and CTB are discussed in Appendix B.

4.3.3 Multi-mode linearity requirements

Any non-linear RF or digital device generates various forms of distortion besides spurious content when it carries a waveform that does not have a constant envelope signal (e.g. EDGE, WCDMA, LTE). The same is true for the sum of several (GSM/EDGE, WCDMA, LTE) signals, or even a group of constant envelope (GSM-GMSK) signals normally amenable to

non-linear amplifiers. Since the distortion components fall into adjacent channels as interference, advanced linearisation schemes have become key technologies in enabling multi-carrier transceivers architectures. Unlike single-carrier radios which rely on filters to remove the undesired components that could corrupt neighboring channels, multi-carrier architectures must instead, inherently limit distortion over the entire transmission bandwidth, requiring a very linear performance, translating to higher power consumption. This toughened linearity requirement coupled with a low EVM specification manifests as an issue of dynamic range, which we will cover in the subsequent sections.

4.3.3.1 GSM/EDGE - linearity requirement

For scenarios involving 3 or more GSM/EDGE carriers, the factor C_n is an empirical correction factor [10] that varies with the transmitted carrier configuration and must correct for:

- **IMD bandwidth spreading**[13]: The two-tone IP3 expression assumes equal bandwidths for the tones and IMD products. This assumption is no longer valid when using modulated signals whose PSD cannot be fully expressed by a singular frequency. A correction factor needs to be incorporated into the two-tone IM3 expression, which can be explained through the mechanism of frequency domain convolution[14] between two similarly shaped spectra. The Figures 4.14 and 4.15 illustrate this mechanism of spreading. Correspondingly, since both carrier and leakage spectrum are measured with the same RBW, a correction factor needs to be incorporated to when considering the select IMD power to apply to the two-tone IP3 calculation. This value is best obtained from measurements as the IMD spectral is not uniform with respect to frequency.

- **Non-linearity measurement and RBW specifications**: GSM/EDGE standards specify several cases of measurement where the resolution bandwidths for both the carrier and the leakage products change with the case. For example, at frequency offsets 1.8-to-6.0 MHz from the carrier, both the carrier and the leakage spectrum are measured in a 100 KHz RBW. With GSM/EDGE having an Occupied Bandwidth (OBW) of 270 KHz and a similarly shaped IMD spectrum, assuming a uniformly shaped spectrum, a corresponding factor of approximately $10\log\left(\frac{\text{RBW}}{\text{OBW}}\right)$ could be incorporated.

- **Shape of the modulated spectrum and IMD products**: The two-tone test in its very definition assumes that both the carriers and their IMD products are defined by singular frequencies. Besides the bandwidth spreading factor discussed above, an additional factor which corrects for the relative marker powers between the modulated spectrum and a tone (for a given RBW), needs to be applied. From simulations, a GSM/EDGE is approximately 6 to 7dB below tone-power in a 30 KHz RBW. For WCDMA and LTE, this is approximately $10\log(\text{OBW})$ assuming uniformly shaped spectrum. Figure 4.15 illustrates this for GMSK modulated (GSM) carriers.

[13] $\left[\frac{\text{IMD BW}}{\text{Carrier BW}}\right] = 3,\ 5,\ 7$ etc.

[14] This is the time domain equivalent of $a_n \cdot x^n(t)$, where $x(t)$ is the input signal and a_n is the nth order coefficient of device non-linearity.

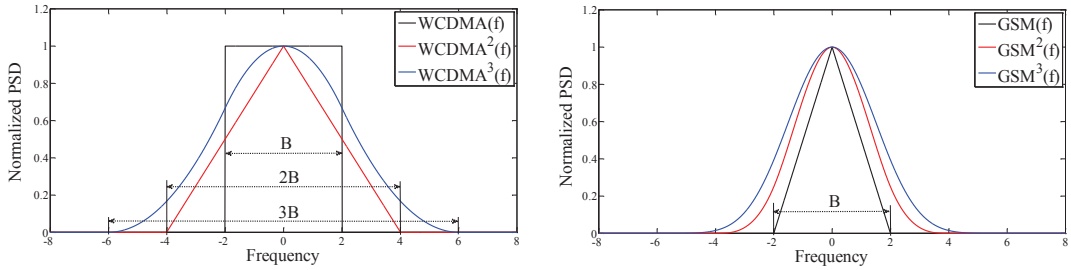

Figure 4.14: Simulated bandwidth spreading for 3rd order coefficient of non-linearity polynomial

- **Number of carriers (N_c) transmitted**: As the number of carriers is increased, the intermodulation products accumulate, with the highest IMD levels being close to the first channel outside the carrier aggregate. Here we assume the worst case that when two IMD products result at the same frequency, they are uncorrelated and add in power without any regard to their relative phases. In other words, their phases are ignored and with that any possibility of destructive interference i.e., cancellation. The same logic is used when cascading the non-linear products of two subsequent blocks. The case for IMD accumulation at the critical carrier-edge, from the simultaneous transmission of GMSK carriers is illustrated in Appendix B. In addition to the accumulation of IMD products, because IM3 is related to OIP3 through carrier power, IM3 power levels need to backed-off 2dB per dB of carrier power reduced when total power is shared among an increasing number of carriers (N_c).

- **Other criteria**: The relative powers between carriers and the frequency separation between them are particularly important as it determines the power levels and frequency offset of the IMD products and the corresponding Leakage specifications that need to be satisfied. The location of the carriers relative to the transmission band is also critical as any IMD products falling outside of the band would need to adhere to the very stringent Spurious Emissions specifications that limit leakage outside of the used Tx band. Due to the number of sub-clauses that govern these limits, we cannot easily generalise them and therefore apply them on a case-by-case basis. For additional details on the special cases, the reader is referred to the Tx specifications in [19, 48, 50].

The above correction factors allow us to use normal two-tone intercept point expressions, applying them to multiple tones or modulated signals. More complex distortion effects such as AM-PM (phase rotation) and memory effects have also to be considered when determining requirements. These however have a greater impact on the modulation signal quality (EVM) and are ignored here for the sake of a first-approximation-only analysis. For IM3 at close carrier offsets, the OIP3 requirement for (N_c) equal powered carriers of GSM/EDGE can be calculated using the relation below. This however is pessimistic as it ignores the phase relationship between the carriers yielding theoretically higher IM3 levels ($\sim$ 7dB) [74, 75].

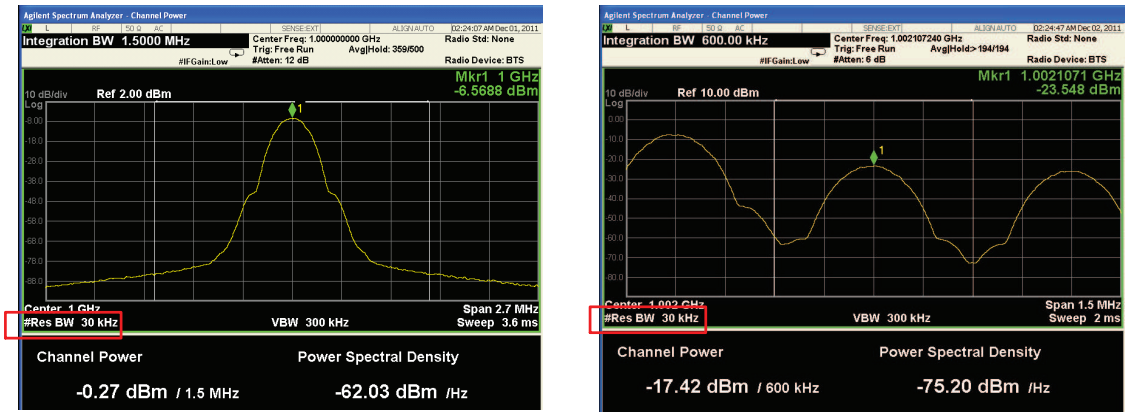

Correction factor between tone and GMSK Modulated waveform ≈ -6.5dB **Correction factor for GMSK IMD shape related to two-tone IM3 ≈ -6.1dB**

Figure 4.15: Correction factors obtained from measurements of GMSK modulated carriers subjected to non-linearity, with RBW = 30KHz. (*Courtesy: NXP Semiconductors*)

$$\begin{aligned} \mathrm{IM3_{dBc}} \geq & \underbrace{2 \cdot (P_{\mathrm{carrier}} - \mathrm{OIP3})}_{\text{IM3 Two-Tone}} + \Bigg[\underbrace{10 \cdot \log_{10}(\eta_3)}_{\text{IMD enhancement factor}} \\ & + \underbrace{2(10 \cdot \log_{10}\left(\frac{\mathrm{RBW}}{\mathrm{OBW}}\right))}_{\text{OBW and RBW correction factor}} + \underbrace{20log_{10}(N_c)}_{\text{Carrier multiplicity factor}} \Bigg] \end{aligned} \tag{4.30}$$

where $\mathrm{IM3_{dBc}}$ is from the system specifications and

$$\eta_3 = \begin{cases} N_c^2 - 1.5N_c & : N_c \ even \\ N_c^2 - 1.5N_c + 0.5 & : N_c \ odd \end{cases} \tag{4.31}$$

The corresponding OIP3 which satisfies the IM3 level specifications of the GSM/EDGE mask will indicate the required linearity at the Antenna Reference Point (ARP, i.e., output of the PA). The above equation is based on the works of [74, 76]. Here we assume that since the each of the carriers holds modulated user-dependent data, they are sufficiently uncorrelated to make our assumption of addition in the power domain reasonable.

The value of η_3 is obtained from both hand-calculations (see Figure B.2) and from (4.31) above, which is scalable for increasing number of carriers. Assuming six GSM/EDGE carriers (typical) equally sharing 80 W (49.0 dBm), this yields a very challenging ARP OIP3 requirement of > 79 dBm satisfying GSM/EDGE Class-1 and also defining multi-mode (GSM/EDGE+WCDMA) requirements, part of which can be supported by Digital Pre-Distortion (DPD) (see Section 4.3.10). We calculate this as follows. For 49.0 dBm of output power, the per-carrier power amounts to 41.2 dBm. If we factor in our correction for shape of the modulated spectrum, this power would be less ≈ 6.5dB with respect to a CW tone in

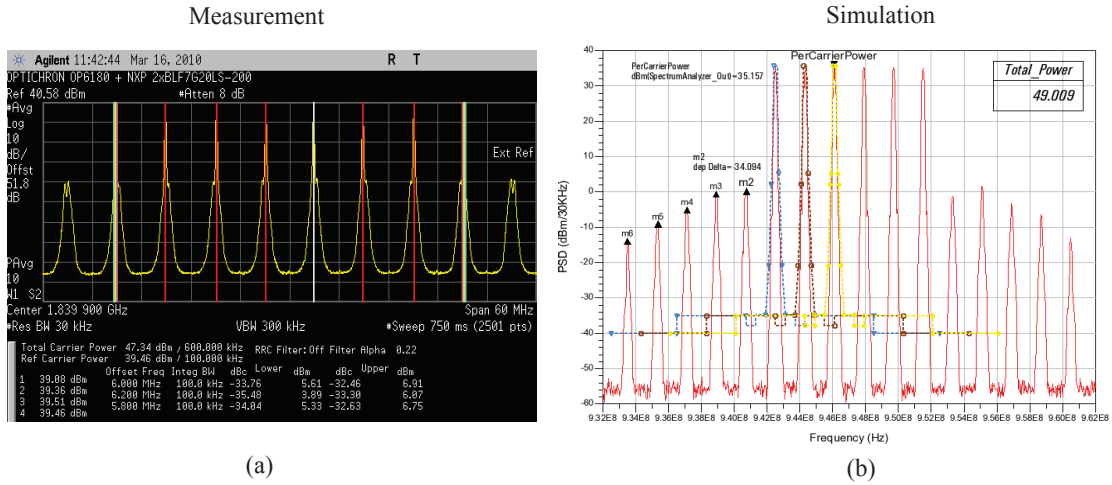

(a) (b)

Figure 4.16: Six-carrier GMSK IMD products (a) Measured (*Courtesy: NXP Semiconductors and Optichron, 2010*) (b) Simulated ($P_{\text{out}} \approx 49.0$ dBm).

an RBW of 30 KHz. This would be the most stringent specification to meet if the carriers were spaced ≈ 1.8MHz apart where the requirement for the IMD levels is -73 dBc/30 KHz. This would be tougher than the -80 dBc / 100 KHz (or -130 dBc/Hz) specification since the spreading due to modulation and broadband noise specification is relaxed by $10 \cdot \log(\mathrm{N_c})$ for multi-carrier BStns. Correspondingly, the two tone (4.30) can be written as

$$-73\text{dBc} \geq \underbrace{2 \cdot (49.0\text{ dBm} - \text{OIP3 dBm})}_{\text{IM3 Two-Tone}} - \underbrace{2 \cdot (6.5\text{ dB})}_{\text{OBW and RBW correction factor}} - \underbrace{2 \cdot (10log_{10}(N_c))}_{\text{Carrier multiplicity factor}} + \underbrace{14.32\text{ dB}}_{\text{IMD enhancement factor}} \tag{4.32}$$

Typical DPD systems (see [77]) achieve up to 25-30 dB reduction in IM3 levels depending on the carriers and the bandwidth of the correction required. While the actual impact of the DPD is more complex, we only interpret its impact of reduced IM3 levels together with increased PAPR (see Section 4.3.10). Consequently, this gives us approximately 12.5 dB of IP3 improvement on applying the DPD IM3 simplification, resulting in an equivalent two-tone OIP3 requirement of greater than 67.5 dBm. It should be noted however, that most PA's are not adequately defined using OIP3 alone and are often, and preferably so, specified in terms of the required IM3dBc, $\mathrm{P}_{-1\mathrm{dB}}$ and $\mathrm{P}_{-3\mathrm{dB}}$ compression points. While numerous measurements and simulations were performed, the special case for six GMSK carriers is shown in Figure 4.16. The measurements were performed on the NXP BLF7G20LS-200 Doherty HPA (including the Tx chain behind it) before applying Digital pre-Distortion. For simulations we used the approximated (or equivalent) two-tone OIP3 for the simulations.

4.3.3.2 WCDMA/LTE linearity requirement

While predicting ACLR (see (4.33)) for a given OIP3 or reverse-engineering OIP3 requirements from ACLR specifications is relatively simpler for the tone-like GDM/EDGE signals, this is more complicated for signals that are statistically *richer*. If we consider GMSK and the EDGE family of modulation schemes, it is readily observable from their frequency spectrum that their statistics closely resemble those of simple modulated waveforms. This is also observable from the manner in which the PAPR changes when a GSM or EDGE signal is subjected to non-linearity (assumed memoryless and described by MacLaurin series for simplicity) or when multiple GSM or EDGE signals are combined together in time domain.

$$\text{ACLR} = 10 \cdot log_{10}\left[\frac{\text{Wanted Signal Power}}{\text{Leakage Power}}\right] \tag{4.33}$$

WCDMA and LTE signals with their numerous channels and layers [78, 79] have characteristics that are closer to Additive White Gaussian Noise, in the voltage domain. The difficulty therefore, in predicting OIP3 requirements is discussed further in Section 4.3.9. In (27) of [80] is a useful analytical single carrier OIP3 expression (memoryless) (4.35) derived by assuming a bandpass Gaussian equivalent WCDMA signal. [81] also presents a simplified but empirical relation (see (4.34)) for OIP3 (memoryless). For multi-carrier wide-band signals, the broadband non-linear distortion power in the neighboring channels would increase by a maximum of $10 \cdot log_{10}(\mathrm{N_c})$, with ($\mathrm{N_c}$) contiguous, similar [15], active carriers. With the higher OBW in LTE, the equation remains roughly the same except for an $\mathrm{ACLR_1}$ (or $\mathrm{IM3_{dBc}}$) degradation of 1 to 2 dB [73]. This would imply a higher Back-off or De-rating on the PA than for a WCDMA signal of the same power and bandwidth. The Table 4.2 summarises the comparisons between measured[16], simulated[17] and calculated[18] values respectively.

$$\begin{aligned}\mathrm{IM3}_{dBc} \approx 2 \cdot [(P_{\text{out}} - 10 \cdot log_{10}(N_c)) - \mathrm{OIP3}] + (-20.75 + 1.6 \cdot \mathrm{PAPR}_{N_c=1}) \\ + 10 \cdot log_{10}(N_c)\end{aligned} \tag{4.34}$$

where, $\mathrm{PAPR}_{N_c=1}$ is the Peak-to-Average-Power-Ratio corresponding to one carrier.

$$\mathrm{OIP3_{dBm}} = 30 - 5 \cdot log_{10}\left[\frac{P_{\mathrm{IM3}} f^3}{(3P_{\text{out,dBW}})^3[\Delta^3_{f,l} - \Delta^3_{f,h}]} - 4.52\right] \tag{4.35}$$

where $f = \frac{3.84\mathrm{MHz}}{2}$, $\Delta_{f,l} = f - |f_{\mathrm{IM3_{low}}} - f|$ and $\Delta_{f,h} = f - |f_{\mathrm{IM3_{high}}} - f|$. Assuming four WCDMA carriers equally sharing 80 W (49.0 dBm), these equations would yield a first-approximation OIP3 of requirement of roughly 68.45 dBm (without DPD), significantly lesser than for GSM, suggesting a potential for reconfigurable blocks, when GSM/EDGE carriers are inactive. The caveat here is that these simulations were performed under controlled circumstances, using device models with polynomial non-linearity (AM/AM, AM/PM included)

[15] Carriers with the same power levels.
[16] These specific measurements were carried out by NXP Applications Engineers located in Smithfield, USA.
[17] Simulations performed using Agilent ADS
[18] Calculations made using MS Excel and MatLab, using the referred equations

Table 4.2: Comparison of ACLR [50] / ORFS [48] values

Transmitted Signal	*ACLR/ORFS/SEM*		
$x = N_c$[ab]	Measured	Simulated [c]	Calculated
1x*WCDMA*	-34.94 dBc	-36.03 dBc	-35.7 dBc
2x*WCDMA*	-31.18 dBc	-33.77 dBc	-32.69 dBc
4x*WCDMA*	-28.86 dBc	-27.22 dBc	-28.17 dBc
6x*EDGE*	-33.76 dBc[d]	-34.08 dBc[d]	-33.09 dBc[d]
8x*EDGE*	-34.43 dBc[d]	-34.64 dBc[d]	-30.48 dBc[d]
4x*EDGE + WCDMA*	-36.58 dBc[e]	-37.83 dBc[e]	-37.5 dBc[e]

[a] Total power shared equally between carriers.
[b] Pout = 49 dBm (approx.), approximated Tx. Two-Tone OIP3 = 67.5 dBm (approx.)
[c] Simulations performed in Agilent ADS.
[d] Power in dBc/100 KHz
[e] Power in dBc/30 KHz

and making simple assumptions for the impact of the DPD on the IM3 levels much like for the GSM/EDGE signals above. This is because, the two-tone OIP3 is a theoretical extrapolation of the IM3 assuming that the IM3 remains the primary contributor that continues until the extrapolated point. As the devices approaches soft-saturation, the extrapolated OIP3 expectedly begins to degrade. At this point first approximations need to be supported by strong assumptions on operating conditions of the amplifier, allowing one to relate this extrapolated OIP3 to the two-tone OIP3 value we derived.

4.3.4 3GPP Spurious, Unwanted Emissions and Co-Existence Emissions Specifications

3GPP refers to unwanted emissions in two categories. Out of band emissions (±10 MHz below and above the lowest carrier frequency and highest carrier frequency respectively) which are essentially unwanted emissions that manifest immediately outside the wanted signal bandwidth and are attributed to the modulation process and non-linearity in the transmitter. These specifications limit the interference to the other operators in the vicinity and also the interference to other users in the same channel. Independently specified, spurious emissions ($>$ ±10 MHz below and above the lowest carrier frequency and highest carrier frequency respectively) are emissions are those that are caused by transmitter effects such as harmonics emissions, parasitic emissions, large-offset intermodulation products and frequency conversion products. These specifications limit the interference to other cellular communications at larger frequency offsets and also the variety of telecommunication technologies, not limited to cellular communications that operate in other parts of the spectrum.

4.3.5 Non-linearity Requirements

A stringent specification arises when a carrier operates near the edge of the transmitted band. In such a case, the distortion products from non-linearity, phase-noise, broadband noise etc., would come under these stringent specifications. The limiting spurious specifications is set by

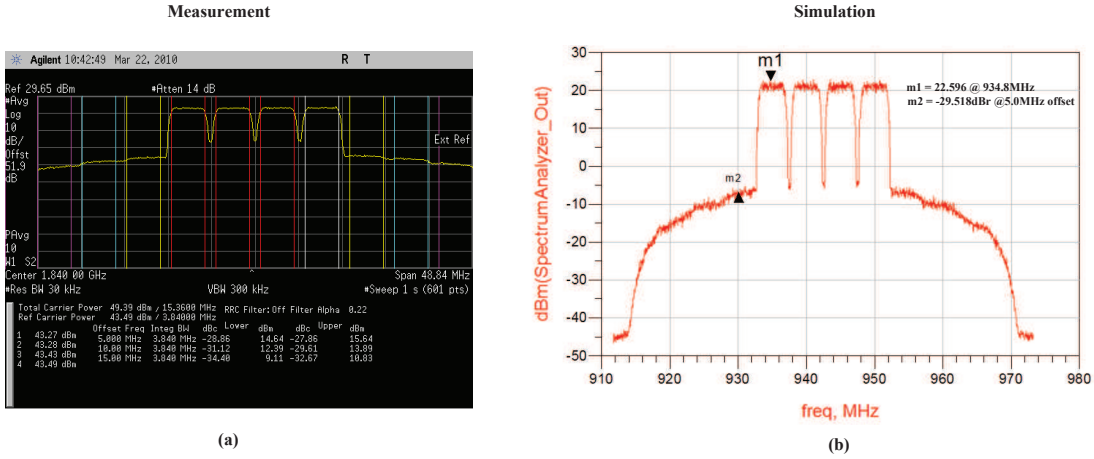

Figure 4.17: Four-carrier WCDMA IMD products (a) Measured (*Courtesy: NXP Semiconductors and Optichron, 2010*) (b) Simulated ($P_{\text{out}} \approx 49$dBm).

the need to protect co-located BStns and to prevent the de-sensitisation of the Rx of the same BStn, against any unwanted emissions from the Tx. The limiting value is -98 dBm/100 KHz (-148 dBm/Hz), in the frequency band corresponding to the receiver. This requirement is similar to the shared broadband noise floor requirement of -30 dBm/MHz (-90 dBm/Hz) if a duplex filter having a isolation of at least 52 dB between the Tx and Rx bands is assumed. We use this to derive requirements for the output-noise of the Tx chain based on assumptions of the duplex filter isolation.

4.3.6 Phase Noise Requirements

The phase noise requirements of the transmitter are specified by both signal distortion limits as well as the leakage spectrum specifications, in particular the clause corresponding to Unwanted Emissions Specifications/Mask. With reference to the in-band or signal quality requirements, we observe from our simulations that the LTE carriers are most sensitive to phase noise distortion at small frequency offsets. Consequently, we derive the small-offset (or 'close-in') phase noise requirements from this metric. For frequency offsets lesser than 200 KHz and down to 100 Hz, the performance specification is derived from the EVM that is budget for small-offset phase noise, based on our analysis of phase noise distortion ($\text{EVM}_{\text{Phase Err.}}$). This will be discussed in the next chapter.

Large-offset (or 'far-away') phase noise requirements are derived from the broadband-noise floor requirements and the Unwanted in-band Emissions specifications. If we were to assume that a maximum of two 20 MHz LTE carriers are supported by the multi-mode transmitter, then the requirements would be determined as follows. For frequency offsets less than 1.8 MHz but above 200 KHz, the phase noise is derived from the specifications corresponding

Table 4.3: Phase noise for frequency offsets < 10MHz

$f_{\mathbf{low}}$ - $f_{\mathbf{high}}$ KHz	**Phase-noise**
$200 \geq f_{\text{offset}} < 400$	-116.50 dBc/Hz
$400 \geq f_{\text{offset}} < 600$	-124.55 dBc/Hz
$600 \geq f_{\text{offset}} < 1200$	-142.00 dBc/Hz
$1200 \geq f_{\text{offset}} < 1800$	-148.00 dBc/Hz
$1800 \geq f_{\text{offset}} < 10000$	-153.77 dBc/Hz

to the Band Category 2 (BC2) specifications[19]. In the case of BC2 the derivation of phase noise assumes six GSM carriers at the edge of the carrier aggregation, requiring the phase noise to satisfy the GSM or EDGE ORFS spectral mask. To derive a first-approximate phase noise mask for these offsets we assume a suitable back-off, an additional margin of $6 - 8$ dB corresponding to the degradation in the transmitter together with a correction factor of $10\log(6)$ corresponding to the number of carriers. The RBW varies with the offset from the carrier (see [48]) and also needs to be taken into account when calculating at each offset. The resulting mask is given by Table 4.3.

If the GSM/EDGE carriers are disabled, then the requirements of BC1 would define the specifications for phase noise performance at offsets less than 5 MHz. While these specifications were derived (and found to be more relaxed[20]), we do not present them here since GSM support is assumed active.

For frequency offsets 1.8 MHz $< \Delta_f <$ 10.25 MHz, the requirement is set by the Spurious Emissions limits of BC2, which stipulates that the emissions must not exceed -30 dBm/3 MHz (-94.77 dBm/Hz). Relating this to the carrier power of 49.0 dBm, this would yield a requirement of -143.77 dBc/Hz or -153.77 dBc/Hz with a margin of 10 dB and uniformly distributed carrier PSD assumed. If GSM/EDGE carriers were not active in the configuration, the 3GPP BC1 Spurious Emissions specification of -13 dBm/3 MHz (-73.77 dBm/Hz) would set the requirement of (-132.77 dBc/Hz) with the same margin incorporated.

The large offset phase noise ($\Delta_f \geq 10.25$ MHz) is set by the Spurious emissions specification of -98 dBm/100 KHz (or -148 dBm/Hz). If a worst case duplex rejection ratio of 50 dB is assumed, this would yield -98 dBm/Hz. Relative to for a carrier power of 49.0 dBm, this would yield, -147 dBc/Hz, given the convolution of phase noise spectrum with the carrier[21]. Typically, there are several contributors to the broadband noise floor, as illustrated

[19] BC1 refers to multi-standard transmissions that do not involve GSM/EDGE carriers while BC2 refers to active GSM/EDGE carriers.

[20] These specifications are derived by placing the carrier configuration at the Tx band-edge and deriving the specifications from the Unwanted-in-band Emissions mask.

[21] The bandwidth of the carrier is irrelevant because the phase noise contributions add up to roughly the same amount in all cases. If a carrier PSD is assumed to comprise of several 1 Hz frequency bins spanning its entire bandwidth, then, assuming each frequency bin is modulated in such a way that it would be uncorrelated with the other bins, i.e., i.i.d., which is consistent with our assumptions of noise-like signals, then the phase noise convolves with each bin and adds up in power at the given frequency offset, to yield the dBm/Hz power level.

in Figure 4.13. As a result, we would need to back-off each of the requirements in addition to providing a margin for implementation. Typically a margin of 10 dB is assumed resulting in approximately −157 dBc/Hz of large-offset phase noise. The phase noise is specified at ARP although this noise is introduced early in the chain, in the sense that the dynamic range between the carrier and the large offset phase noise in dBm/Hz is assumed almost unchanged. This is because the noise in a cascade of blocks is set by the first few blocks in the chain if the gain is sufficiently high near the input. This will become more evident from the budgeting in the next chapter, that the input referred Noise Figure (NF) of the chain does not significantly degrade after the Mixer and the DAC. As a result the 10 dB margin is sufficient to compensate for any subsequent accumulations in the chain.

4.3.7 Image Rejection and LO suppression Requirements

While we considered the signal quality degradation $\text{EVM}_{\text{IQ Imbalances}}$ due to in-band images in Section 4.2.3.2, the IQ image rejection requirement is actually defined by the leakage of the unwanted sideband (i.e., image) signal into the Receive band of the same BStn. This specification is controlled by the transmitter spurious emissions specifications, which defines a limit of −91 dBm/Hz (originally −96 dbm/100 KHz[22] - 55 dB Duplexer isolation), without considering the rejection of the Duplex filter. If six carriers of equal power in a Wide Area 49.0 dBm $P_{\text{max,R.M.S.}}$ BStn are assumed, this amounts to roughly −23.54 dBm/Hz per carrier, assuming all are LTE carriers (OBW=4.51 MHz) and have a flat PSD. Typically a back-off of roughly 3 to 5 dB is added to this specification, resulting in −91 dBm/Hz + −5 dB - −23.54 dBm/Hz ≈ 72.46 dBc/Hz of image suppression across any 1.0 MHz window. Here we have assumed no margins. Typical unaided carrier and sideband rejection values of −45 dBc (< 0.55% EVM) may be chosen, usually enhanced by calibration up to −70 dBc (< 0.03% EVM) depending on the IF frequency. The assumptions for equalization at the receiver vary among standards and need to be taken into account when determining a more exact requirement. In all of our analyses we have assumed six carriers, as this is the most common carrier aggregation supported among contemporary BStns. We begin to see how the system level carrier aggregation scenario (see Chapter 3) defines the performance requirements for the operation of the BStn. It is perhaps worth noting that the requirement of IQ suppression is also closely tied to the tolerance of the carrier to DC-offset and flicker-noise, the choice of IF frequency at the output of the DAC, the dynamic range at the highest clock frequency of the DAC, the Duplex filter stop-band rejection and also the frequency selective IQ imbalance behaviour in the AQM. These are some of the tradeoffs at system level that allow us to compare Zero-IF versus Low/High-IF transmitter architectures.

If the IF is large, then the LO signal can fall outside of the Tx frequency band, but also outside of the Rx band. This is done considering the limited clock frequency of the DSP processors (typically ≈ 245.76 Msps), which limit the IF to relatively small values. The power of the LO carrier between the Rx and Tx bands is limited by the transmitter Spurious Emissions specification for BC2, stipulating a maximum power of −30 dBm/3 MHz (−95 dBm/Hz) at offsets 30 MHz away from the Tx band edge. The specification is 6 dB tougher

[22] This is derived from the requirements which protect or prevent the receiver of the same BStn from desensitisation due to Tx signal leakage.

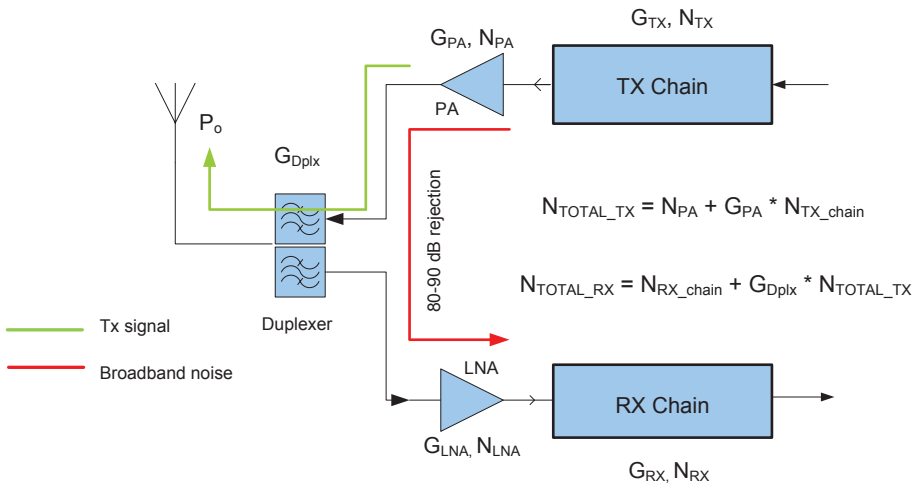

Figure 4.18: Degradation of Rx sensitivity by Tx noise leakage into Rx frequency band

if operating at frequencies < 1 GHz. Depending on offset from the Tx band edge, typically 10 to 40 dB can be gained from duplexer rejection, yielding a relaxation to -95 dBm/Hz $+ 10$ dB $= -85$ dBm/Hz, at a worst case. Since this is measured in a 1.0 MHz RBW, the power with respect to the carrier (dBc) is then -85 dBm/Hz $+ 10\log(10^6)$dB - 49.0 dBm or -69 dBc. A typical margin for implementation would be added to this and is easily measured by a one-tone test. Due to the steep requirement, LO leakage suppression is achieved by a combination of native analog suppression (-40 dBc) and digital compensation (-30 dBc).

4.3.8 Output Noise Requirements

In FDD architectures, the Rx of a BStn is desensitised when the spectrum of the Tx extends into Rx frequency band. The transmitted signal leakage manifests as additive noise in the Rx band, deteriorating the noise figure (NF) of the Rx. This mechanism of degradation of the Rx NF can be explained with the aid of the Figure 4.18.

The cumulative broadband noise that leaks from the transmitter comprises amplified Tx phase noise (at large carrier offsets), spurs, unfiltered LO harmonics, non-linearity products and thermal noise from the various Tx components. This specification is among the most demanding of the transmitter spectrum leakage specifications, especially when applied to unpaired[23] frequency bands with small duplex frequency separation. The degradation of the sensitivity of the Rx can be expressed as

$$10^{\frac{\text{Degraded Rx sensitivity in dBm/Hz}}{10}} = 10^{\frac{\text{Thermal Noise floor in dBm/Hz}}{10}} \cdot 10^{\frac{\text{Rx Noise Figure in dB}}{10}} + 10^{\frac{\text{Tx noise leakage in Rx band dBm/Hz}}{10}} \tag{4.36}$$

[23]This denotes that in FDD the Tx and the Rx do not share the same frequency band, as is done for TDD bands.

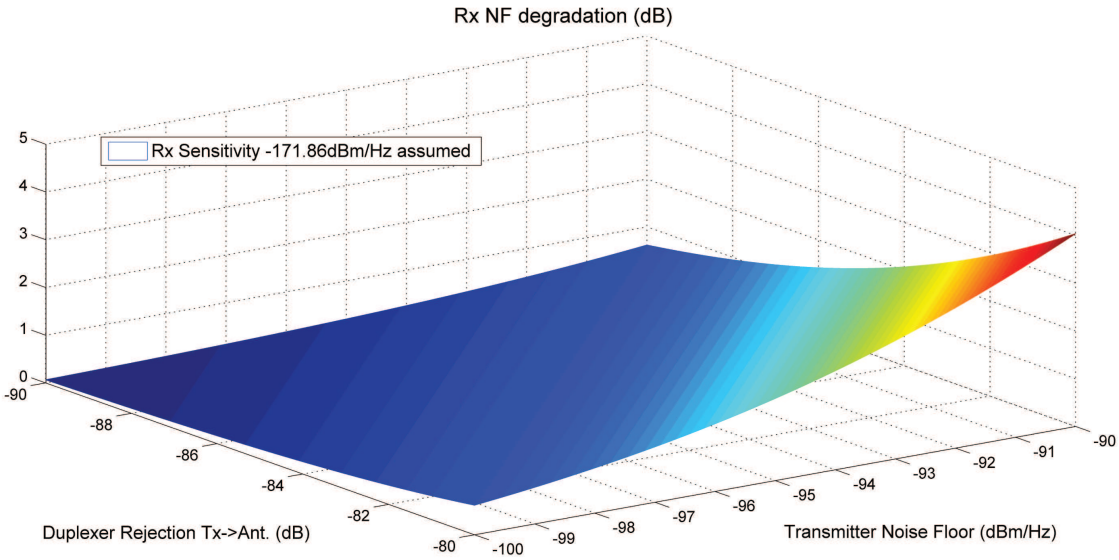

Figure 4.19: Degradation of Rx sensitivity as varying levels of duplexer rejection and Tx noise

The first term on the left hand side refers to the sensitivity of the Rx without Tx noise leakage. If we assume the Rx NF to be 2 dB, the inherent Rx sensitivity is then −171.86 dBm/Hz. Equation 4.36 becomes

$$10^{\frac{\text{Degraded Rx sensitivity in dBm/Hz}}{10}} = 10^{\frac{-171.86\text{dBm/Hz}}{10}} + 10^{\frac{\text{Tx noise leakage dBm/Hz}}{10}} \tag{4.37}$$

The clause protecting the Rx from desensitisation due to Tx leakage stipulates a maximum leakage limit of −98 dBm/100 KHz (−148 dBm/Hz). The specification is most demanding at maximum or rated average output power when the BStn is at its maximum gain setting. If the highest Tx noise floor is set to −148 dBm/Hz, a minimum duplex filter rejection of A_{duplexer} (= 50 dB) in the Rx band results in a degraded sensitivity given by

$$10^{\frac{\text{Degraded Rx sensitivity in dBm/Hz}}{10}} = 10^{\frac{-171.86\text{dBm/Hz}}{10}} + 10^{\frac{-198\text{dBm/Hz}}{10}} = 10^{\frac{-171.849\text{dBm/Hz}}{10}} \tag{4.38}$$

This implies an NF degradation (see Figure 4.19) of (−171.86 dBm/Hz - −171.849 dBm/Hz =) 0.01 dB. While this is desirable, the requirement of −148 dBm/Hz is a very demanding specification for the Tx given that the output noise floor at the DAC (e.g. AD9142) is not better than −160 dBm/Hz. A typical Tx gain of 55 dB from the DAC to the ARP amplifies this to −105 dBm/Hz. In the amplification towards the ARP, the Tx chain further degrades the noise floor by ≈ 10 dB, to yield a broadband noise floor of ≈ −95 dBm/Hz. This is significantly above the −148 dBm/Hz initially assumed. Consequently, typical values for duplexer rejection are between 85 and 90 dB (e.g. Kathrein Duplexer-Combiner 78210192),

allowing the Tx noise leakage in the Rx band to be ≈ -185 dBm/Hz. This adheres to the 3GPP specification and degrades the NF of the Rx by an acceptable ≈ 0.2 dB. If less sensitivity degradation is required, then the Tx noise floor would need to be further reduced, till the impact is minimised to acceptable levels. However, this stresses the Tx and the duplexer further. From (4.27), we have also seen the impact of the filter specifications on the signal quality. As Tx-Rx frequency separations reduce, the performance of the duplex filter/combiner performance[24] becomes particularly critical.

4.3.9 Peak-to-Average Power Ratio (PAPR)

The simplest form of distortion occurs when a signal (envelope) is passed through a non-linear device, generating non-linear distortion products. Assuming a memoryless non-linear system, the distortions that are produced have a one-to-one relationship with the corresponding input signal [82, 83]. In the transmitted signal quality metrics described in previous sections, measurements are both ensemble (i.e., made over several symbols) and time averaged measurements, implying that the impact of the instantaneous distortion mechanisms on these metrics depends on the statistical probability of their occurrences [84].

In analog design the Peak-to-Average-Power-Ratio (PAPR) presents a qualitative estimate of the tradeoff between the linearity and efficiency in the design of the corresponding block. For a device that is biased with a certain back-off from its compression point, a higher PAPR (given a certain average) leads to higher non-linearity and consequently, more spectral regrowth. Simultaneously, this also implies a greater probability of the device being in instantaneous saturation, leading to a higher efficiency[25] The PAPR is determined by observing a signal over a time period and then determining the probability of peaks with respect to the average within the period. For a sinusoid this is relatively straightforward, but is complicated for modulated signals. This characterisation of the PAPR is achieved by observing the statistical distribution of the signal over a reasonable time window. The PAPR of a composite signal $x(t)$ is given by,

$$\text{PAPR[x(t)]dB} = 10log_{10}\left[\frac{\mathbf{Max}\{x(t).x'(t)\}}{\mathbf{E}\{x(t).x'(t)\}}\right] \tag{4.39}$$

where, $\mathbf{E}\{.\}$ is the expected value operator.

Complementary Cumulative Distribution Function (CCDF) The CCDF of the PAPR characterizes the *weighted* probability of the signal excursions i.e., peak-amplitude distributions relative to the envelope average, by indicating the number and probability of instances where the signal peak power exceeds its average power by a certain value [85]. The CCDF of PAPR$[x(t)]$ is denoted $\rho(\cdot)$ and given by

$$\rho(c) = \int_{c+E[xx']}^{\infty} f_{xx'}(p)dp \tag{4.40}$$

[24] We do not specify the performance of the duplex filter here because that would require knowledge of the Rx specifications which are beyond the scope of this work.

[25] A non-linear active device is theoretically more efficient near compression than at a high back-off.

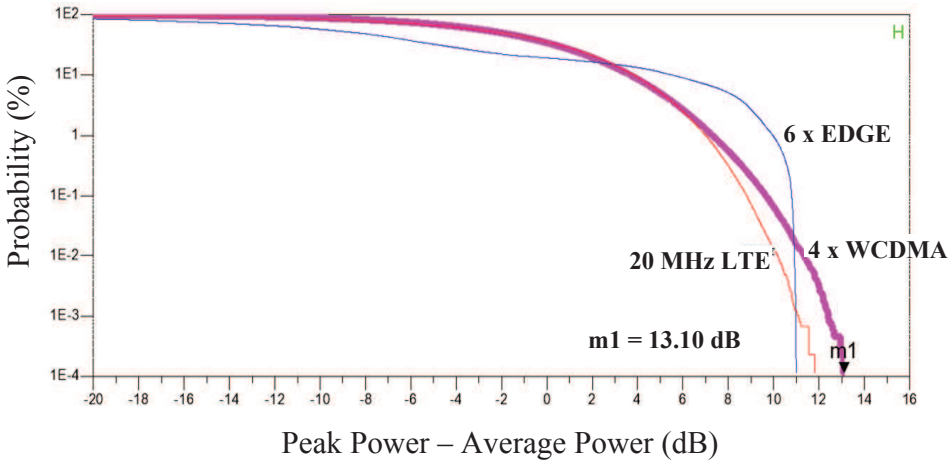

Figure 4.20: Simulated CCDF of the PAPR for multi-carrier transmission

where, c is the value of the PAPR for which probability is recorded and $f_{xx'}$ is the Probability Density Function (PDF) corresponding to the power of the signal $x(t)$. Over a reasonable time window of observation, designers refer to the PAPR at $10^{-2}\%$ to $10^{-4}\%$ (*level-of-confidence*) probability in order to back-off or de-rate the device from compression, or reduce the input signal itself. In modern BStns, the dynamic range of the signal is shared between the DAC and the VGA. If power-control is required per-carrier and is uncoordinated between the carriers, this can only be achieved in the digital domain. As a result, the addition of the large (*static* and *dynamic*) gain control ranges on top of the PAPR of the composite signal stresses the dynamic range required from the components [10]. We will discuss this issue of dynamic range in the following chapter.

The composite signal PAPR depends on the constituent carrier configuration, i.e., the number and type of carriers (including specific modulation scheme used), the relative power levels, the correlation factor between them and also to an extent, the frequency separation between the carriers. One of the challenges in the Baseband of multi-mode transmission in the varying sampling-rate requirements among the various Standards which are completely unrelated. In order for a DAC to convert and transmit a composite signal to the Analog/RF chain, it is necessary to equalise the sampling rates of all the carrier so as to have shared hardware with a common clock rate. While GSM/EDGE signals have a symbol rate of $T_{\text{GSM}} = 1625/6$ Ksps $= 3.692\mu$sec, LTE and WCDMA share the same base rate $T_{\text{WCDMA}} = T_{\text{LTE}}/8 = 1/3.84Msps = 0.2604167\mu sec$, where a 20 MHz LTE signal was assumed. The relation between the two is $T_{\text{GSM}} \cdot \frac{325}{4608} = T_{\text{WCDMA}}$[26]. The total simulation time is 230msec which includes 50 complete GSM/EDGE frames ($50 * 8 = 200$ bursts), and 23 WCDMA frames ($23 * 15 = 345$ slots). It is necessary to ensure complete frames are sampled in order to prevent truncation related errors from clipped frames.

[26]This issue has been addressed by earlier works, using efficient Farrow structures to achieve the fractional re-sampling [3].

Table 4.4: Simulated PAPR values for Downlink signals

Transmitted Signal	**PAPR**	
Probability threshold →	10^{-3}%	10^{-4}%
(20MHz) LTE[a]	11.17 dB	11.79 dB
6x*EDGE*	10.97 dB	10.99 dB
4x *WCDMA*	12.41 dB	13.11 dB
4x *WCDMA* + 6x*EDGE*	11.13 dB	11.33 dB
6x*EDGE* + (20MHz)*LTE*	10.98 dB	11.04 dB
4x *WCDMA* + (20MHz)*LTE*	12.55 dB	13.09 dB
6x*EDGE* + 4x *WCDMA*+(20MHz)*LTE*	11.15 dB	11.23 dB
4x *WCDMA*[b]		13.11 dB
3x *WCDMA*		12.76 dB
2x *WCDMA*		12.13 dB
1x *WCDMA*		10.31 dB
N_cx*EDGE* (*correlated*)[c]	$\approx 3.28 + 10log_{10}(N_c)$	
20MHz *LTE*	-	11.79 dB
15MHz *LTE*	-	11.67 dB
10MHz *LTE*	-	11.70 dB
5.0MHz *LTE*	-	10.76 dB
1.4MHz *LTE*	-	10.34 dB

[a] Similar to Gaussian distribution (of voltage) with PAPR limited according to the Central Limit Theorem.
[b] Contiguous channels, TM1 64 DPCH (full-load) with different scrambling codes per carrier.
[c] 2G signals typically have high degrees of correlation only during transmission of training sequences (presenting higher PAR) and not otherwise. N_c is the number of carriers.

For the purpose of determining dynamic range requirements for this transmitter, the composite PAPR of a composite signal comprising of six GSM/EDGE carriers (400 KHz frequency separation), four UMTS (WCDMA-HSDPA) carriers (Test Model TM1, 64 DPCH) and one LTE carrier (1.4 MHz - 20 MHz, varying bandwidths), in different combinations is simulated and analyzed here. These equal powered carriers are measured at a 'Level-of-Confidence' probability threshold of 0.001% and also 0.0001%. The carriers are combined in the complex domain (with variable frequency offsets) after having their sampling rates using fractional interpolation, as indicated above. The carriers are then qualified after measuring their respective EVM before observing the CCDF of their PAPRs. Simulated PAPR[27] values for different carrier configurations are indicated in the Table 4.4.

Due to the inherently high PAPR in modulated signals, Crest Factor Reduction (CFR)

[27] Although PAPR is the industry standard in determining the de-rating of a non-linear device, Cubic Metric (CM) is gaining prominence and has been shown to be more accurate in describing the distortion of specific modulated signals when subjected to non-linearity [86].

techniques [87, 88] are deployed in the digital domain by statistically altering the behavior of the signal itself or, by brute-force methods (peak-limiting by clipping and filtering/windowing) in order to limit the PAPR of the transmitted signal to an admissible range. However, most methods cause signal distortion (generating noise and signal leakage) affecting both the signal and its neighboring channels, necessitating a tradeoff. For this reason, CFR methods are also characterized by the signal distortion they induce quantified by a corresponding EVM (which is typically a fraction of the defined threshold) and ACLR.

4.3.10 Impact of Digital Pre-distortion (DPD): Assumptions

Efficient Multi-Channel Power Amplifier (MCPA) modules are quickly becoming prerequisites in the effort to make BStns more efficient. However, in order to achieve acceptable PA efficiencies, the input signals need to be digitally *pre-distorted* to compensate for the non-linearity of the device which comprises AM/AM, AM/PM modulation and also memory-effects. Without pre-distortion the un-aided performance requirements of the PAs to achieve the same linearity would otherwise demand an impractical power budget, eliminating any efficiency gained in the small-signal chain. The basic concept of DPD is illustrated in Appendix A. It is easy to notice that instead of transmitting the input signal, a modified polynomial transfer function containing the signal was necessary for the pre-distortion. This expansion implies an increased PAPR which places additional demands on the dynamic range. For this reason CFR techniques are typically co-designed with DPD algorithms, so as to contain the power budget on the highly backed-off, linear small-signal RF blocks.

Assuming time domain addition or combination of multi-mode carriers, their combined statistical distribution is a convolution of individual PDFs of the constituent carriers. To calculate the PA back-off, it is normally sufficient to use the $10^{-2}\%$ PAPR of the composite waveform as expressed in the previous section. This is because the CFR is agnostic to the performance of the amplifier. However, since ACLR is an averaged metric, it is necessary to consider the complete PDF of the signal rather than just one point, because the composite envelope amplitude distribution combines with the amplifier's transfer functions (AM/AM and AM/PM and memory effect etc.) to determine spectral performance. As an example, if $x(t)$ and $y(t)$ are multi-carrier (power) signals of GSM/EDGE and WCDMA signals respectively, the composite signal $z(t)$ obtained by the addition of the two waveforms is given by

$$z(t) = x(t) + y(t) \tag{4.41}$$

Let f_z denote the PDF of $z(t)$. $f_z(z = c)$ is the PDF of $z(t) = c$, where c is any arbitrary value for which the probability is assumed. Consequently,

$$f_z(z = c) = f_z(x + y = c) \tag{4.42}$$

If we assume that x and y are normalised values of $x(t)$ and $y(t)$, normalised to the average value of $z(t)$, we obtain

$$f_z(z = c) = \int_{a=-\infty}^{\infty} \underbrace{f_x(x = a)}_{H(\tau)} \cdot \underbrace{f_y(y = c - a)}_{G(t-\tau)} \underbrace{da}_{d\tau} \tag{4.43}$$

The above resembles a convolution function $h(t) * g(t)$, which implies

$$f_z(z = c) = f_x(x = a) * f_y(y = c - a) \tag{4.44}$$

Now, if c corresponds to a certain PAPR, the probability of $z(t) > c$ is

$$Pr[z > c] = f_z(z = c + 1) + f_z(z = c + 2) + \ldots + f_z(z = c + n)\ n \longrightarrow \infty \tag{4.45}$$

The Cumulative Density Function (CDF) or cumulative PDF is given by

$$\rho[z] = \int_c^\infty f'_z dz' \text{ where } z' = (z = c + 1),\ z = c + 2,\ \ldots,\ z = c + n \quad n \longrightarrow \infty \tag{4.46}$$

where f'_z is the PDF of $z = c + n$, $n > 0$. If c is the average amplitude (i.e., mean of the PDF), then subtracting the above expression from 1 (i.e., $\rho'[z] = 1 - \rho[z]$) yields a simplified mathematical representation of the CCDF of the PAPR of the composite signal. If the signal is subject to a simple polynomial non-linearity given by Appendix B.2, the analysis evidently becomes more complex. Despite the above expression suggesting the effect of the signal PDF on the spectral leakage (e.g. ACLR), we rely primarily on computer simulations to give us a more detailed distribution of the PAPR of composite signal, owing to the complexities involved in its computation. Therefore, with DPD, the analytical OIP3 calculation becomes progressively complex and the ideal of using an empirical correction factor C_n like we did in Section 4.3.3.1 is no longer single valued for a given carrier configuration. This relation highlights an important dependency on the operation and compensation of the HPA as a function of the statistics of the modulated signal. As a simplification, DPD impact can be included as an empirical correction factor (in Equations 4.30-4.34) corresponding to the NdB improvement in IM3 levels specific to the carrier configuration, giving approximately $\frac{N}{2}$dB reduction in the required OIP3. This, we source from previous DPD solutions for Doherty PAs in the market. Typically, in order to have the linearity requirements set by the final active block (PA) in the chain and minimize the (non-linearity) impact of small-signal block that precede the PA, so that the power-intensive DPD compensates only the PA in the transmit chain, the preceding blocks must have a significantly high OIP3 in order to avoid being the linearity-bottleneck (see Figure 4.21).

4.4 Summary

In this chapter, we discussed the translation of 3GPP specifications with respect to signal quality and signal leakage metrics by making first order approximations of the various distortions present in the Tx chain. From the graphs that show simulated EVM degradation against distortion for different access technologies, it is evident that using equations which assume narrow-band signals is suitable for only first approximations in modulated signals that are wide-band. This is due to the fact that these access technologies are provided with several mechanisms to tolerate distortions as in the case of spreading gain ($< 10\log(Spreading\ Factor)$) in WCDMA signals. Nevertheless, these relationships are useful tools in analysing the performance requirements of each block and in highlighting bottlenecks or critical tradeoffs. Following from this chapter, we consider the stringent linearity

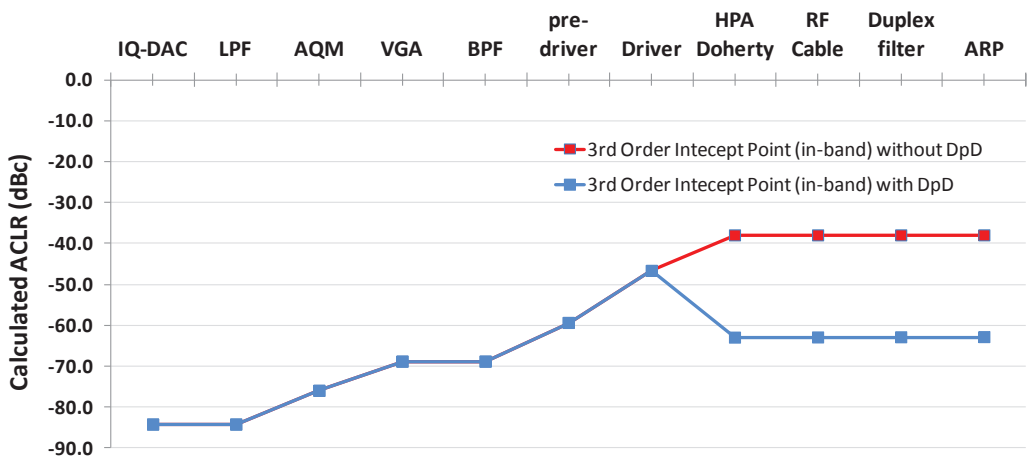

Figure 4.21: ACLR degradation for six EDGE carriers, at the output of each block along the transmit chain, with $P_o = 49.0$ dBm

Table 4.5: RF parameters for Simultaneous Multi-Mode Tx derived from analysing EVM contributions

RF Parameter	Derived value (A.R.P.)		Established by
Noise floor	≤ -95 dBm/Hz		GSM/EDGE/UMTS/LTE
Linearity	≥ 79.0 dBm[A]		GSM/EDGE
IQ Imb.($\Delta\theta$ / ϵ_A)	$\leq 1^\circ$ / ≤ 0.1 dB		-
(uncompensated)	-94.00 dBc/Hz	$f_{\text{offset}} < 10$ KHz	(LTE, w/o CPE correction) [C]
	-106.00 dBc/Hz	$10 \geq f_{\text{offset}} < 100$ KHz	(LTE, w/o CPE correction) [C]
PLL Phase-Noise[B]	-116.50 dBc/Hz	$200 \geq f_{\text{offset}} < 400$ KHz	
Mask	-124.55 dBc/Hz	$400 \geq f_{\text{offset}} < 600$ KHz	
	-142.00 dBc/Hz	$600 \geq f_{\text{offset}} < 1200$ KHz	
	-148.00 dBc/Hz	$1200 \geq f_{\text{offset}} < 1800$ KHz	
	-153.77 dBc/Hz	$1800 \geq f_{\text{offset}} < 10000$ KHz	
	-157.00 dBc/Hz	$f_{\text{offset}} \geq 10$ MHz	

[A] Measured for six GSM/EDGE equidistant, equal powered carriers, 49 dBm total power. Digital pre-distortion will approximately improve IM3 by 25 dB and thereby reduce HPA percentage in EVM_{net}.
[B] PLLs implemented to meet this mask will have lesser EVM contribution. The reference Oscillator (e.g. CCHD-950) contribution to EVM (limited to < 1 KHz) is not significant.
[C] CPE correction in LTE would reduce it's distortion (EVM) from phase noise making it less sensitive to PN. The integrated

requirements from GSM/EDGE specifications, the sensitivity of LTE to phase noise, and a shared requirement of the broadband noise floor in order to budget for OIP3 (and $P_{-1\text{dB}}$), NF, ϕ_n and IQ imbalance. This, we will discuss in the next chapter, where the budgeting of these specifications and a method to analyse or improve the distribution will also be pre-

sented. Another issue facing the transmission of multi-channel signals is the high PAPR of the composite multi-standard signal, which we observed from the CCDF of the PAPR of various carrier configurations. We use these findings in order to isolate the dynamic-range bottleneck, in the next chapter. The DPD plays an important role in improving the efficiency and easing the budgeting of the PA. But, although DPD suppresses IMD at the output of the PA, it increases the inherent non-linearity of the baseband signal which increases the OIP3 requirements of the small-signal blocks. This is accompanied by an increase in the PAPR (or CM) of the pre-distorted signal and therefore needs careful optimisation when budgeting for the small-signal blocks of the chain. The Table 4.5 summarises the Tx performance requirements collated from the analyses above.

Chapter 5

Multi-Mode Transmitter Performance Budgeting

In the previous chapter we described one of the processes involved in system design/analysis, where the transmitter performance requirements are synthesised from the 3GPP system level metrics. Here we will translate or distribute some of these derived requirements into block level performance requirements, in particular OIP3, Phase Noise, Noise Figure and IQ Imbalances. An overview of the methodology is as described in Section 2.7. So far we have made assumptions of the various impairments present in a transmitter and analysed, to a first order of approximation, the sensitivity of GSM/EDGE, WCDMA and LTE signals to these imperfections. We begin with a cascade chain analysis for impairments that are shared among the various blocks. For other impairments that are specific to a block, the budgeting will be rather straightforward.

5.1 Cascade Analysis for Cumulative Errors

Referring to (4.1), in the absence of any other imperfection, the required EVM is inversely related to the minimum required Signal-to-Noise Ratio (SNR) (i.e., $\text{EVM}_{\text{min}} \approx 1/\sqrt{\text{SNR}_{\text{min}}} \simeq \sqrt{\text{noise power}}/\sqrt{\text{signal power}}$) of a modulation scheme (see Section 4.2.3). Each transmitter component block has one or more of the imperfections and distorts the signal, producing an EVM contribution that is weighted as a function of its implementation and its position or role in the transmit chain. We will explain this with the case for block level noise contribution to the Tx noise floor at the ARP.

Let us consider the case of broadband (random) noise budget in the transmitter. For multi-mode operation, the absolute contribution from noise was identified in Section 4.3.8 to be ≤ -95 dBm/Hz. If a total of six to eight carriers[1] are assumed in a transmission bandwidth of 60 MHz (UMTS2100 band with DL frequencies $2110 - 2170$ MHz), the corresponding dynamic range is 49.0 dBm - $10\log(6)$ dB - (-95 dBm/Hz + $10\log(60M)$ dB) = 58 dBc for each carrier. This corresponds to a total EVM contribution from broadband noise, $\text{EVM}_{\text{Random Noise}}$, of $10^{-58/20} * 100 = 0.13\%$. This may seem somewhat relaxed, but it is quite

[1] These are a typical carrier numbers in modern BStns.

a demanding specification not only from the perspective of spectrum leakage, but also in the case of EVM in BStns which can support per-carrier power control (see Section 5.3).

Given a set of sequential blocks 'a', 'b', 'c' and so on, in the transmitter chain, we calculate the EVM contribution per block in the following manner. The EVM of the chain i.e., $\mathrm{EVM_{net}}$, R.M.S.,can be expressed as a quadratic sum of the block-wise R.M.S. contributions, as

$$\mathrm{EVM_{net}} = \sqrt{(\mathrm{EVM_a^2} + \mathrm{EVM_b^2} + \mathrm{EVM_c^2} + \ldots)} \tag{5.1}$$

where, EVM_a, EVM_b are the EVM contributions of block a and b and so on, respectively. Since we are treating only the noise contribution of a block, ignoring other impairments, we obtain

$$\mathrm{EVM_{net}} = \sqrt{\left(\frac{1}{\mathrm{SNR}_N}\right)} \tag{5.2}$$

which is the cumulative EVM after N blocks of the transmitter chain, and SNR_i (SNR_N), the cumulative SNR after the ith block (where, $i = 1, \ldots, N$) in the chain,

$$\mathrm{EVM_1} = \sqrt{\mathrm{EVM_a^2}} = \sqrt{\left(\frac{1}{\mathrm{SNR_1}}\right)} = \sqrt{\left(\frac{1}{\mathrm{SNR}_a}\right)} \tag{5.3}$$

$$\mathrm{EVM_2} = \sqrt{\left(\frac{1}{\mathrm{SNR_2}}\right)} = \sqrt{\mathrm{EVM_a^2} + \mathrm{EVM_b^2}} \tag{5.4}$$

The EVM contribution of block b in the chain is therefore

$$\mathrm{EVM}_b = \sqrt{\mathrm{EVM_2^2} + \mathrm{EVM_1^2}} = \sqrt{\mathrm{EVM_2^2} + \mathrm{EVM_a^2}} \tag{5.5}$$

$$\mathrm{EVM}_b = \sqrt{\left(\frac{1}{\mathrm{SNR_2}} - \frac{1}{\mathrm{SNR}_a}\right)} \tag{5.6}$$

where, $\mathrm{SNR_2}$ is the cumulative signal to noise ratio at the output of blocks a and b and EVM_a $= \sqrt{1/SNR_a}$. Or,

$$\mathrm{EVM}_i = \sqrt{\left(\frac{1}{\mathrm{SNR_{cumulative},}_i} - \frac{1}{\mathrm{SNR}_{i-1}}\right)} \tag{5.7}$$

where, EVM_i, is the EVM of the ith block in the chain, $\mathrm{SNR_{cumulative},}_i$, is the cumulative signal-to-noise ratio up to the ith block and SNR_{i-1}, is the signal-to-noise ratio of the $(i-1)^{th}$ block.

Due to the fact that the EVM_i is in the linear (as opposed to logarithmic) domain, we can easily determine the linear percentage contribution of the block with respect to the entire chain, corresponding to the particular distortion, i.e.,

$$\mathrm{EVM}_i\% = \frac{\mathrm{EVM}_i}{\sum_{i=1}^{N} \mathrm{EVM}_i} \tag{5.8}$$

The cumulative EVM of all the blocks corresponding the a given type of distortion, for example is therefore

$$\mathrm{EVM}_{\text{Random Noise}} = \sum_{i=1}^{N} (\mathrm{EVM}_i)^2 \tag{5.9}$$

The above method makes for a tractable analysis of the block EVM along the lines of the cascaded noise figure and can also be extended to other imperfections such as non-linearity (e.g. in IP3 calculations, by using IM3 as the measured distortion instead of noise and approximating ACLR to be a function of IM3), where the block EVM contribution also depends on its position in the chain. This treatment allows the EVM to be connected to the link budget analysis based on the mechanism highlighted above, and would help to improve on the performance distribution and also to highlight or understand possible tradeoffs. A cautionary note here is that this is only reserved for a preliminary analysis because, while most of the small-signal RF blocks work with high back-off ($\mathrm{P}_{-1\mathrm{dB}}$-$\mathrm{P}_{\mathrm{signal}}$) necessary for pre-distortion of the High Power Amplifier (HPA), the PA itself cannot be sufficiently described using IP3 and/or even IP5 values alone. Effects such as memory effects, frequency dependent non-linearity etc., become evident only with circuit implementation or advanced modeling. With the HPA being among the largest contributors to signal distortion (ignoring signal pre-distortion for simplicity), it is prudent to leave a suitable design margin during the preliminary analysis which can later be tapered down to exact values to minimize power consumption from the assumed excess margin. .

In multi-mode transmission, amplitude and phase cross-modulations (CMD) that occur at carrier frequency, and inter-modulation (IM3, IM5, IM7, for less than 3 carriers) and composite-triple-beat (CTB, for ≥ 3 carriers) products that fall in-band also affect the EVM ($\mathrm{EVM}_{\text{Non-Linear Distortion}}$) of a wanted signal, as indicated in Section 4.2.3.4. These however dependent on relative amplitudes of the active carriers, with the latter also depending on the carrier frequency separations[2]. Approximating $\mathrm{EVM}_{\text{Non-Linear Distortion}} \leq 1/10^{(\mathrm{ACLR}_{\mathrm{dB}}-30)/20}$ and using the EVM/distortion relations cited above, one can ascertain the $\mathrm{EVM}_{\text{Non-Linear Distortion}}$ in a similar manner. The toughest system level linearity requirement for simultaneous multi-mode transmission has been analyzed in Section 4.3.3.1 to need an (two-tone approximated) OIP3 of ≥ 79 dBm (68.45 dBm, for non-GSM) given a 49.0 dBm macro-BStn radio module of six to eight carriers. Since this meets the stringent (GSM/EDGE) spectral mask requirement of ≤ -70 dBc (post DPD), the ACLR requirement is expectedly more demanding than the EVM (assuming equal powered carriers). Given that it consumes a significant amount of power to achieve, the impact of in-channel non-linearity products is therefore well within tolerance limits (≤ -70 dBc $\simeq \leq 0.3\%$).

Now that we have established a mechanism to analyse the EVM contribution of block based on its position in the chain, we can more easily see the impact of the block on the transmitter. We will return to this topic once we have covered how to budget the performance specification.

In order to perform budgeting, we start by giving each block equal percentage of the total

[2]The impact of CMD is typically, greater on the EVM than on the ACLR of the channel. Given a varying number of modulated signals of dissimilar modes and varying power levels, the analysis of cross-modulation becomes complex. Ignoring the PM/PM modulation, the CMD/IM3 ratio is approximately 4.0 (6.02 dB)

EVM (EVM_{net}, see Figure 5.1). For example, with a budget of 3% and 10 blocks in the transmitter, this gives each block 0.3%, assuming the errors are correlated from one block to another. More realistically, if uncorrelated, this would be, 0.95% per block, based on a quadratic summation[3]. We could then calculate the performance requirements for each of the blocks. This would naturally yield unrealistic specifications. From a power perspective, PA is the most power hungry block in the chain. We then give EVM budgets to blocks based on their power consumption. This would end up with the small-signal blocks (e.g. DAC, AQM) having very demanding specifications to satisfy their corresponding EVM budgets, the design for which yields a power budget for these blocks which becomes contrary to the our assumption. If we were to distribute EVM budgets in reverse order, with the PA being given the smallest, then we end up with impossible performance expectations on the PA module. However, we would need to take into the impact of DPD which essentially decouples the native PA performance versus power-consumption relationship, by compensating for its non-linear effects in the baseband. Unfortunately, this would also come with the penalty of increased EVM contribution (CFR included) from the baseband signal processing[4]. Typical[5] EVM values for ASICs and FPGAs implementing the DUC, DPD and CFR varying between 2% and 4%.

This exercise demonstrates two things: that there are several factors not limited to linearity (assumed, due to compression) which determine the total power budget; secondly, the power consumption of a block is not the only factor that determines its distortion contributions. If we consider the example of a simple Mixer (see Section 6.3), the large-signal compression depends to a large extent on LO amplitude swing relative to IF. The LO amplitude and slope of the LO waveform also determine the IQ imbalance to a large extent, which translates into increased power consumption not for the Mixer, but for the LO chain, as we will see in the next chapter. Apart from the LO waveform, the IQ imbalance is also largely influenced by component mismatch, which is determined by the level of process control that has no power budget. Interestingly, the IQ imbalance can be largely compensated in the Baseband and is typically incorporated into modern DPD algorithms, subsequently shifting more of the power and EVM budget into the digital domain. These interactions are therefore not easily incorporated into a first-order approximation of budgeting. With the case of the IF anti-aliasing filter and the RF band-pass filter which attenuate non-linear products, this is more evident as they have no power consumption but require an EVM budget (see Section 4.2.3.5). These filters are invariably passive off-chip filters, because choosing an active filters to meet multi-mode BStn. spectral requirements would involve very high costs and poor trade-offs. Therefore, to reduce complexity and in order to highlight the relevance of analysing trade-offs in the chain, we assume a proven architecture which has already been evaluated against other options.

[3]This is another reason why we highlight Volterra series modeling for non-linearity for future work, as the phase relationships and therefore the correlation between non-linear byproducts is brought into focus.

[4]Baseband signal processing includes Digital Up-Conversion (DUC), DPD, CFR and Interfacing.

[5]e.g. Xilinx - Texas Instruments GC5322 and Altera LogiCORE-IP DPD.

Using Friis'[6] formula [89] for input referred noise

$$F_{ab} = F_a + \frac{F_b - 1}{G_a} \tag{5.10a}$$

also applied to OIP3

$$\frac{1}{OIP3_{ba}} = \frac{1}{OIP3_a \cdot G_b} + \frac{1}{OIP3_b} \tag{5.10b}$$

and OCP

$$\frac{1}{OCP_{ba}} = \frac{1}{OCP_a \cdot G_b} + \frac{1}{OCP_b} \tag{5.10c}$$

where, F_a, F_b, G_a, G_b, OCP_a and OCP_b refer to the noise factor, available power gain and output compression point of any two cascaded blocks 'a' and 'b', respectively, it is easy to observe that a better design is one which focusses only on the linearity of high power blocks (operating near compression) at the output stages of the chain, while also having high dynamic-range, high gain blocks near the input of the chain. Accordingly, the DAC and the AQM define the noise levels of the chain and enjoy a large portion of the $\text{EVM}_{\text{Random Noise}}$, while the PA largely determines the non-linearity of the chain and has a major portion of the $\text{EVM}_{\text{Non-Linear Distortion}}$. With pre-distortion (e.g. DPD), the PA budget is reduced and shifted to the Baseband. Since the Tx output noise floor is specified as an absolute power level (see Section 4.3.8), both NF (i.e,. relative SNR degradation) and also absolute noise contributions need to be minimised to meet specifications. The power gain up to the ARP is the highest from the DAC and the Mixer. Consequently, the noise contributions of these blocks continue to remain the most critical in the chain. Most modern DPD algorithms compensate for the non-linearity of the complete PA module, including the driver amplifier as well at the high-power Doherty PA stage. In order to achieve maximum compensation, the non-linearity contributions from the small-signal chain need to be kept to a minimum within the power budget. The tough dynamic range requirements of the small-signal become evident if we attempt to relate the linearity requirements to the compression point for a given DC bias setting.

Budgeting and verifying performance specifications for each iteration where the corresponding block-level EVM budget is incrementally adjusted in one order or the other is an involved task, so we jump ahead to reasonable assumptions based on inputs by expert designers and arrive at a distribution of performance by means of the cascade chain analysis. The cascade analysis is best begun with an approximate idea of the performance that can be achieved per block to achieve the total system performance.

The EVM expression from (5.7) indicating block level EVM contribution has exactly the same behaviour as that shown by the cascade equation. The relations between the different

[6]The OIP3 using Friis' formula is pessimistic as it assumes all non-linearity products to be additive, with no cancellation among them. With respect to the cascaded NF using Friis' formula, the noise factor 'F' is either larger or smaller than predicted, if the input impedance of a block is lesser or more that the source impedance to the block, respectively. Here we assume 50Ω matching for all stages, i.e., max. Power Gain, but also provide for mismatch in our Excel sheet calculations, where the available- and transducer power gains would be lower than their maximum value.

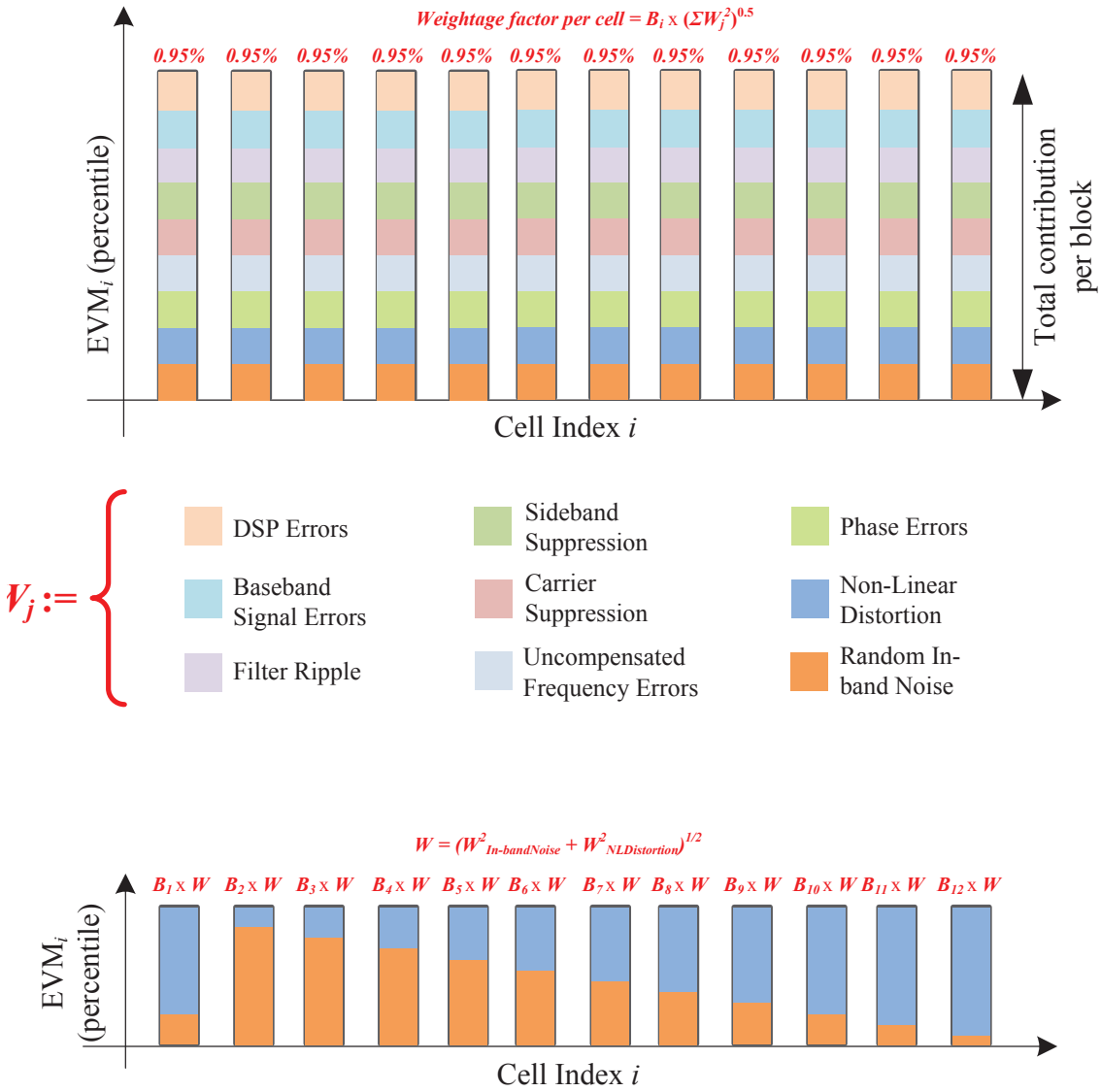

Figure 5.1: Block-wise distribution of EVM

EVM of (4.2) were discussed in the previous chapter. The total EVM of the ith block in the chain EVM_i is quadratic sum of its contributions

$$\begin{aligned}\text{EVM}_i \approx \Big[&(\text{EVM}_{\text{IQ Imbalances},i})^2 + (\text{EVM}_{\text{Phase,Frequency Err.},i})^2 \\ &+ (\text{EVM}_{\text{Non-Linear Distortion}}, i)^2 + (\text{EVM}_{\text{Random Noise},i})^2 \\ &+ (\text{EVM}_{\text{DSP, Baseband Err.},i})^2\Big]^{1/2}\end{aligned} \tag{5.11}$$

5.1.1 Weighting Factors

Returning to the analysis of EVM contribution from a block, it is easy to observe that while the cascade analysis (see (5.7)-(5.9)) brings out the percentage contribution per block (B_i), the specifications analyses from the previous chapter gives the absolute limits (W_j) for the corresponding distortion. By combining the two, it is possible to view the absolute linear EVM contribution per block, for a given type of distortion. The Figure 5.2 shows the relative and absolute $\text{EVM}_i\%$ when budgeting for noise (NF) and linearity (here, OIP3 only). The simplified impact of the DPD is modeled as an IM3 reduction in the cumulative IM3 level at the output of the HPA.

Although in most cases the resulting EVM contribution by each block has a strong relation to its power consumption, it should be noted that there are also other requirements which specify performance more stringently than EVM (e.g. Adjacent Channel Leakage Ratio or ACLR, for OIP3). The contributions have different cost-functions (power consumption, chip area, process control etc.) depending on the block. This can, for example be viewed as a figure-of-merit or a cost-function for each type of distortion from the block.

A diminishing $\text{EVM}_{\text{Non-Linear Distortion}}$ contribution at the output of the chain typically requires an increasing power budget. The case is similar for a smaller $\text{EVM}_{\text{Random Noise}}$ contribution at the ARP, with input blocks given higher priority. The above method would provide several conveniences including insights for budgeting based on cost of implementation. This can be seen as a cost function, where

$$\text{EVM}_i = \sqrt{\sum_{\text{errortype}} \left(\left(\underbrace{C_i}_{\text{Cost Parameter}} \cdot \underbrace{B_i}_{\text{Block Weighting factor}} \cdot \underbrace{W_j}_{\text{Error Weighting Factor}} \right)^2 \right)} \tag{5.12}$$

and, where the C_i is a cost function, B_i is given by the cascade analysis, with the W_j given by the performance specification from our system analyses. The i and j refer to the index of the block in the chain and the type of distortion, respectively, e.g. i = [DAC, AQM, LO, PA, etc.] and j = [Noise, Phase noise, IM3, etc.].

For illustrative purposes the Figure 5.3 shows the (percentile) block-level EVM contributions, as a percentage of the block total, with all the first-order of errors incorporated. The distortion depends also on the power and type/mode of carriers (GSM/EDGE, UMTS, LTE), the neighbouring carriers, and the relative powers between them, requiring a worst-case carrier-configuration specific weighting factor, W_j, for every distortion type, to be combined

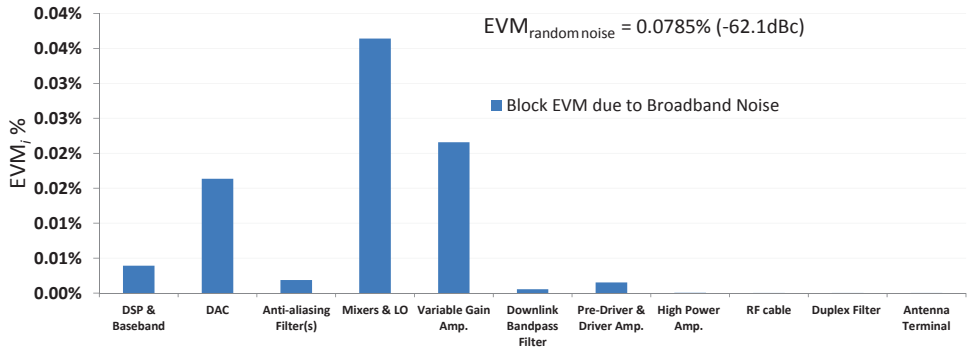

(a) Noise

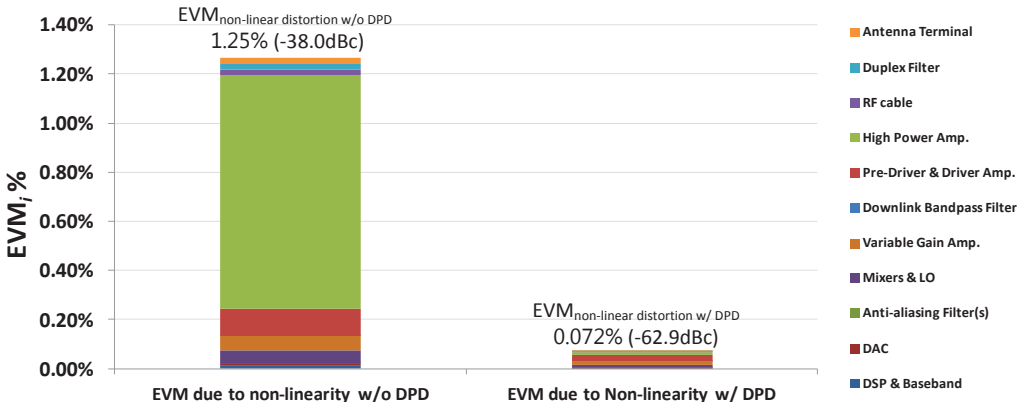

(b) Non-linear Distortion

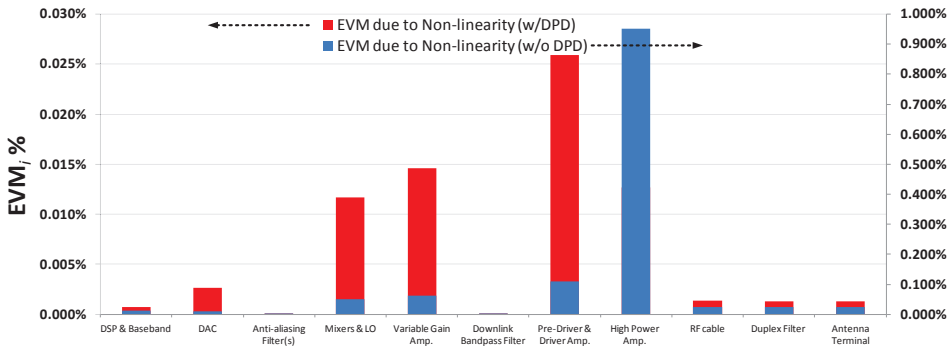

(c) Non-linear Distortion with and without DPD

Figure 5.2: Actual block-wise percentage EVM contributions for IP3 and Noise in figures 5.2(a) and 5.2(b). Figure 5.2(c) indicates the total actual EVM contributions, before and after DPD. The block level contributions in this case are equivalent percentages of the total and not actual.

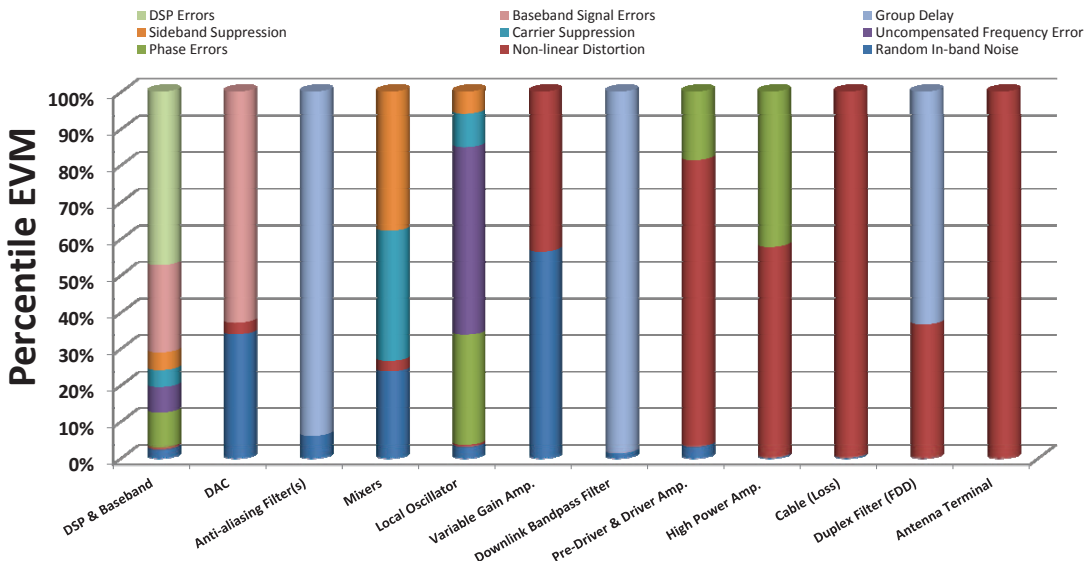

Figure 5.3: Percentile block-wise impairments in a multi-mode BStn transmitter (Pre-distortion, Baseband/DSP contributions and design margin not accurately represented.)

with the block's EVM contribution, B_i. For our analysis, W_j is obtained from simulations (see Figures 4.6, 4.9 and 4.11) and measurements. For example, in-channel noise has a greater impact on GSM/EDGE carriers than UMTS carriers (not shown here), requiring a higher W_{noise} for GSM/EDGE. The block-wise weighting for noise is shown in Figure 5.2(a). The information contained in W_j would be particularly useful for reconfigurable systems which employ software-defined run-time reconfiguration (refer Section 2.1) where reconfiguration decisions can be made depending on which carriers are active. The case for reconfigurable linearity was made in Section 4.3.3.2.

However, being very use-case-scenario and architecture dependent it is difficult to generalise based on a universal weighting factor and we consider worst case scenarios, by assuming that all carriers are active. For multi-mode transmitter design, the weighting corresponding to the toughest supportable carrier configuration is chosen, as mentioned in Section 4.4. This, when combined with the block and distortion weighting factors, allows one to conditionally optimize the power budget of the transmitter by a careful distribution the imperfections along the chain.

Referring to the cost-function, if we consider for example the linearity requirement (OIP3, $\text{OCP}_{-1\text{dB}}$, $\text{OCP}_{-3\text{dB}}$, etc.) of a block, the function could take the simple form $\frac{\text{P}_{\text{IM3}}}{\text{P}_{\text{dc}}}$ (for $\text{P}_{\text{signal,max}}$) or $\frac{\text{OIP3}}{\text{P}_{\text{dc}}}$. While this does not give a combined figure of merit for the block, it reflects the power consumption associated with achieving a certain OIP3 requirement. A simplified relationship between power consumption and the linearity requirement can be examined, by assuming a fixed ratio between the OIP3, $\text{OCP}_{-1\text{dB}}$ and the output signal swing. For a class-A amplifier (see Figure 5.4) with a resistive load R_L and collector resistance R_c ,

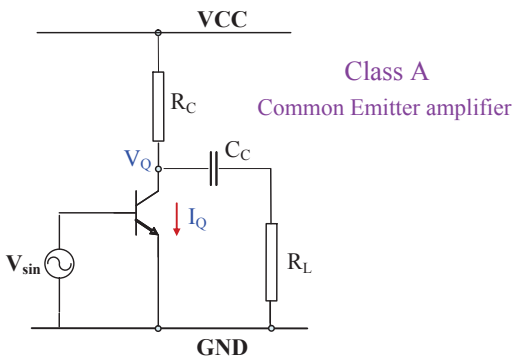

Figure 5.4: Class A amplifier stage linearity versus static power relationship

this would yield the basic expression[7]

$$\mathrm{OIP3} = \frac{V_{\max} R_{\mathrm{c}}}{0.05 V_{\mathrm{CC}}(R_{\mathrm{c}} + R_{\mathrm{L}})} \tag{5.13}$$

where

$$V_{\max} = \frac{V_{\mathrm{CC}} - V_{\mathrm{CEsat}}}{2} \tag{5.14}$$

The graph shown in Figure 4.21 illustrates the increase in leakage spectrum power, at the output of each block in the transmit chain, based on the outcome of one iteration of performance budgeting. Regions of increased slope relative to the input of the block indicates a bottleneck in the distribution of the OIP3 specification. This occurs when the IIP3 of a block is lesser than the cumulative OIP3 of the blocks preceding it. Inversely, a flatter curve with a high cost function would indicate an over-dimensioned block. Our budgeting was performed with the objective of maintaining a relatively smooth gradient of the indicated curve, while arriving at the input of the PA module with the lowest absolute IMD power achievable.

Similar relationships can be developed for other classes of amplification or other types of operation (e.g. Mixer), allowing one to optimize power consumption by tradeoffs among design objectives, among the active blocks in the transmitter. A case of optimisation between an ADC and the baseband filter was examined by [90]. Our expression above, however, assumes a simple relationship between linearity and power consumption of a block. This was shown to be insufficient, with the case of the Mixer, earlier. On a similar note, it is possible to have different architectures for the same design criteria, but with numerous tradeoffs which cannot easily be modeled by generalisations. We do not develop this further here, but is strongly suggested for future development of this work.

Apart from digital baseband signal errors, the IQ imbalances, phase noise and non-linearity are the major contributors to EVM requiring a significant part of the energy budget to achieve. From a noise-floor perspective, it can be observed that the D/A converter (DAC) and the Mixer/LO set the broadband noise floor requirements for the chain and carry the

[7] P. Jean, M. Perin, S. Kowlgi, 2009, personal communication

highest weighting factors for noise contribution. Similarly, the unaided HPA being the most power hungry, is the biggest contributor to the non-linear-distortion budget, thereby needing the largest portion of the EVM budget. The typical baseband EVM contribution (not indicated) is also comparable to that of the un-aided HPA. Figure 5.5 from one of several iterations required for the analysis, shows the resulting 'weighted' percentage error contributions by each of the blocks in a multi-mode base station transmission chain.

5.2 Other Errors

5.2.1 LO Leakage and IQ path imbalances

Treatments for other major imperfections such as IQ imbalances and (integrated) phase errors although cumulative, are not treated in the manner similar to IP3 or NF of the chain. The uncompensated baseband and analog modulator (IQ mixers) imbalances are independent of the signal being transmitted, but depend on the carrier frequency spacing and choice of IF frequency (zero- or low/high-IF architecture i.e., in-band or out-of-band image,) which adversely impact the DAC and ADC power consumption where the use of the NCO and higher interpolation factors proportionally impact the small-signal power budget, assuming contiguous carriers. From Section 4.3.7, we identified the requirements of roughly -40 dBc of rejection for both the unwanted Image the LO fundamental. The sharp transmission of the LO signal implies rich harmonic content which also need to conform to the Spurious Emissions specifications, much like the LO leakage. For these large frequency offsets the Duplex filter should provides adequate rejection (see Section 4.3.8).

Non-ideal sideband suppression and LO leakage can together be attributed to several sources in the transmitter, among them[8], -

- BB DC offsets and residual DC in modulator
- DAC output termination mismatch
- Reconstruction Filter gain and phase mismatch
- I and Q path PCB trace mismatch
- AQM input termination mismatch
- IQ differential imbalances: phase, gain

  Mixer IF, LO, RF port mismatches

  LO duty cycle asymmetry

  IF port I/Q path gain and phase imbalance
- Miscellaneous (parasitic-)capacitive and substrate EM couplings[9]

[8] Here we ignore Frequency selective impedance

[9] In our conceptual design, we only considered capacitive coupling and substrate coupling was ignored. This would become more critical during actual implementation of the design.

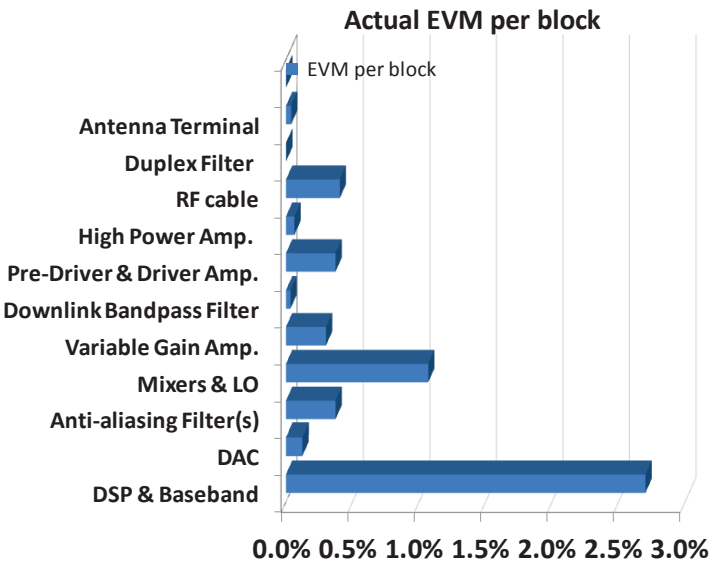

(a)

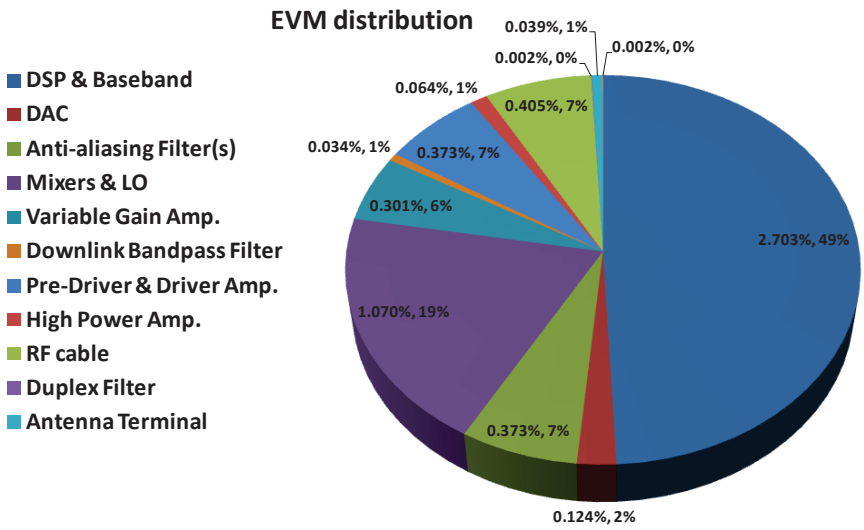

(b)

Figure 5.5: Block-level actual and percentage EVM contributions across a multi-mode BStn transmitter at rated power

IQ imbalances after the DAC are largely attributed to non-idealities in the AQM and the −40dBc rejection is incorporated into the AQM design by means of tolerances of the on-chip passives, matching in differential stages and the IRR of the LO polyphase filter (see Section 6.4). Assuming purely resistive input impedance, the gain mismatch is dominant. The most prominent DACs include an (8-bit or 10-bit) auxiliary DAC which is typically capable of providing up to 2.0 mA (in 2μA steps) of compensation current in order for DC offset cancellation, and also to reduce mismatch between the DAC output and the subsequent (AQM) stage. Typically, better than 10% tolerance[10] is required on the matching resistors. This translates into tens of mV of correction, depending on the matching impedances chosen. Loose tolerances worsen the imbalance and can potentially be beyond the compensation capability of the DAC chip. Similarly, a phase adjust of approximately 3.5° in $3.5°/2^{\text{N bits}}$ steps is also available for phase imbalance correction. IQ compensation can also be done in the baseband, before the DAC. The DAC is then used to calibrate against or compensate PCB mismatch issues from product sample to sample.

5.2.2 Phase noise

'Close-in' Phase Noise (PN) is given by degradation of the signal quality as suggested by $\text{EVM}_{\text{Phase,Frequency Err.}}$ indicated in Section 4.2.3.3. On the other hand, 'Far-out' PN levels at larger frequency offsets from the carrier manifest as leakage in neighboring channels and also degrade wanted-channel SNR via reciprocal cross-mixing (with neighboring carriers), depending on the relative multi-mode carrier powers. Un-attenuated large offset phase noise also appears in other frequency bands, degrading sensitivity or causing interference. These levels are set by the most stringent multi-mode ACLR (or ORFS) and SEM (Spurious Emissions Mask) requirements[11] as was indicated in Section 4.3.6. From our previous analyses and from several original works highlighted in the previous chapter, we note that the variance of the PN mask is the determining factor in the distortion of the signal. A variety of PN masks can be implemented, all having the same variance. Consequently, the choice of PN profile is dependent on the cost of implementing the PLL satisfying that mask. In the same analysis, we also noted the pronounced sensitivity of LTE to PN for small offsets, which was used to determine the close-in phase noise specifications. The Table 4.5 summarizes the synthesised phase noise conformance mask at all critical offsets, corresponding to PLL mask of the Tx. For the transmitter, phase noise is introduced in two stages, firstly, when Baseband data is converted into the analog signal and the clocks introduces timing jitter and secondly, the LO Synthesiser (PLL) which multiplies with the wanted signal in time domain i.e., convolution in frequency domain to give rise to spectral leakage. We use a budgeted reference EVM value of $< 0.5\%$ (≤ -45 dBc or $\phi_{n,\text{rms}} \leq 0.3°$ R.M.S.) which is confirmed by means of a simple piece-wise log-linear approximation (see Figure 5.6) as suggested by [91, 92]. The HPA also introduces random phase rotation ($\text{EVM}_{\text{Phase,Frequency Err.},HPA}$) as a function of its modulated input. Typical unaided Doherty HPAs produce between 15°-20° of AM-PM.

[10] This is obtained by calculating the residual DC offset after compensation by the DAC.

[11] With typical values approaching −160 dBm/Hz at $f_{\text{offset}} \geq 10$MHz, the levels are comparable to broadband in-channel/in-band noise, at the output of the mixing stage. Therefore, this value is equally useful in determining the Duplexer rejection. Here we do no make the distinction between AM noise and Phase Noise.

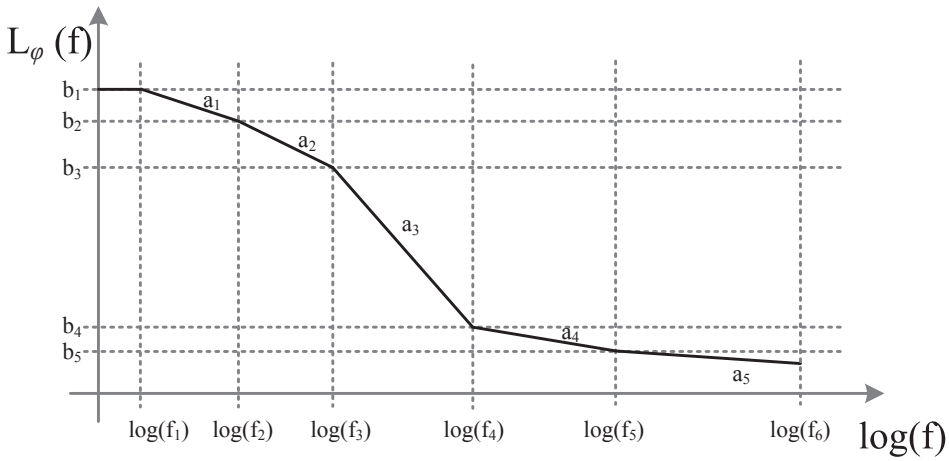

Figure 5.6: Piecewise linear approximation of the Phase noise mask for the calculation of integrated phase noise and jitter

At the time of writing, no exact inputs were available on corresponding compensation provided by the DPD. Any uncompensated errors could have a significant effect on the EVM, as demonstrated by 4.9. An additional margin would need to be included for this, where the $\text{EVM}_{\text{Phase,Frequency Err.},HPA}$ is quadratically summed[12] with that of the PLL and the Digital clocks to produce a net $\text{EVM}_{\text{Phase,Frequency Err.}}$.

Given the one side PSD of the PN, $L_{\phi_n}(f)$ dBc/Hz, as defined by Table 4.5

$$\phi_{n,\text{rms}} = \sqrt{2 \cdot \sum_{N-1}^{i=1} 10^{\frac{b_i}{10}} \cdot f_i^{\frac{-a_i}{10}} \cdot \left(\frac{a_i}{10}+1\right)^{-1} \left(f_{i+1}^{\frac{-a_i}{10}+1} - f_i^{\frac{-a_i}{10}+1}\right)} \tag{5.15a}$$

where N is the number of frequency points over which the $\phi_{n,\text{rms}}$ is integrated and

$$a_i = \frac{L_{\phi_n}(f_{i+1}) - L_{\phi_n}(f_i)}{\log f_{i+1} - \log f_i} \tag{5.15b}$$

$$b_i = L_{\phi_n}(f) \tag{5.15c}$$

assuming the piecewise approximation

$$\underbrace{L_{\phi_n}(f)}_{y} = \underbrace{\sum_{N-1}^{i=1} \left[a_i(\log f_{i+1} - \log f_i) + b_i\right] \cdot \left[U(f-f_i) - U(f-f_{i+1})\right]}_{\text{m}x+\text{c}} \tag{5.15d}$$

[12]This would mean that the two phase rotations are uncorrelated despite referring to the same modulated signal. If the errors are indeed correlated, the AM-PM effect is much worse [93] adding linearly, and needs to be treated carefully.

where $U(.)$ is the unity step function. The values corresponding to the above equations are summarised in Table 5.1.

5.3 Power Control Issues in a Multi-mode Transmitter

Power control in the Down-Link (DL) is of paramount significance as it aims to balance the need for sufficient transmitted energy per bit to achieve the required Quality-of-Service (QoS), against the needs to minimize interference to other UEs or BStns in the system. The power control mechanism adapts to the characteristics of the channel medium, including path loss, shadowing and fast fading, as well as overcoming interference from other BStns – both within the same cell and in neighbouring cells. This it does in order to move the cell's Signal-to-Interference-Ratio (SIR), particularly at the cell-edges (where interference is highest), closer to the network-optimum for throughput. While the mechanisms of DL power control are beyond the scope of this report, the specifications for power control range significantly affect system and block level design, more so in convergent multi-mode systems.

Through all of our previous discussions we have highlighted the increased dynamic range requirements from the higher PAPR and the stringent spectral leakage specifications. Future evolutions of BStns face yet another issue when carrier specific power control is required. The small EVM budget ($< 5\%$) available for simultaneous multi-mode transmission is a challenge especially with the large power-control dynamic-range required and increasing numbers of carriers. In RAN-shared BStns (see Section 3.4.4), typically, a maximum of 30 dB (dynamic) + 12 dB (static) gain control [13] [48] could be per carrier to achieve independent yet collaborative, interference and QoS management for each operator sharing the same BStn. However, the mechanisms and depth of power control in GSM/EDGE, UMTS and LTE differ significantly. Consequently, this $P_{max,rms}-$ [0 dB to 42 dB], formerly shared between the DAC and the VGA, can now, theoretically be achieved only in the digital/Baseband domain prior to the DAC. This causes significant problems for low power signals (at lowest gain settings), both, due to low SNR given the fixed noise floor (typically -164 dBm/Hz at the DAC port) and also due to the IM3/CTB products from higher powered carriers (at higher gain settings) which fall into the lower power channels failing the EVM at the antenna connector (A.R.P. where the dynamic range, DR, of the signal is reduced compared to the DAC port requiring a higher DR from all the blocks in the chain).

In legacy/older systems, this is achieved by varying the R.M.S. power of a Variable Gain Amplifier (VGA) by changing digital-control bits or adjusting the analog-control-voltage which accordingly modifies the gain setting of the block (see Figure 5.7). Contemporary systems effect power-control in the digital or Baseband-domain instead of the VGA, requiring a high-dynamic range on the Digital-to-Analog Converter (DAC).

Per-carrier power control is best placed in the analog domain RF-VGA for single carrier systems as this allows the DAC to have a simpler DR. This also simplifies the DAC solution, particularly where Digital Pre-Distortion (DPD) is employed, which requires a larger bandwidth (BW). For multi-carrier systems having shared or common power control settings, it remains simpler to implement the gain in the VGA. Shared power control implies that all the

[13] This is different from the Code domain power control in UMTS-WCDMA [50]

Table 5.1: Integrated-Phase-noise and Jitter Calculation

Frequency (Hz)	**'b' dBc/Hz**	**SSB→DSB**	**Slope 'a'**	**k (linear)**	**RMS Phase Jitter (rad.)**	**Frequency Jitter (Hz)**
1000	-94.00	-91.00				
2000	-94.00	-91.00	0.0000	7.94328E-10	7.9433E-07	1.853432548
5000	-94.00	-91.00	0.0000	7.94328E-10	2.3830E-06	30.97880115
10000	-94.00	-91.00	0.0000	7.94328E-10	3.9716E-06	231.6790685
200000	-116.57	-113.57	-1.7349	0.006910195	9.6132E-06	27158.67511
250000	-120.00	-117.00	-3.5381	25034049.08	1.4973E-07	7391.619438
400000	-124.00	-121.00	-1.9596	0.075504817	1.8870E-07	18898.14829
600000	-142.01	-139.01	-10.2276	1.56899E+45	3.3616E-08	6658.356087
1200000	-145.01	-142.01	-0.9966	7.20096E-09	5.2300E-09	4075.536224
1800000	-153.84	-150.84	-5.0138	1.89909E+16	1.5124E-09	3014.406418
3000000	-156.02	-153.02	-0.9835	1.17019E-09	7.6121E-10	4294.69214
6000000	-157.04	-154.04	-0.3382	7.73617E-14	1.3161E-09	26959.37869
10000000	-157.04	-154.04	0.0000	3.94576E-16	1.1837E-09	67472.48059
Total		**$\mathbf{EVM_{\phi_n}}$ = 0.3891%**			**$\phi_{n,rms}$ = 0.237 deg.**	
	$\mathbf{J_n}$ (rad.) = 0.00414055		**$\mathbf{J_n}$ (psec.) = 0.30793881**		**$\mathbf{J_n}$ (Hz) = 407.661384338799**	

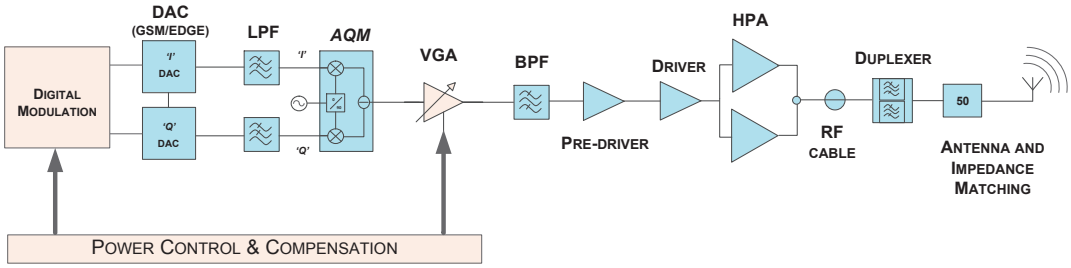

Figure 5.7: Block diagram of Power (Gain) control in legacy Base Stations

carriers will have their carrier powers lowered or raised at the same time. We can imagine of a use-case scenario where a user's throughput is spread over several carriers (Frequency Domain Multiplexing) as is done in MC-GSM/EDGE in order to improve or guarantee a certain minimum throughput. This reflects the multi-carrier scenario with shared power control because power control is executed on a per user SIR basis i.e. per user QoS setting. The case is the same for both GSM and WCDMA, independently. As of 2012, all the 3GPP standards assumed that the power distribution between carriers of the same access technology, was egalitarian.

Contrary to the assumption, which is also under investigation for implementation in Release 12 [94, 95], it is not necessary that all carriers will share gain settings because a single carrier with a independent/unshared power control could also used by the Network Operator to guarantee a maximum coverage setting while others could be used to guarantee throughput in a given area. These are contradictory requirements. Given the variety of sharing possibilities, it is likely that a BStn can have multiple transmission objectives for the different carriers. An example scenario of a multi-carrier BStn with multiple sectors is briefly described in [96]. Given this, collectively changing the powers of all carriers in the analog domain will yield undesirable effects [14], degrading the EVM of the lower powered carriers in the ensemble. This is particularly true for the interference scenarios that currently form the background for the 3GPP specifications.

Consequently the gain will need to be implemented fully in the DAC (see Figure 5.8), with the VGA retained for its remaining task of gain/loss compensation for any drift in output power from the required value although typically only a few dB. As is evident from the Figure 5.9 increasing number of carriers for a given output power, the power-control dynamic range and the increased PAPR (Section 4.3.9) in multi-mode operation, will imply that either the DAC headroom (Full Scale or FS signal swing) should be increased or the noise floor be reduced further (see Appendix C) in order not to violate the stringent EVM requirements[15] (see Table 4.1) for each carrier, particularly of the GSM/EDGE family. However, reducing the noise floor in Tx presents a fundamental challenge even with existing calibration methods. Increasing the Full-Scale swing of the DAC could be explored, but with discouraging

[14] It should be pointed out that whilst our solution does not alleviate this issue, it helps when the number of carriers is increased and the DAC cannot sustain all of the gain control range.

[15] The EVM requirement remains fixed irrespective of carrier power levels.

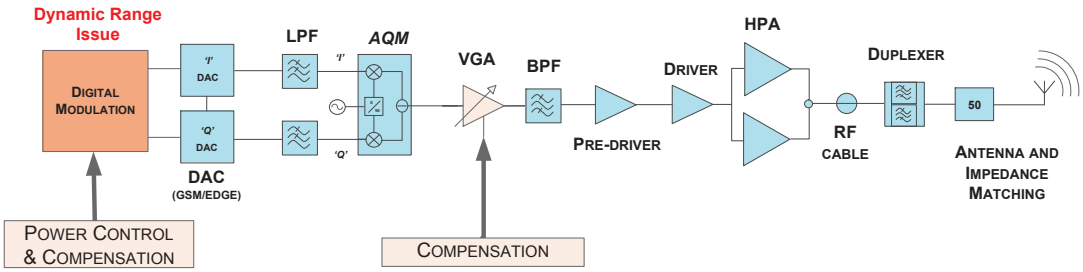

Figure 5.8: The (DAC) bottleneck in the Multi-mode Gain-control scheme

consequences on the performance of the succeeding blocks, alongside an increasing power consumption. This is primarily because the noise floor set by the DAC and the AQM is high enough for the SNR to not be significantly degraded by the rest of the blocks in the chain, made evident by the cascaded-noise-factor analysis in Section 5.1. With each carrier requiring at most 30dB dynamic range reducing carrier power reduces SNR by the same amount, because the noise floor is typically constant for all levels of signal power varying only with the gain.

Due to the increasing $\text{EVM}_{\text{Random Noise}}$ for low-power carriers, the noise-floor becomes increasingly critical when dividing the total power among an increasing number of carriers. This also diminishes the ACLR margin for each carrier, that the DAC presents at the input of the RF chain. Modern high-performance DACs boast of approx. 85dB ACLR for single carrier transmission (e.g. AD9779A). Taking away 30 dB signal power will leave a very small margin for other transmitter impairments. With this we briefly highlight one of the major bottlenecks in a multi-mode BStn Tx.

5.4 Multi-mode AQM with Mode-specific Gain Control

This issue highlighted above is reflective of the changing trend in DACs from low DR / high BW [97] to high DR / (low, but) increasing BW [98]. A plausible solution for the fundamental difficulties of implementing a Tx for such a large dynamic range, would be to separate the gain-control for GSM/EDGE and WCDMA/LTE carriers. This could, for example, be achieved by having a separate DAC and gain-control path for each standard followed by a shared Tx chain (see Figure 5.10), thereby retaining most of the advantages of a shared RAN. Here the power-control dynamic range is achieved together by the Baseband and the exclusive gain-stage for each access technology. An added advantage is that the signals being in analog domain, need not be re-sampled or equalised to a common clock rate ($\frac{t_{GSM}}{t_{WCDMA}} = \frac{270Kbps}{3.84Mcps}$), thereby not needing the highly selective filtering requirements for fractional re-sampling (Section 4.3.9). While the issue of distortion due to CMD (cross-modulation) was not studied in depth, its impact is manifestly aggravated particularly when low power GSM/EDGE carriers are combined with high powered WCDMA or LTE carriers. The marked EVM degradation of a low powered EDGE carrier (P=40dB) in a four-carrier

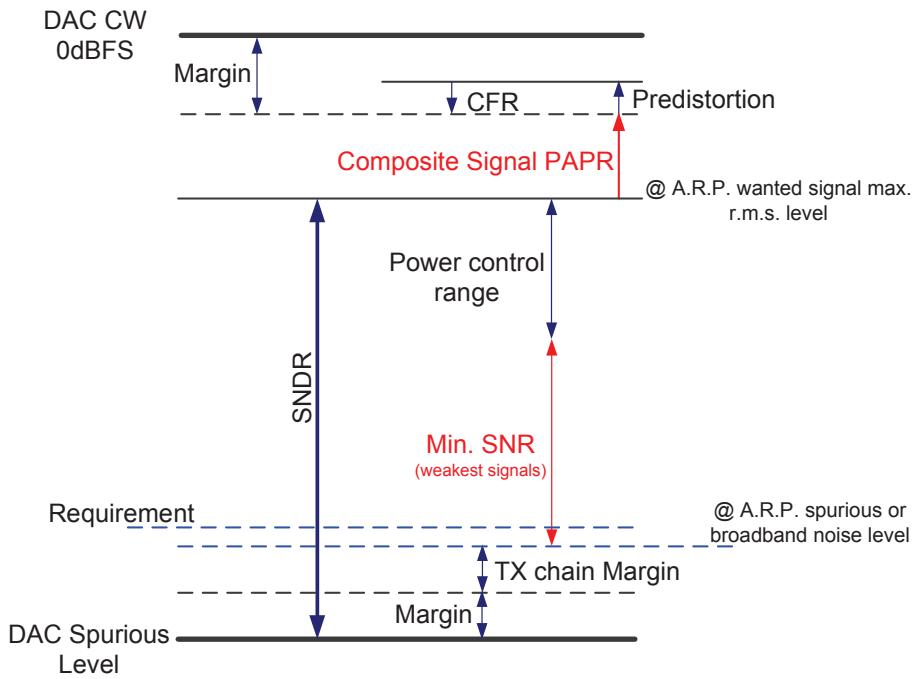

Figure 5.9: The issue of dynamic range requirements for the DAC from multi-mode signal transmission

aggregate, is illustrated in Figure 4.11.

In the following chapter we present the conceptual design of one such AQM along with arguments and deliberations, starting from the fundamentals.

5.5 Summary

Here we have shown the distribution of performance specifications derived in the Chapter 4, into block level requirements. The cascade analysis using EVM and ACLR allows designers to connect system level distortion to block level performance specifications. The primary contributors to EVM, non-linearity (i.e.,OIP3), noise (i.e., NF), phase noise and IQ imbalances are considered for the distribution. Table 5.2 summarises the budgeting for gain, linearity and noise performance. More detailed modeling, especially of the PA module, is suggested for further development of this work. Simplified assumptions are made here, such as assuming an equivalent two-tone OIP3 approximation for non-linearity of the HPA, taking into account the impact of the DPD in the soft-compression zone of the Doherty PA. Further modeling of small-signal RF non-linearity and the HPA characteristics is suggested for future work. A method of incorporation cost functions and weighting factors when distributing performance specifications towards a goal is also suggested. We also briefly highlighted miscellaneous EVM contributions in Section 4.2.3.5 for which no analysis was presented. While most of those errors excluding those originating from DSP manipulations and Baseband impairments, are

Table 5.2: Transmitter Performance Budgeting for six EDGE carriers

Parameters	Transmitter blocks			
	IQ-DAC	**LPF**	**AQM (w/ LO)**	**VGA**
Available Power Gain Gp,av [dB]	0.0	-1.0	**1.50**	15.6
CUMULATIVE GAIN [dB]	0.0	-1.0	0.5	16.1
NF [dB]	13.0	1.0	**17.50**	10.2
OIP3 [dBm]	29.0	100.0	**27.5**	40.0
OIP2 [dBm]	80.0	100.0	60.0	80.0
Output CP1 [dBm]	100.0	100.0	**13.9**	30.0
Output Resistance [Ohm]	50	50	**50**	50
Neqin = (Noise Temperature * k)	7.59E-20	1.04E-21	2.21E-19	3.77E-20
Neqin [dBm/Hz]	-161.20	-179.84	-156.55	-164.23
Noise_out (cumulative) [W/Hz]	7.99E-20	6.43E-20	4.03E-19	1.61E-17
Noise out (cumulative) [dBm/Hz]	-160.98	-161.92	-153.94	-137.92
k*T [W/Hz]	4.00E-21			
	Block Available Output Power			
TOTAL Wanted Signal Power [dBm]	**-9.0**	-10.0	-8.5	7.1
Per-Carrier Wanted Signal Power [dBm]	-13.8	-14.8	-13.3	2.3
Carrier Power [W]	4.1667E-05	3.3097E-05	4.6751E-05	1.7117E-03
Carrier Peak Signal Power [dBm]	-2.5	-3.5	-2.0	13.6
Cumulative Gain [dB]	0.0	-1.0	0.5	16.1
Noise [dBm] in system noise bandwidth	-82.8	-83.8	-75.8	-59.8
Cumulative SNR [dB] in system bandwidth	69.0	69.0	62.5	62.1
Cumulative EVM due to noise [%]				
Corresponding EVM contribution per block	**0.0353%**	**0.0040%**	**0.0659%**	**0.0229%**
	Noise Figure			
cumulative Input referred NF [dB]	13.0	13.06	19.53	19.92
	2rd Order Intercept Point (in-band)			
Cumulative IP2 [dBm] in-band	20.8	20.8	19.8	22.2
Cumulative OIP2 [dBm] in-band	80.0	79.0	60.0	74.3
Cumulative ACLR IMD2 [dBc]	-93.8	-93.8	-73.3	-71.9
Cumulative ACLR [dBc] Peak	-82.5	-82.5	-62.0	-60.6
Cumulative ACLR2 [dBc] due to Noise	-69.0	-69.0	-62.5	-62.1
Cumulative PIMD2 [dBm] at output	-107.6	-108.6	-86.6	-69.6
Cumulative IMD2 [dBc]	-93.8	-93.8	-73.3	-71.9
Cumulative EVM due to IP2 [%]				
	3rd Order Intercept Point (in-band) without DpD			
Cumulative IP3 [dBm] in-band	20.2	20.8	19.8	22.2
Cumulative OIP3 [dBm] in-band	29.0	28.0	25.4	37.4
Cumulative ACLR IMD3 [dBc]	-84.3	-84.3	-76.0	-68.9
Cumulative ACLR [dBc] Peak	-63.0	-63.0	-54.8	-47.7
Cumulative ACLR [dBc] due to Noise	-69.0	-69.0	-62.5	-62.1
Cumulative PIMD3 [dBm] at output	-99.4	-100.4	-90.7	-67.9
Cumulative IMD3 [dBc]	-85.6	-85.6	-77.4	-70.2
Cumulative EVM due to IP3 [%]				
Corresponding EVM contribution per block	**0.0017%**	**0.0017%**	**0.0043%**	**0.0098%**
	3rd Order Intercept Point (in-band) with DpD			
Cumulative PIM3 [dBm] with DpD	-99.4	-100.4	-90.7	-67.9
Cumulative OIP3 [dBm]	29.0	28.0	25.4	37.4
Cumulative ACLR IMD3 [dBc]	-84.3	-84.3	-76.0	-68.9
Cumulative ACLR [dBc] Peak	-63.0	-63.0	-49.9	-45.9
Cumulative EVM due to IP3 [%]				
	1dB Compression Point (in-band)			
cumulative CP1 [dBm] @ block output	100.0	96.5	13.4	21.9
Cumulative CP1 [dBm] OIP3-13	16.0	15.0	12.9	21.0
DPD IM3 improvement	**25 dB**			
PAPR assumed	**11.3 dB**			
Signal Bandwidth	**65 MHz**			

Transmitter Performance Budgeting (...continued)

Transmitter blocks						
BPF	**pre-Driver**	**Driver**	**HPA Doherty**	**Cable loss**	**Duplex filter**	**A.R.P.**
-1.5	12.0	17.0	16.0	-1.0	-0.2	0.0
11.3	23.3	40.3	56.3	55.3	55.1	55.1
1.5	5.0	8.0	4.0	1.0	0.2	0.0
100.0	45.0	55.0	67.5	100.0	100.0	100.0
100.0	90.0	90.0	100.0	100.0	100.0	100.0
100.0	30.0	42.0	55.0	100.0	100.0	100.0
50	50	50	50	50	50	50
1.65E-21	8.66E-21	2.13E-20	6.05E-21	1.04E-21	1.89E-22	9.23E-24
-177.82	-170.63	-166.72	-172.18	-179.84	-187.24	-200.35
1.14E-17	1.81E-16	9.09E-15	3.62E-13	2.87E-13	2.74E-13	2.74E-13
-139.42	-127.42	-110.42	-94.42	-95.42	-95.62	**-95.62**
Block Available Output Power						
5.6	17.6	34.6	50.6	49.6	49.4	**49.4**
0.8	12.8	29.8	45.8	44.8	44.6	44.6
1.2118E-03	1.9205E-02	1.0	38.3	30.4	29.1	29.1
12.1	24.1	41.1	57.1	56.1	55.9	55.9
14.6	26.6	43.6	59.6	58.6	58.4	58.4
-61.3	-49.3	-32.3	-16.3	-17.3	-17.5	-17.5
62.1	62.1	62.1	62.1	62.1	62.1	**62.1**
						0.0783%
0.0008%	**0.0022%**	**0.0008%**	**0.0001%**	**0.0000%**	**0.0000%**	**0.0000%**
Noise Figure						
19.92	19.92	19.92	19.92	19.92	19.92	**19.92**
2rd Order Intercept Point (in-band)						
37.9	36.4	49.0	67.3	95.9	97.1	100.0
72.7	83.6	89.6	99.0	95.8	94.3	93.3
-71.9	-70.8	-59.8	-53.1	-51.0	-49.7	-48.6
-60.6	-59.5	-48.5	-41.8	-39.7	-38.4	-37.3
-62.1	-62.1	-62.1	-62.1	-62.1	-62.1	-62.1
-71.1	-57.9	-30.0	-7.3	-6.2	-5.0	-4.0
-71.9	-70.8	-59.8	-53.1	-51.0	-49.7	-48.6
						0.1011%
3rd Order Intercept Point (in-band) without DpD						
37.9	36.4	49.0	67.3	95.9	97.1	100.0
35.9	43.2	53.9	65.5	64.5	64.3	**64.3**
-68.9	-59.5	-46.7	-38.0	-38.0	-38.0	**-38.0**
-47.7	-38.2	-25.5	-16.8	-16.8	-16.8	-16.8
-62.1	-62.1	-62.1	-62.1	-62.1	-62.1	-62.1
-69.4	-47.9	-18.2	6.5	5.5	5.3	5.3
-70.2	-60.8	-48.0	-39.4	-39.4	-39.3	-39.3
						1.25%
0.0098%	**0.0291%**	**0.1257%**	**0.3420%**	**0.3421%**	**0.3421%**	**0.3422%**
3rd Order Intercept Point (in-band) with DpD						
-69.4	-47.9	-18.2	-18.5	-19.5	-19.6	-19.6
35.9	43.2	53.9	78.0	77.0	76.8	**76.7**
-68.9	-59.5	-46.7	-63.0	-63.0	-63.0	**-62.9**
-45.9	-41.3	-31.6	-48.6	-48.6	-48.6	-48.5
						0.0715%
1dB Compression Point (in-band)						
20.4	28.0	40.2	52.6	51.6	51.4	51.4
19.5	28.7	40.5	52.4	51.4	51.2	51.2

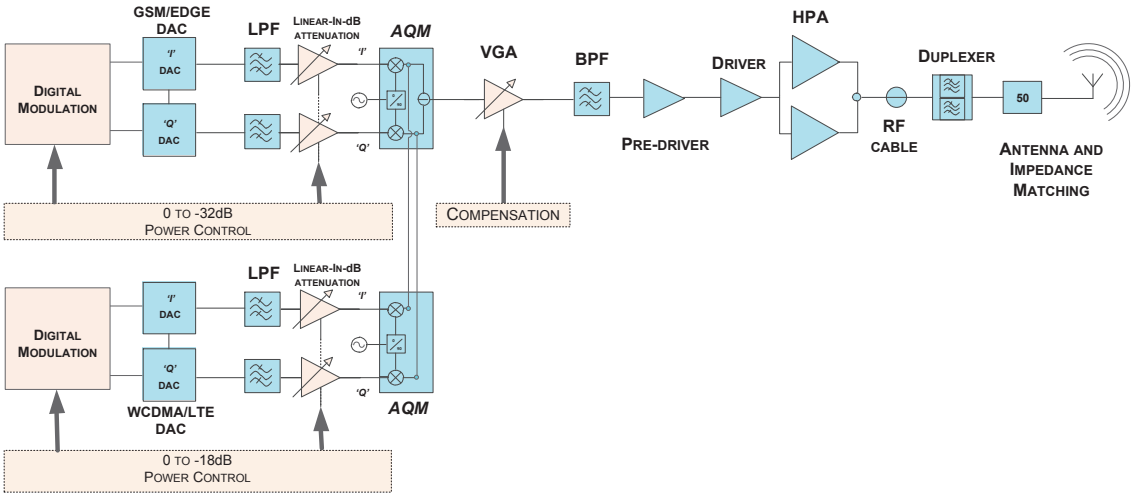

Figure 5.10: The proposed multi-mode transmitter gain control scheme with separate gain control paths

compensated or nullified through calibration, it would be prudent to leave sufficient margin for any uncompensated errors that remain (see Figure 5.5).

The high dynamic range requirements arising from the increased PAPR for multi-mode signals together with the carrier-specific power control poses a challenge for implementation. The same is true when increasing the number of carriers, possible with resource-sharing scenarios in BStn, as highlighted in Chapter 3. The limited output noise floor of the DAC illustrates one of the bottlenecks of dynamic range in the multi-mode Tx, which is also shared the blocks that succeed the DAC. A multi-mode Analog-Quadrature-Modulator with dual gain/mixing paths and a shared output stage is presented as a possible architectural solution. The AQM requires a significant EVM budget as it introduces random noise, LO phase noise, LO leakage, IQ imbalance and non-linearity related distortions in the analog chain. We therefore delve into the conceptual design of the multi-mode AQM in the next chapter, in order to relate circuit level issues to system level performance criteria, as previously highlighted in this work and also to understand the various design tradeoffs for future implementation.

Chapter 6

The Design of a Multi-Mode Variable Gain AQM

The Analog Quadrature Modulator (AQM) serves the purpose of translating the baseband or low-frequency band-pass (IF) signal to radio-frequency (RF). The IF signal could be a multi-mode carrier configuration comprising several carriers of different air-interface standards, sometimes referred to as a multi-mode *carrier aggregation scenario*. For the sake of simplicity if we assume a sinusoidal input signal, the function of the AQM as a block can be expressed as

$$\begin{aligned}
\text{BB signal} &= I(t) + j \cdot Q(t) \\
\text{LO signal} &= \cos(\omega_{\text{LO}} t) + j \cdot \sin(\omega_{\text{LO}} t) \\
\text{RF signal} &= \Re[I(t) + j \cdot Q(t)] \cdot [\cos(\omega_{\text{LO}} t) + j \cdot \sin(\omega_{\text{LO}} t)] \\
&= I(t) \cdot \cos(\omega_{\text{LO}} t) - Q(t) \cdot \sin(\omega_{\text{LO}} t)
\end{aligned} \tag{6.1}$$

where $\Re(\cdot)$ denotes the real part of a complex expression. The above procedure rejects the image frequency, in this case, the Lower Side-Band, the design for which will be discussed in Sections 6.3 and 6.4. In this section, we attempt to present the design of an Analog-

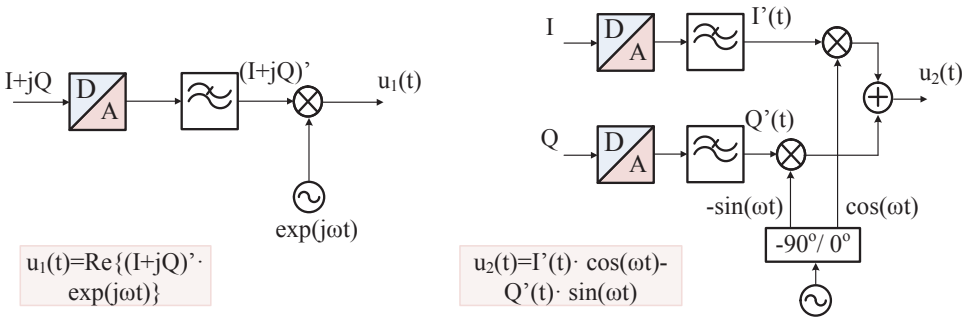

Figure 6.1: Frequency translation to the upper sideband by the Analog Quadrature Modulator

Quadrature-Modulator with gain/attenuation control and capable of supporting dual IQ inputs, based on established theories. The objective is to highlight some of the tradeoffs that exist in the design. Based on the system level EVM analysis in Chapter 5 and the performance requirements calculated in Table 5.2, the performance requirements for the dual-input AQM are summarised in the Tables 6.1 and 6.2 below.

Table 6.1: Summary of AQM performance requirements

Parameter	**Specification**	Units
Supply Voltage	3.3	Volts
Total supply current (max.)	< 300m	Amps
Operating temperature	-45 to $+80$	deg. Cel.
LO frequency range	700 to 3700	MHz
RF frequency range	700 to 3700	MHz
Modulator IF frequency band (1dB)	DC to 350	MHz
LO input signal level	0	dBm
LO input match return loss	< -10	dBm
Modulator input impedance (Diff)	50 (per pin)	Ohms
Peak I,Q input voltage/pin	500m pk, 1000m pk-pk	Volts
Typical I,Q DC common mode	2.8	Volts
Output noise floor without LO	-158	dBm/Hz
Output noise floor with LO	-155	dBm/Hz
Nominal output power	-5 to -10	dBm
Modulator gain I or Q to output (SE)	-25.5 to +1.5	dB
Output impedance (SE)	50	Ohms
Linearity : output IP3	> 25	dBm
Linearity : output CP1	> 10	dBm
Linearity ACPR (6xEDGE)	≤ -72	dBc
Power out for spec. ACPR	-12	dBm
Linearity EVM (rms)	$\leq 1.5\%$	-
Unadjusted carrier leakage	< -40	dBc
Unadjusted image feed-through	< -40	dBc
LO to RF isolation (nominal)	> 40	dB

Table 6.2: AQM electrical performance requirements

DAC output values (per channel 'I' or 'Q')	**Value**	**Units**	**Comments**
DC common-mode current	10.00	mA	fixed by design
AC Peak-Peak current	20.00	mA pk-pk	(diff)
Peak AC current	10.00	mA pk	(diff)
DAC supply voltage	3.30	V	DC supply
Input common mode DC voltage	2.80	Vdc	3.3 Vsupply - 10 mA_dc * 50 Ohms.
Full scale peak-peak voltage	2.00	Vpk-pk	per I or Q channel (diff) across 100ohms_diff per I or Q channel
Full scale peak voltage	1.00	Vpk	per I of Q channel (diff) across 100ohms_diff per I or Q channel
Full scale peak voltage per pin	0.50	Vpk	per Pin (se)
Output impedance (diff) per channel	100.00	R_diff (Ohms)	(diff)
Output impedance (single-ended) per pin	50.00	R_se (Ohms)	(se)
Max. peak output power from the DAC	10.00	dBm	(differential) across 50Ohms/pin/channel or 100ohms_diff/channel
PAPR	**10.00**	dB	depends on the number of carriers.As measured by Optichron
RMS output power for all carriers combined	0.00	dBm	
DAC output transformer turns ratio	1.00	Npri/Nsec	Transformers are typically used at the output of the DAC to increase voltage swing
Max Power control range (attenuation)	25.00	dB	power levels are reduced as the power cannot be increased with respect to the Max average value
Min Power level (max power control level)	-3.01	dBm	
Peak Power Developed at AQM input pin	0.97	dBm	
RMS output power for all carriers combined (loaded with AQM Z_{in})	**-9.03**	dBm	Power delivered into the load

Continued on the next page ...

Table 6.2: (continued)

DAC output values (per channel 'I' or 'Q')	**Value**	**Units**	**Comments**
Corresponding RMS signal voltage into Modulator per pin	79.06	mVrms	differential voltage swing per (I or Q) channel of the DAC
Modulator output values			
I & Q channel power gain	**1.49**	dB	IRR assumed high. Measured from matched SE O/P to matched DIFF I/P I/Q, 50Ohms system
Peak Output power	2.47	dBm	should be less than OCP1_vga - Gp,av,max_vga in order to avoid compression
Peak Output voltage	0.42	Vpk	across 50 Ohms (se)
Peak-Peak Output voltage	0.84	Vpk-pk	across 50 Ohms (se)
RMS Output Power	-7.53	dBm	depending on PAPR assumed (filter loss not subtracted)
RMS Output voltage	0.30	Vrms	
RMS Output current	5.94	mA rms	
Peak Output current	8.40	mA pk	
Peak-Peak Output current	16.81	mA pk-pk	
Linearity requirements			
Minimum OIP3 requirement for modulator	**27.50**	dBm	across matched output (as calculated in link budget analysis) = IIP3 if Power Gain = 0 dB
Difference between OIP3 and OCP-1dB	13.60	dB	assuming AQM is operating in the 2dB/dB region with sufficient back-off
OCP-1dB requirement for modulator	**13.90**	dBm	across 50 Ohms output
OCP-1dB (in dBm) Corresponds to a Peak output referred voltage of	1.57	Vpk	50 ohms. Should be much higher than peak voltage of the signal
Corresponding Peak output signal current swing	31.34	mA	across 50 Ohms output load
OCP-1dB (in dBm) Corresponds to a Peak-Peak output referred voltage of	3.13	Vpk-pk	50 ohms. Should be much higher than peak-peak voltage of the signal

Continued on the next page . . .

Table 6.2: (continued)

DAC output values (per channel 'I' or 'Q')	Value	Units	Comments
If transformer is used at the output			
Turns ratio (N_{pri}/N_{sec})	1.00		
Noise floor requirement			
Relative to Peak input voltage	5.41	dBV	
Output noise floor required from TX system calculations	**-158.05**	dBm/Hz	excluding LO noise
Corresponds to an output noise voltage of	**2.80**	nV/sqrt(Hz)	in a 50 Ohm system
Corresponding SNR	72.74	dBc	
Output noise floor at maximum attenuation	**-166.00**	dBm/Hz	obtained from simulations
Corresponds to an output noise voltage of	**1.12**	nV/sqrt(Hz)	in a 50 Ohm system
Corresponding SNR with gain control	65.69	dBc	across 60 MHz signal BW, based on simulated noise floor of -163.7 dBm/Hz at minimum gain or maximum attenuation setting

In order to achieve the different performance specifications, the AQM (see block diagram in Figure 6.2,) is divided into three stages:

- Current-mirror based transconductance-amplifier with linear-in-dB gain/attenuation control
- I and Q path Mixers (including LO buffers and Poly-Phase-Filter)
- Output buffer with an on-chip RF Transformer

6.1 NXP-QUBiC4X Technology

The designs in this work are based on the NXP QUBiC4X [99] 0.25μm SiGe:C HBT BiCMOS technology. The process has an $f_{\mathrm{T}}/f_{\mathrm{max}}$ of 110/180GHz (or 60/140GHz) for the (High Voltage) HBT NPN transistors and 80GHz f_{max} for the nMOS transistors in the process. The high f_{T} of the HBT together with a 3.3V breakdown voltage makes it ideal for up to 30GHz systems and ultra low noise applications, requiring the intrinsically high dynamic range.

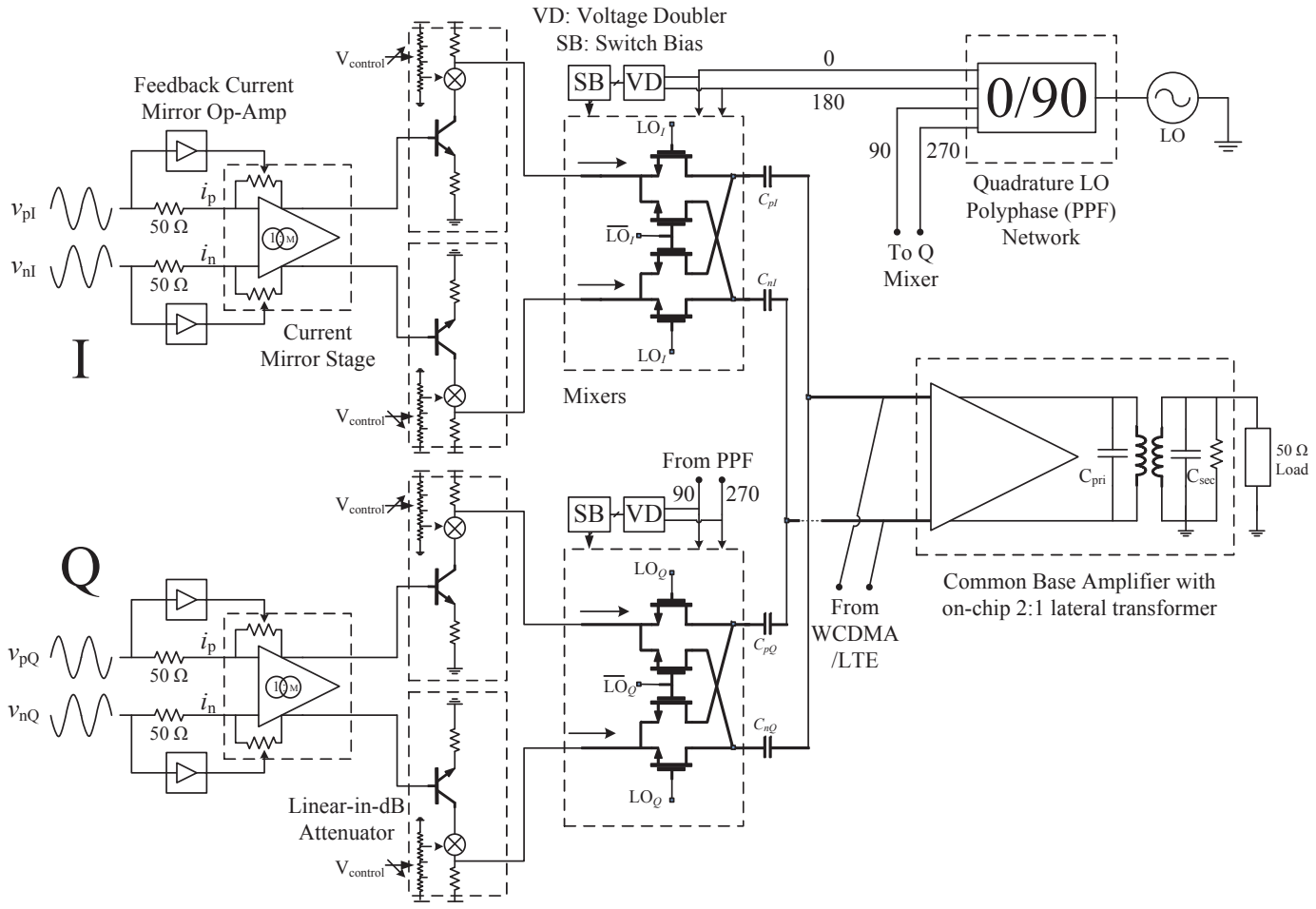

Figure 6.2: Block diagram of the Analog Quadrature Modulator showing the input matching resistor, current mirror stage, linear-in-dB attenuator, mixers, common-Base output amplifier and on-chip lateral transformer.

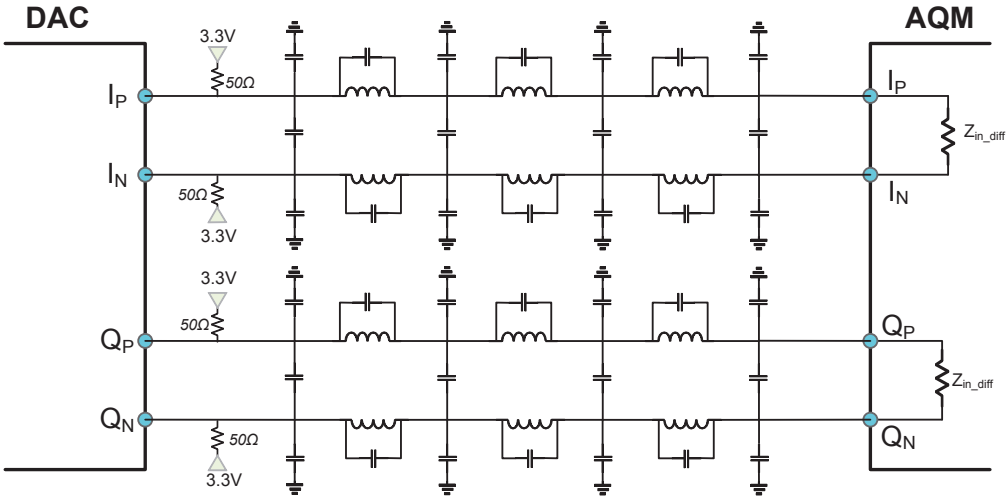

Figure 6.3: The interfacing between the DAC and the AQM

It features buried layers, deep-trench isolation and provides a comprehensive set of active and passive elements including, 0.25μm nMOS and pMOS devices, vertical NPN transistors (both high speed and high voltage versions), lateral PNP transistors, mono- and poly-silicon resistors, thin film resistors (optional), diodes, capacitors (including a high density MiM capacitor) and five layers of metal interconnect. For this design, a supply voltage of 3.3V is chosen which allows it to be easily integrated with majority of the DACs in the market.

6.2 AQM Input Stage

The input of the AQM is interfaced to the Digital-to-Analog-Converter (DAC) via a reconstruction or anti-imaging (low-pass) filter which comprises lumped L and C elements to filter out Nyquist images and the broadband noise of the DAC. The order of the filter (typically of 5th order) depends on the sampling frequency of the DAC. The interface (see Figure 6.3) lacks AC coupling to retain the DC component of the spectrum making it amenable to zero-IF signal transmission[1]. The signal swing and dynamic range at the output of the DAC are optimised for a specific common-mode output voltage, in this case 2.8V.

The changing of common-mode DC of the DAC to that of the input of the AQM is typically done using resistive dividers, as depicted in Figure 6.4, shown here ignoring the reconstruction filter. However, this level shifting using a passive network entails a loss in the AC signal and degrades the SNR by an equal amount. To counter this, a shunt bypass capacitor (shown in red) can be introduced, with area restrictions limiting the capacitor's size. The capacitor introduces a (high-pass) pole, increasing the risk of attenuating/loosing

[1] Zero-IF allows to halve the clock rate for transmission at best, which becomes useful when using DPD systems that often require 5× to 7× the signal bandwidth to correct the PA's non-linearities. Furthermore, for zero-IF, the Numeric Complex Oscillator (NCO) that facilitates baseband to pass-band frequency translation in the DAC is switched off, conserving power.

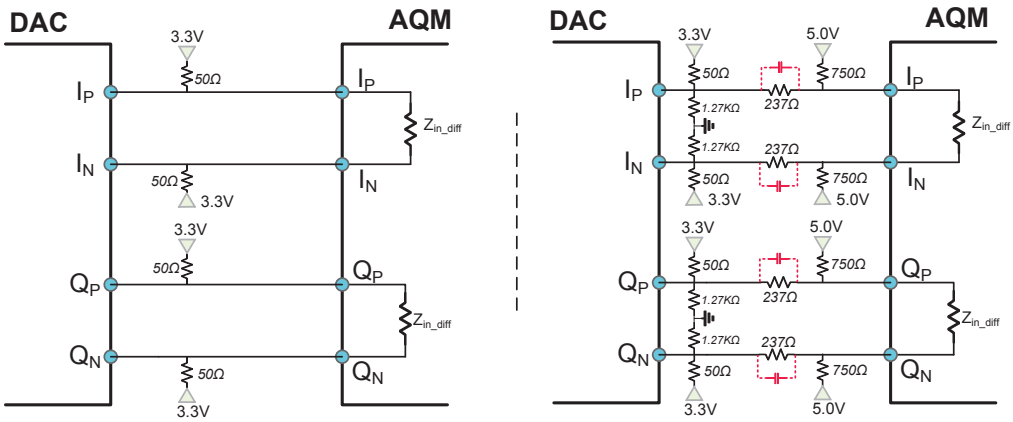

Figure 6.4: Level shifting the common-mode output voltage from 2.8V (left) at the DAC (aux. DAC not shown) to 3.3V(right) at the AQM input

signal close to DC, if not properly dimensioned.

While most commercial DACs are available with either a current-source or current-sink output stage, it is assumed to be an open-Drain (output impedance in MΩs) current sink [100] for this work.

In either case, any DC current that is drawn away from the DAC results in a shift of this common-mode 'sweet-spot' resulting in reduced signal swing and/or potentially higher distortion. The output voltage swing for the DAC is illustrated in Figure 6.6.

The input (Gain/Attenuation) stage cannot therefore not be a Common-Base or Common-Gate stage in spite of their better linearity than Common-Emitter or Common-Source stages [101], because the DAC cannot source or sink DC current into the Mixer (as explained above) and is also not AC coupled. Furthermore, due to the DC content in the signal, the operational bandwidth and the frequencies involved, a large discrete transformer coupling the DAC and the AQM at the input becomes necessary, which, practically, is unwieldy. Also, the performance of such transformers is typically quite poor at this frequency range. For this purpose, the input of the AQM features a 'cold' node or a low impedance node (Y_a, Y_b) at the input that is held at a fixed voltage which tracks the common-mode voltage (nodes X_a, X_b) at the output of the DAC. See Figure 6.7.

The concept works by negative feedback as shown in the Figure 6.8 below. The voltage $V_{j,\mathrm{cm}}$ gathers the average (common-mode) voltage of the input pins I_p, I_n (Q_p, Q_n) but also unfortunately has a low frequency drift due to the non-zero pole frequency of the low-pass filter, which allows the signal component at this frequency and even noise to filter through. Typical DACs are equipped with an Auxiliary DAC that tracks and internally enables compensating of the DC and IQ (gain, phase) offsets, making this compensated average voltage that is sensed, also the common-mode voltage of the pins. $V_{k,\mathrm{cm}}$ holds the average (common-mode) voltage of the input nodes that track the $V_{j,\mathrm{cm}}$. $V_{j,\mathrm{cm}}$ and $V_{k,\mathrm{cm}}$ form

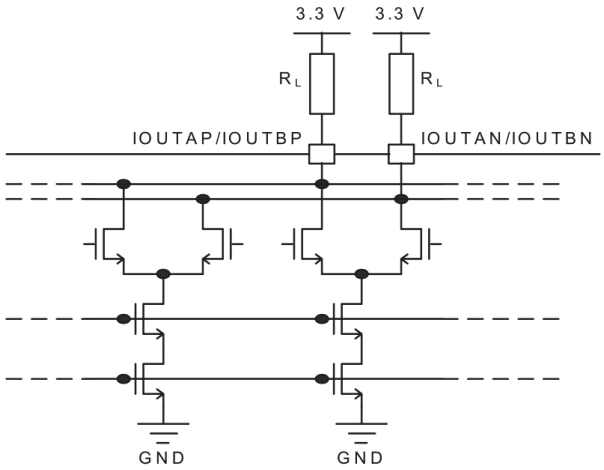

Figure 6.5: Output stage of the 16-bit DAC1627D1G25 Digital to Analog Converter (*Courtesy: NXP Semiconductors, 2011*)

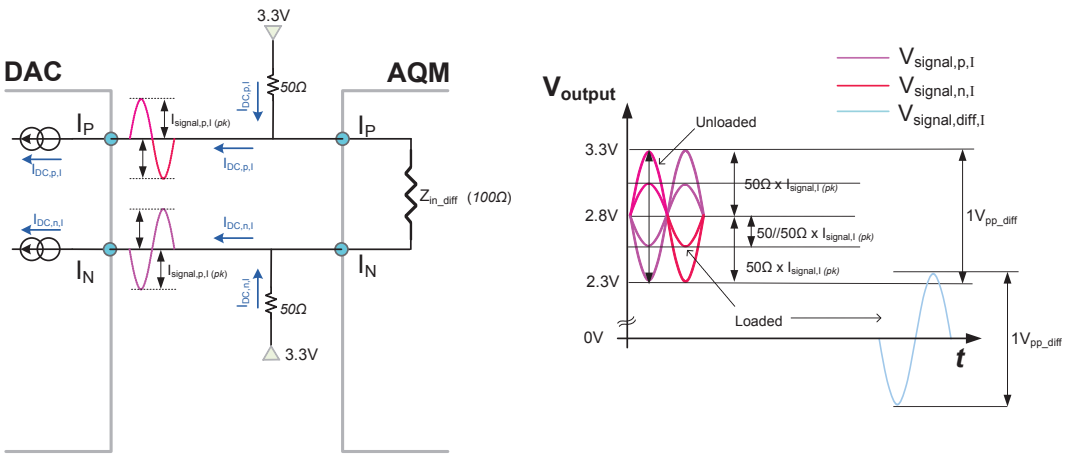

Figure 6.6: Unloaded and Loaded Full-Scale voltage swing at the output of the DAC

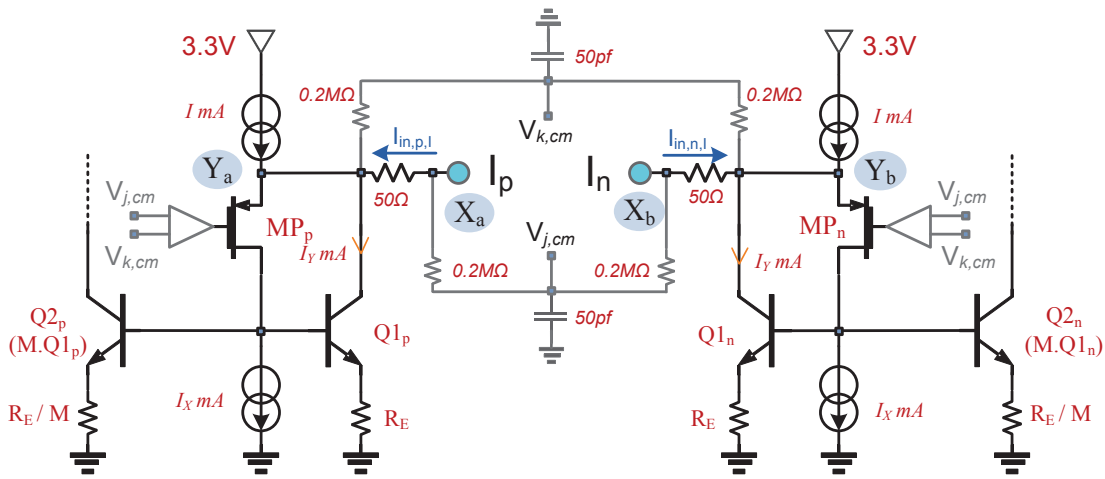

Figure 6.7: Input stage of the AQM for the In-phase path

inputs to an Op-Amp comparator which is connected in an inverting amplifier configuration. Thereby this negative feedback allows nodes Y_a and Y_b to track nodes X_a and X_b respectively.

Due to the low supply voltage of 3.3V, the comparator chosen for the design is a Current Mirror Op-Amp (see Figure 6.11) with wide-swing current mirrors. The majority of the gain occurs in the second stage, resulting in the Op-Amp having a relatively poor noise performance. The output referred noise however can be filtered by forcing a dominant pole at the output using large capacitor C_{L}. The dominant pole is at $1/RC$, with $C = C_{\mathrm{L}}+C_{\mathrm{db2}}+C_{\mathrm{gd2}}$ and $R = r_{\mathrm{ds1}}(g_{\mathrm{m2}} + g_{\mathrm{mb2}})r_{\mathrm{ds2}}$. The dominant pole also ensures stability as is evident from the margins in Figures 6.9 and 6.10.

The wide-swing configuration not only provides a larger output swing but also provides the correct output phase necessary for the correction. The pMOS is chosen to have a large size in order to minimize the mismatch [102] and also to minimize the flicker noise, as will be discussed in Section 6.2.4. Ignoring the degeneration resistances, the input common-mode voltage range that the comparator can track varies within the range $2 \cdot V_{\mathrm{D,sat}} + V_{\mathrm{T}} \leq V_{\mathrm{cm,in}} \leq V_{\mathrm{DD}} - V_{\mathrm{D,sat}}$ (which is approximately 0.9V to 3.1V) assuming the saturation ($V_{\mathrm{D,sat}}$) and threshold V_{T} voltages of input stage and current mirror load transistors are similar. Similarly, the output common-mode voltage which tracks the input common-mode is limited to $V_{\mathrm{DD}} - V_{\mathrm{D,sat}} \geq V_{\mathrm{cm,out}} \geq V_{\mathrm{D,sat}}$. It is also necessary to further reduce by $V_{\mathrm{ov}} + V_{\mathrm{T}}$ to account for the last 'feedback' pMOS transistor which can be viewed as a source-follower configuration. The voltage is also limited by the current source that feeds the pMOS. A drawback in the design (and also in most AQMs in production) is that the tracking will not be effective if I_{p} and I_{n} pins shift equally, but in opposite directions. For example, the average of $2.8 + 0.1 = 2.9$V and $2.8 - 0.1 = 2.7$V is still 2.8V. Typical DACs are built with internal mechanisms to ensure that this anti-phase drift does not occur. However, variations in the

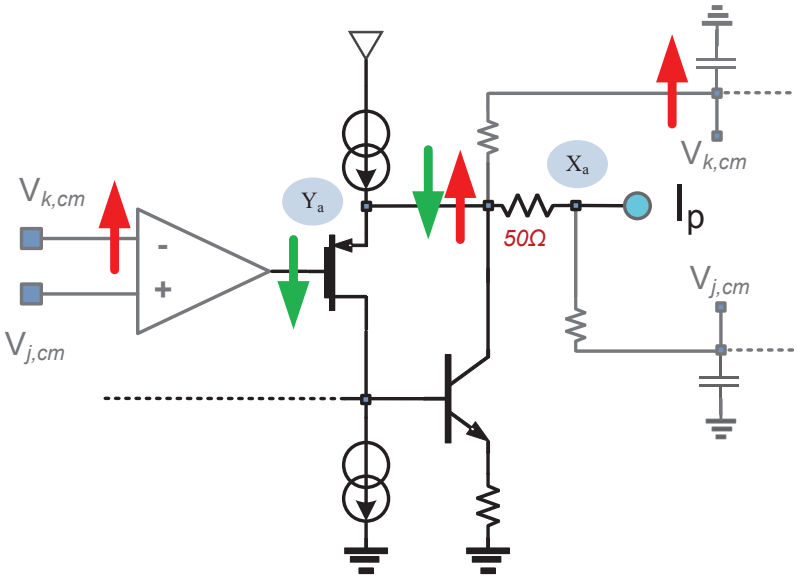

Figure 6.8: Feedback compensation of common-mode drift at the input of the AQM

impedance matching, filter performance etc. can still lead to such drifts that require explicit mechanisms to correct because these deviations manifest as IQ imbalance, as discussed in the pervious chapter.

6.2.1 Input Impedance

With the voltage at Y_a, (Y_b) held at a fixed DC value, the IF signal voltage is converted into a current across the 50Ω impedance matching series resistor R_{in}. The low frequency input impedance ($R_{\text{in}} = \frac{v_{\text{i}}}{i_{\text{i}}}\big|_{i_{\text{o}}=0}$) of the input stage at node Y_a, (Y_b) is calculated similar to the output resistance of a super-Source follower, as in (6.2). Most of the IF signal current follows the lowest impedance to ground. At node Y_a, (Y_b) this would be the $1/(g_{\text{m}} + g_{\text{mb}})$. The stage works by negative feedback [2] through $Q_{1\text{p}}$ ($Q_{1\text{n}}$) to further lower this input impedance by a factor β, as illustrated in the equation for R_{in}.

Applying a test voltage v_t at the input and KVL at the smallest input loop (see Figure 6.12, we obtain

$$v_t - \left(i_t - i_{\text{x}} - \frac{\beta_1 . i_{\text{x}}}{2}\right) r_{\text{o},1} - i_t \cdot R_{\text{e},1} = 0 \tag{6.2a}$$

where, $R_{\text{e},1} = R_{\text{E},1} + r_{\text{e},1}$. $1/(g_{\text{m}} + g_{\text{mb}})$ is a small fraction and can be ignored because $g_{\text{m}} + g_{\text{mb}}$ is chosen to be large in order to present a very low impedance to ground at the internal node. The choice of the pMOS g_{m}, later referred to as $g_{\text{m,MP}}$, has significant impact on the other

[2] Qualitatively, if the Gate voltage of MP_{p} (MP_{n}) is held constant, if the voltage at node Y_a rises, the V_{gs} increases causing an increase in drain current of MP_{p} (MP_{n}) which leads to a higher current flowing into $Q_{1\text{n}}$ ($Q_{1\text{p}}$). This effects a higher V_{be} which consequently causes more current to flow into the input node. This is in effect a lowering of resistance at the node.

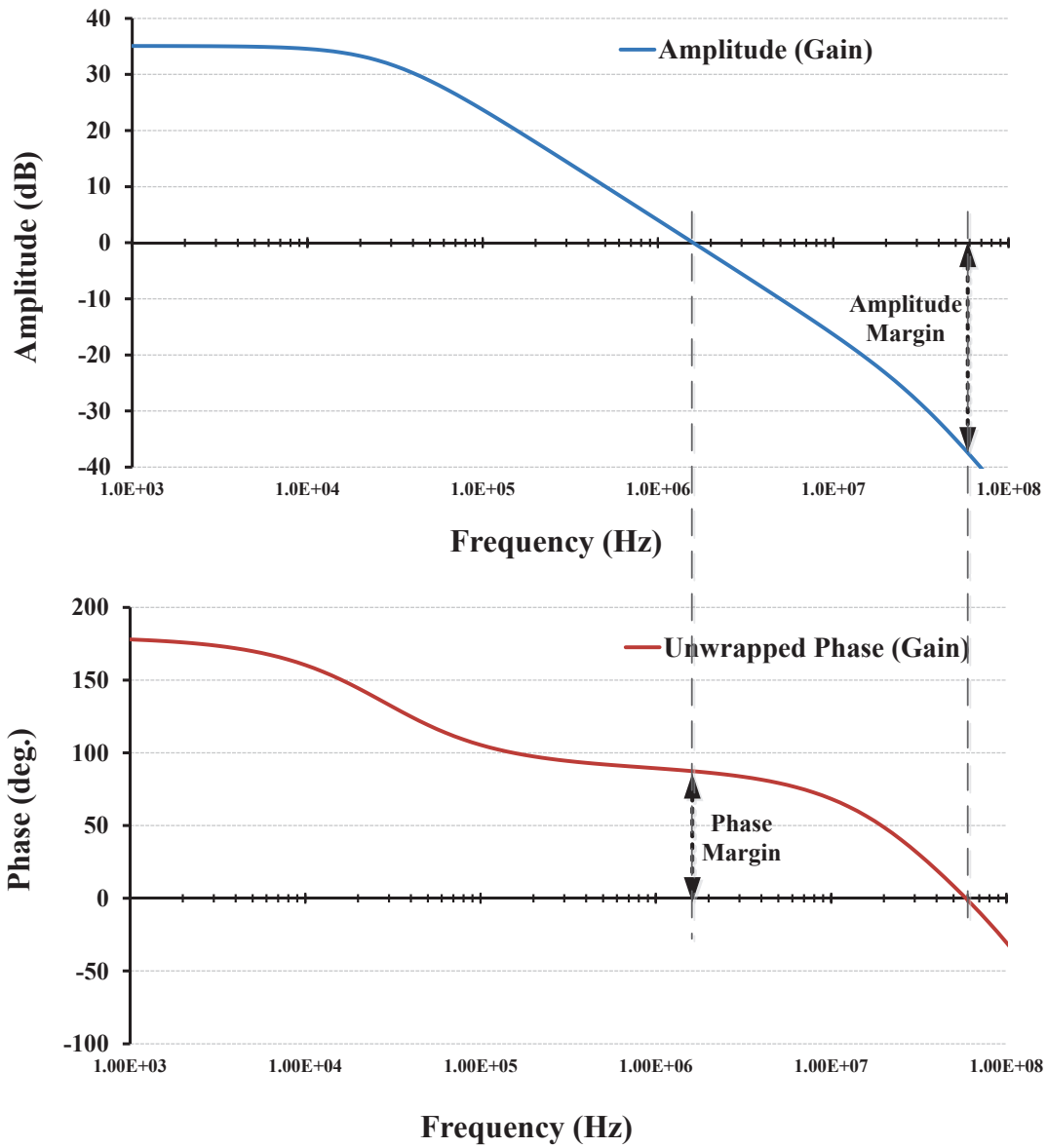

Figure 6.9: Phase and amplitude of the comparator gain, versus frequency

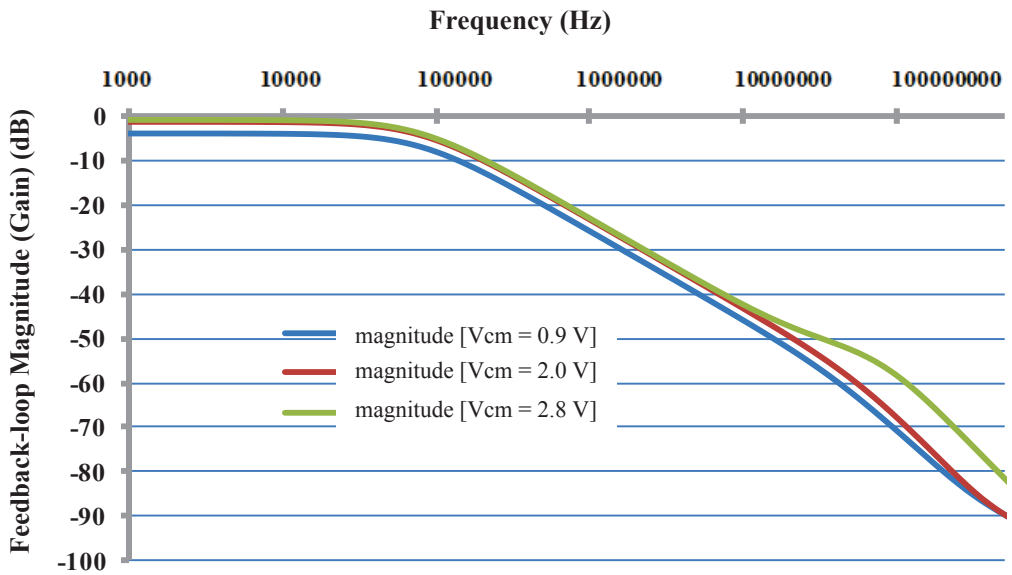

(a) Gain

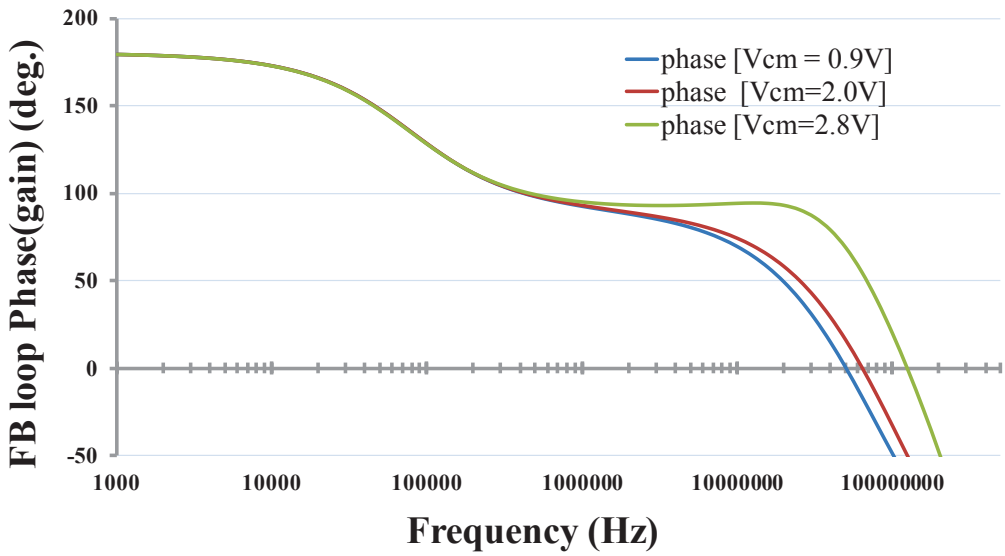

(b) Phase

Figure 6.10: Phase and amplitude of the feedback loop gain between the pMOS and the comparator, versus frequency

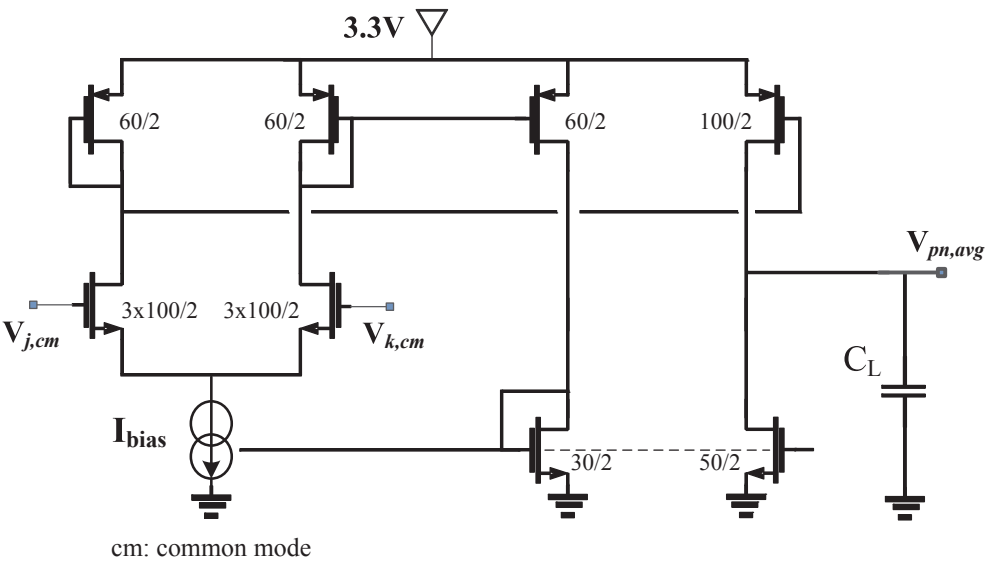

Figure 6.11: Schematic of the feedback Op-amp comparator

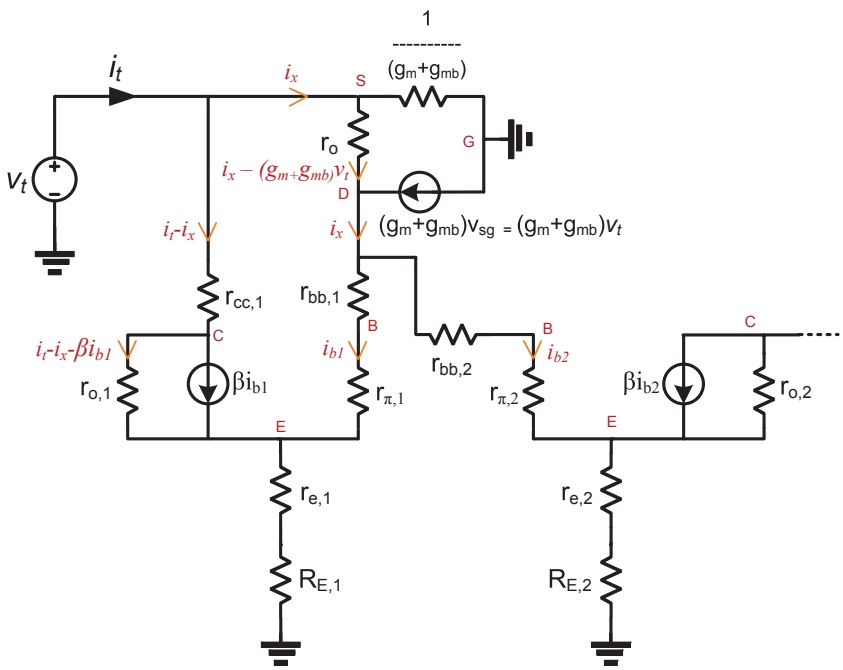

Figure 6.12: Circuit for the analysis of the input resistance looking into node Y_a,(Y_b)

performance parameters of the circuit, as will be discussed in the following sections.

$$v_t - \left(i_t - i_{\mathrm{x}}(1 + \frac{\beta_1}{2})\right) r_{\mathrm{o},1} - i_t \cdot R_{\mathrm{e},1} = 0 \tag{6.2b}$$

This is because the current i_{x} can be assumed to split equally into parts, one of which flows into the Base of the Q_2, the output half of the current mirror (CM). The output impedances of the current source and sink are large and therefore, ignored. The input resistance looking into the Base of Q_2, r_{in,Q_2} is easily calculated to be

$$r_{\mathrm{in},Q_2} = r_{\mathrm{bb},2} + (\beta_2 + 1)(R_{\mathrm{E},2} + r_{\mathrm{e},2}) \tag{6.2c}$$

For the sake of simplicity we can ignore r_{bb} (simulated value of 3.3Ω) and r_{cc} (simulated value of 4.6Ω). The current i_{x} is given by

$$\begin{aligned} i_{\mathrm{x}} &= (g_{\mathrm{m}} + g_{\mathrm{mb}}).v_{\mathrm{sg}} \\ v_{\mathrm{sg}} &= v_t \\ i_{\mathrm{x}} &= (g_{\mathrm{m}} + g_{\mathrm{mb}}).v_t \end{aligned} \tag{6.2d}$$

where, g_{m} is the incremental transconductance and g_{mb} the body transconductance of the pMOS transistor $\mathrm{MP_p}$ ($\mathrm{MP_n}$).

$$v_t - \left(i_t - ((g_{\mathrm{m}} + g_{\mathrm{mb}}).v_t)\,(1 + \frac{\beta_1}{2})\right) r_{\mathrm{o},1} - i_t \cdot R_{\mathrm{e},1} = 0 \tag{6.2e}$$

$$v_t \left(1 + (g_{\mathrm{m}} + g_{\mathrm{mb}})\,(1 + \frac{\beta_1}{2})\right) r_{\mathrm{o}} - i_t \cdot (r_{\mathrm{o},1} + R_{\mathrm{e},1}) = 0 \tag{6.2f}$$

$$R_{\mathrm{in}} = \frac{v_t}{i_t}\Big|_{i_{\mathrm{o}}=0} = \frac{r_{\mathrm{o},1} + R_{\mathrm{e},1}}{\left(1 + (g_{\mathrm{m}} + g_{\mathrm{mb}})\,(1 + \frac{\beta_1}{2})\right) r_{\mathrm{o},1}} \tag{6.2g}$$

Qualitatively, the input stage comprising the current mirror and the feedback pMOS can also be visualised as a Trans-Impedance Amplifier if the output half of the current mirror is ignored. The input impedance is then $R_f/(1 + A)$, where R_f is analogous to $1/(g_{\mathrm{m}} + g_{\mathrm{mb}})$ and A can be compared to the $\beta \cdot g_{\mathrm{m}} \cdot r_{\mathrm{o}}$ of the transistors. For the given current and the chosen dimensions, the β_{DC} was approximately 290 resulting in a much lower impedance than 50Ω. This can be further lowered by increasing the current into the pMOS, with the penalty of higher power consumption. A low impedance at this node is necessary because voltage fluctuations at this node could cause the (finite r_{o}) non-linearity of the source current-mirror at node Y_a (Y_b) to become an issue. The low impedance input node facilitates current mode operation. The in-phase and quadrature IF signal currents $i_{\mathrm{in,p,I}}$, $i_{\mathrm{in,n,I}}$, and $i_{\mathrm{in,p,Q}}$, $i_{\mathrm{in,n,Q}}$ flow into the $(1 : N)$ current mirror comprised of transistors $Q1_{\mathrm{p}}$:$Q2_{\mathrm{p}}$ and $Q1_{\mathrm{n}}$:$Q2_{\mathrm{n}}$. The $Q2$ transistors are N times larger than the $Q1$ and proportionately amplify the current. The $Q2$ actually comprises of an array of $N = 40$ HBTs in parallel. A transistor in this array also forms the tail or CE (Common Emitter) stage of a linear-in-dB gain/attenuation-control stage discussed in Section 6.2.5.

6.2.2 Gain

The voltage gain at the output of the current mirror is easily analysed to be

$$\frac{V_{\text{out}}}{V_{\text{in}}} = \frac{M \cdot I_{\text{in}} \cdot R_{\text{out}}}{I_{\text{in}} \cdot R_{\text{in}}} = \frac{M \cdot R_{\text{out}}}{R_{\text{in}}} \tag{6.3}$$

where, R_{out} is the impedance seen at the output of the cascode stage of the current-mirror and M is the current-mirror ratio,

$$M = \frac{I_{\text{C,Q2}}}{I_{\text{C,Q1}}} \approx \frac{A_{\text{e,Q1}}}{A_{\text{e,Q2}}} = \frac{r_{\text{bb,Q1}}}{r_{\text{bb,Q2}}} = \frac{R_{\text{E,1}}}{R_{\text{E,2}}} = \frac{r_{\text{e,Q1}}}{r_{\text{e,Q2}}} \tag{6.4}$$

It must be pointed out that this gain is at minimum (zero) attenuation setting and the output current will therefore be subjected to the attenuation settings that are described in the next section. The Mixers at the output of this stage will load the output stage impacting the gain and its effect is included in the R_{out} above. For the voltage gain to be large, R_{out} would have to be large, Mixers included.

We are however, manipulating current all the way to the output stage, and not voltage. Consequently, we will refer only to current gain hereafter. Although the current gain has been assumed to be the current-mirror ratio M, its accuracy is limited by the non-idealities of the current-mirror. For a current mirror with identical devices that have no mismatch, the current gain as a function of systemic errors [103], is expressed as

$$\frac{I_{\text{C,Q2}}}{I_{\text{C,Q1}}} = \frac{I_{\text{S}_2}}{I_{\text{S}_1}} \frac{1 + \overbrace{\frac{V_{\text{CE}_2} - V_{\text{CE}_1}}{V_{\text{AF}}}}^{\text{finite } r_{\text{O}} \text{ error}}}{1 + \underbrace{\frac{1 + \frac{I_{\text{S}_2}}{I_{\text{S}_1}}}{\beta_{\text{F}}}}_{\text{finite } \beta_{\text{F}} \text{ error}}} \tag{6.5}$$

Since the input to the stage is current and there are in fact N devices that make up $Q2$, this is multiplied with M/R_{in} to obtain the gain of the stage with respect to the input voltage.

$$\frac{I_{\text{C,Q2}}}{V_{\text{in}}} = \frac{M}{R_{\text{in}}} \frac{I_{\text{S}_2}}{I_{\text{S}_1}} \frac{1 + \frac{V_{\text{CE}_2} - V_{\text{CE}_1}}{V_{\text{AF}}}}{1 + \frac{1 + \frac{I_{\text{S}_2}}{I_{\text{S}_1}}}{\beta_{\text{F}}}} \tag{6.6}$$

Cascading of $Q2$ with the attenuator stage, will enhance the output resistance minimising the corresponding finite r_{O} error. The above expression is determined under the assumption that $V_{\text{BE}_1} = V_{\text{BE}_2}$. With mismatch[3], these voltages are no longer equal and the deviation in the output current as given by [103], becomes

$$\frac{\Delta I_{\text{C,Q2}}}{I_{\text{C,Q2}}} \approx \left(\frac{1}{1 + \frac{g_{\text{m}} R_{\text{E}}}{\alpha_{\text{F}}}} \right) \frac{\Delta I_{\text{S}}}{I_{\text{S}}} + \frac{\frac{g_{\text{m}} R_{\text{E}}}{\alpha_{\text{F}}}}{1 + \frac{g_{\text{m}} R_{\text{E}}}{\alpha_{\text{F}}}} \left(- \frac{\Delta R_{\text{E}}}{R_{\text{E}}} + \frac{\Delta \alpha_{\text{F}}}{\alpha_{\text{F}}} \right) \tag{6.7}$$

[3] This is the mismatch between the 40 degenerated transistors that make up the Q2. Consequently, $\Delta I_{\text{C,Q2}}$ is arrived by linear or quadratic addition or subtracting individual mismatches, depending on their correlation.

Here $\alpha_F = \beta_F/(\beta_F + 1)$ and β_F being the arithmetic mean[4] nominal forward current gain of the transistor for the given mean current I_C. I_S and R_E refer to the averaged saturation current and degeneration resistor respectively. Delta values indicate the mismatch. With good matching, the signals at the output add linearly while uncorrelated noise adds quadratically. This would provide some improvement in dynamic range. In order to minimise the mismatch, large devices are chosen to have the highest F_t for the chosen bias current. R_{E1} and R_{E2} are chosen to be as large as permissible with the given headroom, to minimise impact of the I_S mismatch. The degeneration resistors R_E also help to reduce temperature sensitivity. While the leakage current I_{CO} and β of the transistor both increase with temperature, V_{be} has a negative temperature coefficient. However this is not necessarily a canceling effect. The R_Es act as ballast resistors such that when the transistor draws more current at increasing temperatures, the voltage drop across the ballast resistor increases, increasing current, thus regulating the output current to a certain degree by providing negative feedback.

6.2.3 Non Linearity

The BJT has several known forms of non-linearity mechanisms (see Chapter 9 in [101]):

- nonlinear transconductance (g_m and its coefficients)
- nonlinear EB conductance (g_{be}) (i.e., $1/r_\pi$)
- nonlinear capacitances (C_{be}, C_{bc} and C_{cs})
- avalanche multiplication current (I_{CB})
- finite forward Early effect voltage (r_o,V_{AF})

The non-linearity associated with the limited output resistance $r_o = V_{AF}/I_{C,Q2}$ of the current mirror output stage is minimised by the use of the attenuator as a cascode stage. Fluctuations of $I_{C,Q2}$ due to variations in V_{CE} across $Q2$ are minimised by the increased output resistance of the cascode current-mirror. This also creates a low-impedance node at the Collector of $Q2$, owed to the input impedance of the upper-stage, reducing the C_{bc} non-linearity. Due to the fact that the $1/(g_m + g_{mb})$ of the pMOS is a finite value, it will produce a finite-impedance node instead of a virtual-ground that is desired here. The current across R_{in} is modulated by the nth-order coefficients of this transconductance g_m, producing voltage fluctuations that are amplified to appear the Base of $Q2$. This contribution of the finite g_m of the pMOS is significant, so a large pMOS is chosen, driven by a high current. This also increases the pMOS current noise, decreases the corresponding flicker-noise and is traded-off with linearity performance of the stage, for a given power budget. The non-linear g_m, g_{be} and C_{be} further add to this non-linearity[5] and are among the primary contributors.

6.2.4 Noise performance

The noise performance of this stage is critical and contributes significantly to the up-converted noise of the Modulator. The noise of the input matching resistor R_{in}, appears at the Collector

[4] This average value is that obtained by averaging the two β_Fs.

[5] It should be noted that the exponential (see Chapter 9 in [101]) V_{BE}/I_C relationship is incorporated into the coefficients of g_m.

nodes of the BJTs that make up $Q2$, as $\sqrt{\frac{4kT}{R_{\text{in}}}(M \cdot \rho)^2}$. Here, ρ is the loss[6] associated with the finite input impedance of the feedback pMOS. We make the simplification that the current mirror has the ratio $1 : M$, as specified. If we consider the pMOS together with its current-source (also pMOS) and current-sink (nMOS) transistors, we can analyse this as a cascode structure where the output node is the Base of $Q2$. The approximate noise at this node, taking into account the noise of only the three MOSFETs, is given by (6.8).

The noise of the Source and Sink MOSFETs is determined by simply adding them up. The noise of the Source sees MP as a Common-Gate transistor and is visible at the junction of the Base terminals. The contribution of Source and Sink are given by

$$\overline{V^2_{\text{n,out,B,a}}} = \left(\underbrace{4kT(\gamma g_{\text{m,src}} + \gamma g_{\text{m,snk}})}_{\text{Thermal noise}} + \underbrace{\frac{K_{\text{a}} I_{\text{D,src}}}{f} + \frac{K_{\text{a}} I_{\text{D,snk}}}{f}}_{\text{Flicker noise}} \right) \cdot R_{\text{b}}^2 \tag{6.8a}$$

$$R_{\text{b}} = \frac{\beta_{\text{Q1}} R_{\text{E,1}}}{(M+1) + (\frac{g_{\text{m,MP}} R_{\text{in}} \beta_{\text{Q1}}}{1 + g_{\text{m,MP}} R_{\text{in}}})} \tag{6.8b}$$

$$\overline{V^2_{\text{n,out,B,b}}} = 4kT \frac{\gamma R_{\text{b}}^2}{r^2_{\text{O,src}} g_{\text{m,MP}}} + \frac{K_{\text{a}} I_{\text{D,MP}}}{f} \cdot \frac{R_{\text{b}}^2}{r^2_{\text{O,src}} g^2_{\text{m,MP}}} \tag{6.8c}$$

$$\overline{V^2_{\text{n,out,B}}} = \overline{V^2_{\text{n,out,B,a}}} + \overline{V^2_{\text{n,out,B,b}}} \tag{6.8d}$$

$$= 4kT(\gamma g_{\text{m,src}} + \gamma g_{\text{m,snk}} + \frac{\gamma}{r^2_{\text{O,src}} g_{\text{m,MP}}}) \cdot R_{\text{b}}^2 \tag{6.8e}$$

$$+ \frac{K_{\text{a}} I_{\text{D,MP}}}{f} \cdot \frac{R_{\text{b}}^2}{r^2_{\text{O,src}} g^2_{\text{m,MP}}} \tag{6.8f}$$

$$+ \left(\frac{K_{\text{a}} I_{\text{D,src}}}{f} + \frac{K_{\text{a}} I_{\text{D,snk}}}{f} \right) \cdot R_{\text{b}}^2 \tag{6.8g}$$

where K_{a} is a technology constant, I_{D} is the drain current and R_{b} is the impedance at the junction of the Base terminals. The noise of MP at this junction is given by $\overline{V^2_{\text{n,out,B,b}}}$. This gives us a total noise contribution of $\overline{V^2_{\text{n,out,B}}}$, as shown above.

It is evident from the above that there exists a tradeoff between the noise contribution of these transistors and the various other constraints that define $g_{\text{m,MP}}$. This voltage-domain

[6] $\rho = 1 - 3/(\beta + 3)$

noise is amplified by the transconductance of $Q2$ to give

$$\begin{aligned}\overline{I^2_{\text{n,out,casc.}}} &= G^2_{\text{m,Q2}} \cdot \overline{V^2_{\text{n,out,B}}} \\ &= G^2_{\text{m,Q2}} \cdot \left(\overline{V^2_{\text{n,out,B,a}}} + \overline{V^2_{\text{n,out,B,b}}}\right) \\ &= G^2_{\text{m,Q2}} \cdot \Bigg[4kT(\gamma g_{\text{m,src}} + \gamma g_{\text{m,snk}} + \frac{\gamma}{r^2_{\text{O,src}} g_{\text{m,MP}}}) \cdot R^2_{\text{b}} \\ &\qquad + \frac{K_{\text{a}} I_{\text{D,MP}}}{f} \cdot \frac{R^2_{\text{b}}}{r^2_{\text{O,src}} g^2_{\text{m,MP}}} \\ &\qquad + \left(\frac{K_{\text{a}} I_{\text{D,src}}}{f} + \frac{K_{\text{a}} I_{\text{D,snk}}}{f}\right) \cdot R^2_{\text{b}}\Bigg]\end{aligned} \tag{6.9}$$

where, $G_{\text{m,Q2}} = (1/g_{\text{m,Q2}} + (R_{\text{E,2}} + 1/g_{\text{m,Q2}} + r_{\text{bb}}/\beta_{\text{Q2}})/\beta_{\text{Q2}} + R_{\text{E,2}})^{-1}$ is the degenerated transconductance of $Q2$.

The current-mirror functionality of $Q1 - Q2$ is evidently retained, even with the addition of the feedback network. So, if we treat the rest of the circuit as a simple current-mirror with degeneration, then the total approximate noise contribution of the components can be readily calculated [104].

$$\overline{I^2_{\text{n,wn,CM}}} = 2qI_{\text{C,Q1}}(1+M)^2 \Bigg[\frac{1 + \frac{g_{\text{m,Q1}} r_{\text{bb,Q2}}}{M} + \frac{g_{\text{m,Q1}} r^2_{\text{bb,Q1}}}{M r_{\pi,\text{Q1}}} + 2g_{\text{m,Q2}} R_{\text{E,2}}(1 + \frac{r_{\text{bb,Q2}}}{M r_{\pi,\text{Q2}}})}{\left(1 + \frac{r_{\text{bb,Q1}}}{M r_{\pi,\text{Q1}}} + g_{\text{m,Q2}} R_{\text{E,2}}\right)^2} \tag{6.10a}$$

$$+ \frac{(1+M)\frac{g_{\text{m,Q2}} R^2_{\text{E,2}}}{r_{\pi,\text{Q2}}}}{\left(1 + \frac{r_{\text{bb,Q1}}}{M r_{\pi,\text{Q1}}} + g_{\text{m,Q2}} R_{\text{E,2}}\right)^2}\Bigg] \tag{6.10b}$$

$$\overline{I^2_{\text{n,fl,CM}}} = \frac{K_{\text{a}} I^{\gamma}_{\text{B,Q1}}}{f} \Bigg[\frac{M^{2-\gamma}\left(1 - \frac{g_{\text{m,Q1}} r_{\text{bb,Q1}(1-\frac{1}{\beta_{\text{Q1}}})}}{M}\right)^2}{\left(1 + \frac{r_{\text{bb,Q1}}}{M r_{\pi,\text{Q1}}} + g_{\text{m,Q2}} R_{\text{E,2}}\right)^2} \tag{6.10c}$$

$$+ \frac{\left(M + \frac{g_{\text{m,Q1}} r_{\text{bb,Q1}(1+\frac{M}{\beta_{\text{Q1}}})}}{M} + (1+M) g_{\text{m,Q2}} R_{\text{E,2}}\right)^2}{\left(1 + \frac{r_{\text{bb,Q1}}}{M r_{\pi,\text{Q1}}} + g_{\text{m,Q2}} R_{\text{E,2}}\right)^2}\Bigg] \tag{6.10d}$$

$$\overline{I^2_{\text{if,wno}}} = \overline{I^2_{\text{n,sh,CM}}} + \overline{I^2_{\text{n,fl,CM}}} \tag{6.10e}$$

where γ is a technology dependent constant. The total noise is given by the sum of the shot, thermal and flicker noise (in units of $\text{A}/\sqrt{Hz}$) calculated above.

6.2.5 Gain/Attenuation Stage

The IF voltage swing is converted into current across the 50Ω (matching) and R_{in} resistors, corresponding to a gain $1/(50+R_{\text{in}})$. The $1:M$ current mirror ratio provides an approximate gain given by (6.6). The signal current is then driven into the attenuation stage by the transistor array that comprises $Q2_{\text{p}}(Q2_{\text{n}})$ also forms part of the attenuation stage illustrated in Figure 6.13.

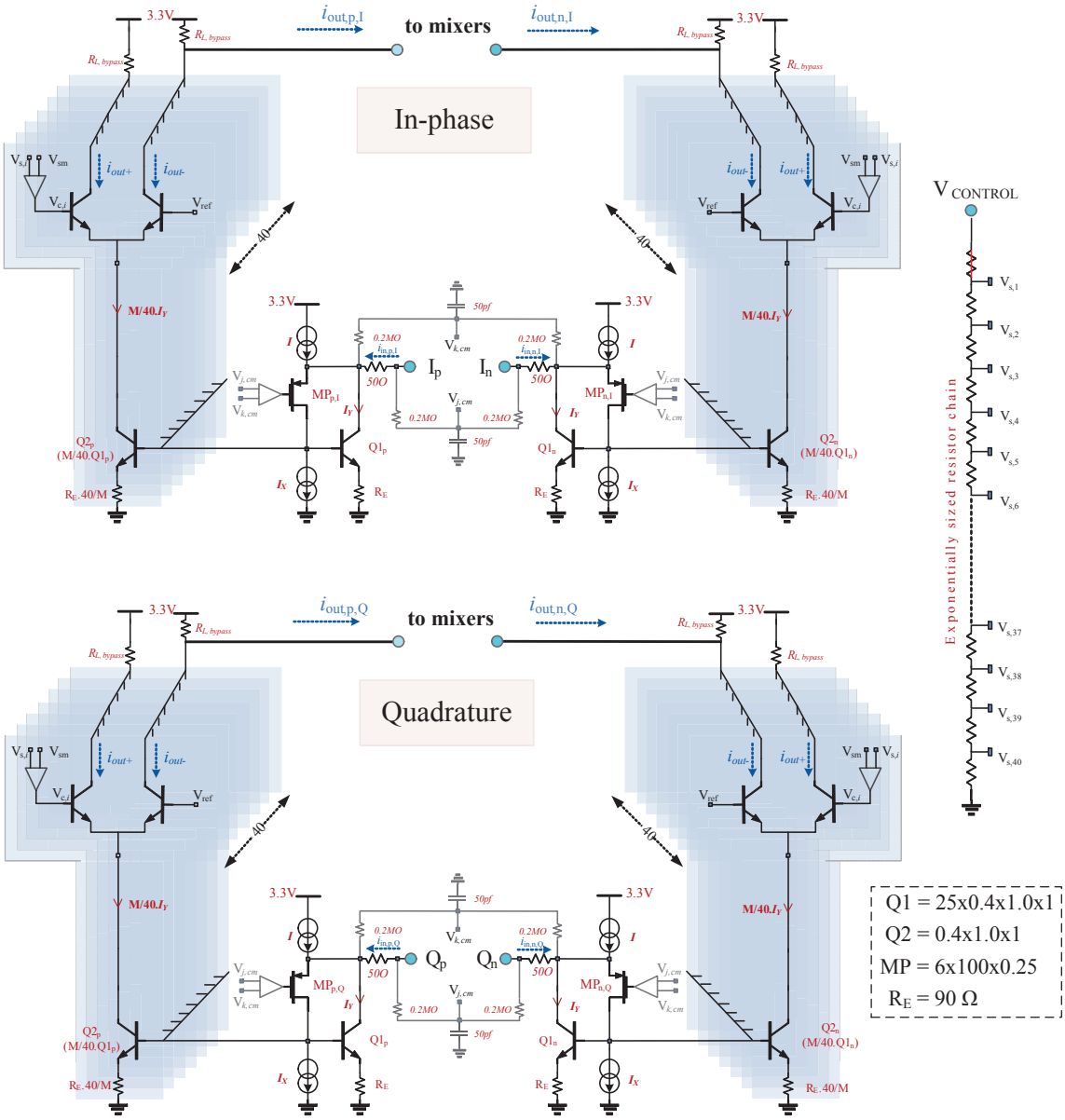

Figure 6.13: Input stage with the linear-in-dB analog Gain-control stage using exponentially-sized resistor string

Succinctly, the IF signal current from a resistive degenerated transconductance cell (output stage of the current mirror) is split within a Gilbert-Mixer type cell between a 'signal' node and a 'bypass' node, using an attenuation stage similar to that in [105], previously demonstrated for a Low Noise Amplifier. The ratio of currents in the two paths is determined by the voltage difference between the Base terminals of the BJTs in the two paths, much like a symmetrical differential-pair with a known unbalance. This would be a noisy solution, as the differential-pair would contribute noise to output[7], in addition to any noise that is generated from its bias circuitry. This is because the differential-pair, when in transition (i.e., both transistors or both paths are active,) acts as a difference amplifier to the uncorrelated noise at its inputs, and almost does not experience the degeneration of the under-stage. We simplify this structure by splitting the differential pair into N cells and combining the respective output nodes of these cells. A control voltage V_{control} then determines which cell is ON and specifically, whether the 'signal' or 'bypass' BJT is conducting. In this manner, the issue of noise in transitionary cells is avoided to a large extent. The method of controlling the current and achieving the linear-in-dB gain necessary for controlling the output power of the Base Station is explained below.

The attenuation stage works in a manner similar to a Multi-Tanh [106–108] in that it uses parallel combinations of Emitter-coupled pairs (diff-pair) to achieve gain control. However, the diff-pairs in this design are not unbalanced in size or their tail currents and the IF signal is not coupled to the Base but forms part of the tail current, as is done in typical diff-pairs. Since the attenuation stage is operated as a Common-Base transistor, the attenuation has a larger dynamic range[8] than the Multi-Tanh topologies. Therefore, this should not be compared with a Trans-linear cell where the exponential relationship between Base-Emitter voltage and Collector current is exploited. The attenuation stage diff-pair simply serves as a cascode stage to the signal sunk by the current-mirror beneath, leaving little importance for the g_{m} of the pair other than, perhaps, to analyse the noise behaviour. Outputs of differential pairs with the same phase current are connected together to form two separate branches - the 'bypass' and the 'signal' paths. The signal path is DC coupled in current mode to the input port of a Mixer, which is discussed in the following sections. Increasing V_{control} bleeds more current away from the *signal* path and into the *bypass* path, effecting the attenuation. We will aim to establish a relationship between the V_{control} and the attenuation factor for the entire stage.

The attenuation stage comprises of a resistive ladder or chain with N (= 40) taps, supplied by the attenuation control voltage V_{control}. Each of these taps serves as an input $V_{\text{s},i}$ to a comparator provided with a preset reference voltage V_{sm}. The individual comparators generate an output voltage $V_{\text{c},i}$ corresponding to the tap i ($i = \{1, \ldots, 40\}$). These $V_{\text{c},i}$ serve as control voltages for a differential pair whose other terminal is connected to a reference voltage V_{ref}. [9]

Now, the current in each branch of the differential pair making up one attenuation stage

[7] Uncorrelated noise at the inputs of the differential-pair is simply amplified to the output by the gain of the cell, when both elements of the pair are conducting.

[8] This is typically measured by range of input voltage over which the aggregated g_{m} of the $'N'$ collective stages has minimum acceptable ripple.

[9] The V_{ref} is set based on the required compression point of the entire stage between V_{cc} and *Ground*.

(see (6.11)) is given by a simple but well known analysis of the diff-pair,

$$\begin{aligned} i_{\text{out},+} &= \frac{\alpha.I_{\text{tail}}}{1+e^{-\frac{V_{\text{x}}^{+}-V_{\text{x}}^{-}}{V_{\text{T}}}}} \\ i_{\text{out},-} &= \frac{\alpha.I_{\text{tail}}}{1+e^{\frac{V_{\text{x}}^{+}-V_{\text{x}}^{-}}{V_{\text{T}}}}} \end{aligned} \tag{6.11}$$

where, $\alpha = \beta/(\beta+1)$, β being the forward current gain $I_{\text{tail}} = N/40 \cdot I_{\text{Y}}$, and V_{x}^{+}, V_{x}^{-} refer to cell control voltage $V_{\text{c},i}$ and the reference voltage V_{ref}, respectively.

As mentioned earlier, this primary control voltage V_{control} is divided into control or tap voltages, $V_{\text{s},i}$, for $i = \{1,\ldots,40\}$ (see (6.12)). The control voltage for each of the N(= 40) branches can be expressed as

$$\begin{aligned} V_{\text{s},1} &= V_{\text{control}} \quad \text{and} \\ V_{\text{s},i} &= \frac{\sum_{j=i}^{40} R_j}{\sum_{j=1}^{M=40} R_j}.V_{\text{control}} \quad \forall\, 2 \leq i \leq 40 \end{aligned} \tag{6.12}$$

The control voltages, $V_{\text{s},i}$, are compared with a band-gap referenced voltage V_{sm}, to generate the comparator output control-voltage $V_{\text{c},i}$ that serves as a control voltage at the Base terminal, in the bypass path of the diff-pair making up one cell of the attenuator. As the control voltage V_{control} is increased, the comparators generate proportionally larger voltages $V_{\text{c},i}$ which cause a corresponding increase in the flow of current into the bypass path or consequently, an attenuation of the signal path current. For the sake of easier understanding, the V_{control} can be expressed as having two components,

$$V_{\text{control}} = V_{\text{sm}} + A_{\text{dB}} \cdot \Delta V_{\text{c}} \tag{6.13}$$

where, V_{sm} is the fixed offset voltage that comes from the comparator reference of V_{sm}. Control voltages below this comparator reference do not actuate the stage to produce any attenuation. A_{dB} that is used in the expression is the slope of the linear-in-dB attenuation curve and ΔV_{c} is the change in control voltage required to obtain unit dB attenuation. If we rearrange the above expression, we obtain

$$\frac{V_{\text{control}} - V_{\text{sm}}}{\Delta V_{\text{c}}} = A_{\text{dB}} \tag{6.14}$$

The expression above gives the change in attenuation $A_{\text{dB}_{\text{n}}} - A_{\text{dB}_{\text{n-1}}}$ for a step change (ΔV_{c}) in the control voltage V_{control}. Evidently, for A_{dB} to be linear-in-dB, the L.H.S. of the above expression must vary linearly-in-dB. This will be achieved by sizing the resistances which provide the tap voltages, and will be derived below. Analytically, when V_{control} is increased, the $V_{\text{s},i}$ increases till such a point that it trips the comparator whose output voltage $V_{\text{c},i}$ rises sharply in response, as a function of its own gain. When $V_{\text{c},i}$ is larger than the V_{ref} this draws away more of the I_{tail} current from the signal path effecting the attenuation. The comparator

trip voltage (V_{sm}) is set low at approximately 0.2V)in order to allow a relatively low value of V_{control} to modify the attenuation, thereby maximising the effective control attenuation range of the V_{control}. V_{sm} can be visualised as a sensitivity setting between the attenuated output current and the input control voltage.

It might be interesting to look at the Attenuation as having voltage gain, but since we refer to current gain from the current mirror and follow it up with a passive current driven mixer, the current gain or attenuation is therefore more instructive when dealing with such cascaded stages. Since we are measuring the current gain of the input stage, we must facilitate a current mode operation, i.e., the IF signal current is manipulated. The empirical expression for the output current is as given by

$$I_{\text{out,signal}} = I_{\text{IF}} - \sum_{i=1}^{M=40} \frac{\frac{N}{40} I_{\text{IF}}}{M} . B_i \tag{6.15}$$

where $I_{\text{IF}} = I_{\text{Y}} + i_{\text{IF}}$ is the sum of bias and signal currents in the IF path, which make up the tail current of the Bipolar differential-pair. M refers to the number of stages, here, 40 and where N is the current mirror ratio from the under-stage. B_i is a decision variable ('ON' or 'OFF', '1' or '0'), which captures the state of the cell. [10] For a cell i that is in transition, $V_{\text{c},i} \approx V_{\text{ref}}$, implying the corresponding tap on the resistive chain $V_{\text{s},i}$ should be close to the comparator reference V_{sm}, giving us an idea of the gain for the comparator. The corresponding B_i takes on a value of 1/2, because the current is divided approximately equally between the signal and the bypass paths when $V_{\text{c},i} \approx V_{\text{ref}}$.

From the above expression, it is evident that the attenuation of the of the output current can be expressed in dB as

$$20 \log \left[\frac{I_{\text{out,signal}}}{I_{\text{IF}}} \right] = 20 \log \left[1 - \frac{\frac{N}{40}}{M} \sum_{i=1}^{M=40} (B_i) \right] \tag{6.16}$$

where the decision variable B_i can take any of the following values,

$$B_i = \begin{cases} 1 \; V_{\text{s},i} > V_{\text{sm}} \Rightarrow V_{\text{c},i} > V_{\text{ref}} \\ 0 \; V_{\text{s},i} < V_{\text{sm}} \Rightarrow V_{\text{c},i} < V_{\text{ref}} \\ \frac{1}{2} \; V_{\text{s},i} = V_{\text{sm}} \Rightarrow V_{\text{c},i} \approx V_{\text{ref}} \end{cases} \tag{6.17}$$

For easier understanding, we refer to the attenuated IF current that enters the Mixers as I_{IF} from here on, although it actually refers to $I_{\text{out,signal}}$. This is deliberate because we intend to highlight the effect of attenuation on the input signal while it traverses the signal path.

By comparing Equations (6.16) and (6.14), the value of A_{dB} can be established, as given by

$$A_{\text{dB}} = 20 \log \left[1 - \frac{\frac{N}{40}}{M} \sum_{i=1}^{M=40} (B_i) \right] \tag{6.18}$$

[10] We can also have cells that are in between the 'ON' and 'OFF' states, i.e., in a state of transition. As explained above, this implies that $V_{\text{c},i} \approx V_{\text{ref}}$, owing to the limited gain of the comparator. The noise contribution of the differential pair (noise from the biasing circuit) is the highest in this state and is to be avoided.

6.2.5.1 Comparator

The construction of the comparator is similar to, but an inverted version of the input stage of a $\mu A741$ Operational amplifier. Since the comparator threshold voltages are closer to ground and because the NXP QuBiC4 process does not support vertical PNPs, we replace them with pMOS transistors o achieve a similar effect. The active load in the $uA741$ input stage is replaced in this circuit, by resistors. Both the comparator inputs are formed by a pMOS Common-Source stage. One of these is driven by the V_{sm}. The Gate of the other Common-Source stage is driven by the voltages $V_{\text{s},i}$ of the resistive taps. The output of the comparator $V_{\text{c},i}$ if obtained from a Common-Base Stage which stacks above the Common-Source in cascade. $V_{\text{c},i}$ rises with increasing $V_{\text{s},i}$ as a function of the gain setting of the comparator.

The comparator has the same gain for all cells and therefore mismatch between any two cells introduces ripple or a step change in the useful part of the attenuation curve. This is because if the voltage difference between two adjacent cells is too high, the i cells starts its transition when the $i-1$ cell has already been turned OFF. The transition from one cell to another while the V_{control} is changing, is no longer smooth, resulting in a step or ripple in the slope of output current versus V_{control}. On the other hand, if the voltage difference is too small, then several cells conduct current at the same time and the noise contribution increases as more cells are in the transition zone.

The comparator in this design is composed of two halves, as illustrated in Figure 6.14. While one half of each comparator is local to that cell, the other half is not replicated and is in fact a common (half) block shared by all comparators. This achieves $\sqrt(2)$ times less [102] mismatch [11] between any two neighboring cells. Mathematically, the total deviation between two neighbouring but uncorrelated cells, $\sigma_{\text{i,i+1}} = \sqrt(\sigma_i^2 + \sigma_{i+1}^2)$ is reduced by a factor of $\sqrt{2}$ if either of σ_i^2 or σ_{i+1}^2 is set to zero. This is achieved by the split-sharing explained here. The common half-pair is also given a higher multiplicity in dimensioning (≈ 4) to further reduce its total spread in threshold voltage. However, this is just to obtain a more accurate value for the threshold and not to reduce the differences between the value for neighbouring cells.

For the linear-in-dB relation that is required between V_{control} and $I_{\text{out,signal}}$, the right-hand side expression of (6.16) must also vary linearly on the dB scale, with a negative slope because attenuation is required. To achieve this, the R.H.S. of the above equation should be an exponential function or a power of 10. It is more practical to size the resistive chain as an inverse exponential series than as an inverse power of 10. Furthermore, the lesser slope of the exponential also ensures lesser sensitivity to unwanted fluctuations in the V_{control}.

In order for the current gain of the input stage to drop linearly on a log-scale, the resistors R_j are sized such that when V_{control} increases, the voltages $\Delta V_{\text{s},i}$ rise exponentially (see (6.19)). Since V_{control} sets the value of $\Delta V_{\text{s},i}$, it highlights the relation between $\Delta V_{\text{s},i}$ and B_i which gives the linear-in-dB relationship between V_{control} and $I_{\text{out,signal}}$. We know the attenuation

[11] This is because there is only one half of the comparator differential-pair present in each individual cell, and the differences between individual cells is what produces the offsets. Since the other half of the differential pair is also present but is common to all cells it does not contribute to threshold differences between the cells. If each cell had a complete differential pair as input comparator then there would be 4 half-pairs contributing to the mismatch between the threshold of 2 cells. By splitting and sharing the comparator structure, only two half-pairs are contributing.

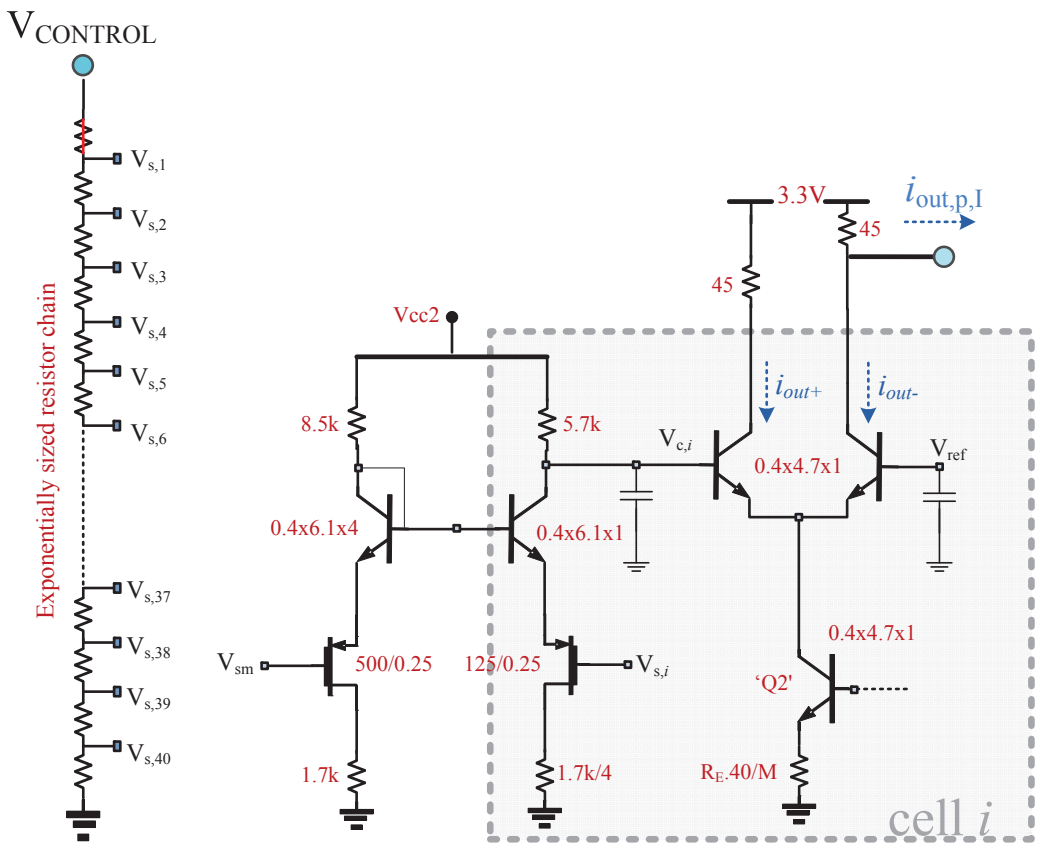

Figure 6.14: A single cell of the Gain (Attenuation) stage, showing the comparator and the resistor string

factor A_{dB} of (6.14) from (6.16).

The Figure 6.15 plots tap voltage $V_{\mathrm{s},i}$ and the $\Delta V_{\mathrm{s},i}$ as a function of the cell index 'i'. $\Delta V_{\mathrm{s},i}$ can be expressed as

$$\begin{aligned}\Delta V_{\mathrm{s},i} &= V_{\mathrm{control}} \cdot \frac{\sum_{j=i}^{40} R_j}{\sum_{j=1}^{M=40} R_j} - \frac{\sum_{j=i+1}^{40} R_j}{\sum_{j=1}^{M=40} R_j} \\ &= V_{\mathrm{control}} \cdot \frac{R_i}{\sum_{j=1}^{M=40} R_j}\end{aligned} \tag{6.19}$$

From the perspective of current, the currents of the output (*signal*) path are offset (on the x-axis) by $\Delta V_{\mathrm{s},i} = V_{\mathrm{s},i+1} - V_{\mathrm{s},i}$. It is evident from the above that the voltage differences $\Delta V_{\mathrm{s},i}$ between the contiguous resistances are part of an exponential series with a certain

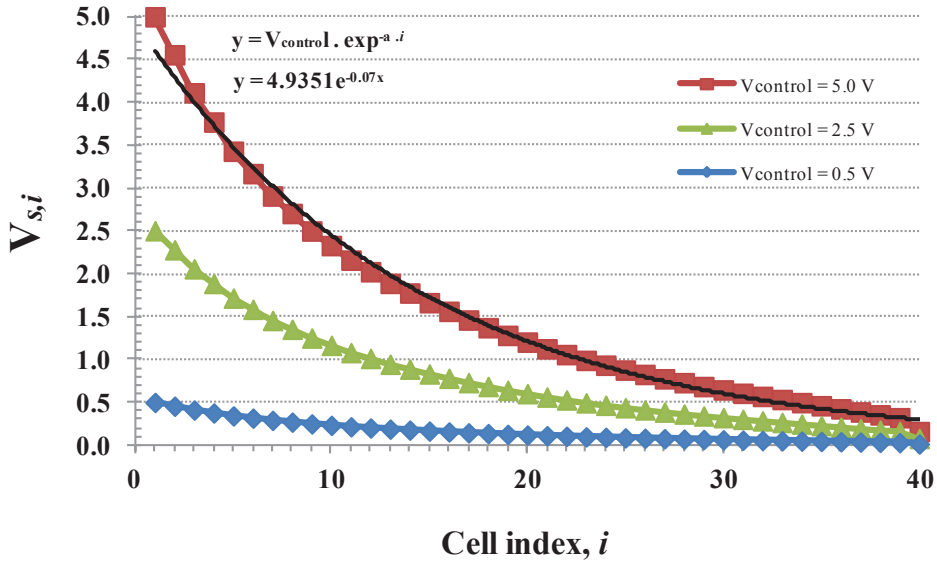

(a)

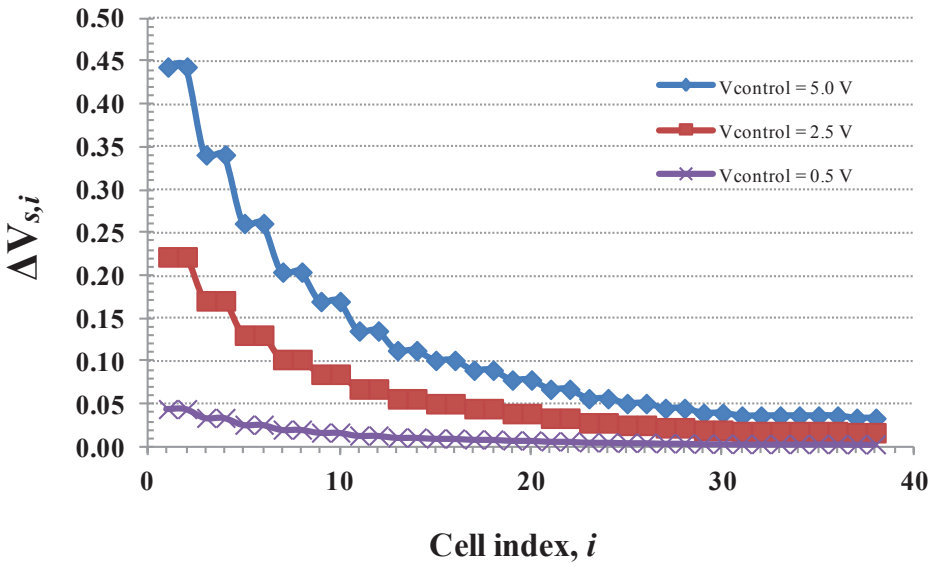

(b)

Figure 6.15: (a) Tap voltages $V_{s,i}$ of the resistor string and, (b) difference $\Delta V_{s,i}$ between tap voltages, at $V_{control}$ = 5.0 V, 2.5 V, 0.5 V

slope chosen by design. The ratio of the resistances and the gain of the comparators are both collectively derived from the minimum voltage change ΔV_c required to provided a unit change in the attenuation. The delta values expressed above and the voltage gain of the comparators together can be represented in the form $\exp^{-ax}$, where a is a constant multiplier and x is the index. Taking logarithm of this expression yields,

$$\log(\exp^{-ax}) = \log\exp \cdot \log\exp^{-ax} = -0.434ax \tag{6.20}$$

where, -0.434 is a multiplicative constant, a refers to a chosen gain which determines the sensitivity to the input (V_{control}) and x corresponds to the index of the gain cell. Due to the fact that the resistors are sized based on the exponential series while the required gain is linear-in-dB, this combines together with the $\ln_e$ to $\log_{10}$ conversion ($\log(\exp^{-ax}) = \log(\exp) \cdot \ln(\exp^{-ax})$) to yield the slope of the exponential series which determines the slope of (6.14).

6.2.5.2 Linearity

The biasing of the input stage is set here based on the required back-off from the compression point. The output compression point of the C-E/C-B cascode is determined by the bias point of the upper stage of the cascode. Accordingly a bias voltage of $V_{\text{ref}} = 2.6\text{V}$ is chosen to maximise the compression point. The selection also aims to minimise non-linearity associated with the C_{bc} and C_{be} non-linear junction capacitances. At minimum control voltage (attenuation setting of 0dB), the bypass path NPN is completely switched off. As the control voltage is increased, the high comparator gain increases the Base bias voltage to the corresponding cell, to the same level as the signal path NPN, turning it ON. The following equations attempt to determine the compression point of the attenuator stage, based on compression due to reaching $V_{\text{CE,sat}}$ [12].

$$V_{\text{peak}} = V_{\text{CE,Q}} - V_{\text{CE,sat}} \tag{6.21}$$

This essentially gives us the lower half of the swing that is permissible without entering into saturation. By substituting for $V_{\text{CE,Q}}$ we obtain

$$V_{\text{peak}} = \underbrace{(V_{\text{CC}} - I_{\text{C}} \cdot Z_{\text{bypass}})}_{V_{\text{C}_\text{Q}}} - \underbrace{(V_{\text{ref}} - V_{\text{BE,ON}})}_{V_{E_Q}} - V_{\text{CE,sat}} \tag{6.22}$$

where $V_{\text{BE,ON}}$ is the diode voltage drop of $\approx$ 0.7V. Substituting values (($V_{\text{CC}} = 3.3\text{V}$, $I_{\text{C}} \approx 6\text{mA}$, $Z_{\text{bypass}} = 45\Omega$, $V_{\text{ref}} = 2.6\text{V}$, $V_{\text{CE,sat}} \approx 0.3\text{V}$), we obtain $V_{\text{peak}} \approx 830\text{mV}$. The corresponds to a voltage-swing limited compression point of $10\log\left(2^2 \cdot V_{\text{peak}}^2/(2\cdot 50)\right) = 14.40\text{dBm}$ referred to a 50Ω load or simply $20\log\left(V_{\text{peak}}/(\sqrt{2})\right) = -1.62\text{dB}V_{\text{rms}}$.

Similarly, the large-signal compression of the transconductor under-stage is determined by

$$V_{\text{peak}} = \underbrace{(V_{\text{ref}} - V_{\text{BE,ON}})}_{V_{C_Q}} - \underbrace{(V_{\text{b}} - V_{\text{BE,ON}})}_{V_{E_Q}} - V_{\text{CE,sat}} \tag{6.23}$$

[12] From the well established analysis, as $V_{\text{CE}} = V_{\text{CE,sat}}$, the forward current gain β_{DC} drops drastically causing I_{C} to be determined by other circuit elements as it no longer behaves as a source.

where V_{b} refers to the voltage at the Base of ($Q2$,) the output stage of the current-mirror, which is dependent on the input common-voltage. This allows to also take into account the compliance range of the current mirror.

For such large signals, high-voltage devices with high Collector-Emitter breakdown voltages (Base open, BV_{CEO} and high Collector-Base breakdown voltages (Emitter open, BV_{CBO}) are chosen. This ensures better reliability under stress and also reduces non-linearity associated with avalanche currents to a degree.

The attenuation stage contributes to the overall non-linearity by a combination of the mechanisms listed in Section 6.2.3 above. Of these, the non-linear conductance g_{be} and the junction capacitances showed the most significant non-linearity for the given bias setting and signal swing. [13]. The significant degeneration of the g_{m} of the 'signal' path transistor via the current-mirror output stage causes its contribution to the overall non-linearity to be reduced. The effect of negative feedback (i.e., degeneration) on n^{th}-order coefficients of the transconductance of a BJT has been presented in detail in [101]. To improve linearity, the authors of [110] suggest using a transistor driven by a signal or voltage of opposite polarity at the Base, connected across the 'signal' path transistors. While this could produce a cancelling effect on the C_{bc}, it would also increase current consumption and noise associated with the additional transistor. We were however unable to verify the suggested method in detail. The size of the transistors has been chosen with a view to maximise the f_{T} for the current set by the large-signal compression. This way the impact of the non-linear capacitances on the non-linearity and the contribution of the Base resistance r_{bb} to the noise of the attenuation stage is minimised.

Based on the expression for junction capacitance, a larger V_{CB} would reduce the fluctuations of the C_{bc}, reducing its non-linearity (see Figure 6.16). However, reducing the DC voltage at the Collector (output) terminals of the attenuation by reducing the DC load would also reduce the current flowing towards the Mixer, as will be shown in (6.44). The choice of this load Z_{bypass} also impacts the noise performance as the current noise of the resistor itself, $4kT/R_{\mathrm{bypass}}$ (ignoring parasitic capacitors), increases as the resistance is lowered to achieve a more favourable linearity. This here presents a point of tradeoff between noise, linearity and current gain of the input stage.

While some consideration was given to minimising process variations, the gain control is unfortunately not compensated against variations in ambient and junction temperature. Temperature-stability plays an important role in the gain control in a wide-area Base station for which this design is suggested. Without temperature stability, then burden of compensation falls onto the circuitry that generates the control Voltage. This therefore, remains among the drawbacks of this AQM design and is highlighted for future work.

The attention given to matching also influences the temperature drift of the offsets in this

[13] This can be compared with the analog π-attenuator that was studied, where non-linearity performance was primarily due to the g_{ds} of the nMOS transistors with the non-linear capacitances (C_{db}, C_{gs} and C_{gd}) beginning to contribute at higher frequencies. With Silicon-on-Insulator technologies, the significant effect of the C_{db} has been proven [109] to be somewhat diminished.

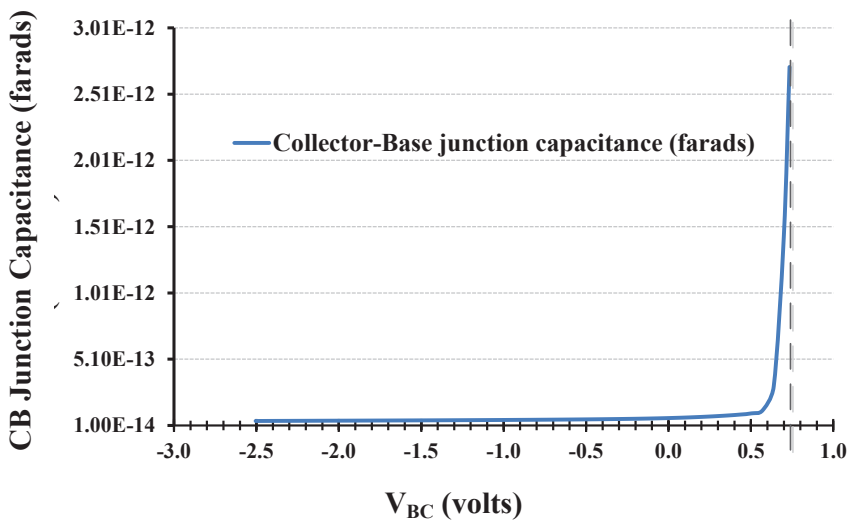

Figure 6.16: Variation of the Collector-Base junction capacitance C_{bc} with respect to V_{BC}

stage. The voltage and current offsets (see [103]) are given to be

$$V_{\mathrm{OS}} \simeq V_{\mathrm{T}} \left(-\frac{\Delta R_{\mathrm{load}}}{R_{\mathrm{load}}} - \frac{\Delta A_{\mathrm{e}}}{A_{\mathrm{e}}} + \frac{\Delta(N_{\mathrm{A}} W_{\mathrm{B},V_{\mathrm{CB}}})}{(N_{\mathrm{A}} W_{\mathrm{B},V_{\mathrm{CB}}})} \right) \tag{6.24a}$$

$$I_{\mathrm{OS}} \simeq \frac{I_{\mathrm{c}}}{\beta_{\mathrm{F}}} \left(-\frac{\Delta R_{\mathrm{load}}}{R_{\mathrm{load}}} + \frac{\Delta \beta_{\mathrm{F}}}{\beta_{\mathrm{F}}} \right) \tag{6.24b}$$

where, A_{e} is the Emitter area, N_{A} is the acceptor density in the Base and $W_{\mathrm{B},V_{\mathrm{CB}}}$ is the width of the Base as a function of V_{CB}. The last two terms make up the mismatch in saturation current, $\Delta I_{\mathrm{s}}/I_{\mathrm{s}}$.

Clearly, both of the above expressions are temperature dependent, implying a drift in offsets with temperature variation. Low temperature coefficient resistors with good process control ($T_{\mathrm{c}} = 160\mathrm{ppm}/^{\circ}\mathrm{Cel.}$ and $\sigma \approx 2.6\%\mu\mathrm{m}$) are therefore chosen for the load, degeneration, input matching resistors and also for the resistive ladder. The objective is to have resistors with similar temperature coefficients, play equal role in increasing as well as decreasing the current in the circuit, in the event of temperature variations. With the comparator supply and reference voltages both already band-gap referenced, a suggested method for temperature compensation in the resistive chain could involve driving the resistive chain with a CTAT current source derived from V_{control}, in order to achieve relatively stable tap voltages for gain control.

6.2.5.3 Noise Performance

We know from the noise performance of a differential-pair in [103] that the noise from each of the transistors making up the pair is amplified when both are in the ON state or a state

of transition for the cell, with respect to the gain control. For this reason, the comparators provide reasonable gain so as to not have cells in this transition zone and also to ensure that no two cells are transitioning at the same time. For cells that are 'ON' in the bypass path, the signal path BJT supplies neither IF signal current nor noise to the output. For those that are in the 'OFF' state, the signal path BJT supplies most part of the differential-pair tail current to the output. In this case, its noise contribution [14] and that of the current mirror stage that makes up the tail current, go through to the Mixer stage. The differential-pair signal path BJT that is 'ON' in this case, acts as a Common-Base transistor and therefore any noise from the previous stages and also noise from its bias network, both experience roughly the same attenuation as the IF signal current. For use later, we shall present the noise from the IF stage as $i_{\mathrm{fno,IF}}$.

An nMOS 9-stage π-network based attenuator with $0-27$dB, with 3dB per stage was also studied and analysed in comparison, but is not discussed here. While the noise performance of the π-attenuator [15] is relatively poor (see also [111,112]), its bandwidth is larger than the differential-pair structure chosen for this design. This bandwidth limitation comes from the several C_{bc} capacitances which appear in parallel at the Mixer input node. Furthermore, the Common-Base structure chosen, does little to degrade the noise figure due to the cascoding, or high degeneration of the cascode transistors by the output impedances of the CM stage. The choice of attenuator structure was based on linearity and noise performance rather than bandwidth, because of the DC -to- low-IF frequencies at which this stage is required to function.

6.2.6 Frequency Response

The bandwidth of the entire input stage is of importance as it defines the range of DC -to- mid-band frequencies from the output of the DAC which can be usefully up-converted. We deal here with half-circuit equivalents because of the symmetry of the positive and negative phase circuits in the schematic. Since no decoupling capacitors are used between the stages, this design also support signals at DC. Most telecommunication standards typically have little/no information at DC. This is especially true in the case of LTE, where the sub-carrier(s) with (around the) DC-index is (are) usually ignored. In the case of WCDMA, the use of a notch filter in the receiver to reject noise around DC involves little loss of information because the signal is of sizeable bandwidth. This system level adaptation is helpful because the biasing circuits have been identified through simulations to be among the primary contributors of side-band noise that is up-converted by the Mixers and the Output stage to RF. This is comparable with LO phase-noise. Large shunting capacitors are used to low-pass filter noise coming from the bias networks, but their size is often constrained by area limitations [16].

[14] This includes the noise of the Base resistance $4kTr_{\mathrm{bb}}$, the biasing network $kT/(C_{\mathrm{shunt}})$ and the shot noise $2qI_{\mathrm{c}}/N$ of the transistor itself. Large shunt capacitors C_{shunt} are used to filter the signals to the Ground. But, since the shunt capacitors can only force a non-zero pole and because the attenuation stage is DC coupled to the Mixer circuit, this noise, like the IF signal, also experiences a frequency up-conversion by the Mixer.

[15] Typically, because the passive-attenuator is comprised of resistances, its noise increases almost dB-per-dB with the attenuation, much like any passive network of resistors.

[16] These large capacitors here may not always present a significant area penalty since they are MiM capacitors (using M5, M6 metal layers, at 5fF/μm^2) which can be placed above active devices not using the same upper-

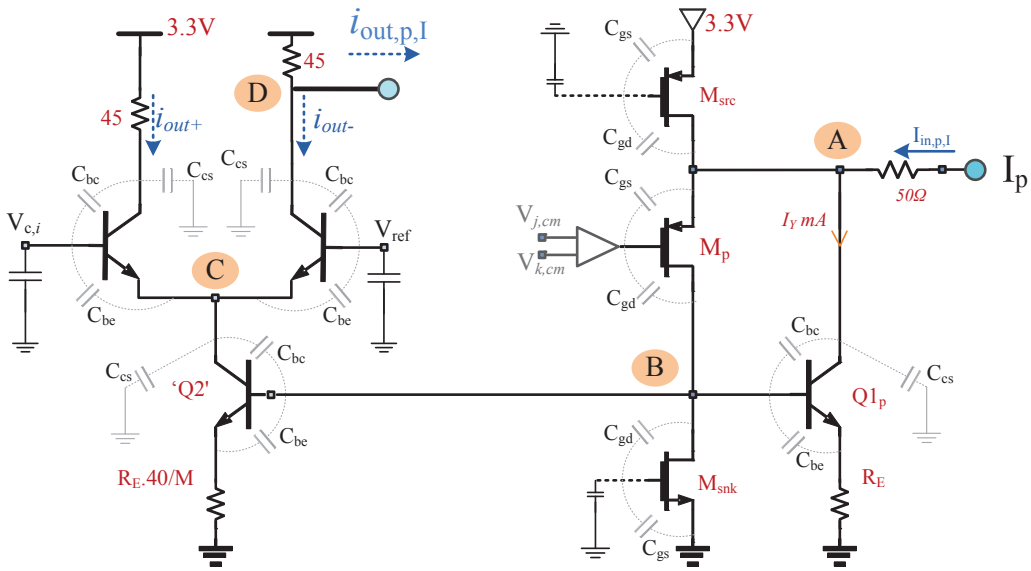

Figure 6.17: Simplified schematic showing critical nodes for DC-to-IF bandwidth analysis

In order to determine the dominant pole, the most critical nodes in the input stage are identified, Ⓐ - Ⓓ, as show in Figure 6.17. An approximate calculation of the poles at the critical nodes indicate that the dominant pole is located at node Ⓓ. The structure of the attenuator, which was discussed earlier mentions details of the nature of this IF output node. The low-frequency pole at this node is mainly due to the large number of C_{bc} capacitors in parallel with the 45Ω IF load resistor. Reducing the load resistor to have better current mode operation (i.e., higher IF bandwidth) is somewhat complicated as there also exist other constraints that dictate the sizing of this resistor. This has been addressed earlier. Although C_{gs} capacitances of the Mixer occur at this point, they are connected via large biasing resistors to Ground in one path. C_{sb} with its low value (of $<$ 40fF from simulations) does not impact the IF bandwidth. At input node Ⓐ, if we ignore the Collector and Base intrinsic resistances r_{cc} and r_{bb} the capacitances of C_{gs} of MP and C_{sb} of $Q1$, appear in parallel with the $\frac{1}{g_{\mathrm{m}}+g_{\mathrm{mb}}}$. This intrinsic resistance is broadband and has a value of $\approx 2-3\Omega$s at a common-mode input voltage of 2.8V. [17] This is the *cold*-node at the input that was discussed in the previous section. Consequently, voltage fluctuations across this node are at a minimum and the node is amenable to fast charging-discharging, implying a high frequency pole.

At Ⓑ between the Base terminals of the $Q1$ and $Q2$, there exist several capacitances if we were to ignore the influences of the Base and Collector terminal intrinsic resistances. This

metal layers. Where matching critical devices are used, these capacitors are distributed symmetrically over the matched devices. Care has also been taken to ensure the reliability and lifetime of these capacitors is not degraded, by limiting the voltages that appear across these capacitors.

[17] This resistance value remains almost unchanged even if the common-mode voltage is set to a lower value since the Gate voltage tracks the input common-mode voltage within its range to ensure that the same overdrive voltage and current are maintained for the pMOS device.

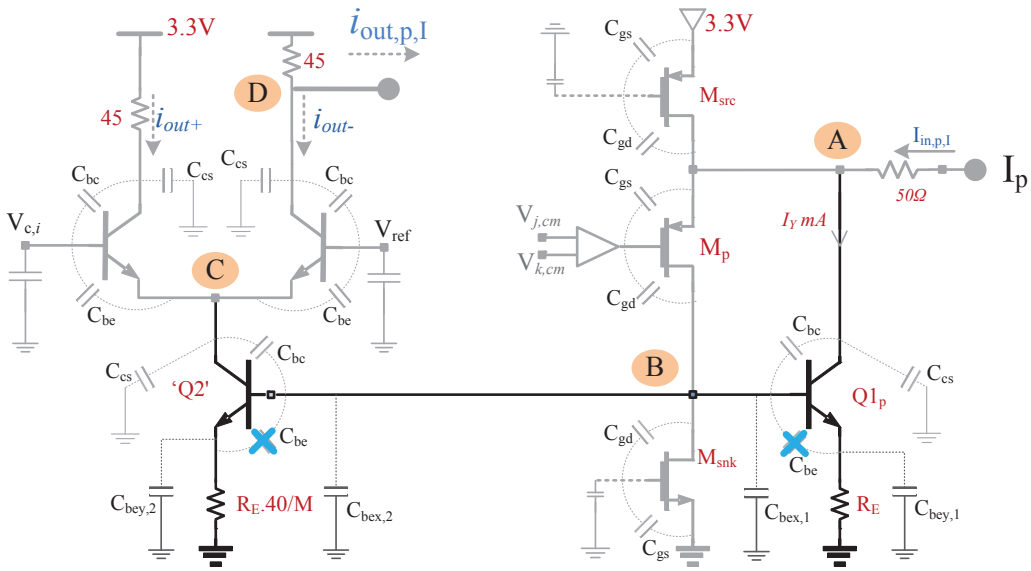

Figure 6.18: Dividing the C_{be} capacitance to calculate equivalent capacitance at the internal node Ⓑ

would indicate the secondary critical node in terms of bandwidth. C_{bc} of $Q1$ appears shunted, to Ground. This is because the input node is a low-impedance node and the capacitance does not experience the Miller effect. The C_{be} can be split into two capacitances as shown in the Figure 6.18. These appear as $C_{be,x}$ from Base of $Q1$ to Ground and $C_{be,y}$ which appears across the degeneration resistor $R_{E,1}$. The values of $C_{be,x}$ and $C_{be,y}$ are given by

$$C_{be,x} = C_{be}(1 - A_v) = \frac{C_{be}}{1 + g_m R_{E,1}} \tag{6.25a}$$

$$C_{be,y} = C_{be}\left(1 - \frac{1}{A_v}\right) = -\frac{C_{be}}{g_m R_{E,1}} \tag{6.25b}$$

where $A_v = R_{E,1}/(1/g_m + R_{E,1})$ is the gain of what can be seen as an Emitter-follower circuit formed between the cold-node at the Collector of $Q1$ and its Base. Similarly the $C_{be,x}$ and C_{bc} capacitances of $Q2$ also appears between Ⓑ and Ground, but M times in size, due to the current-mirror ratio. $Q2$ is actually made N devices in parallel, coming from the attenuator structure, so C_{be} and C_{bc} are the net capacitances that result from this parallel combination. The C_{bc} of $Q2$ also appears between Ⓑ and Ground because of the low-impedance node at the Collector of $Q2$. The relatively smaller C_{gd} of the current sink is ignored for this analysis. The equivalent capacitance therefore is $(1 + M)C_{be,x} + (1 + M)C_{bc}$. The corresponding equivalent resistance at Ⓑ is $(1 + 1/M)(r_\pi + R_E)||(r_O + 1/(g_m + g_{mb}))$. Much like the case with the capacitors, the resulting input impedances of the $Q2$ is actually that of N devices in parallel. Although the capacitances at this node are not significantly large, the equivalent resistance at this node could be very high, resulting in a bandwidth limiting node.

Lastly, at node Ⓒ, which is between the Current-Mirror stage and the Attenuation stage,

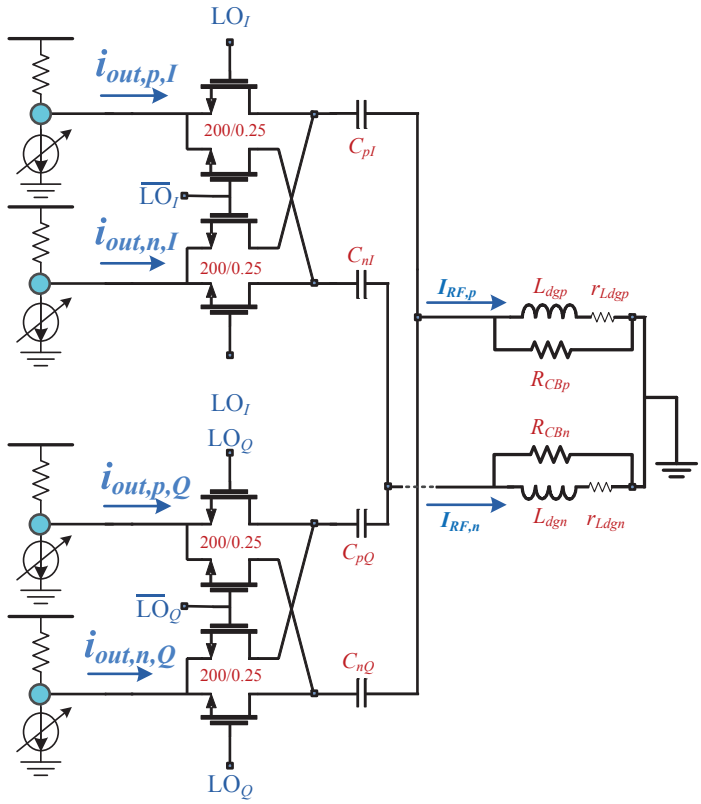

Figure 6.19: Simplified operating principle of the Passive Current-Driven Mixer

the impedance looking into the Emitters of the 'bypass' and 'signal' path transistors is approximately $1/g_{\mathrm{m}} + Z_{\mathrm{bypass}}/g_{\mathrm{m}}r_{\mathrm{O}}$ which is quite small, implying that this does not limit the bandwidth in the IF stage.

6.3 Mixers

The Mixers in the design achieve the critical task of frequency translation or up-conversion from the IF signal at the output of the previous stage to RF. In keeping with the current-mode approach of this design, the commutation is achieved in the current domain, with the aid of a quadrature phase LO signal (see Section 6.4), towards a low impedance node of the subsequent (see Section 6.5) stage. By this mechanism, an RF *current* is driven into the next stage. The Figure 6.19 shows the current mode operation and interface between the various stages of the modulator.

The nMOS transistors that make up the time-variant switches of the Mixer are current driven in that the IF-signal current from the attenuation stage follows a path of least impedance to ground, in this case, through the large switches of the Mixers and eventually through the Emitter of the Common-Base stage. The Mixers are *passive*-mixers as

no/negligible DC current passes through them, owing to the large decoupling capacitors at the Mixer's output port. It is relevant to note here that although the input stage discussed earlier is capable of achieving a decent large-signal voltage gain, because the Mixer is terminated into a low-impedance node, only the current gain is relevant. The voltage across the Mixer and the load are consequently, small, hence the appellation, *current mode* or passive current-driven. We will therefore calculate the voltage- or corresponding power-gain only at the output stage of the modulator. This might seem counter-intuitive because of the sizeable 45Ω load at the output of the attenuation stage indicating a voltage gain already available at the IF port. However, by simply examining the RF-impedance of the mixing path to ground, it is easy to visualise the current-mode operation. This also ensures a highly linear operation of the Mixer, as will be pointed out in the sections below.

The ON resistance R_{ON} of the mixers can be expressed as given in [111]

$$R_{\mathrm{ON}} = \frac{1 + \theta.(V_{\mathrm{GS}} - V_{\mathrm{Th}})}{\mu C_{\mathrm{ox}}(\frac{W}{L})(V_{\mathrm{GS}} - V_{\mathrm{Th}} - \eta V_{\mathrm{DS}})} \tag{6.26}$$

where θ models the resistance of the source and drain nodes, mobility degradation and other short channel effects. The parameter η models the exponential increase of the drain current with the value of $\mathrm{V_{GS}}$ in the subthreshold region. The figure 6.20 shows the simulated value of resistance for the nMOS switch under different bias conditions.

Being operated as a passive device that is simply switched ON and OFF, the poor reverse isolation causing translation of output signals back to the input, becomes an issue. This might seem to be particularly troublesome with the architecture of the output stage indicated in Figure 6.40, where the Mixers from the two separate signal paths combine their output currents into the Common-Base stage. In receivers this is particularly troublesome, as has been previously analysed in [113]. The authors suggest that the reverse isolation causes image signals to become visible at the RF input port leading to distortion. A complication of this issue involved I and the Q channels that combine at the high impedance IF node allowing currents to leak into the low-impedance node in the opposite channel, causing further distortion and deteriorating linearity and noise performance. This lack of reverse isolation also has a positive effect since a low-pass filter response at the output IF port is easily translated into a high-Q band-pass response at the RF port that helps reject unwanted signals, improving selectivity.

In the case of transmitters, closer examination of the impedance when looking towards the generator reveals a switched capacitor resistor, as shown in Figure 6.21. The capacitances that appear at the IF port have been discussed in Section 6.2.6.

The impedance of the IF node as seen from the RF port of switch is given by

$$I = \frac{2 \cdot C_{\mathrm{par}} V_{\mathrm{x}}}{T_{\mathrm{LO}}} \tag{6.27a}$$

$$\Rightarrow R_{\mathrm{par,IF}} = \frac{T_{\mathrm{LO}}}{2 \cdot C_{\mathrm{par}}} \tag{6.27b}$$

which occurs in parallel ('——') with $R_{\mathrm{L,bypass}}$ to result in

$$z_{\mathrm{IF,sc}} = \frac{T_{\mathrm{LO}}}{2 \cdot C_{\mathrm{par}}} || R_{\mathrm{L,bypass}} \tag{6.27c}$$

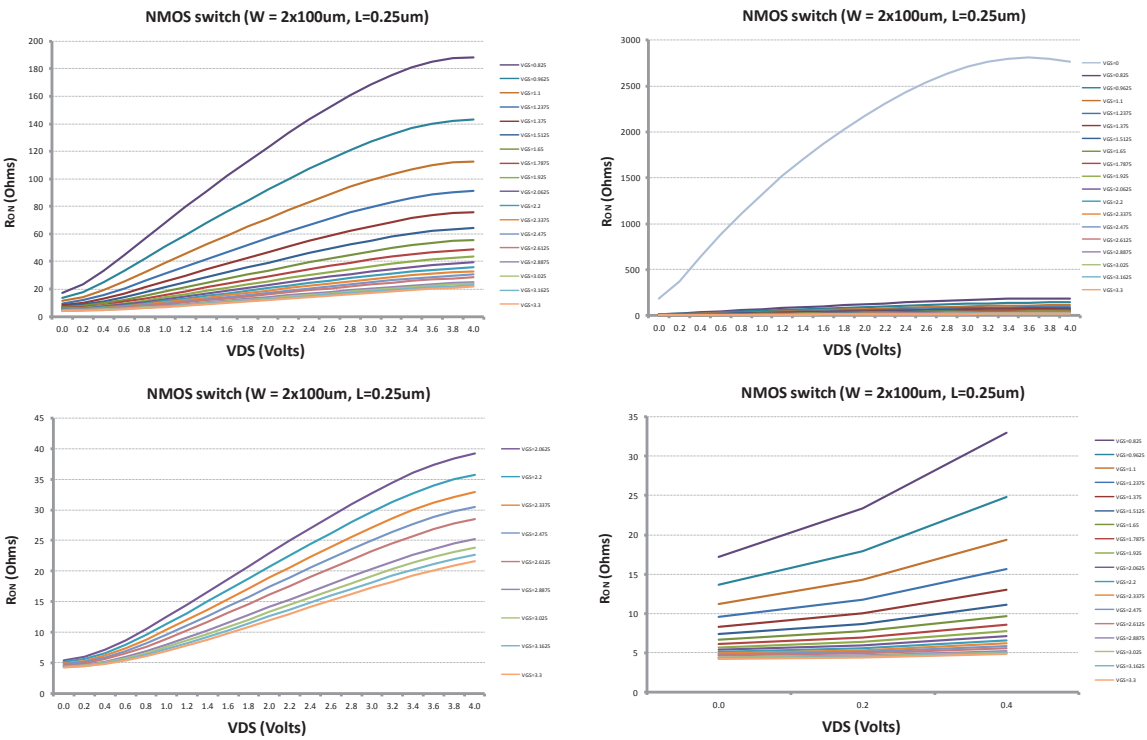

Figure 6.20: Mixer nMOSFET switch ON resistance R_{ON} for different values of V_{GS} and V_{DS}

where, T_{LO} is the fundamental time-period of the LO waveform.

This switched capacitance presents a relatively high impedance node, giving lesser incentive for the currents from I channel to leak into the Q channel and vice-versa, rather than into the much smaller RF port load. Any voltage that develops at the RF node owing to the leakage currents is observed at the IF wanted and image frequencies (see (6.29)).

Ignoring higher odd-order harmonics for simplicity, the voltage developed across the RF load is given by

$$v_{\mathrm{RF}}(t) = \left(\frac{2}{\pi} i_{\mathrm{IF}}(t)\cos(\omega_{\mathrm{LO}}t) * z_{\mathrm{RF}}(t)\right) \tag{6.28}$$

where $*$ indicates the convolution function.

If we consider that voltages and currents across only one of the Mixer's switches, we see that owing to the poor reverse isolation of the switch, the voltage at RF node is visible at the IF node due to the same LO switch action. In other words, if the RF load implements a low-pass function, this is frequency translated to IF. This is evident from (6.29) after having incorporated (6.28) into the second term.

$$v_{\mathrm{IF}}(t) = i_{\mathrm{IF}}(t).R_{\mathrm{ON}} + \left(\frac{2}{\pi} i_{\mathrm{IF}}(t)\cos(\omega_{\mathrm{LO}}t) * z_{\mathrm{RF}}(t)\right)\frac{2}{\pi}\cos(\omega_{\mathrm{LO}}t) \tag{6.29}$$

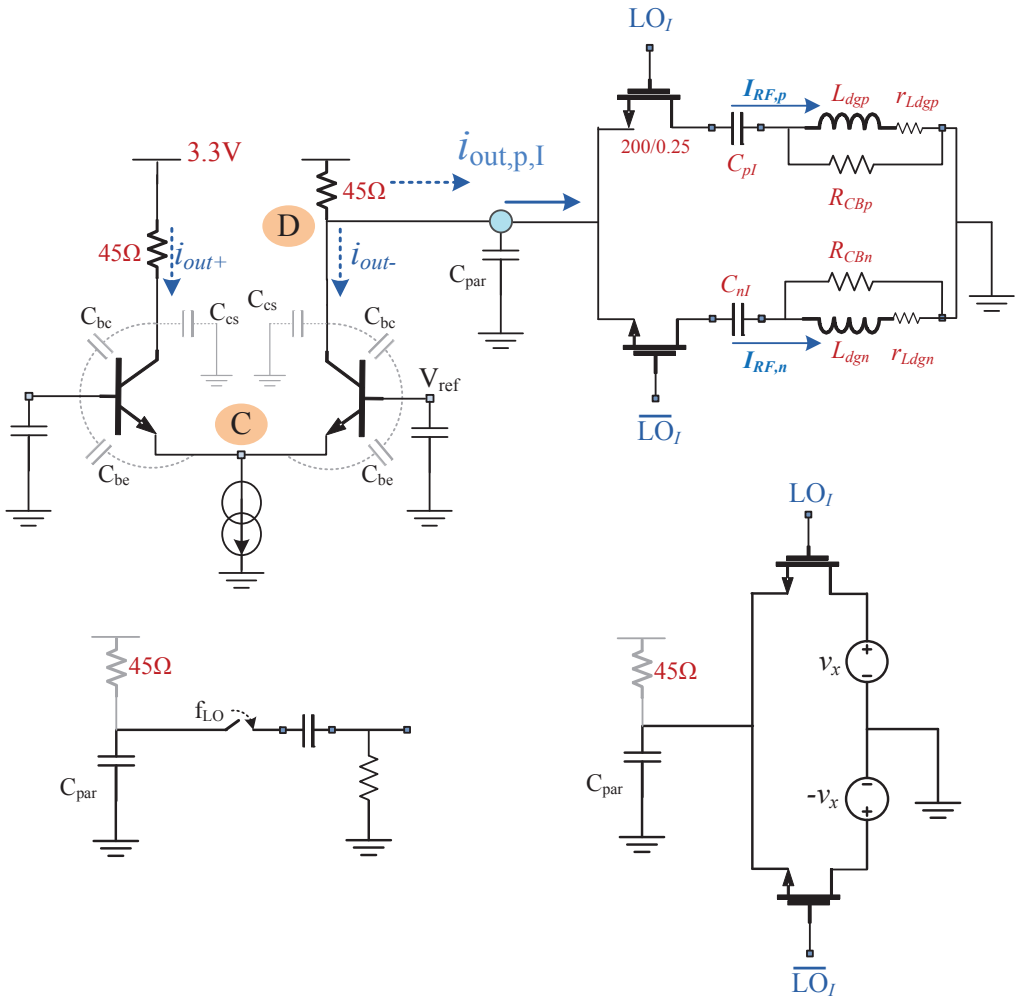

Figure 6.21: Impedance at the output of the Mixer looking back towards the source

where $i_{\mathrm{IF}}(t)$ is the IF signal current, $z_{\mathrm{RF}}(t)$ is the impedance at the RF node, ω_{LO} is the fundamental frequency of the LO square wave and $*$ represents the convolution operation. Although, R_{ON} is also a time varying quantity, by assuming a fixed amplitude signal (for simplicity) and ignoring LO harmonics, the switches could appear as having a fixed resistance, given the LO frequency and can be represented by a constant term. Essentially, the IF signal current develops a voltage across the RF node due to the switching action, at the LO frequency and its odd harmonics. Due to the fact that there is little reverse isolation across the Mixer RF and IF ports, this voltage is translated in frequency (across $n\omega_{\mathrm{LO}}, \forall$ odd n.

Further analysis of the above equation (see Appendix D, Section D.1) reveals that at the input frequencies (ω_{IF}), the impedance observed is that of the R_{ON} of the mixer and the RF impedance Z_{RF} (see Section 6.3.3,) at ω_{RF} and also $\omega_{\mathrm{IF}} - \omega_{\mathrm{LO}}$.

The I and the Q channels combine currents at the RF node. If the impedance at this

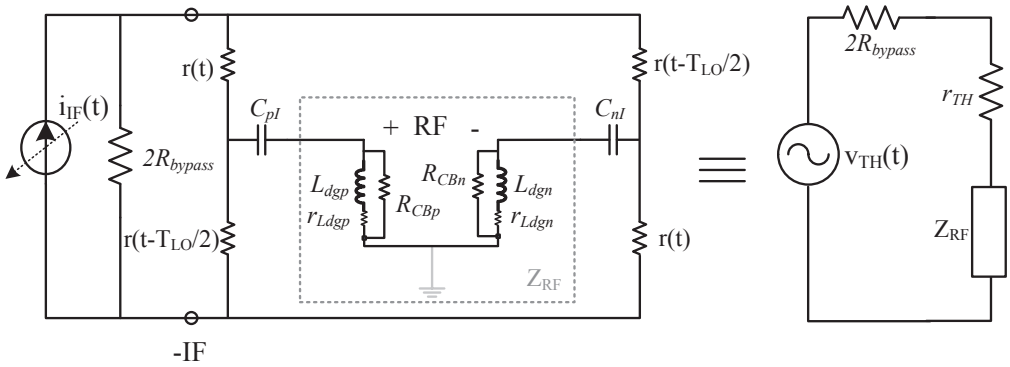

Figure 6.22: Time varying conductance of the switches and its Thevenin equivalent circuit

node is designed to be sufficiently low, this, together with the small fraction of I↔Q current leakage (see Figure 6.21) ensures that any voltage that develops at this node (and which is translated to the IF node by the LO action, as indicated above) is small enough to cause only minimal disturbance at the IF node. The fraction of leakage current can be determined from the current divide ratio. Maintaining the RF node at low impedance has other benefits, as will be pointed out shortly.

We could consider the switches to be time-varying resistances $r(t), r(t - T_{\mathrm{LO}}/4), r(t - T_{\mathrm{LO}}/2), r(t - T_{\mathrm{LO}}/2 - T_{\mathrm{LO}}/4)$ which correspond to the four phases of the LO signal under ideal and well-matched conditions. The Figure 6.22 illustrates the equivalent circuit of the Mixer together with the RF load.

$$v_{\mathrm{TH}} = \left[\frac{r(t) - r(t - \frac{T_{\mathrm{LO}}}{2})}{r(t) + r(t - \frac{T_{\mathrm{LO}}}{2})}\right] v_{\mathrm{IF}} \tag{6.30}$$

$$r_{\mathrm{TH}} = \frac{r(t) + r(t - \frac{T_{\mathrm{LO}}}{2})}{2} \tag{6.31}$$

The dimensionless multiplicative factor in (6.30) represents a mixing function which depends on the LO drive and the DC bias voltage on the Gates. The resistances $r(t), r(t - T_{\mathrm{LO}}/4), r(t - T_{\mathrm{LO}}/2), r(t - T_{\mathrm{LO}}/2 - T_{\mathrm{LO}}/4)$ are in fact different values of R_{ON} of the switches depending on their respective overdrive voltage, in the manner represented in (6.26), where

$$V_{\mathrm{G}} = \begin{cases} V_{\mathrm{LO,DC}} + A_{\mathrm{LO}}\left(\frac{1}{2} + \frac{2}{\pi}\Sigma_{n=0}^{\infty}\frac{(-1)^n}{2n+1}\cos((2n+1)\pi f_{\mathrm{LO}}t)\right) & \text{Phase } 0^\circ, V_{\mathrm{LO}_{\mathrm{I}}^{+}} \\ V_{\mathrm{LO,DC}} + A_{\mathrm{LO}}\left(\frac{1}{2} - \frac{2}{\pi}\Sigma_{n=0}^{\infty}\frac{(-1)^n}{2n+1}\cos((2n+1)\pi f_{\mathrm{LO}}t)\right) & \text{Phase } 180^\circ, V_{\mathrm{LO}_{\mathrm{I}}^{-}} \\ V_{\mathrm{LO,DC}} + A_{\mathrm{LO}}\left(\frac{1}{2} + \frac{2}{\pi}\Sigma_{n=0}^{\infty}\frac{(-1)^n}{2n+1}\cos((2n+1)\pi f_{\mathrm{LO}}t - \frac{\pi}{2})\right) & \text{Phase } 90^\circ, V_{\mathrm{LO}_{\mathrm{Q}}^{+}} \\ V_{\mathrm{LO,DC}} + A_{\mathrm{LO}}\left(\frac{1}{2} - \frac{2}{\pi}\Sigma_{n=0}^{\infty}\frac{(-1)^n}{2n+1}\cos((2n+1)\pi f_{\mathrm{LO}}t - \frac{\pi}{2})\right) & \text{Phase } 270^\circ, V_{\mathrm{LO}_{\mathrm{Q}}^{-}} \end{cases} \tag{6.32}$$

and $V_{\mathrm{LO,DC}}$ is the DC level on the Gates and A_{LO} is the amplitude of the LO voltage. The voltage at the Source terminal, V_S, is given by (6.29). The IF signal current $i_{\mathrm{IF}}(t)$ could be

a sum of several cosines of varying amplitudes.

$$i_{\mathrm{IF}}(t) = \sum_{n=1}^{N} I_{\mathrm{IF}}.\cos(\omega_{\mathrm{IF}} - n\Delta\omega_{\mathrm{IF}})t + I_{\mathrm{IF}}\cos(\omega_{\mathrm{IF}} + n\Delta\omega_{\mathrm{IF}})t \text{ for 'N' tones.} \tag{6.33}$$

where, $\Delta\omega_{\mathrm{IF}}$ is the frequency separation between a pair of tones. We convert the Thevenin network into a Norton equivalent for the purpose of determining the RF current, arriving at

$$i_{\mathrm{IF}}(t) = -v_{\mathrm{IF}}(t) * \mathcal{F}^{-1}\left(\frac{1}{2Z_{\mathrm{bypass}}}\right) \tag{6.34}$$

where, Z_{bypass} is the (frequency domain) bypass impedance (bias resistance together with any parasitic capacitances) at the output of the attenuator stage (see Figure 6.13). The operator $*$ is the convolution operator and $\mathcal{F}^{-1}$ is the inverse Fourier transform. The inverse Fourier of the impedances is used because we are interested in the steady-state response to a sinusoidal input.

Referring to Figure 6.22, if we assume $m(t)$ to be the multiplicative mixing function of (6.30), then from (6.30), (6.44) and (6.34) we can express the resulting RF current $i_{\mathrm{RF}}(t)$ in the following form (see (6.35)). It is evident that the mixing function has no DC component and is periodic with a period $T_{\mathrm{LO}} = \frac{1}{f_{\mathrm{LO}}}$. We are therefore able to arrive at a similar expression as in [114].

$$\begin{aligned} i_{\mathrm{RF}}(t) &= v_{\mathrm{TH}} * \mathcal{F}^{-1}\left(\frac{1}{Z_{\mathrm{RF}} + r_{\mathrm{TH}}}\right) \\ &= \left[v_{\mathrm{IF}} \cdot \left(\frac{r(t) - r(t - \frac{T_{\mathrm{LO}}}{2})}{r(t) + r(t - \frac{T_{\mathrm{LO}}}{2})}\right)\right] * \mathcal{F}^{-1}\left(\frac{1}{Z_{\mathrm{RF}} + r_{\mathrm{TH}}}\right) \\ &= \left[-\left(i_{\mathrm{IF}} * 2\mathcal{F}^{-1}(Z_{\mathrm{bypass}})\right) \cdot \left(\frac{r(t) - r(t - \frac{T_{\mathrm{LO}}}{2})}{r(t) + r(t - \frac{T_{\mathrm{LO}}}{2})}\right)\right] * \mathcal{F}^{-1}\left(\frac{1}{Z_{\mathrm{RF}} + \frac{r(t) + r(t - \frac{T_{\mathrm{LO}}}{2})}{2}}\right) \end{aligned} \tag{6.35}$$

where, Z_{RF} is the (frequency domain) differential impedance at the Drains of the switches, which is a combination of the RF port impedance (see Section 6.3.3) and the two DC blocking capacitances C_{pI}, C_{nI}. At the RF port however the I and the Q branch currents add in anti-phase for image rejection, to give twice the RF current expressed above.

Calculating the exact current gain of the Mixer is more involved as it depends on the bias conditions of the switch and the relative voltages between the LO and IF voltages, as will be evident in 6.3.2. The calculation involves taking the Fourier transform of the above expression, evaluated at the fundamental LO frequency f_{LO} (and its harmonics). It is useful to note that with good matching, the mixing function $m(t) = -m(t + T_{\mathrm{LO}}/2)$ therefore only contains odd-order harmonics of f_{LO}, while the even-order components and the DC are canceled out. If we assume that the RF port impedance is significantly larger than that of the switch, and the LO drive is an ideal square wave (i.e. $\frac{\Delta v_{\mathrm{LO}}(t)}{\Delta t} = \infty$) much larger than the IF signal, operating without the DC bias, $m(t)$ evaluates approximately to a square wave (see Figure 6.23 and Figure 6.47). The conversion gain expression G_{c} evaluates to the coefficients

of $m(t)$,

$$G_c \cong \frac{2}{\pi}\left(\frac{\sin(\pi\Delta f_{LO})}{\pi\Delta f_{LO}}\right) \tag{6.36}$$

which is the typical expression for Mixer gain, used in literature.

The authors of [115] provide an expression for the mixer gain based on similar biasing conditions, as given in (6.37).

$$G_c = \begin{cases} \frac{\arcsin(r)/r+\sqrt{1-r^2}}{\pi} & 0 \leq r \leq 1 \\ \frac{1}{2r} & 1 \leq r < \infty \end{cases} \tag{6.37}$$

where $r = |V_{Th} - V_{LO,DC}|/A_{LO}$. Using this expression, the Mixer gain was simulated to be $-4.41dB$, which is in agreement with the above equation.

The Mixer is arranged in the make-before-break configuration where the $V_{LO,DC} > V_{Th}$. This preconditioning enables a smaller LO signal swing to adequately turn ON the FET switch at the Gate in the presence of large-signal modulation at the Source (or Drain) terminal(s). The is advantageous and important because in the event that the LO signals have a finite rise-time, complementary phases of the LO can cause all switches to momentarily remain in the 'OFF' state with a very large voltage swing at the IF terminal. This can be particularly troubling for the reliability of the FET switches. This preconditioning however also implies that with overlapping LO waveforms, complementary paths can be turned 'ON' momentarily leading to the noise translating to the output, much like the offset voltage [18] in a differential pair, but a slowly varying quantity. This is treated further in the section on Mixer noise below. The Figure 6.23 depicts the dimensionless the switching function

6.3.1 Linearity and Noise performance

When the Mixer is 'ON', the FET (nMOS) switches operate in the triode region due to the small V_{DS}. This low resistance channel is preferred to the parasitic capacitances, for signal conduction. As a result, the coupling through the substrate and the LO paths are minimal and can be ignored. When the Mixer is in the 'OFF' state, the parasitic capacitances become preferred leakage paths, resulting in a deterioration of isolation between the three ports. The use of the an nMOS with an isolated well and surrounded by deep-trenches, as depicted in Figure 6.24, helps reduce the impact of some of these parasitic capacitances to a certain degree.

This construction allows to independently control the bias voltages on the four terminals of the FET. By appropriately choosing the relative biasing voltages (i.e. the Bulk relative to the others), it is possible to reduce the width of the depletion region and thereby the capacitances (C_{sb} and C_{db}) associated with the Bulk. The low voltage swing across the Mixer by design also works in its favour, as it reduces any coupling-induced fluctuation of the Bulk. For this to work, the Bulk (p-well) terminal needs to be biased at a voltage lower than the Drain/Source terminals of the Mixer. A Buried-n-well 'BN' isolates the Bulk (p-well)

[18] The input referred flicker noise in each of the switches are not correlated to each other and can be analysed by principle of superposition.

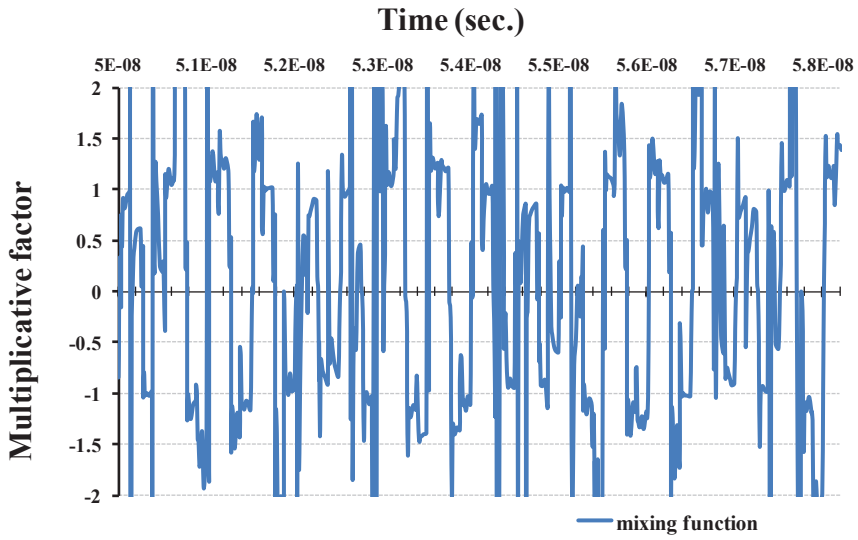

Figure 6.23: The actual simulated mixing function of the double-balanced mixer based on the (dimensionless) multiplicative factor of (6.30)

from the Substrate and is biased at the highest available DC voltage in order to ensure better isolation.

Although the DC common-mode voltage at the IF load increases with the control voltage reaching V_{cc} at maximum attenuation (when the current across the load is negligible), this does not present an issue to maintaining the required overdrive across the FET switch because the signal amplitude also reduces in a logarithmic manner with increasing control voltage, limiting the swing on the Source/Drain terminals with respect to the Gate.

The leakage caused by the C_{gs} and C_{gd} [19]and the increased load on the LO drive remain, to be traded off against the R_{ON} of the nMOS. From simulations however, their contributions to non-linearity were negligible as the Mixer linearity well above the rest of the circuit and thereby ignored.

The size of the Mixer switches also influences the noise performance, other forms of non-linearity and the power consumption associated with the mixer. Although Mixer linearity is a two-port definition it depends significantly on the third port, the LO drive. The Mixer's compression and linearity performance is, in large part, due to the LO signal strength and biasing. This is applicable also to active mixers where the bias and LO drive of the 'Gilbert' stage determines the linearity due to compression in the load and the bottom stages. An exercise in determining the power factor of the Mixer is envisioned for further development of this work. Passive mixers operate in the triode region when turned On. From the perspective

[19]These capacitances include the bias dependent gate-oxide parasitic capacitances $C_{\mathrm{gs},p} = C_{\mathrm{gd},p} = 1/2C_{\mathrm{ox}}WL$ and the bias independent overlap capacitances $C_{\mathrm{gs,ov}} = C_{\mathrm{gd,ov}} = C_{\mathrm{ox}}WL_D$, where C_{ox} is the capacitance per unit gate area and W, L, L_{D}, the channel width, length and length of the diffusion overlap region, respectively.

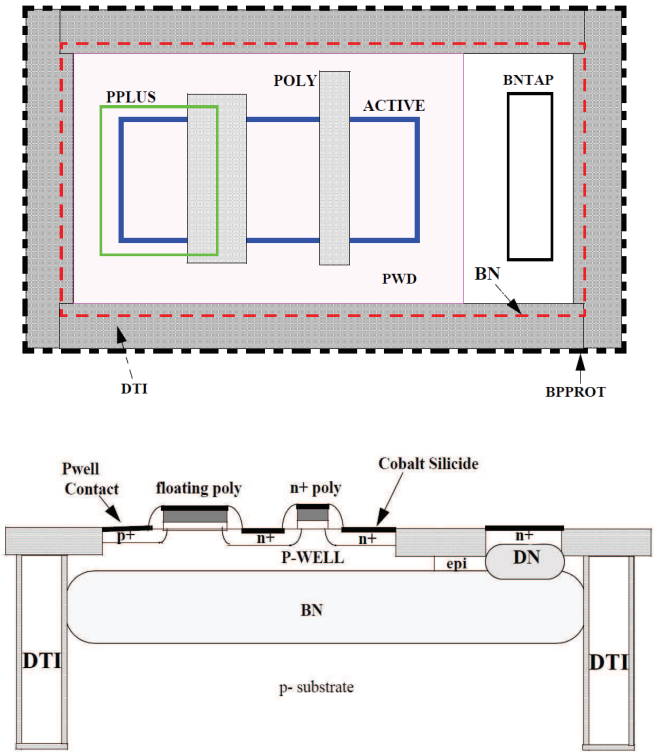

Figure 6.24: Block diagram of the QUBiC4 Isolated nMOS transistor showing the isolating Deep-Trench and the isolated Bulk (*Courtesy: NXP Semiconductors*)

of linearity, choosing a larger FET (for low R_{ON}) pushes the device further into triode, given the same overdrive ($V_{\mathrm{ov}} = V_{\mathrm{GS}} - V_{\mathrm{Th}}$). Hence for a first order analysis, a large overdrive or a larger device could improve linearity, more so because the V_{DS} modulation of the ON resistance of the FET switch is minimised. This is discussed further in Section 6.3.2.

Non-linearity in a passive MOSFET Mixer that is driven by a square-wave LO is mainly due to combinations of the following:

- non-linear parasitic capacitances C_{gs}, C_{gd} and the C_{db},
- finite rise and fall time of the LO waveform,
- and the non-linear I_{DS} versus V_{DS} relationship

Most of these capacitances are bias dependent, so, reducing the (modulating) voltages across these devices significantly reduces their non-linear contribution. Typically, for short channel length devices, the non-linear capacitances are relatively smaller and hence, their contribution to non-linearity is well below the other non-linear components in the circuit, with their influence growing with increasing signal strength. Their contribution is thereby ignored. A significant source of non-linearity is due to the non-linear (non-square-law) relation [103,

116,117] between the Drain current I_{DS} and the Drain-Source voltage V_{DS} of an nMOS device operating in strong inversion, biased in the triode region. This is known to be of the form

$$\begin{aligned} I_{\mathrm{DS}} &= \mu_{\mathrm{n}} C_{\mathrm{OX}} \frac{W}{L} \left\{ \left[(v_{\mathrm{G}} - V_{\mathrm{FB}} - 2\phi_{\mathrm{F}}) \cdot (v_{\mathrm{D}} - v_{\mathrm{S}}) - \frac{1}{2}(v_{\mathrm{D}}^2 - v_{\mathrm{S}}^2) \right] \right. \\ &\qquad \left. - \gamma \frac{2}{3} \left[(v_{\mathrm{D}} - 2\phi_{\mathrm{F}})^{\frac{3}{2}} - (v_{\mathrm{G}} - 2\phi_{\mathrm{F}})^{\frac{3}{2}} \right] \right\} \\ &= \Sigma_{k=0}^{\infty} (a_k V_{\mathrm{DS}}^k) \end{aligned} \tag{6.38}$$

where V_{FB} is the flatband voltage, γ is the body-effect constant and ϕ_{F} is the Fermi level of Silicon. V_{DS} in the second part of the equation is the result of the incident LO and IF waveforms [118, 119]. This is discussed in further detail in [120–122]. The relationship between the RF current $i_{\mathrm{RF}}(t)$ and its bias conditions is evident from Figure 6.22, (6.26) and (6.35). Minimising V_{DS} across the switch will evidently reduce this aspect of Mixer non-linearity. The large size (low R_{ON})of the Switches and the low (Mixer-) RF port impedance Z_{RF} facilitate this.

6.3.2 LO Drive

Several types of LO drives exist. For its several advantages in this case a square wave LO waveform is preferred over a sinusoidal drive. When both device and drive strength in the double-balanced Mixer are well matched, a square wave ensures zero or minimum common mode, thereby reducing second-order harmonic terms in the output. This is because the simultaneous turn-on time for any two complementary switches is minimized by minimizing the low-high and high-low transitions in the LO voltage signal. A square wave also ensures better linearity performance as it minimises the modulation of the switching transition point by the large-signal at the IF port[20]. It has been well established from previous works of [120–122] that the IF (large) signal *phase*-modulates the switching function or the mixing function. This is because the instant or more practically, the region of switching between ON and OFF, which occurs when the condition $V_{\mathrm{GS}} > V_{\mathrm{Th}}$ is satisfied across the FET switch, is actually modulated at a rate equal to the difference in frequency of LO and IF port signals. This extent of modulation depends on the ratio of the IF and LO signal amplitudes and is specified by a modulation index k which carries the depth of modulation as a function of their amplitudes. The extent of interference can be decreased by reducing the modulation index, i.e., by providing the LO swing with sharper transition times, thus reducing the dependency on the IF signal. This is achieved easily by increasing the amplitude of the LO signal swing[21]

Having a rail-to-rail signal in the LO drive path also rejects any variation in common-mode gain between the different output paths of the Poly-Phase-Filter (PPF) (see Section 6.4). This

[20] The fact that the fundamental sinusoid in the Fourier expansion of a square wave has an amplitude which is $4/\pi$ times that of the square wave, gives it better performance than a sinusoidal LO drive of matching amplitude. Larger amplitude sinusoids have sharper zero-crossing transitions, assuming zero DC offset.

[21] The large IF port signal also deteriorates the Mixer linearity, as a function of the input signal swing. This for of distortion has been previous expressed as a dynamic range, $\mathrm{DR} = 20\log\left(\frac{V_{\mathrm{Gate}}/T_{\mathrm{LO}}}{V_{\mathrm{Source}}/T_{\mathrm{IF}}} - 4\right)\mathrm{dB}$, in [123]. However, we observed from simulation results that the Switch linearity is significantly better than the other blocks, thereby having little the contribution to the overall IP3.

benefits image-rejection because an offset in any of the switching pairs results in a greater ON (or OFF) time for that switch, which impacts the duty-cycle (half-wave symmetry), resulting in LO signal harmonics at the RF port that do not cancel out by differential signaling. Asymmetric *ON* time for one of the transistors also brings common-mode noise from the Gate drive (i.e.LO noise), and also noise from the IF port, albeit somewhat attenuated and translated in frequency. The analysis (see [124]) of this is very similar to that of a differential-pair and is therefore not dealt with in further detail.

A higher voltage to charge or discharge will lead to sharper(shorter) turn-ON or turn-OFF time, respectively [22]. This implies duty cycle errors and therefore more harmonics apart from the usual odd-harmonics of the square wave LO, will creep in. However, having good common-mode rejection will imply good rejection of even-harmonics. For this reason, the LO is AC coupled to the Mixer and the signal is driven rail-to-rail in order to minimise the DC offset and gain errors.

6.3.3 Input Impedance of the Output-Buffer Stage

The RF port of the Mixer is terminated by an impedance Z_{RF} composed of an RLC load, with a large series decoupling capacitor ($C_{\mathrm{p}}, C_{\mathrm{n}} \approx 10\mathrm{pF}$) in series with a parallel R-L network.

$$\begin{aligned} Z_{\mathrm{RF}}(s) &= \frac{C_{\mathrm{p}} L_{\mathrm{dg}} R s^2 + L_{\mathrm{dg}} s + R}{C_{\mathrm{p}} L_{\mathrm{dg}} s^2 + C_{\mathrm{p}} R s} \\ s &= \frac{\pm\sqrt{L_{\mathrm{dg}}^2 - 4 C_{\mathrm{p}} L_{\mathrm{dg}} R^2} - L_{\mathrm{dg}}}{2 C_{\mathrm{p}} L_{\mathrm{dg}} R} \end{aligned} \tag{6.39}$$

where R is actually the input impedance of the buffer that makes up the output stage. The RLC load has a high-pass transfer function, with a low R value extending the bandwidth. The Q factor of the inductor L_{dg} together with the capacitance determines the sharpness of the response. To implement the R, a trans-impedance buffer was considered. This is because a net voltage-gain is desired at the output (converting it into a net power-gain) with a matched 50Ω output load. Two output stages were compared for this purpose - a Common-Base (CB) amplifier and a Common-Emitter (CE) with dual-feedback. The input impedance of the Common-Base stage is given by (6.40) [23]

$$\begin{aligned} Z_{\mathrm{in,CB}} = &\frac{1}{\frac{1}{r_\pi} + sC_\pi + g_{\mathrm{m}}} \left(1 + \left(r_{\mathrm{bb}} + \frac{R_{\mathrm{B}} s C_{\mathrm{B}}}{R_{\mathrm{B}} + sC_{\mathrm{B}}}\right)\left(\frac{1}{r_\pi} + sC_\pi\right)\right) \\ &+ \frac{r_{\mathrm{o}}(1 + g_{\mathrm{m}} Z_s')}{1 + g_{\mathrm{m}} Z_{\mathrm{mixer,out}} Z_{\mathrm{s}}'(1 - Z_{\mathrm{L}})} \end{aligned} \tag{6.40}$$

where, $Z_{\mathrm{s}}' = Z_{\mathrm{mixer,out}} || Z_{\mathrm{E}} || Z_\pi$, $Z_{\mathrm{mixer,out}}$ is the output impedance of the IQ Mixers as illustrated in Figure 6.21, Z_{E} is the impedance of the degeneration inductor L_{dg}, Z_{L} is the

[22] This could potentially worsen a non-linearity phenomenon not analysed here. Given the non-linear parasitic capacitances associated with the Gate, large voltage fluctuations could yield large current fluctuations at the tail-node, i.e., $i_{\mathrm{Cp,tail}} = C_{\mathrm{gs}} \frac{d(v_{\mathrm{LO}} - v_{\mathrm{IF}})}{dt}$, proportionally worsening the linearity

[23] The feedback capacitor across the Collector and Emitter terminals, C_γ should appear (with a CE stage voltage-gain) [125], in parallel with the $Z_{\mathrm{in,CB}}$, but we ignore this for simplicity as the capacitance was of small value when simulated.

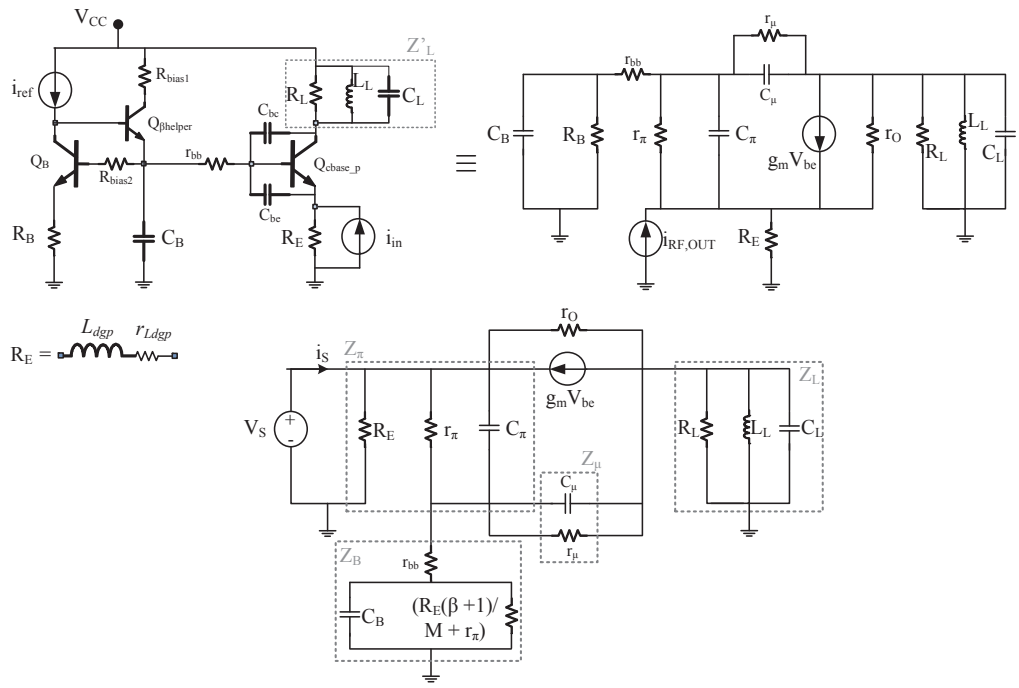

Figure 6.25: Small-signal representation of the Common-Base amplifier showing the output balun and the bias network.

load impedance at the Collector (discussed in 6.5.1), r_{bb} and r_{o} are the resistance of the Base terminal and small-signal output resistance of the NPN transistor, respectively, R_{B} and C_{B} make up the impedance of the bias circuit of the Common-Base amplifier, as shown in Figure 6.25.

Closer examination of the high-frequency response using the *Open-Circuit Time Constant* analysis reveals the high-frequency cutoff to be

$$f_{\mathrm{H}} = \frac{1}{2\pi C_{\pi}(\frac{r_{\pi}}{\beta_{\mathrm{F}}}||Z_{\mathrm{s}}||Z_{\mathrm{E}}) + C_{\mu}(Z_{\mathrm{c}}||Z_{\mathrm{L}})} \tag{6.41}$$

where, Z_{s} is the impedance of the generator, Z_{E} is the degeneration impedance at the emitter and Z_{c},Z_{L} are the collector and load impedances respectively.

Similarly, the input impedance of the CE stage with series-series (Emitter degeneration) and shunt-shunt feedback is given by

$$Z_{\mathrm{in,cew/fb}} = \frac{1}{Y_{11,\mathrm{cew/fb}} + \frac{Y_{12,\mathrm{cew/fb}}Y_{21,\mathrm{cew/fb}}}{Y_{22,\mathrm{cew/fb}}+Y_{\mathrm{L}}}} \tag{6.42}$$

Although the two stages were not compared with respect to their noise performances, a closer look at the values of impedance would reveal that the CB stage achieves a lower impedance, higher power-gain and a greater bandwidth than the CE-stage with dual feedback,

for the same power consumption, under the assumed constraints. The low impedance on the Base terminal creates a *cold* node preventing modulation (fluctuation) of the Base thereby reducing the impact of the inherently non-linear C_{bc} junction capacitor. The CB stage also allows to exploit the higher breakdown voltage BV_{CEO}, one effect of which is a reduced non-linear avalanche current [24], in this configuration. The relatively higher linearity of the CB stage operating in current mode has been shown to be more linear than a CE stage in previous works, better linearity [101]. The design of the CB stage will be discussed in further detail in the next section.

Reverting to the issue of low-impedance at the RF node of the mixer, having a low value benefits reverse isolation, as indicated above, while also ensuring a low current-loss at IF Although it has been shown that increasing the RF port impedance increases the loss at the IF output stage (see Section 6.2), it also brings benefits by reducing the (voltage domain) non-linearities associated with the Mixer switches, by dominating the voltage drop when looking into the Mixer's IF port. The Mixer and the RF port impedance form a current divide together with the output impedance of the attenuation stage as show in Figure 6.26. The output impedance (resistance) of the attenuator-stage is chosen with the objective of minimising the loss while also optimising the dynamic range ($IM3_{\mathrm{dB}} - Noise_{\mathrm{dB}}$) of the gain/attenuation stage. The gain/loss at the IF load can be determined according to the (6.44).

$$\begin{aligned} i_{\mathrm{IF}}(f) = i_{\mathrm{IF}}(f) - i_{z_{\mathrm{bypass}}}(f) &= i_{\mathrm{IF}}(f) * -\frac{Z_{\mathrm{bypass}}}{Z_{\mathrm{bypass}} + Z'_{\mathrm{on}}} \\ A_i &= -20log_{10}\left(\frac{Z_{\mathrm{bypass}}}{Z_{\mathrm{bypass}} + Z'_{\mathrm{on}}}\right) \end{aligned} \tag{6.44}$$

where, A_i is the current gain (loss), i_{IF} is the output current from the linear-in-dB attenuator network, Z'_{on} is a combination of the $R_{\mathrm{ON},h}$ of the mixer corresponding to h^{th} harmonic the LO waveform and the RF port impedance Z_{RF} together with the decoupling capacitors, referred to the IF port. The RF load (see Figure 6.26 comprises of a series capacitor ($10pF$) together with a parallel combination of an inductor ($L = 2.67$nH, $Q = 9.84$) and the input impedance of the Common-Base (CB) stage. With the low input impedance of the CB stage amplifier (see (6.40)), the RF current from the Modulator finds a preferred path to ground. The inductance value (higher than the CB stage $Z_{\mathrm{in,cb}}$) was so chosen, as to provide adequate degeneration (Z_E) for the amplifier, while still maintaining enough headroom at the Collector node.

[24] [99]The Avalanche mechanism is illustrated by a current source between the Collector and the Base terminals. The magnitude of the current is given by the expression,

$$\begin{aligned} I_{\mathrm{av}} &= I_{\mathrm{in}}(M-1) \\ M &= \frac{1}{1-\left(\frac{V_{\mathrm{CB}}}{BV_{\mathrm{CBO}}}\right)^n} \\ BV_{\mathrm{CEO}} &\approx \frac{BV_{\mathrm{CBO}}}{\beta_{\mathrm{F}}^{\frac{1}{n}}} \end{aligned} \tag{6.43}$$

where, M is a multiplicative factor whose magnitude is dependent on the electric field intensity, i.e., the CB voltage relative to the CB breakdown voltage, β_{F} is the forward current gain and $n \approx 4$.

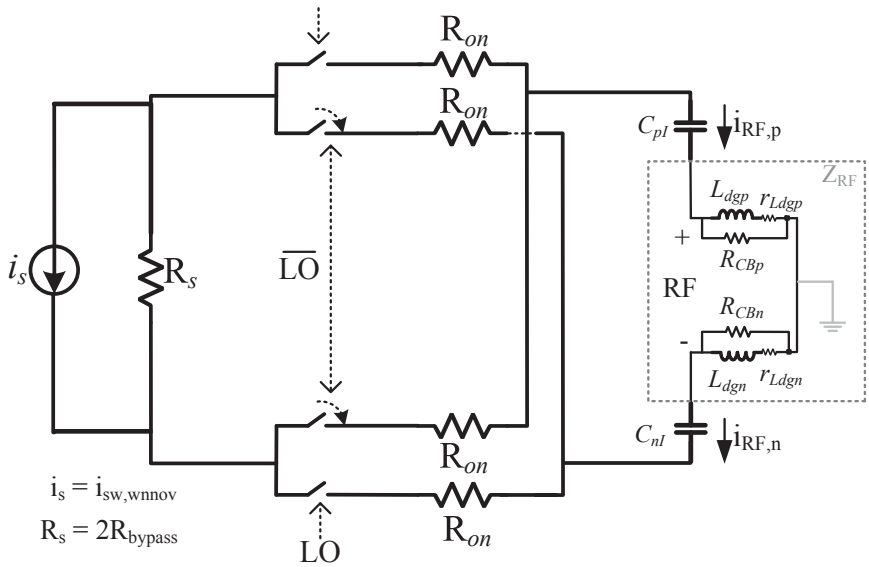

Figure 6.26: Current division at the output of the attenuation stage impacting the overall current gain

6.3.4 Noise Performance

The Mixer has several mechanisms by which it contributes noise at the output port. While some of these mechanisms are indirect, attributed to the frequency translation mechanism of the Mixer, others are more direct, attributed to the noise of the Mixer itself or from the multiple ports that connect to it. We discuss some of these noise transfer mechanisms, beginning with the Flicker noise which is dominant at low frequencies and appears as sideband distortion on the carrier.

Flicker noise exists in the presence of a current flow through the MOS. If the impedance at the Source and Drain terminals is unequal, the large overlap capacitances of the Switch create a potential difference across the nMOS channel producing an RF (i.e. cyclostationary) current through it. Flicker noise in the FET is expressed as an input referred Gate voltage $\overline{v_{\mathrm{sw,fn}}} = \sqrt{K_{\mathrm{f}}/WLC_{\mathrm{ox}}f}$, that is valid for all regions of operation of the device. In the current-commutating passive Mixer, the flicker noise at each switch randomly modifies or modulates the instant of ON/OFF transition. This is because the Gate-referred flicker noise appears in series with the Gate-Source voltage (V_{GS}), with the Gate bring driven by a large, quick-transiting LO signal and the Source floating along with a smaller IF signal. The flicker noise is similar in behaviour to a slowly varying offset voltage in a diff-pair. Due to the nature of the make-before-break[25] biasing on the Gate of the switches, the flicker noise voltage leaks from

[25] In this configuration, the LO common-mode voltage exceeds the threshold voltage of the MOSFET and an LO/$\overline{\mathrm{LO}}$ overlap causes the complementary phase switches to be On at the same time, resulting in diff-pair like amplification of Gate referred noise, to the output. In the break-before-make configuration, where the LO common-mode voltage is below the threshold voltage, this is less likely to occur, although the LO amplitude requirement is increased.

the Mixer through to the RF path. The noise appears momentarily as pulses during regions of overlap, which occurs twice during a single LO cycle. It therefore appears translated in frequency $(2 \cdot \omega_{\mathrm{LO}})$, corresponding to a periodicity $\delta(t + n\frac{T_{\mathrm{LO}}}{2})$, as shown in Figure 6.27.

Assuming an noiseless LO signal, the shift, Δt, in the switching instant is dependent on the flicker noise voltage $v_{\mathrm{fn}}(t)$ and is inversely proportional to the transition slope 'K' (where $K = V_{\mathrm{LO}}(t)/\Delta t$) of the LO signal. Since we are interested in the RF output current of the Mixer due to flicker noise, its value can be calculated (see [124, 126]) as,

$$i_{\mathrm{sw,fno}}(t) = \sum_{n=-\infty}^{\infty} \left(2i_{\mathrm{IF}}(t).\Delta t.\delta(t + n\frac{T_{\mathrm{LO}}}{2})\right) \quad = \sum_{n=-\infty}^{\infty} \left(2i_{\mathrm{IF}}(t).\frac{v_{\mathrm{sw,fn}}(t)}{K}.\delta(t + n\frac{T_{\mathrm{LO}}}{2})\right) \tag{6.45}$$

where, $i_{\mathrm{IF}}(t)$ is given by (6.34), $v_{\mathrm{sw,fn}}(t) = [k_{\mathrm{f}}/(WLC_{\mathrm{ox}}f)\Delta f]^{1/2}$ is the Gate referred flicker noise voltage and T_{LO} is the time period of the fundamental harmonic of the LO. Taking the Fourier transform of the above equation gives,

$$I_{\mathrm{sw,fno}}(f) = \sum_{n=-\infty}^{\infty} \left(\frac{4}{K.T_{\mathrm{LO}}} I_{\mathrm{IF}}(f) * V_{\mathrm{sw,fn}}(f).\delta(f + 2nf_{\mathrm{LO}})\right) \tag{6.46}$$

During the LO/$\overline{\mathrm{LO}}$ overlap in the 'I' phase, both differential pairs (i.e. $\mathrm{I_p}$ and $\mathrm{I_n}$) are On. Consequently, the flicker noise current into the RF port impedance can be calculated as a quadratic sum of the i.i.d. switch noise currents. The flicker noise current from each switch taking into account the current divider is given by,

$$I_{\mathrm{sw,fno,RF,n/p}}(f) = \sum_{n=-\infty}^{\infty} \left(\frac{4}{K.T_{\mathrm{LO}}} V_{\mathrm{IF}}(f) * V_{\mathrm{sw,fn}}(f).\delta\left(f + 2nf_{\mathrm{LO}}\right)\right)^{1/2} \left(\frac{\mathcal{F}(R_{\mathrm{on}}(t))/2}{Z_{\mathrm{RF}} + \mathcal{F}(R_{\mathrm{on}}(t))}\right) \tag{6.47}$$

where, $Z_{\mathrm{RF}} = \mathcal{F}(z_{\mathrm{RF}})$, $R_{\mathrm{on}}(t) = 1/g_{\mathrm{ds}}(t)$ is the modulated switch ON' (channel) resistance and $K = V_{\mathrm{LO}}(t)/\Delta t$, Δt being the width of the pulse shown in Figure 6.27. The sum total of the Mixer flicker noise currents in the 'I' phase is therefore given by,

$$I_{\mathrm{sw,fno,RF}}(f) = 2\sum_{n=-\infty}^{\infty} \left(\frac{4}{K.T_{\mathrm{LO}}} V_{\mathrm{IF}}(f) * V_{\mathrm{sw,fn}}(f).\delta\left(f + 2nf_{\mathrm{LO}}\right)\right)^{1/2} \left(\frac{\mathcal{F}(R_{\mathrm{on}}(t))/2}{Z_{\mathrm{RF}} + \mathcal{F}(R_{\mathrm{on}}(t))}\right) \tag{6.48}$$

The factor of 2 is obtained by quadratically summing (i.e., $\sqrt{1^2 + 1^2 + 1^2 + 1^2}$) all the i.i.d. currents, ignoring any mismatch.

Flicker noise, from the above, does not occur at LO harmonic frequency but at twice the harmonic of the LO frequency in the square-wave as has also been previously analysed for down-conversion Mixers in [124, 126]. For the sake of better understanding, this can easily be compared with the operation of Mixer on the IF signal itself,

$$RF(f) = H(f) * IF(f) \tag{6.49}$$

where, $H(f) = \sum_{n=-\infty}^{\infty} C_{\mathrm{n}} \cdot \delta(f + nf_{\mathrm{LO}})$ represents the mixing function, i.e., in the ideal case,

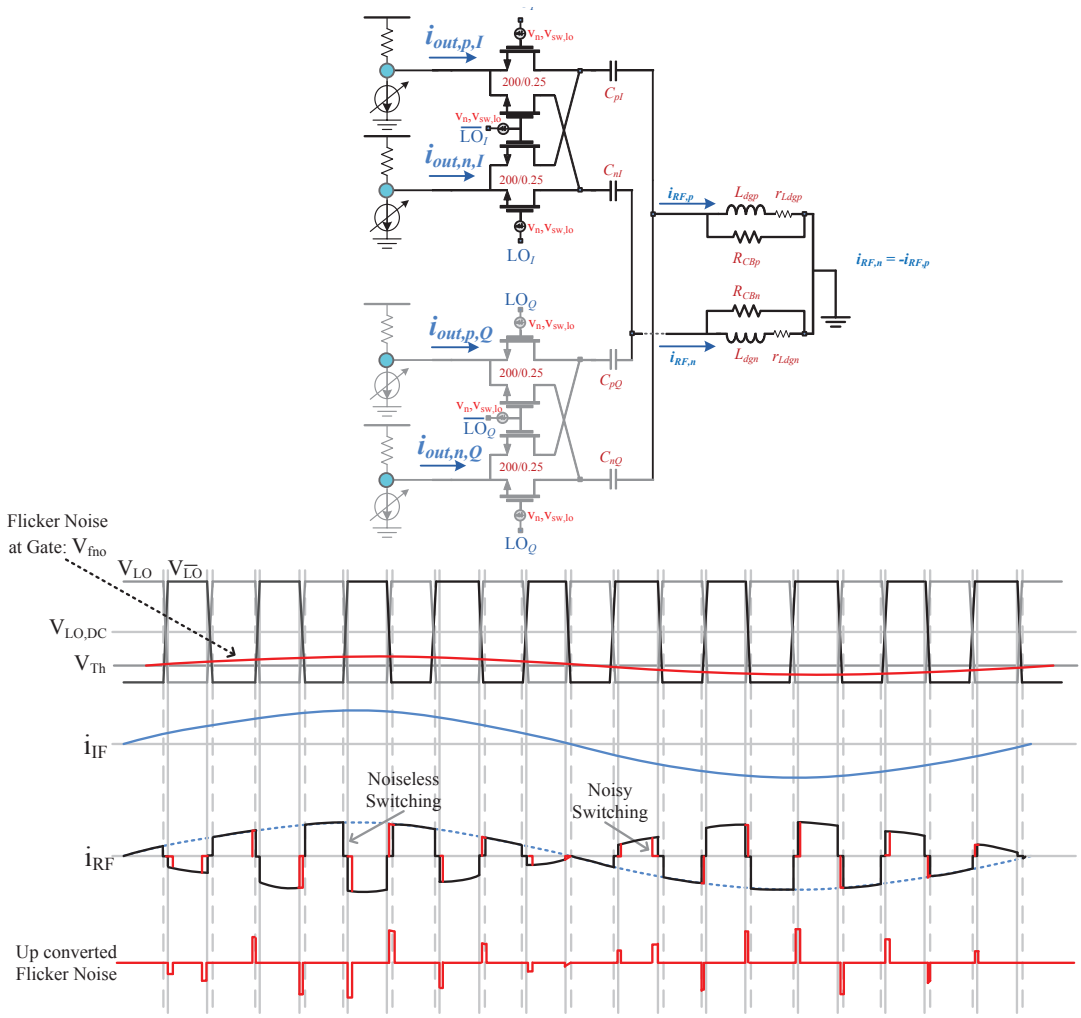

Figure 6.27: Flicker noise during 'ON' overlap in the current-commutating switches

the frequency spectrum of the LO and its harmonics.

$$
\begin{aligned}
RF(f) &= \left[\sum_{n=-\infty}^{\infty} C_{\mathrm{n}} \cdot \delta\left(f + n f_{\mathrm{LO}}\right)\right] * IF(f) \\
&= \sum_{n=-\infty}^{\infty} C_{\mathrm{n}} \int_{-\infty}^{\infty} \delta(f + n f_{\mathrm{LO}}) \cdot IF(f - \sigma) d\sigma \qquad (6.50) \\
&= \sum_{n=-\infty}^{\infty} C_{\mathrm{n}} \cdot IF(f + n f_{\mathrm{LO}})
\end{aligned}
$$

where '$*$' represents the convolution function and C_{n}, the amplitude of the n_{th} harmonic of

the LO. It can be seen that the LO signal translates the input signal $IF(f)$ by nf_{LO} and not $2nf_{\mathrm{LO}}$ as is the case for the flicker noise. [26]

Flicker noise is independent of the bias and is inversely proportional to the Gate area. The noise is minimised by increasing the size of the switches. However, the flicker noise also leaks into the RF path via the switch leakage capacitances mentioned earlier which increase with switch size. Therefore, increasing the size of the switches has a detrimental effect on the noise performance. Hence a tradeoff is necessary here. This highlights another reason why a CE stage with dual-feedback was not preferred for the output stage. The output stage would have a gain function that is inversely proportional to the impedance of the generator. Increasing the size of Mixer FET's would increase the parasitic capacitors which would reduces the value of the switched-capacitor resistance that forms the generator impedance to the CE stage. As a consequence, the signal gain increases; the signal referred to here being the noise. Increasing the LO frequency would have a similar effect due to its relation to the switched-capacitor resistance.

In the triode region operation of the switch, white noise is the major noise mechanism. This arises from the channel material that is resistive. In this region, a continuous channel exists in the presence of a Gate-Source voltage exceeding the threshold, irrespective of the presence of absence of direct current. White noise in a FET is expressed as a current source ($i^2_{\mathrm{sw,wn}}(t) = 4kT\gamma g_{\mathrm{ds}}$) in parallel with the channel resistance, where γ is the excess noise factor of the MOS, g_{ds} is the MOS small-signal conductance[27] in the triode region, k and T are the Boltzmann's constant and absolute temperature, respectively. The switches contribute noise in two states. Firstly, when one of the switches is in the 'ON' state while the complementary path is 'OFF' and secondly, during the 'ON' overlap period explained earlier. We first analyse the gain of this noise current leading to the noise current at the output port. This we can do by the principle of superposition, because they are uncorrelated.

The channel conductance ($g_{\mathrm{ds}} \approx 1/R_{\mathrm{ON}}(t)$) is modulated by the RF and IF voltages, similar to the previous analyses for the Mixer conversion gain. To analyse the switch thermal noise contribution to the output, we can first convert the thermal noise current into a Thevenin equivalent series voltage for simpler analysis. Based on a simple voltage divider, the contribution of a the double-balanced mixer thermal noise contribution can be expressed as,

$$\begin{aligned} v^2_{\mathrm{sw,wnnov}}(t) &= 8kT\gamma R_{\mathrm{ON}}(t)\left(\frac{z_{\mathrm{RF}}}{z_{\mathrm{RF}} + R_{\mathrm{ON}}(t) + 2.z_{\mathrm{bypass}}}\right)^2 . 2N \\ i^2_{\mathrm{sw,wnnov}}(t) &= 8kT\gamma R_{\mathrm{ON}}(t)\left(\frac{1}{z_{\mathrm{RF}} + R_{\mathrm{ON}}(t) + 2.z_{\mathrm{bypass}}}\right)^2 . 2N \end{aligned} \tag{6.51}$$

where the latter is obtained by reverting to the Norton network representation, and $R_{\mathrm{on}}(t) = 1/g_{\mathrm{ds}}(t)$ is the modulated switch 'ON' (channel) resistance and $N = (2/\pi)^2 \sum_0^\infty (1/(2n+1)^2) = 0.5$ represents the accumulated noise after aliasing from all the LO harmonics, without

[26] Given a combination of poor reverse isolation highlighted in (6.29), coupling mechanisms and stray tones in the IF signal, it is likely but remains to be evaluated in further development of this work, or further researched if the up-converted flicker noise falls into the wanted RF bands.

[27] Thermal noise in a MOS is modeled as $4kT\gamma(g_{\mathrm{m}} + g_{\mathrm{ds}} + g_{\mathrm{mbs}})$. In the triode region, where this Mixer is biased to operate, g_{ds} dominates.

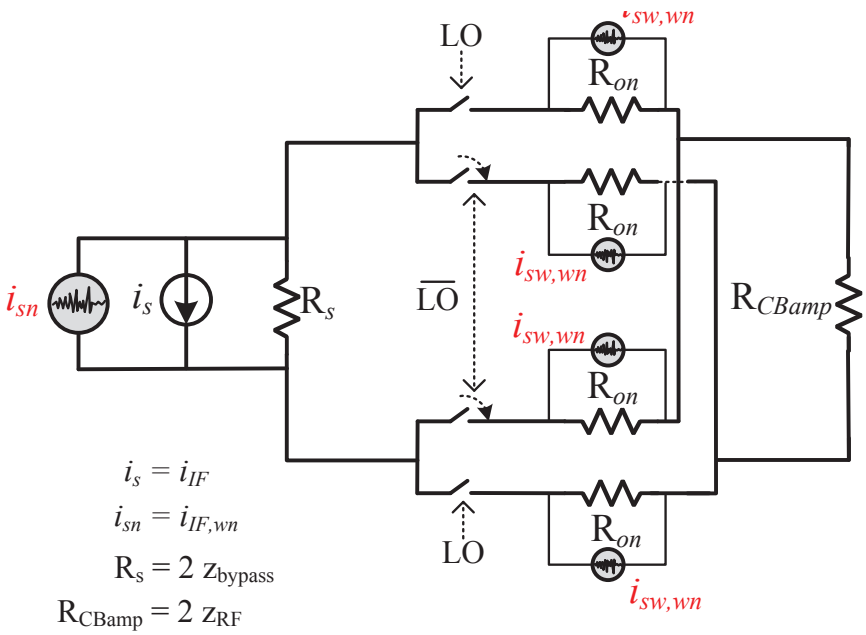

Figure 6.28: White noise transfer in the current-commutating switches

any filtering of the harmonics at the output. The multiplication by two takes into account noise from both wanted and image bands. The factor N arises from a simplification because we assume an ideal square wave LO. For a more practical LO waveform, we would need to time average the resulting signal over one time period (i.e., T_{LO}) in order to incorporate all available aliases of the fundamental within that period. This frequency translated noise is cyclo-stationary and therefore its time-averaged spectral density is obtained by time-averaging over one time-period of the fundamental LO signal, giving,

$$\begin{aligned} I^2_{\mathrm{sw,wnnov,RF}}(f) &= \sum_{n=-\infty}^{\infty} \frac{2}{T_{\mathrm{LO}}} \int_0^{T_{\mathrm{LO}}} i^2_{\mathrm{sw,wnnov,RF}}(t).e^{j(2n+1)2\pi f_{\mathrm{LO}}} dt \\ &= \sum_{n=-\infty}^{\infty} \frac{1}{T_{\mathrm{LO}}} \int_0^{T_{\mathrm{LO}}} 16kT\gamma R_{\mathrm{ON}}(t) \left(\frac{1}{z_{\mathrm{RF}} + R_{\mathrm{ON}}(t) + 2.z_{\mathrm{bypass}}} \right)^2 .e^{j(2n+1)2\pi f_{\mathrm{LO}}} dt \end{aligned} \tag{6.52}$$

where, $2n+1$, with $n = -\infty$ to ∞ refers to all the LO harmonics. The multiplication by 2 is because the up-converted noise in the image band also overlaps with the RF band, as is the case above. During the overlap phase and the non-overlap phase, the resistances are modulated by the both LO and RF waveforms and this is reflected in the channel resistance factor $R_{\mathrm{ON}}(t)$.

It is perhaps worth noting that because we do not need a power gain at the output of the IF stage, we can increase z_{bypass} in order to reduce the noise impact of the Mixers and the trans-impedance (Common Base) Output stage while simultaneously reducing the current loss (see (6.44)). The current noise contribution of z_{bypass} is not affected by the degeneration (which impacts the noise of the unbalanced differential pairs in the attenuation stage) and

finds the lowest impedance path to ground, in this case, through the Switches. However, doing so will also have an adverse impact on the linearity due to increased non-linear junction capacitances and saturation related compression of the attenuation-stage.

During the 'ON' overlap phase, we can assume the conductance of both the channel to be a constant. The thermal noise contribution here is therefore the sum of the noise from the complementary paths. In the case of finite transition time for the LO, both switches of the 'differential pair' contribute noise and the method to determine output noise [114] is similar to that presented for the flicker noise. Although the authors of [126] [28] assume that passive-FET mixer contribute white noise only during the 'ON' overlap, a detailed analysis of switch white noise performance during the 'ON' overlap phase is presented.

During the overlap phase, both complementary switches conduct, contributing to the output noise. The corresponding input referred voltage noise for each switch is $4kT\gamma 1/g_{\mathrm{m}}$.

The instantaneous combined transconductance of the differential-pair of switches is given by,

$$G_{\mathrm{m}}(t) = 2\frac{g_{\mathrm{m}}(t).g_{\mathrm{m}}(t-\frac{T_{\mathrm{LO}}}{2})}{g_{\mathrm{m}}(t)+g_{\mathrm{m}}(t-\frac{T_{\mathrm{LO}}}{2})} \tag{6.53}$$

where, $g_{\mathrm{m}}(t)$ and $g_{\mathrm{m}}(t-T_{\mathrm{LO}}/2)$ are the trans-conductances of the respective switches with respect to signals at the Gate. If they are both equal (at the cross-over point), this simply evaluated to the $g_{\mathrm{m}}(t)$ that we are familiar with in balanced differential pairs. The combined transconductance converts this voltage noise into an output current noise.

The total combined noise is therefore,

$$\begin{aligned} i^2_{\mathrm{sw,wnov}}(t) &= 2\ \cdot\ 4kT\gamma\left(\frac{1}{g_{\mathrm{m1}}}\left(\frac{g_{\mathrm{m1}}}{1+g_{\mathrm{m1}}/g_{\mathrm{m2}}}\right)^2+\frac{1}{g_{\mathrm{m2}}}\left(\frac{g_{\mathrm{m2}}}{1+g_{\mathrm{m2}}/g_{\mathrm{m1}}}\right)^2\right) \\ &= 2\ \cdot\ 4kT\gamma G_{\mathrm{m}}(t) \end{aligned} \tag{6.54}$$

The noise here is doubled because there are two differential pairs. To obtain the total noise contribution, we take the time-averaged PSD as this is cyclostationary noise.

$$\begin{aligned} I^2_{\mathrm{sw,wno,RF}}(f) &= \sum_{n=-\infty}^{\infty}\frac{2}{\Delta T_{\mathrm{LO}}}\int_0^{\Delta T_{\mathrm{LO}}} i^2_{\mathrm{sw,wnov,RF}}(t).e^{j(2n+1)2\pi f_{\mathrm{LO}}}dt \\ &= \sum_{n=-\infty}^{\infty}\frac{1}{\Delta T_{\mathrm{LO}}}\int_0^{\Delta T_{\mathrm{LO}}} 16kT\gamma\frac{1}{G_{\mathrm{m}}(t)}\left(\frac{1}{z_{\mathrm{RF}}+R_{\mathrm{ON}}(t)+2.z_{\mathrm{bypass}}}\right)^2 e^{j(2n+1)2\pi f_{\mathrm{LO}}}dt \end{aligned} \tag{6.55}$$

where ΔT_{LO} is the overlap period.

In order to determine the total white noise contribution of the Mixer, we are required to sum up the noise in the two phases taking into account the effective duty cycles for the two

[28] To our understanding, this assumption is perhaps not entirely true. This is the case only for active mixers where the noise of switching stage is diminished compared to transconductance stage, to which it is in cascode. The contribution of the cascode stage to SNR degradation is small as it is heavily degenerated by the r_{o} of the transconductance stage, which can be easily visualised by using the superposition principles for noise analysis.

phases. This would also give them their frequency domain characters, as was shown for the flicker noise earlier. This has been partially treated in (1) of [127].

The white noise (and flicker noise) translation from the IF to the RF port (as $I_{\text{if,wno,RF}}(f)$) of the Mixer is similar to the analysis of current gain expressed in (6.35). This combines the noise of the attenuator stage and that of the bypass resistance z_{bypass}. It is perhaps useful to note that during periods of 'ON' overlap given finite LO signal rise-times, the noise at the IF port appears as common-mode noise at the RF port. This is because during the overlap, the complementary paths are both in the 'ON' stage and form a differential pair. The noise resembles tail current in a typical differential pair, which, if the matching is ideal, appears as a common mode noise at the output of the differential pair (i.e., at the RF port).

Noise sources also exist at the Gate terminal. The noise here refers to both the Gate resistance and the LO noise expressed as a voltage in series with the Gate voltage. The analysis of LO noise in depth is somewhat more involved because of the nature of the jitter, which contains components of varying time-periods, some of which are close to the LO harmonics themselves and vary with the mixing function. As a result, the noise sources at this port cannot be considered Wide-Sense-Stationary (WSS) (i.e., stationary if observed within the time period). By a simplified assumption of cyclo-stationary (i.e., only white-noise) noise at the LO port, we can give the LO noise and the Gate noise both the same treatment. The noise at the LO port can therefore be represented as a resistor R_{LO} in series with the Gate resistance r_{g} of the switch. During the 'ON' overlap, the differential pair formed by the switches amplifies the noise from the LO buffers and the Gate noise of the switches themselves. It is not possible to reject the contributions from the LO harmonics at the Gate because they are characteristic to the mixing operation itself. Rejecting LO harmonics at the Gate would degrade the performances of the Mixer, including the noise performance.

The combined noise associated with R_{LO} and r_{g} is simply a voltage source ($v^2_{\text{sw,lo}} = 4kT\gamma[R_{\text{LO}}+r_{\text{g}}]\Delta f$) in series with the Gate. The time-averaged power spectral density (PSD) of the cyclostationary noise at the output is therefore expressed as,

$$\begin{aligned} I^2_{\text{sw,lo,RF}}(f) &= \sum_{n=-\infty}^{\infty} V^2_{\text{sw,lo}}(f+nf_{\text{LO}})\frac{1}{T_{\text{LO}}}\left(\int_0^{T_{\text{LO}}} |G_{\text{m}}(t)|^2.e^{j(2n+1)2\pi f_{\text{LO}}}dt\right) \\ &= \sum_{n=-\infty}^{\infty} 8kT\gamma(R_{\text{LO}}+r_{\text{g}})(f+nf_{\text{LO}})\frac{1}{T_{\text{LO}}}\left(\int_0^{T_{\text{LO}}} |G_{\text{m}}(t)|^2.e^{j(2n+1)2\pi f_{\text{LO}}}dt\right) \end{aligned} \tag{6.56}$$

where, $V^2_{\text{sw,lo}}(f)$ is the PSD of the WSS Gate noise. It is easy to observe that $G_{\text{m}}(t)$ has a period $T_{\text{LO}}/2$, but unlike the flicker noise, the LO noise is (assumed) WSS (at large carrier offsets) and therefore its PSD is flat (for large carrier offsets) in the output spectrum. This noise is different and in addition to the noise from the leakage of the LO and its harmonics to the RF port. The LO port contribution to noise is therefore significant to the Mixer's performance. The authors of [114] provide a more exact expression for noise translation from the LO port.

The total R.M.S. output noise contribution of the Mixer is obtained by quadratically

summing the expressions flicker, IF, Thermal, LO above.

$$\overline{I^2_{n,\text{mixer,out}}} = \Bigg(\underbrace{2I^2_{\text{sw,fno,RF}}(f)}_{\text{Mixer Flicker Noise}} + \underbrace{I^2_{\text{sw,wnnov,RF}}(f) + I^2_{\text{sw,wnov,RF}}(f)}_{\text{Mixer White Noise}} + \underbrace{I^2_{\text{if,wno,RF}}(f)}_{\text{Up-converted IF White Noise}} + \underbrace{I^2_{\text{if,fno,RF}}(f)}_{\text{Up-converted IF Flicker Noise}} + \underbrace{I^2_{\text{sw,lo,RF}}(f)}_{\text{LO Noise}} \Bigg)^{\frac{1}{2}} \tag{6.57}$$

Since we deal here with an image reject Mixer, the quadratic summation of noise $((\overline{I^2_{n,\text{mixer,out}}} + \overline{Q^2_{n,\text{mixer,out}}})^{0.5})$ from the I and Q paths needs to be considered at the Mixer's RF port, which forms the input noise to the CB stage.

6.4 Quadrature LO Generation

We refer to Chapter 4, where the EVM of a modulated signal was shown to be significantly affected by the unwanted image in a multi-channel up-conversion process. If we consider the (6.1), we can readily observe that the up-conversion process in both I and Q branches produces both upper ($\omega_{\text{LO}} + \omega_{\text{IF}}$) and lower ($\omega_{\text{LO}} - \omega_{\text{IF}}$) sidebands. The act of subtraction at the output of the two paths eliminates the unwanted (in this case, the lower) sideband to the extent defined by the Image Rejection Ratio (IRR), discussed below. Any deviation from this ideal expression will result in crosstalk or unwanted signal components in other channels, degrading their quality.

The details of this design are not discussed here for the sake of confidentiality. However, we illustrate some basic concepts of this block to show the impact of non-idealities from this stage, on the distortion of the signal. From the Hartley based Quadrature up-conversion architecture [29], we know that a 0°/90° Quadrature LO is required for the translation expressed in (6.1). These In-phase (I) and Quadrature-phase (Q) LO signals are actually generated from a single or differential phase LO by means of an on-chip passive n-stage RC - Poly Phase filter (PPF). The PPF [128, 129] is ubiquitous in contemporary circuits for Base stations, being preferred for its simplicity, better matching and noise characteristics compared with Frequency-division [30] based LO generation techniques.

For this design a 3-stage RC-CR PPF is chosen which is composed of three cascaded stages of the four-phase RC polyphase network. ABCD parameters lend themselves to easy manipulation when dealing with cascaded networks and are therefore preferred for representing and analysing cascaded PPFs. The general ABCD parameter matrix for a single-phase PPF cell [130] shown in Figure 6.29 is given by (6.58)

[29] In the Hartley up-conversion, the IF signal is available as separate I and Q streams at the output of the DAC, requiring a Quadrature LO signalling scheme.

[30] Latch based Quadrature generation techniques need twice the LO frequencies implying a higher power consumption besides requiring a reference clock with comparable phase-noise performance, but at double the clock frequency. Furthermore, when the duty-cycle between the I and Q paths deviates from the required 50%, the phase mismatch is worsened, degrading image rejection.

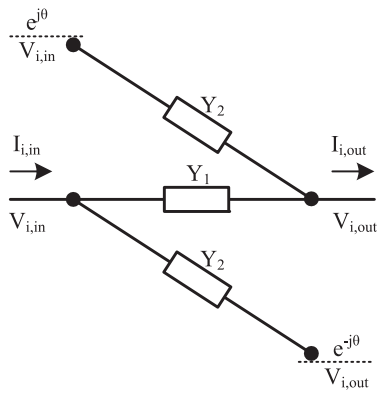

Figure 6.29: Single-phase illustration of a PPF cell

$$\begin{bmatrix} V_{i,\text{in}} \\ I_{i,\text{in}} \end{bmatrix} = \frac{1}{Y_1 + e^{j\theta} Y_2} \begin{bmatrix} Y_1 + Y_2 & 1 \\ 2Y_1Y_2(1-\cos\theta) & Y_1 + Y_2 \end{bmatrix} \begin{bmatrix} V_{i,\text{out}} \\ I_{i,\text{out}} \end{bmatrix} \tag{6.58}$$

where, $V_{i,\text{in}}, I_{i,\text{in}}$ are the input vectors of one phase (i corresponding to the stage, with $i = 1, 2, 3...., N$ for N stage PPFs) and $V_{i,\text{out}}, I_{i,\text{out}}$, the outputs corresponding to the input signals of the same phase. $Y_1 = 1/R$ and $Y_2 = j\omega C$. The $e^{j\theta}$ indicates the phase of the inputs relative to the other inputs, with $\theta < 0$ indicating negative phase, $\theta > 0$ indicating positive phase. In typical PPF's we deal with four phases, $\theta = \{0, 90, 180, 270\}$ or $\{I_+, Q_+, I_-, Q_-\}$ [31]. The four-phase network forms one PPF stage (see Figure 6.30)which is cascaded in order to achieve the required image rejection. The network in symmetrical in that there is a physical symmetry in the path from input signal to corresponding output, irrespective of the phase.

If we rewrite (6.58) using only circuit elements and analyse for the 0° phase, we obtain,

$$\begin{bmatrix} V_{i,\text{in}} \\ I_{i,\text{in}} \end{bmatrix} = \frac{1}{1 + \omega RC} \begin{bmatrix} 1 + j\omega RC & R \\ 2j\omega C & 1 + j\omega RC \end{bmatrix} \begin{bmatrix} V_{i,\text{out}} \\ I_{i,\text{out}} \end{bmatrix} \tag{6.59}$$

The above representation corresponds to one sequence of inputs. If the sequence were to be reversed, i.e., ω replaced by $-\omega$ or negative frequencies, now referred to as the negative sequence, we obtain the following representation,

$$\begin{bmatrix} V_{i,\text{in}} \\ I_{i,\text{in}} \end{bmatrix} = \frac{1}{1 - \omega RC} \begin{bmatrix} 1 + j\omega RC & R \\ 2j\omega C & 1 + j\omega RC \end{bmatrix} \begin{bmatrix} V_{i,\text{out}} \\ I_{i,\text{out}} \end{bmatrix} \tag{6.60}$$

The unloaded voltage transfer functions of the single stage PPF for positive and negative sequences are given by,

[31] We have only the I components (I_+, I_-) of the LO signal as available inputs. The other phase inputs can either be shorted to the available inputs, be left open or be connected to the LO input ports via inductors to the available inputs. The addition of the inductors creates an additional notch filter, which improves the overall image rejection in both phase and magnitude, above the typical unaided IRR value of −30 to −40 dB.

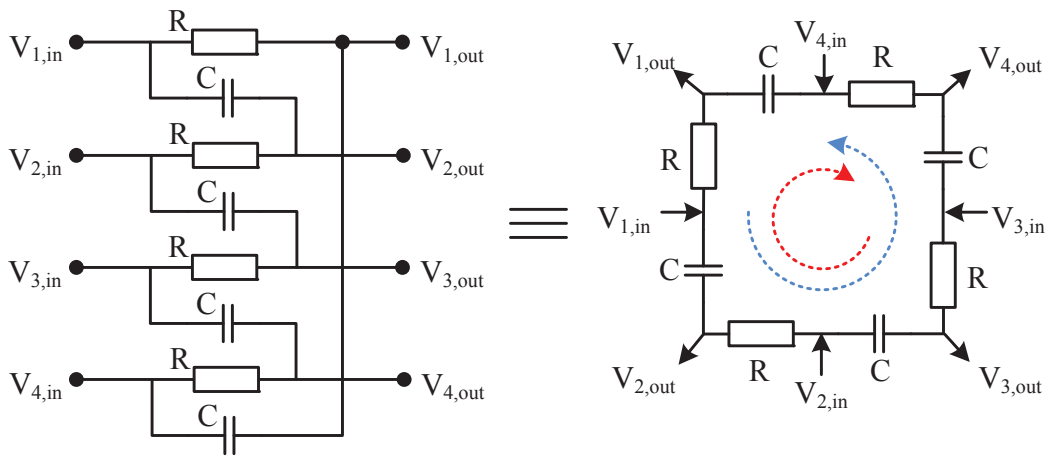

Figure 6.30: A single stage or Four-phase PPF network showing positive (anti-clockwise) and negative (clockwise) sequences

$$H(\omega) = \frac{1 + \omega RC}{1 + j\omega RC} \tag{6.61}$$

and,

$$H(-\omega) = \frac{1 - \omega RC}{1 + j\omega RC} \tag{6.62}$$

If we consider the above transfer functions for the four ($i = 1, 2, 3, 4$) positive sequence phases with $\theta = \{0, 90, 180, 270\}$ corresponding to $\{I_+, Q_+, I_-, Q_-\}$, by assuming that the inputs are similarly excited (i.e., $V_{1,\text{in}} = V$, $V_{2,\text{in}} = jV$, $V_{3,\text{in}} = -V$ and $V_{4,\text{in}} = -jV$) [32] we obtain,

$$\begin{aligned} V_{\text{I}_+} = V_{1,\text{out}} &= \frac{V}{2}\{H(\omega) + H(-\omega)\} \\ V_{\text{Q}_+} = V_{2,\text{out}} &= -j\frac{V}{2}\{H(\omega) - H(-\omega)\} \\ V_{\text{I}_-} = V_{3,\text{out}} &= -\frac{V}{2}\{H(\omega) + H(-\omega)\} \\ V_{\text{Q}_-} = V_{4,\text{out}} &= j\frac{V}{2}\{H(\omega) - H(-\omega)\} \end{aligned} \tag{6.63}$$

The image rejection ratio (IRR) for a single phase PPF is given by a ratio of the transfer functions for the positive and negative sequences, i.e., dividing (6.62) by (6.61), to obtain,

$$\text{IRR}(\omega)_{\text{dB}} = 20\log\left[\frac{1 - \omega RC}{1 + \omega RC}\right] \tag{6.64}$$

[32] For the negative sequence, this would be $V_{1,\text{in}} = -V$, $V_{2,\text{in}} = -jV$, $V_{3,\text{in}} = V$ and $V_{4,\text{in}} = jV$

This discrimination between positive and negative sequences characterises the PPF's performance[33]. Evidently, a 1-stage PPF rejects a negative sequence of inputs fully only at a singular frequency $\omega = 1/RC$. This is easily analysed by considering the pole and zero of the above equation. At other frequencies, this rejection is understandably, diminished. This image rejection can be stretched or made broadband by cascading two or more stages together, producing a net rejection over the wanted bandwidth which exceeds a stipulated design value (in this case, better than -40dB [34]). The number of stages is often a trade-off between the rejection it achieves, the sensitivity to component tolerances and the amount of noise it introduces together with the layout area it requires. Noise that is introduced in the LO path can be added as a Gate voltage and follows the analysis in (6.56).

For this design, a 3-stage structure is used, as the result of a tradeoff between bandwidth and sensitivity of the IRR, and noise. For 3 stages in cascade, the representation (6.58) evolves to,

$$\begin{aligned}\begin{bmatrix} V_{\text{in}} \\ I_{\text{in}} \end{bmatrix} &= \frac{1}{1+\omega R_1 C_1}\begin{bmatrix} 1+j\omega R_1 C_1 & R_1 \\ 2j\omega C_1 & 1+j\omega R_1 C_1 \end{bmatrix} \\ &\cdot \frac{1}{1+\omega R_2 C_2}\begin{bmatrix} 1+j\omega R_2 C_2 & R_2 \\ 2j\omega C_2 & 1+j\omega R_2 C_2 \end{bmatrix} \\ &\cdot \frac{1}{1+\omega R_3 C_3}\begin{bmatrix} 1+j\omega R_3 C_3 & R_3 \\ 2j\omega C_3 & 1+j\omega R_3 C_3 \end{bmatrix}\begin{bmatrix} V_{i,\text{out}} \\ I_{i,\text{out}} \end{bmatrix}\end{aligned} \tag{6.65}$$

For this, the unloaded voltage transfer function [116] is given by

$$\begin{aligned}H(\omega) = &\Big((1+\omega R_1 C_1)(1+\omega R_2 C_2)(1+\omega R_3 C_3)\Big)/\Big(1-\omega^2[R_1C_1R_2C_2 + R_1C_1R_3C_3 \\ &+ R_2C_2R_2C_3 + 2R_1C_3(R_2C_1 + R_3C_2 + R_2C_2)] + j[\omega(R_1C_1 + R_2C_2 \\ &+ R_3C_3 + 2(R_1C_2 + R_1C_3 + R_2C_3)) - \omega^3(R_1C_1R_2C_2R_3C_3)]\Big)\end{aligned} \tag{6.66}$$

By using (6.63) and (6.66) we can have a relationship between the I and Q phases at the output of the 3-stage PPF [130], as represented in (6.67).

$$\frac{V_{\text{Q}_+} - V_{\text{Q}_-}}{V_{\text{I}_+} - V_{\text{I}_-}} = \frac{s(R_1C_1 + R_2C_2 + R_3C_3) - s^3(R_1C_1R_2C_2R_3C_3)}{1 - s^2[R_1C_1R_2C_2 + R_1C_1R_3C_3 + R_2C_2R_2C_3)} \tag{6.67}$$

Deviations in the IRR accuracy caused by physical imperfections, arise due to component mismatch, process variations and parasitics. A non-ideal IRR degrades signal quality and a design with sufficient margins is therefore required. Process variations for example, are dealt with by introducing an additional margin in the design.We know for example, $\omega = 1/RC$. So, with ΔR being the process variation in R for a given σ and ΔC, the process variation in C for the same multiple of standard deviation, we obtain a deviation for the time-constant,

[33] This essentially 20log[(I+jQ)/(Q+jI)] dB

[34] Due to the significant impact of IQ imbalances on the signal EVM, Base Stations manufacturers often improve this value by further by enhancing image rejection through digital calibration. In addition to the DAC IQ control suggested earlier, an improvement of $15-20$ dB by calibration and compensation, is possible.

Table 6.3: Simulated design values for the passives of the 3-stage PPF

Stage	Resistor	Value	Capacitance	Value	Inductance	Value
1	R_1	112.7Ω	C_1	4.5pF	L_+, L_- [a]	3.5nH
2	R_2	112.7Ω	C_2	2.904pF	-	-
3	R_3	112.7Ω	C_3	845fF	-	-

[a] L_+ and L_- are connected at the inputs, between the phases I_+/Q_+ and I_-/Q_-, respectively.

$$\Delta_{\mathrm{RC}} = \frac{(\Delta R + R)(\Delta C + C)}{RC} \cdot 100\% \tag{6.68}$$

Typically, in order to guarantee the minimum IRR within the band of interest, all the main poles of (6.66) are spaced at equal intervals on a logarithmic frequency axis. The process-variation affects all components in a similar manner and thereby causes the poles to shift from their intended frequencies, resulting in a desired IRR that is shifted due to the spreading. Therefore, in order to guarantee the bandwidth for the minimum required rejection, the lowest RC notch (pole) and the highest RC notch (pole) need to be extended by the percentage $\mp\Delta_{\mathrm{RC}}$ determined above. The chosen values for the passive components of the 3-stage RC PPF are as specified in Table 6.3.

Component mismatch causes dissimilarity between the gain and phase of the I and Q paths. This causes the IRR within the bandwidth of interest to deviate from the intended value, i.e., the cancellation of the image signal will not be exact, or within the tolerance required. [131] shows a simple analysis of the requirements for matching accuracies on R and C to within a certain yield deviation ($n.\sigma$). Analysis of the propagation of errors [132] due to component mismatch in 3-stage PPF's is rather involved, so we refer to the 1-stage expression for IRR due to amplitude and phase mismatch between the I and Q paths of the PPF, as determined by [133] shown in (6.69).

$$\mathrm{IRR}_{\mathrm{dB}} = 20\log\left[\frac{(1+\frac{\epsilon}{A_{\mathrm{LO}}})^2 - 2(1+\frac{\epsilon}{A_{\mathrm{LO}}})\cos\Delta\phi + 1}{(1+\frac{\epsilon}{A_{\mathrm{LO}}})^2 + 2(1+\frac{\epsilon}{A_{\mathrm{LO}}})\cos\Delta\phi + 1}\right] \tag{6.69}$$

where, ϵ/A_{LO} is the relative gain error between the I and Q paths and $\Delta\phi$ is the corresponding relative phase mismatch (in radians). Figure 6.31 depicts the impact of mismatch on the IRR in dB.

For a 1-stage PPF, if we were to assume a mismatch between the passive components of the I and Q paths, in the form of $R_1, R_1 + \Delta R$ and $C_1, C_1 + \Delta C$, this would yield the following expression for gain imbalance, given by [134],

$$\frac{\epsilon}{A_{\mathrm{LO}}} \approx \frac{(R_1 + \Delta R_1)(C_1 + \Delta C_1)\omega - 1}{\sqrt{(R_1 + \Delta R_1)^2 (C_1 + \Delta C_1)^2 \omega^2 + 1}} \div \frac{1}{\sqrt{R_1^2 C_1^2 \omega^2 + 1}} \tag{6.70}$$

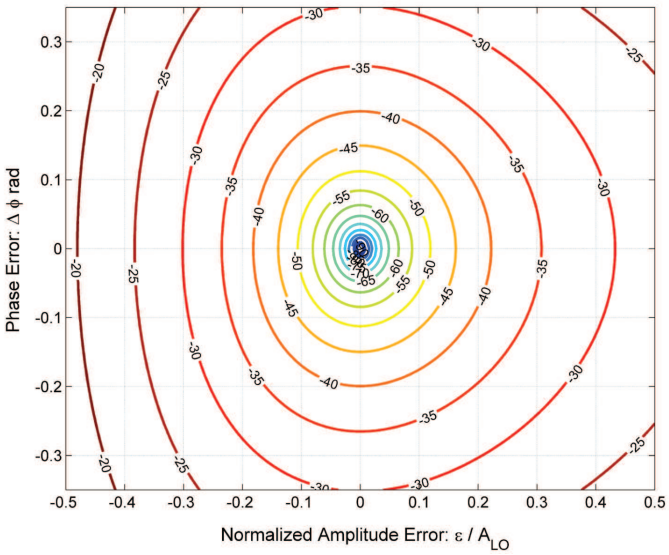

Figure 6.31: Simulated Image Rejection Ratio (dB) as a function of IQ phase and amplitude mismatch

At frequencies close to $\omega = 1/RC$, (6.70) simplifies to,

$$\begin{aligned} \frac{\epsilon}{A_{\mathrm{LO}}} &\approx \frac{\frac{\Delta R_1}{R_1} + \frac{\Delta C_1}{C_1}}{\sqrt{2 + \frac{\Delta R_1}{R_1} + \frac{\Delta C_1}{C_1}}} \div \frac{1}{\sqrt{(2)}} \\ &\approx \frac{\Delta R_1}{R_1} + \frac{\Delta C_1}{C_1} \end{aligned} \tag{6.71}$$

With a multi-stage PPF, the extent of component mismatch is clearly further aggravated given the greater number of components at work. However, the effect of component mismatch on the IRR in multi-stage PPFs is reduced when compared to single-stage PPFs, due to its wide-band frequency response which minimises the deviation of the IRR from the required or designed value. Matching between the two paths is nonetheless critical to ensure that any additional imbalance is not introduced. Mismatch and parasitics are best tackled by incorporating proper component choices and layout techniques [35] Fine tuning is more easily possible by iterations of design following Monte-Carlo simulations (see Figure 6.32) for a large number of samples, as there are several RC networks and also active stages involved making hand-calculations unwieldy given varying statistical distributions and the frequency dependency of the impact on the IRR.

[35] MiM capacitors have a higher Q factor, i.e., lower parasitic resistance than poly-well, poly-poly and MOS capacitors and are preferred for the design as the parasitic poles ($f = 1/2\pi R_{\mathrm{par}} C$) fall outside of the wanted band. Similarly, resistors with large surface areas are shown to be less prone to variations [135].

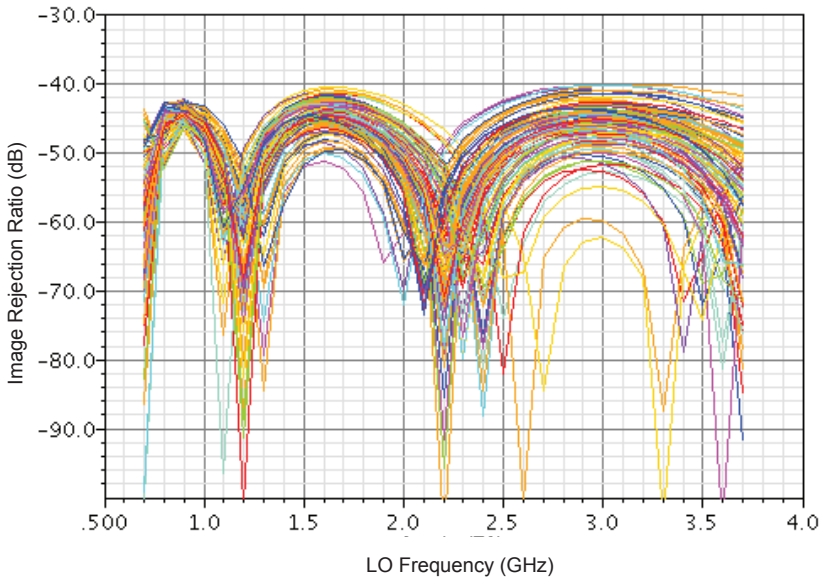

Figure 6.32: Monte Carlo simulations illustrating the degradation of IRR due to process variations and component mismatch (*Courtesy: NXP Semiconductors*).

Due to the fact that the RC stages are in fact passive filters (whose function is to introduce a phase shift), they introduce a loss and correspondingly, noise [36]. The noise has an impact similar to the Gate voltage noise described in the previous sections. The loss demands intermediate-stage amplifiers following the passive PPF network, in order to increase the voltage swing to fully switch the nMOSs of the Mixer. The active chain comprises of BJT differential-pairs followed by CMOS Inverter stages building up the swing from $0.5V_{\text{pp}}$ to the $2.5V_{\text{pp}}$ required. This corresponds to A_{LO} indicated in (6.32) above. The stages are AC coupled to each other to allow independent bias settings for each of the stages. This allows the voltage swing to be gradually built up to (the rails, at) approximately $2.5V_{\text{pp}}$ and ensures that the $R_{\text{load}}C_{\text{load}}$ product at the output of each stage does not limit the bandwidth [37]. Driving the amplifiers/buffers to the rails comes with the added advantage that the amplitude clipping also cuts out any amplitude noise which would otherwise permeate through to the Gates of the Switches, degrading their function. The advantages of this 'hard' switching on the switching function has been covered in previous sections discussing Switch noise and linearity. It is also important to ensure that a common mode DC offset is not introduced as this would shift the zero crossing and consequently, the phase relationship between the I and Q paths. Furthermore DC offsets introduce duty-cycle variations in the LO signal which produce harmonic frequencies that may not be cancelled out if unbalanced. Fast rise times also reduce the phase error as the following simulation result shows (see Figure 6.33).

[36] The noise produced by the active stages will be in addition to the passive RC network.

[37] Typically the load time constant is $5 - 10$ times the maximum operating frequency, until the last stage.

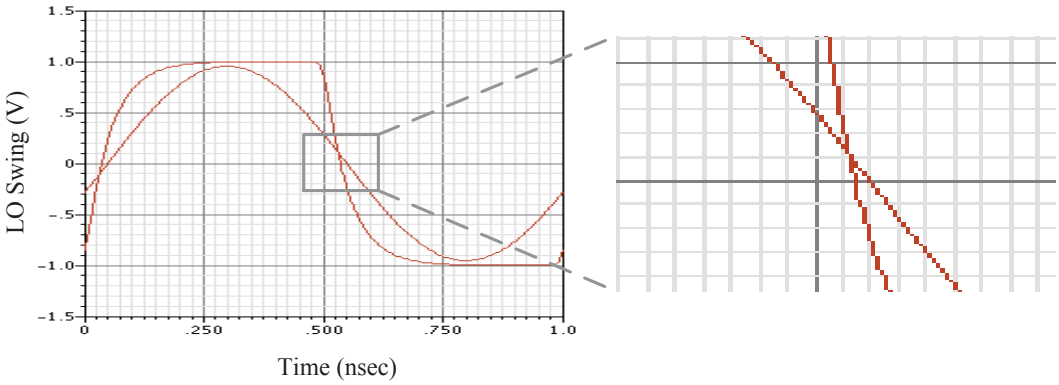

Figure 6.33: Illustration of the variation in zero-crossing due to finite rise-time (bandwidth limitation) (*Courtesy: NXP Semiconductors*).

The differential-pair gain (per stage, two stages) given by $2g'_{\mathrm{m}}R_{\mathrm{load}}$ has to be high within the bandwidth of interest, while allowing for a high slew rate despite the limitations on the biasing current by the power budget. The slew rate and also the common-mode rejection are enhanced by resistive degeneration in the tail current (source). The biasing current can be increased to compensate for a degraded switching speed at higher frequencies, but needs to be traded off with increased shot-noise and the worsening contribution of the non-linear C_{bc} [38], because the junction voltage V_{cb} will decrease. The second Bipolar stage features of an all-NPN push-pull (Class AB) buffer that helps to reinforce the symmetric rise and fall times while also being a more efficient implementation. The BJTs are sized for highest f_{T} at the given current. This minimises the contribution of r_{bb} and also impact of the junction capacitances. Detailed dimensioning and biasing are not discussed here for reasons of confidentiality. Nevertheless the primary objectives would be to ensure that the load and any capacitors in the active path do not limit rise and fall times together with minimising noise contribution, while remaining with the power budget. The final stage of the LO buffer comprises of a two-stage CMOS inverter which not only prevents loading of the BJT stage but also increases the output swing to ±1.25V about the common mode in order to fully switch both the nMOS Switches. Similar to the earlier stages, the pMOS and nMOS of the inverters are sized (according to their resistances) so as to have sharp, symmetric rise and fall times while at the same time minimising the dynamic power consumption, $P_{\mathrm{dynamic}} = f_{\mathrm{LO}}C_{\mathrm{load}}V_{\mathrm{DD}}^2/2$ [39].

All the stages are AC coupled, hence the common-mode mismatch or the DC-offset voltage is diminished, but additional phase mismatch is still introduced as a result of the finite

[38] The junction capacitor is dependent on the voltage across its junctions as discussed earlier, resulting in an AM-to-PM non-linearity.

[39] The load capacitance is actually a series combination of all the capacitances that exist between the output node and the incremental ground, ($V_{textrmDD}$ and GND). This also includes the decoupling capacitor which isolates the inverter output stage DC from the Gate bias network (see Section 6.4.1)

bandwidth of the stages which causes the AM-PM distortion (even in the absence of component mismatch or process variations,) worsening the $\Delta\phi$. The clipping of the output swing aides by absorbing most of the amplitude mismatch ΔA, reducing the $\Delta\phi$ from the AM-PM, to some extent. The LO buffer stage is AC coupled to the Gates of the Mixer by means of a decoupling capacitor $C_{\text{LO,iso}}$ which is sized according to the voltage ratio [40] expressed in (6.72).

$$\frac{V_{\text{LO}}}{V_{\text{Inv,out}}} \approx \frac{C_{\text{LO,iso}}}{C_{\text{LO,iso}} + 2 \cdot C_{\text{Mixer}}} \tag{6.72}$$

where, C_{Mixer} includes the associated capacitances of the nMOS Switches together with any capacitances which link them to V_{DD} or GND directly, or via relatively low impedances. The Switches are each sized 200 x 0.25μm. With $C_{\text{ox}} \approx 6.9\text{fF}/\mu m^2$, this amounts to 2x690fF ($= 2 \cdot C_{\text{Mixer}}$) per LO line.

6.4.1 Switch Biasing

The channel (ON) resistance of a R_{on} of the Mixer varies inversely with the V_{GS}, for a given V_{DS} as shown in Figure 6.20. Having a large overdrive ($V_{\text{GS}} - V_{\text{Th}}$) allows for a low ON resistance. As indicated above, the Mixer is biased to enable a make-before-break switching action (i.e., $V_{\text{LO,DC}} = V_{\text{th}} + V_{\text{eff}}, V_{\text{eff}} > 0$). With only a 3.3V supply available to the circuit, the high overdrive voltage for the switches ($V_{\text{G}} - V_{\text{com}}$) can be achieved by means of a voltage-doubler, illustrated in Figure 6.35.

The operation of a generic voltage doubler can be summarised as a combination of a clamp and a peak-detector (see Figure 6.35). The clamp consists of a cascade of capacitor/diode cells with the bottom plate of the capacitor connected to the LO pulse train. If the diodes are assumed ideal, i.e., $V_{\text{diode,ON}} = 0V$ and A_{LO} be the peak amplitude of the LO waveform, then during the negative half cycle, the capacitance charges via the forward biased diode, developing a potential difference of A_{LO} across its plates. During the positive half cycle, the diode is reverse biased and does not conduct. As a result the voltage across the capacitance becomes twice the amplitude of the LO pulse train. Now, because the diode of the peak-detector is also forward biased, the voltage across the capacitor of the peak-detector is $2*A_{\text{LO}}$. If we take the diode voltage drop into account, the voltage at the output of the peak-detector is then,

$$\begin{aligned} V_{\text{dbl,out}} &= -(V_{\text{dbl,in,pk}} - 2 \cdot V_{\text{diode,ON}}) + V_{\text{in,pk}} \\ V_{\text{dbl,out}} &= -2 \cdot (V_{\text{dbl,in,pk}} + V_{\text{diode,ON}}) \end{aligned} \tag{6.73}$$

Here, $V_{\text{dbl,in,pk}}$ corresponds to the peak LO voltage swing (A_{LO}) and $V_{\text{dbl,out}}$, the output voltage of the Doubler. A variant of this Doubler used in this design features a DC voltage source (here, V_{DD} itself,) forward biasing the diode by $V_{\text{DC}} = V_{\text{DD}}$. As a result, during the negative half cycle of the LO pulse train, the clamp capacitance is charged to $A_{\text{LO}} + V_{\text{DD}}$ which builds to $2 \cdot A_{\text{LO}} + V_{\text{DD}}$ over a complete cycle, from the description above. With practical

[40] In order to allow for faster switching time, the full CMOS voltage swing is used, i.e., $V_{\text{LO}}/V_{\text{Inv,out}} \approx 1$, giving $C_{\text{LO,iso}} >> C_{\text{Mixer}}$.

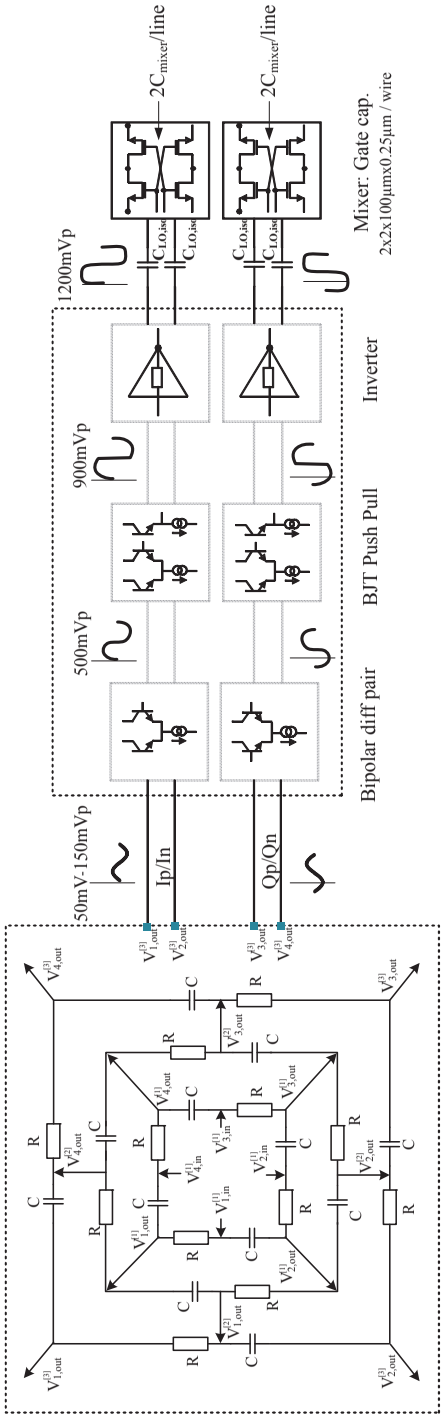

Figure 6.34: Illustration of the LO chain including the PPF network and the LO buffer-amplifiers

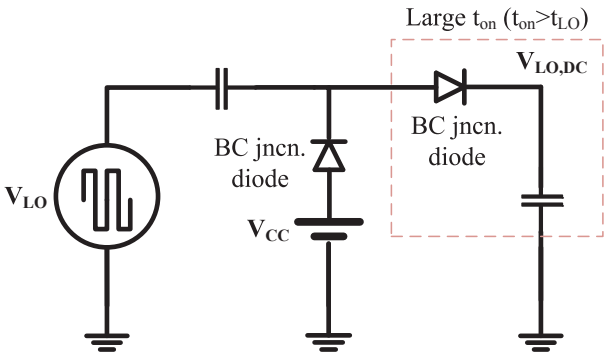

Figure 6.35: Concept of the voltage doubler showing the clamp

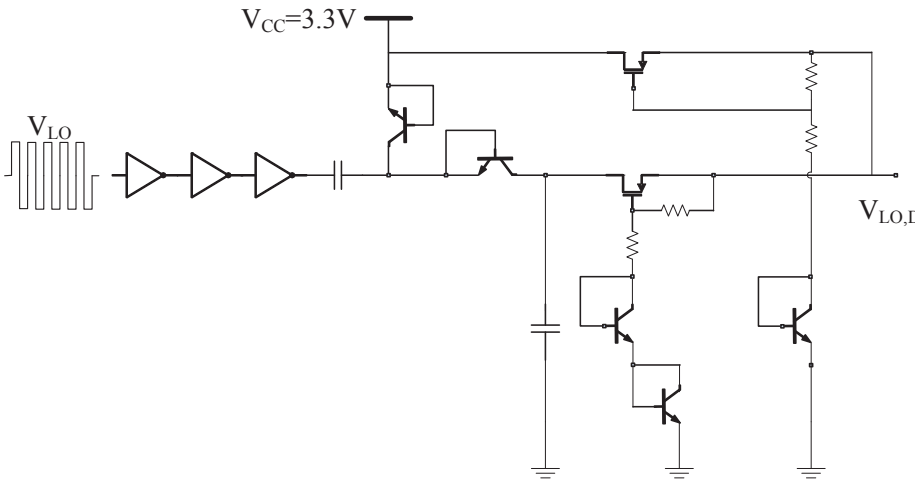

Figure 6.36: Circuit schematic of the voltage doubler

diodes, as in (6.73) above, the output voltage settles at $V_{\text{out}} = 2 \cdot A_{\text{LO}} + V_{\text{DD}} - 2 \cdot V_{\text{diode,ON}}$. Given $A_{\text{LO}} \approx 1.25V$, $V_{\text{DD}} = 3.3V$ and $V_{\text{diode,ON}} \approx 0.8V$, we obtain $V_{\text{dbl,out}} \leq 4.2V$. The diodes (formed by the BC junctions of NPN BJT's) are sized together with the capacitors to have a T_{ON} several factors lower than the fundamental time period of the LO pulse train. The inverter chain shown in the schematic 6.36 merely prevents the voltage-doubler capacitances from loading the LO buffers as they appear in parallel with the capacitances of the Switches.

The input of the bias network comprises of a low-pass filter (LPF) with a near zero frequency cutoff, which senses the common-mode voltage of the differential IF waveforms. This LPF forms part of a programmable bias network whose current can be coarsely tuned in order to set the right output voltage for this network. This output is connected (by large biasing resistors) to the Gates of the Switches. By controlling the current of this bias network, a coarse adjustment of the overdrive voltage on the Switches can be made.

The supply voltage for this bias network is derived from the $2.5V_{\text{pp}}$ rail-to-rail LO swing

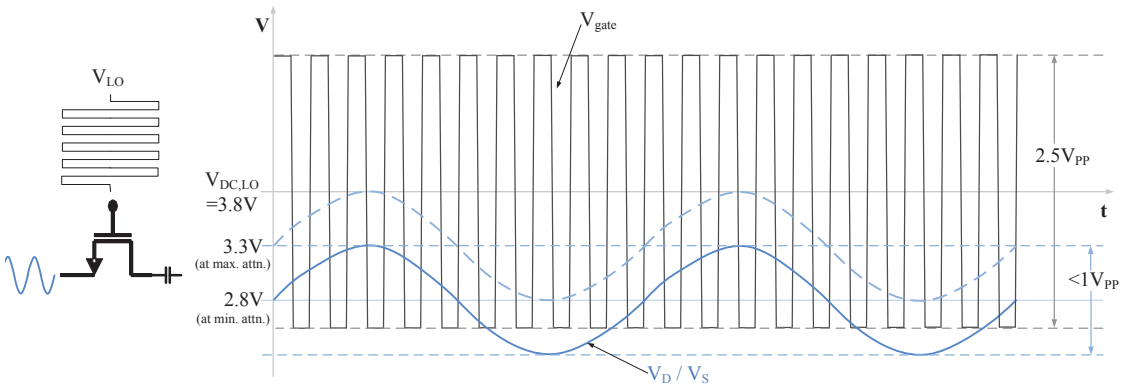

Figure 6.37: Voltage swing on the Gate and Source terminals of a switch in the passive Mixer

(see (6.32)), with the objective of maintaining the symmetry of ON and OFF times[41]. Without the symmetrical ON-OFF (i.e., deviation from the 50% duty cycle) cycles, the finite rise and fall times generate a waveform that has even harmonic components. If the common-mode rejection (i.e., matching) of the balanced Mixer is insufficient, this could result in a leakage of second-order harmonics especially those that are greater than the RC output filter cutoff frequency, to leak into to the RF path. The peak of the LO swing also determines the compression point of the mixer because the input IP3 in a passive mixer tends to be determined most directly by the rise time and the difference between swings of the LO and IF waveforms, as pointed out in the earlier sections. The Gate bias voltage of the Switches is therefore set with (a pre-determined but programmable) DC overdrive of $\approx 0.3V$, with $V_{\mathrm{GS}} \approx 0.8V$ and $V_{\mathrm{Th}} \approx 0.55V$. The switching action is achieved by the changing overdrive voltage due to the oscillating voltages on the Gate and Source/Drain terminals (see Figure 6.37).

Due to the fact that the Source terminal is DC coupled to the output of the attenuator stage, the common-mode voltage of the Source/Drain terminal rises towards the $3.3V$ supply voltage (V_{DD}) as the current through the load reduces with increasing attenuation. Despite this, switching action is not significantly affected because the LO voltage ($2.5V_{\mathrm{pp}} + V_{\mathrm{LO,DC}}$) at the Gate is sufficiently higher than the Source/Drain terminal voltage [42].

6.5 Common Base Output Stage

The Common Base (CB) stage at the output of the AQM functions as a Trans-Impedance Amplifier (TIA) by transforming input current into an output voltage while simultaneously providing gain. This relation or translation is in fact a trans-impedance Z_{T}, which we will determine for the mid to high frequency operation.

[41] A swing which saturates the LO buffers is chosen, in order to minimise IQ DC offset and gain errors. Without this, larger rise times could result for a given LO fundamental frequency, apart from unequal gains on the I and Q paths which could permeate to the switches uncorrected.

[42] Furthermore, the Source/Drain IF swing also diminishes as the attenuation increases

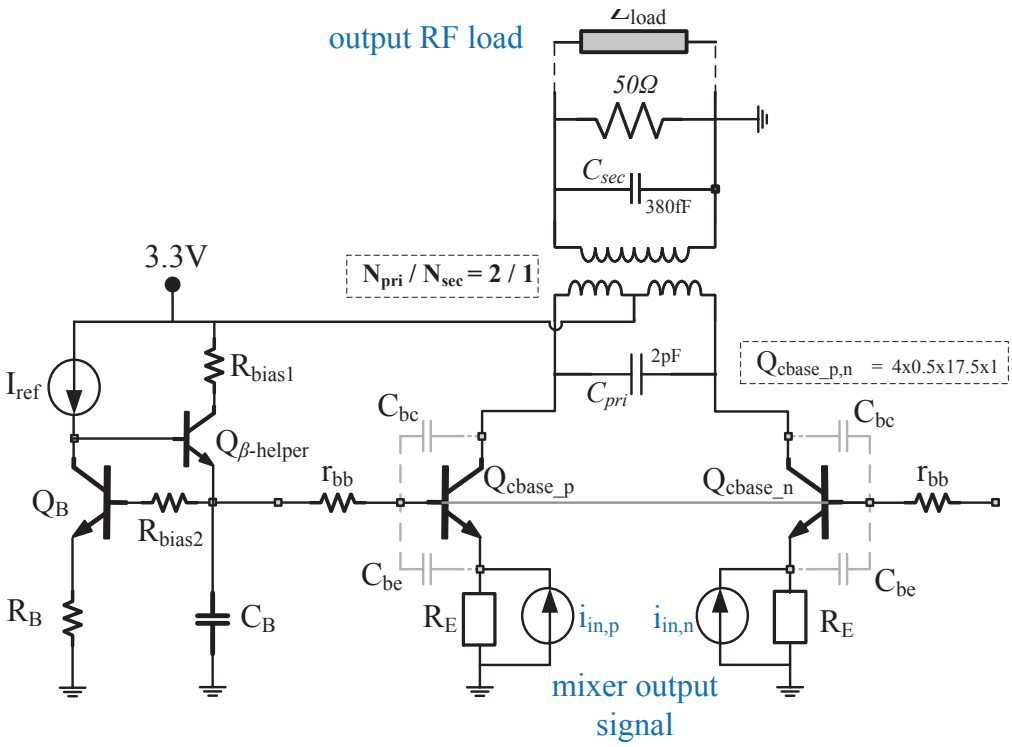

Figure 6.38: Common Base Output Stage and RF transformer at mid to high frequencies

$$Z_{\mathrm{T}} = \frac{V_{\mathrm{L}}}{I_{\mathrm{in}}} = \frac{1}{\left(\frac{1}{Z_{\mathrm{ec}}||r_{\mathrm{o}}} + \frac{1}{Z_{\mathrm{cb}}||Z_{\mathrm{L}}}\right)\left(\frac{1}{g_{\mathrm{m}}+\frac{1}{Z_{\mathrm{ec}}||r_{\mathrm{o}}}}\right)\left(\frac{1}{R_{\mathrm{S}}} + \frac{1}{Z_{\mathrm{eb}}}\right) + \left(\frac{1}{Z_{\mathrm{cb}}||Z_{\mathrm{L}}}\right)} \tag{6.74}$$

where, $Z_\pi = r_\pi||\frac{1}{sC_\pi}$, $Z_\mu = \frac{1}{sc_\mu}$, $Z_b = r_{\mathrm{bb}} + R_{\mathrm{B}}||\frac{1}{sC_{\mathrm{B}}}$ [43] and, $Z_{\mathrm{ec}} = (Z_\pi Z_\mu + Z_\mu Z_{\mathrm{b}} + Z_{\mathrm{b}} Z_\pi)/Z_{\mathrm{b}}$, $Z_{\mathrm{eb}} = (Z_\pi Z_\mu + Z_\mu Z_{\mathrm{b}} + Z_{\mathrm{b}} Z_\pi)/Z_\mu$ and $Z_{\mathrm{cb}} = (Z_\pi Z_\mu + Z_\mu Z_{\mathrm{b}} + Z_{\mathrm{b}} Z_\pi)/Z_\pi$. Z_{L} is the load impedance which will be discussed further in 6.5.1. We could simplify this by assuming that $Z_{\mathrm{b}} \approx 0$ and $Z_{\mathrm{ec}} = \infty$. This yields (6.74) being simplified to

$$\begin{aligned} Z_{\mathrm{T}} &= \frac{1}{\left(\frac{1}{r_{\mathrm{o}}} + \frac{1}{Z_\mu||Z_{\mathrm{L}}}\right)\left(\frac{1}{g_{\mathrm{m}}+\frac{1}{r_{\mathrm{o}}}}\right)\left(\frac{1}{R_{\mathrm{S}}} + \frac{1}{Z_\pi}\right) + \left(\frac{1}{Z_\mu||Z_{\mathrm{L}}}\right)} \\ &= \left[\frac{1}{r_{\mathrm{o}}||Z_\mu||Z_{\mathrm{L}}}\frac{1}{\frac{1}{g_{\mathrm{m}}}||r_{\mathrm{o}}}\frac{1}{R_{\mathrm{S}}||Z_\pi} + \frac{1}{Z_\mu||Z_{\mathrm{L}}}\right]^{-1} \end{aligned} \tag{6.75}$$

[43] At mid to high frequencies, if we momentarily ignore other capacitances, we have $Z_{\mathrm{in,CB}} \approx R_{\mathrm{g}} + R_{\mathrm{e}} + r_\pi/(\beta+1) \Longrightarrow 1/\omega C_{\mathrm{B}} << ((R_{\mathrm{g}}+R_{\mathrm{e}})(\beta+1)+r_\pi)$, where R_{g} is the generator/source resistance. Consequently, this yields a minimum design value of, $C_{\mathrm{B}} = N/(\omega_{\min}((\beta+1)(R_{\mathrm{g}}+R_{\mathrm{e}})+r_\pi))$ where N is a reasonably large number. This creates a dominant low frequency pole at the Base ensuring a stable incremental Ground node.

If we were to ignore the Early-effect ($r_o = V_A/I_C \approx 1.27K\Omega$), this reduces to

$$Z_T \approx \left[\frac{1}{g_m}\frac{1}{Z_L||\frac{1}{sC_\mu}}\frac{1}{R_S||R_E||r_\pi||sC_\pi} + \frac{1}{\frac{1}{sC_\mu}||Z_L}\right]^{-1} \tag{6.76}$$

Now, if we set $Z'_L = 1/(\frac{1}{sC_\mu}||Z_L)$ [44], $Z'_{in} = 1/(R_S||R_E||r_\pi||sC_\pi)$, Z_T evaluates to

$$\begin{aligned} Z_T &\approx \left(\frac{1}{g_m Z'_L}\frac{1}{Z'_{in}} + \frac{1}{Z'_L}\right)^{-1} \\ &\approx \frac{g_m}{\frac{1}{Z'_{in}} + g_m}.Z'_L \end{aligned} \tag{6.77}$$

As is evident from the foregoing equation, in order to achieve a broadband performance necessary for this design, the current must be increased. This yields a higher input pole ($g_m/(C_\pi + C_{mixer,out})$) at the input but reduces the headroom at the output. Although the (first order derivative of) g_m is uniform for a large bandwidth, it is constrained in its minimum value, as $1/g_m$ as $g_m = I_c/V_T$ and reducing this increases Mixer RF port impedance, worsening the current gain looking into the input of the Mixer (see (6.44)). At the same time, reducing the load resistance will reduce gain and increase output current noise. To simplify the tradeoffs, a (tuned) transformer load is chosen whose benefits are two-fold. The transformer's inductance can be used, to tune out the capacitance (referring to C_{bc} or C_μ at the quiescent bias point,) at resonance, achieving a higher power gain when a turns ratio larger than 1 : 1 is used [45]. Secondly, the transformer, when used as a balun, shifts the common-mode to ground, i.e., converting from differential to single-ended signalling, necessary for interfacing to subsequent blocks in the transmit chain.

6.5.0.1 Noise Performance

In order to simplify the noise analysis we make a few assumptions. The Early-effect is neglected (as above) and a large $\beta(\approx 250)$ is assumed. The load is evaluated at resonance, when the Transformer's turns ratio reaches it intended design value (of 2 : 1, see Section 6.5.1).

The noise of the bias stage needs to be taken into account, although it is mostly filtered by the large shunt capacitance C_B. The output noise current of the current mirror reference bias is determined to be

$$I_{n,\text{out,CBb}} \approx \frac{V_{n,r_{bb}} - I_{n,R_B}.R_B + I_{n,Q}(\frac{R_B+r_{bb}}{\beta} + \frac{1}{g_m})}{\frac{r_{bb}}{\beta} + R_B + \frac{1}{g_m}} \tag{6.78}$$

where $V_{n,r_{bb}} = 4kTr_{bb}$ is the voltage noise of the resistance of the Base, $I_{n,R_B} = 4kT/R_B$ is the equivalent current noise of the degeneration resistor used in the Current Mirror bias

[44] We make an assumption here that r_{bb} in the CB stage has little impact on the gain and therefore C_μ can be placed from the collector to ground, in parallel with the tuning capacitance at the Primary, C_{pri}.

[45] By using a high primary-to-secondary turns ratio 'N_{pri}/N_{sec}', the transformer performs an impedance translation of the impedance Z_{sec} (50 Ω) at the secondary of the transformer to its equivalent at the primary, $Z_{sec,\ pri} = (N_{pri}/N_{sec})^2.Z_{sec}$. This impedance $Z_{sec,\ pri}$ is part of (6.77) above, indicating how an enhancement in gain is achieved. For the sake of simplicity, we only refer to the effective turns ratio at resonance.

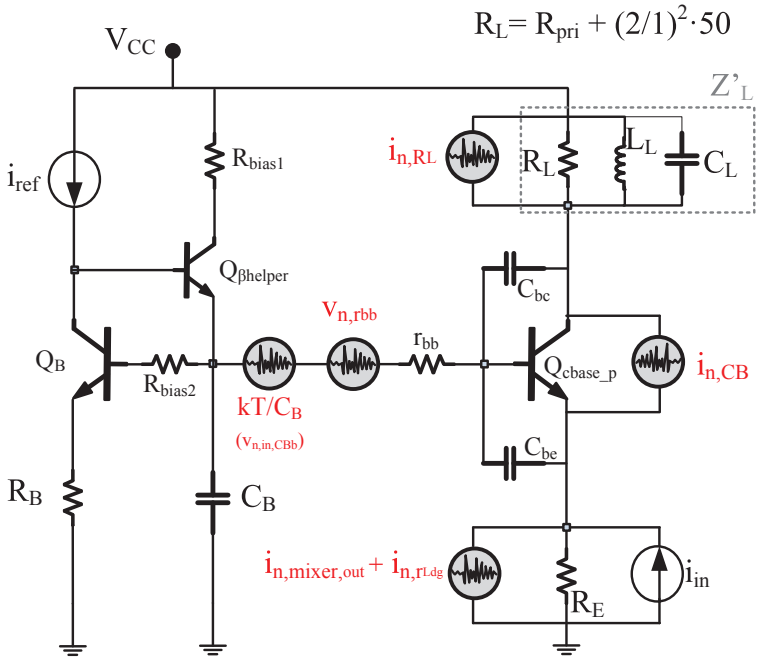

Figure 6.39: Network to calculate output current noise of the Common Base stage

reference and $I_{\mathrm{n,Q}} = 2qI_{\mathrm{C}}$ is the shot noise current of the BJT. The noise contribution of the beta-helper is not taken into account. The output noise of the Current Mirror bias reference can be converted into an equivalent voltage Base noise so that it can be added to the noise at the Base of the CB stage.

$$V_{n,\mathrm{in,CBb}} \approx \frac{1}{\frac{g_{\mathrm{m}}}{1+g_{\mathrm{m}}.R_{\mathrm{B}}}} . \frac{V_{n,r_{\mathrm{bb}}} - I_{\mathrm{n,R}_B}.R_{\mathrm{B}} + I_{\mathrm{n,Q}}(\frac{R_{\mathrm{B}}+r_{\mathrm{bb}}}{\beta} + \frac{1}{g_{\mathrm{m}}})}{\frac{r_{\mathrm{bb}}}{\beta} + R_{\mathrm{B}} + \frac{1}{g_{\mathrm{m}}}} \tag{6.79}$$

The noise can be represented by an equivalent noise source, $4kTR'_{\mathrm{eq,CBb}}$, where,

$$R'_{\mathrm{eq,CBb}} = \left(\frac{1+g_{\mathrm{m}}.R_{\mathrm{B}}}{g_{\mathrm{m}}}\right)^2 . \frac{r_{\mathrm{bb}} + \frac{1}{2g_{\mathrm{m}}} + \frac{g_{\mathrm{m}}}{2\beta^2}(R_{\mathrm{B}}^2 + r_{\mathrm{bb}}^2) + R_{\mathrm{B}}}{(R_{\mathrm{B}} + \frac{1}{g_{\mathrm{m}}} + r_{\mathrm{bb}})^2} \tag{6.80}$$

This noise appears as a series voltage at the Base terminal, as pointed out above. But, when the noise is integrated over its bandwidth to determine its total contribution, this results in a value kT/C_{B} due to the filtering by the large shunt capacitor C_{B}. With C_{B} being set (see 43) to a large value, the contribution of the bias network is relatively negligible. The CB stage in itself, however, has the following noise contribution to the output. To make the analysis less complicated, several simplifications are made. We express it as an output

voltage noise across the load network.

$$\begin{aligned} V_{n,\mathrm{out,CB}} &= \frac{Z'_{\mathrm{L}}}{Z_{\mathrm{in,dg}}}.\frac{I_{n,\mathrm{CB}} + g_{\mathrm{m}}\frac{Z_{\pi}}{Z_{\pi}+Z_{\mathrm{b}}+Z_{\mathrm{in,dg}}}V_{n,r_{\mathrm{bb,CB}}}}{g_{\mathrm{m}} + \frac{1}{Z_{\mathrm{in,dg}}}} + Z_{\mathrm{T}}(I_{n,\mathrm{mixer,out}} + I_{r_{L,\mathrm{dg}}}) \\ &= Z'_{\mathrm{L}}\frac{I_{n,\mathrm{CB}} + g_{\mathrm{m}}\frac{Z_{\pi}}{Z_{\pi}+Z_{\mathrm{b}}+Z_{\mathrm{in,dg}}}V_{n,r_{\mathrm{bb,CB}}}}{g_{\mathrm{m}}Z_{\mathrm{in,dg}} + 1} + Z_{\mathrm{T}}(I_{n,\mathrm{mixer,out}} + I_{r_{L,\mathrm{dg}}}) \end{aligned} \tag{6.81}$$

where $Z_{\mathrm{in,dg}}$ [46] is the impedance of the degeneration network including C_{π} of the CB stage and any parasitic capacitance ($C_{\mathrm{par,dg}}$) of the degeneration inductor L_{dg}. g_{m} is the transconductance of the CB stage and $I_{r_{L,\mathrm{dg}}}$ and $I_{n,\mathrm{CB}}$ are the current noise associated with the resistance $r_{L,\mathrm{dg}}$ of the degeneration inductor and the DC current shot noise of the Bipolar transistor, respectively. An inductor with a high Q factor will have lower parasitic resistance which will yield a high current noise ($\sqrt{4kT/r_{L,\mathrm{dg}}}$ nv/$\sqrt{\mathrm{Hz}}$). Given the high trans-impedance ratio of the CB stage, this presents a tradeoff between the linearity and noise performance of this stage. It is also worth noting that the impedance Z'_{L} seen at the output of the CB stage, is in fact the impedance of the primary of the transformer (used as a balun), which also takes into account the C_{μ} of the CB stage. This voltage noise ($\sqrt{4kT \cdot 50}$ nv/$\sqrt{\mathrm{Hz}}$) of the 50Ω output matching resistor and the noise of the metal resistance of the transformer are not included in the above expression and will contribute additional noise to the output. Moreover, because the stage is a differential one, the total noise output will increase by 3dB (with the wanted signal increasing by 6 dB). Any voltage noise at the primary input will experience a transformation factor given by (6.82). The above expression sums up the total noise contribution of the AQM.

Due to constraints of time, we were not able to fully validate each of the above noise expressions through simulations. However our understanding of the primary noise contributors is similar to that indicated in Table 6.4.

6.5.1 Double Tuned Transformer

The differential to single ended signaling conversion is achieved by means of a RF transformer whose one output terminal at the secondary is shorted to ground. For an ideal case, this does not result in a loss ($-3dB$ if half the signal power is lost) as the common mode voltage of the primary terminals is merely shifted from $V_{\mathrm{cc}} = 3.3V$ to ground and the signal swing is retained. The transformer is a 'matched' or 'double-tuned' transformer in that, both sides of the transformer (see Figure 6.38) are tuned to approximately the same frequency but with a flexibility that permits to change the shape of the selectivity curve. This would otherwise be very narrow-band, if the resonances of the primary and secondary are not staggered. Such flexibility is useful because AQMs that are typically designed for Base Stations are very wide-band covering several octaves. Choosing a balun to achieve higher gain and linearity trades off against the requirement of large bandwidth. Unfortunately however, due to time constraints, we were only able to tune the balun for a single frequency (see Figure 6.41) of

[46] $Z_{\mathrm{in,dg}} = \frac{r_{L,\mathrm{dg}}+s(L_{\mathrm{dg}}(1-\omega^2 L_{\mathrm{dg}}C_{\mathrm{in}}))-r^2_{L,\mathrm{dg}}C_{\mathrm{in}}}{(1-\omega^2 L_{\mathrm{dg}}C_{\mathrm{in}})^2+(\omega)^2 r_{L,\mathrm{dg}}C_{\mathrm{in}}}$, where $C_{\mathrm{in}} = C_{\pi} + C_{\mathrm{par,dg}}$. The mixer output series cap will not change the design very much.

Table 6.4: Primary contributors of noise at the output port, simulated at 20 MHz carrier offset, LO power = 0 dBm, 40° Cel.

Device	**Noise type**	**Noise Contribution ($nV/\sqrt{/Hz}$)**	**% of Total**
I+ phase Input Current Mirror Bias Resistor	thermal	1.13E-09	17.76
I- phase Input Current Mirror Bias Resistor	thermal	1.13E-09	17.75
Q+ phase Input Current Mirror Bias Resistor	thermal	4.94E-10	3.41
Q- phase Input Current Mirror Bias Resistor	thermal	4.94E-10	3.41
RF output port (not part of design)	rn	4.54E-10	2.89
Q- phase Input feedback pMOS	Sth	4.04E-10	2.28
I- phase Input feedback pMOS	Sth	4.04E-10	2.28
Q+ phase Input feedback pMOS	Sth	4.02E-10	2.26
I+ phase feedback pMOS	Sth	4.02E-10	2.26
Q+ phase Input PTAT Current Bias pMOS (source)	Sth	3.47E-10	1.69
I+ phase Input PTAT Current Bias pMOS (source)	Sth	3.47E-10	1.69
Q- phase Input PTAT Current Bias nMOS (sink)	Sth	3.47E-10	1.68
I+ phase Input PTAT Current Bias nMOS (sink)	Sth	3.47E-10	1.68
Q+ phase Input PTAT Current Bias nMOS (sink)	Sth	3.46E-10	1.68
I- phase Input PTAT Current Bias nMOS (sink)	Sth	3.46E-10	1.68
Total Noise at 20 MHz carrier offset =		2.67	**$nV/\sqrt{/Hz}$**

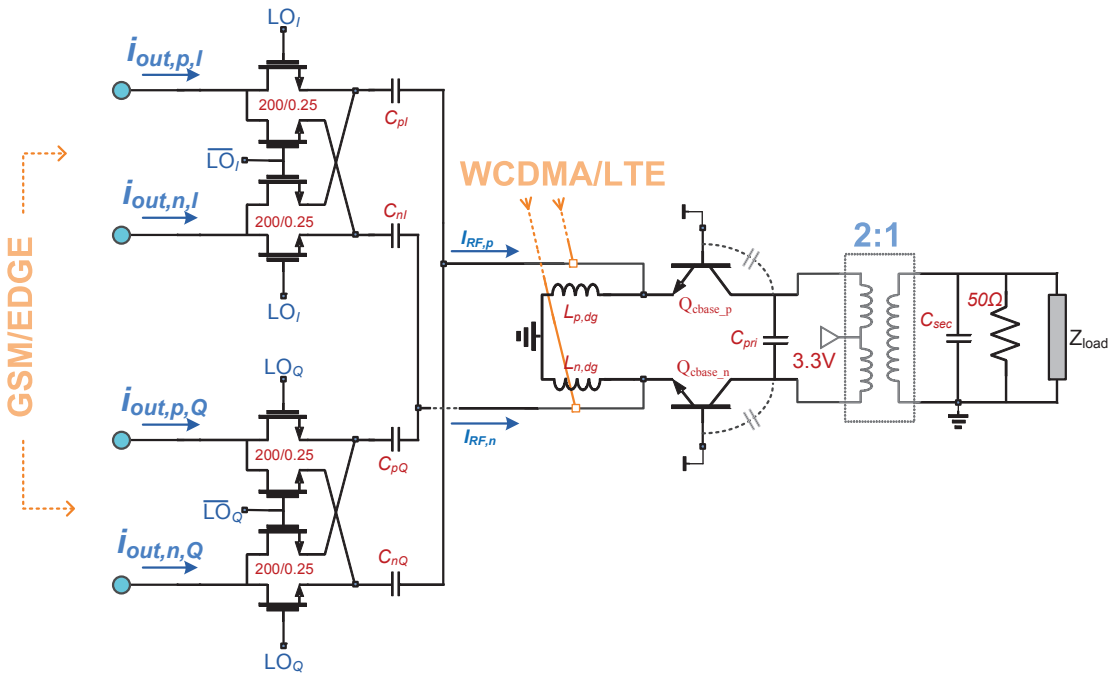

Figure 6.40: Mixing and output buffer stages of the AQM

2.140GHz (centre frequency for Band-I). The design therefore suffers from low bandwidth at the output. Staggered tuning of the balun is therefore earmarked for future work.

As suggested above, the transformer was chosen for a higher power gain (> 1 turns ratio) while providing single to differential conversion with high linearity and relatively negligible noise penalty. A balun with higher turns ratio might be more interesting, but the tuning with additional parasitics would involve more effort to make the stage broadband. For future designs, perhaps a more broadband and equally linear active-stage could also be investigated to replace the CB stage. Alternatively, the single-to-differential conversion with the balun could be introduced at an earlier stage within the AQM where the current transformation ratio of the transformer is exploited. Due to the fact that this design operated in the current mode (i.e., with low impedance nodes), such a step would be beneficial for broad-banding the (parallel RLC) transformer's frequency response. The output impedance matching is achieved by a $\geq 50\Omega$ resistor placed across the secondary of the transformer. This also helps with the power gain and makes the balun frequency response more broadband because the effective Q of the parallel RLC circuit is reduced.

We determine a voltage transformation across the transformer because we have identified the trans-impedance from the input of the CB stage where input current manifests as an output voltage at the transformer-primary terminals. The transformation or 'turns' ratio is

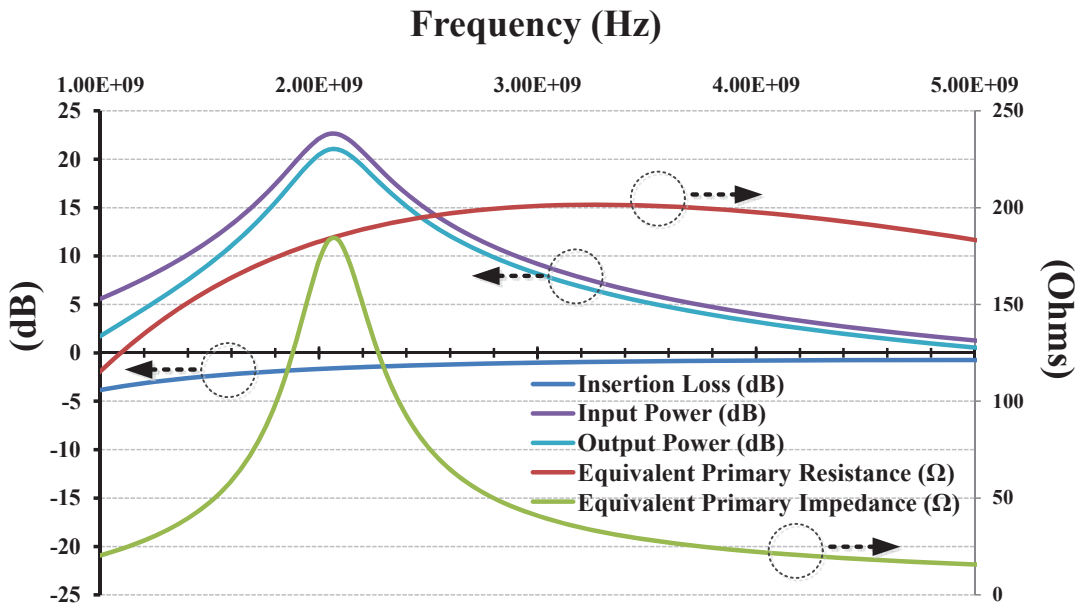

Figure 6.41: 2 : 1 lateral transformer RF characteristics versus frequency, showing the effective resistance and impedance of the primary and corresponding input power, output power and calculated insertion loss

given by the following expression [136].

$$\frac{E_{\text{pri}}}{E_{\text{sec}}} = \frac{Z_{\text{pri}}}{Z_{\text{pri}} + r_{\text{o}}} \frac{r_{\text{o}}\sqrt{C_{\text{pri}}C_{\text{sec}}}}{k} \left\{ \frac{\omega_{\text{pri}}}{\omega_{\text{sec}}} . \frac{1}{R_{\text{L}}C_{\text{sec}}} + \frac{\omega_{\text{sec}}}{\omega_{\text{pri}}} . \frac{1}{r_{\text{o}}C_{\text{pri}}} - \omega^2 \left(\frac{1-k^2}{\omega_{\text{sec}}\omega_{\text{pri}}} . \left(\frac{1}{R_{\text{L}}C_{\text{sec}}} + \frac{1}{r_{\text{o}}C_{\text{pri}}} \right) \right) \right. \tag{6.82}$$

$$\left. + j \left(\frac{-(\omega)^3}{\omega_{\text{pri}}\omega_{\text{sec}}}(1-k^2) + \omega \left[\frac{\omega_{\text{sec}}}{\omega_{\text{pri}}} + \frac{\omega_{\text{pri}}}{\omega_{\text{sec}}} + \frac{1-k^2}{\omega_{\text{sec}}\omega_{\text{pri}} r_{\text{o}} R_{\text{L}} C_{\text{pri}} C_{\text{sec}}} \right] - \frac{\omega_{\text{sec}}\omega_{\text{pri}}}{\omega} \right) \right\} \tag{6.83}$$

where r_{o} is the small signal output resistance of the transistor, C_{pri} is the Primary terminal tuning capacitance, C_{sec} is the Secondary terminal tuning capacitance, k is the coefficient of mutual coupling, given by $M = k\sqrt{L_{\text{pri}}L_{\text{sec}}}$, $\omega_{\text{pri}} = 1/\sqrt{L_{\text{pri}}C_{\text{pri}}}$, $\omega_{\text{sec}} = 1/\sqrt{L_{\text{sec}}C_{\text{sec}}}$ and R_{L} is the 50Ω resistor for output matching. We evaluate Z_{pri}, which is the impedance looking into the Primary of the transformer for a more realistic case, taking into account also the winding resistance r_{pri} and r_{sec} of the Primary and Secondary respectively. This is given by the expression,

$$\begin{aligned} Z_{\text{pri}} &= \left[r_{\text{pri}} + sL_{\text{pri}} - \frac{s^2M^2(1+R_{\text{L}}C_{\text{sec}})}{(r_{\text{sec}}+L_{\text{sec}})(1+sC_{\text{sec}}R_{\text{L}}) + R_{\text{L}}} \right] \\ Z'_{\text{pri}} &= Z_{\text{pri}} || \frac{1}{sC_{\text{pri}}} \end{aligned} \tag{6.84}$$

As is evident, C_{pri} is used to tune out the imaginary part of Z_{pri} at resonance to yield a scaled impedance $N^2 R_{\text{L}}$ to the CB stage which produces the gain. It is also important to note that the choice of turns ratio also has an impact on the input impedance of the CB stage [103] as it is not a unilateral stage (see (6.40) and (6.41)). By assuming $Q_{\text{sec}} = \omega L_{\text{sec}}/r_{\text{sec}}$, $Q_{\text{pri}} = \omega L_{\text{pri}}/r_{\text{pri}}$, we can define the efficiency of the transformer η, as a ratio between the power dissipated in the load resistance R_L to the powers dissipated in r_{pri}, r_{sec} and R_{L}, as given by the following expression.

$$\begin{aligned}\eta = \frac{P_{\text{load}}}{P_{\text{total}}} &= \frac{I_{\text{load}}^2 R_{\text{L}}}{I_{\text{load}}^2 R_{\text{L}} + I_{\text{pri}}^2 r_{\text{pri}} + I_{\text{sec}}^2 r_{\text{sec}}} \\ &= R_{\text{L}} \Big/ \Bigg(R_{\text{L}} + \frac{\omega L_{\text{sec}}}{Q_{\text{sec}}} (1 + \omega L_{\text{sec}} r_{\text{sec}})^2 \\ &\quad + \frac{1}{\omega^2 M^2} \frac{\omega L_{\text{pri}}}{Q_{\text{pri}}} \big[(R_{\text{L}} + r_{\text{sec}} - \omega^2 R_{\text{L}} L_{\text{sec}} C_{\text{sec}})^2 \\ &\quad + (\omega L_{\text{sec}} + \omega C_{\text{sec}} R_{\text{L}} r_{\text{sec}})^2 \big] \Bigg)\end{aligned} \tag{6.85}$$

The insertion loss of the transformer is inverse of its efficiency. Hence, if we set $L_{\text{pri}} = N^2 L_{\text{sec}}$[47], $\omega L_{\text{sec}} = A R_{\text{L}}/(1 + A^2)$, $\omega C_{\text{sec}} = A/R_{\text{L}}$, with $A = Q_{\text{sec}}/\sqrt{1 + k^2 Q_{\text{pri}} Q_{\text{sec}}}$, we note that the efficiency η becomes a function of the L_{sec} and C_{sec}, with $k, Q_{\text{pri}}, Q_{\text{sec}}$ being given. Differentiating (6.85) with respect to $L_{\text{sec}} C_{\text{sec}}$, efficiency η is maximum when the denominator is at a minimum and the corresponding insertion loss[48] IL_{dB} is given by,

$$\begin{aligned}\eta_{\max} &= \frac{1}{1 + 2\sqrt{(1 + \frac{1}{Q_{\text{pri}} Q_{\text{sec}} k^2}) \pm \frac{1}{Q_{\text{pri}} Q_{\text{sec}} k^2} + \frac{1}{Q_{\text{pri}} Q_{\text{sec}} k^2}}} \\ \text{IL}_{\text{dB}} &= \frac{1}{\eta_{\max}}\end{aligned} \tag{6.86}$$

where, IL_{dB} is the corresponding insertion loss. This relationship allows to more accurately define values for L_{sec}, C_{sec} for a more optimized efficiency. As pointed out above, C_{pri} is not part of this expression below and its purpose is used to cancel out the reactive components of Z_{pri} in (6.85).

6.6 Simulation results

The schematic was simulated using Spectre-RF in the Cadence environment. We present the corresponding results in this section. If not specified, the temperature for the simulation is set at +40° Cel.

[47] This is only a simplification as the inductances of the transformer vary with frequency

[48] It is possible to obtain the total gain using the (6.86), together with the gain of the input resistor ($1/R_{\text{in}}$), the current-mirror ratio ($M/1$), the attenuator loss (see (6.18)), the current divider loss at input of the Mixer (see (6.44)), the Mixer conversion function (see (6.36)) and finally the trans-impedance of the CB stage where the input current is converted into a voltage (see (6.77)). However, the combined equation becomes quite complex unless simplifications are made.

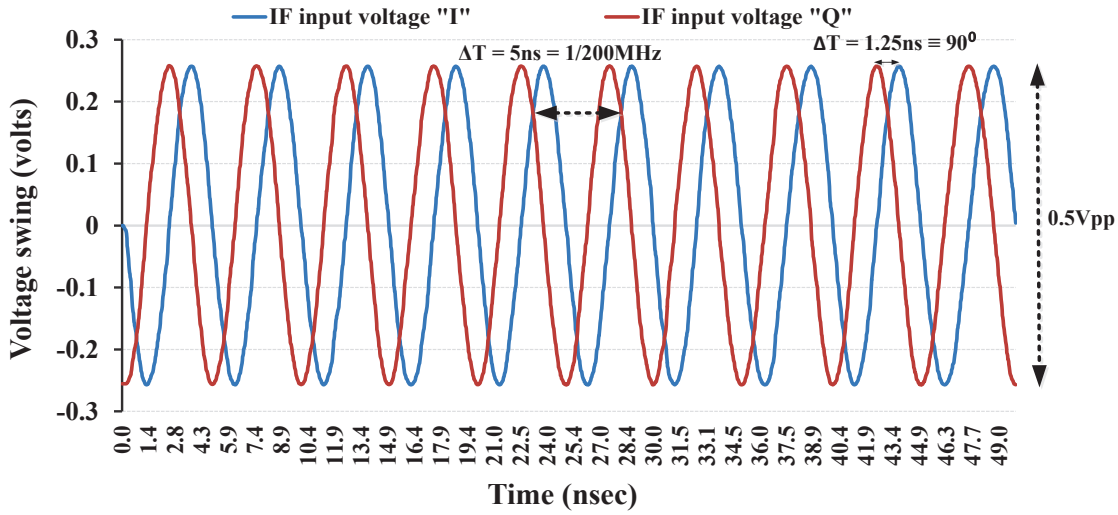

Figure 6.42: Differential voltage swing at the input of the I and Q pins of the AQM

6.7 Time domain waveforms

We first look at the time domain waveforms at various junctions in the circuit. The Figure 6.42 indicates a differential voltage of 500 mV peak-to-peak (pp), at the I and Q path input pins of the AQM, for a DAC output current of 10 mApp, with a single-tone input frequency at 200 MHz. The voltage swing at the input of the AQM is halved relative to the unloaded voltage swing of 1 Vpp at the output of the DAC (corresponding to 10 mApp), indicating an approximate input impedance of 100Ω differential, at the given frequency.

The differential input current swing to the I and Q mixers, together with differential output voltage swing of the I and Q path attenuators are shown in Figure 6.43, for the same input.

As the control voltage increases (range 0.0 V to 5.0 V), the currents from each of the 40 parallel cells respond in the manner illustrated in Figure 6.44.

The total current in the signal branch reduces in logarithmic fashion causing the input DC (common-mode) voltage to increase towards the supply. The overdrive of the switch is reduced as shown in Figure 6.45, but the LO waveform is sufficiently larger than the (now) attenuated IF signal, thereby maintaining proper switching functionality.

The polyphase filter produces the four-phase LO waveforms necessary for the mixer operation. This is illustrated in Figure 6.46. The switch is biased at a DC voltage of 3.8V and has a voltage swing of approximately 2.125V. The IQ combined output current from the mixer is also shown.

The waveforms in Figure 6.47 show the relationship between the mixer input and output currents, clearly showing the switching (up-conversion) action.

The output current from the mixer is buffered into the load via the CB stage and the

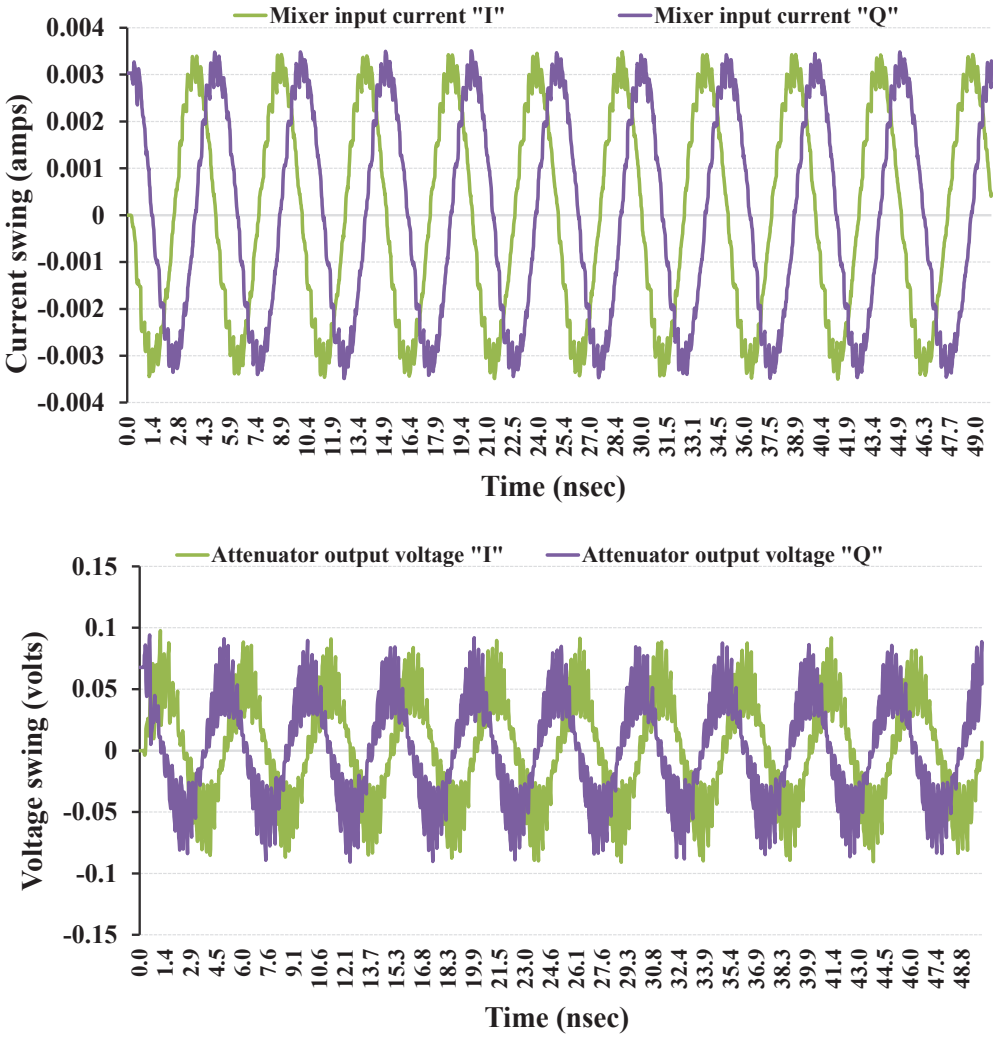

Figure 6.43: Attenuator differential output voltage swing (a) and Mixer differential input current(b)

on-chip transformer. The Figure 6.48 shows the output (unloaded) voltage and current at the secondary of the balun.

6.8 S-parameter simulation results

The two-port Scattering parameters were simulated at the IF and RF ports, with the LO provided by an ideal source, matched to 50Ω. The corresponding S11 and S22 are depicted in Figure 6.49. While the S11 indicates a return loss better than 10 (VSWR $\leq$ 2) dB wide-band match, the output return loss given by S22, is better than 10dB for approximately 250 MHz. This is due to improper tuning of the double-tuned transformer at the RF output.

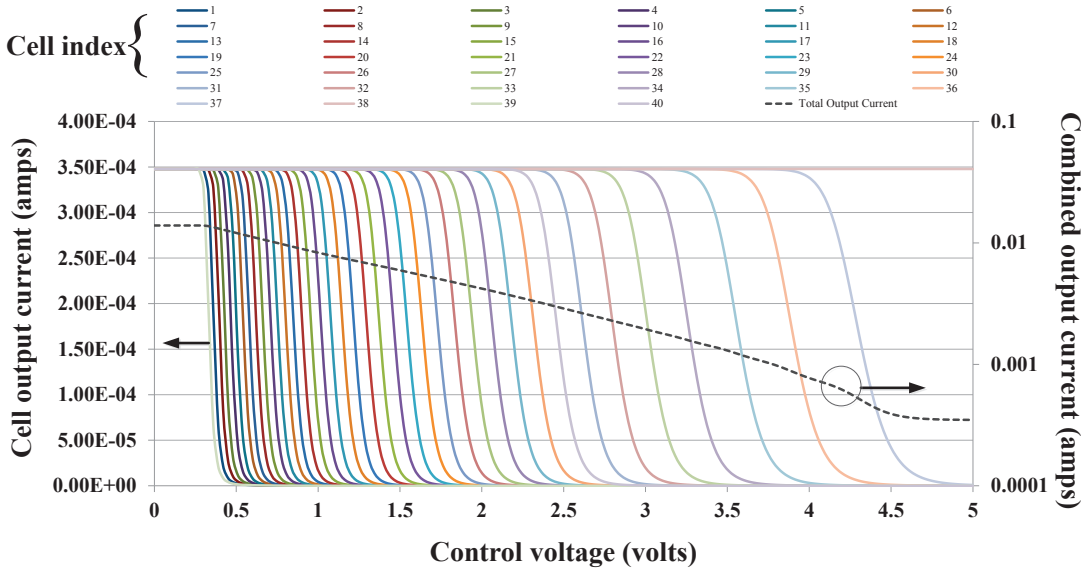

Figure 6.44: Variation of attenuator cell currents with control voltage

The S22 can be improved if the capacitive and inductive values of primary and secondary are properly chosen, to provide two resonances which are spaced to as to provide a more broadband response. While this design does not achieve the bandwidth of the best-in-class product(s) (e.g. TRF3703), the rest of the performances are approximately at par and in certain cases better than several products in the market.

6.9 Parametric sweeps

Here we characterise the design for parametric sweeps of the control voltage, input frequency, LO power and input common-mode voltage. The simulations were performed for a DAC output current of 5 mApp, which corresponds to -17.1 dBm per tone across the (100Ω) input impedance of the AQM. The setup was made such that two tones split the total DAC output current equally instead of the power. This allows us to characterise the design for increasing PAPR values and also observe the large signal compression in time domain since the total current and swing remain the same, even if the number of tones is increased. For two tone simulations, the two tones are spread 20 MHz apart to keep simulation data to a minimum[49].

The Figure 6.50 output power of a single tone at the output of the attenuator, against input frequency (swept from 50 MHz to 500 MHz). The IF bandwidth at the output of the attenuator (i.e., the mixer input port) is visibly larger than 500 MHz and is comparable to several best-in-class products.

[49]This unfortunately does not allow us to observe sharper transitions in the signal which would be the case if the frequencies of the two tones were spaced far apart.

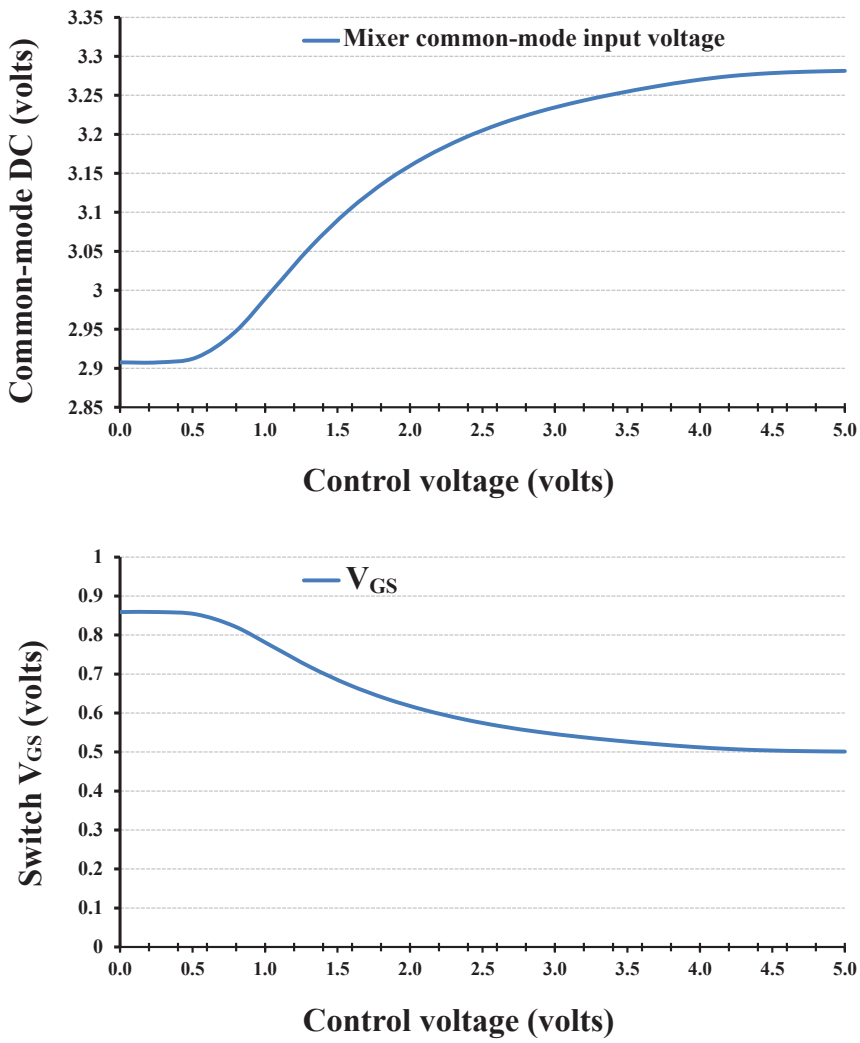

Figure 6.45: Variation of Mixer input common-mode voltage and switch V_{GS}, with respect to the control voltage V_{control}

Similarly, the RF output bandwidth is also evident from the Figure 6.51.

The following simulation shows the variation in the performance parameters, primarily, OIP3, IIP3, output noise (at 20 MHz carrier offset), image suppression and carrier suppression (i.e. LO leakage). The simulations were made for 50 MHz, 200 MHz, 350 MHz. The corresponding image suppression (60dBc at $V_{\text{control}} = 0$V), LO carrier leakage (-80dBc at $V_{\text{control}} = 0$V) and $2 \cdot F_{\text{LO}}$ amplitude (-90dBc at $V_{\text{control}} = 0$V) were all well within limits for all IF frequencies. However, these values need to be validated with post-layout simulation and measurements for the same. We observe that a significant part of the non-linearity is due to

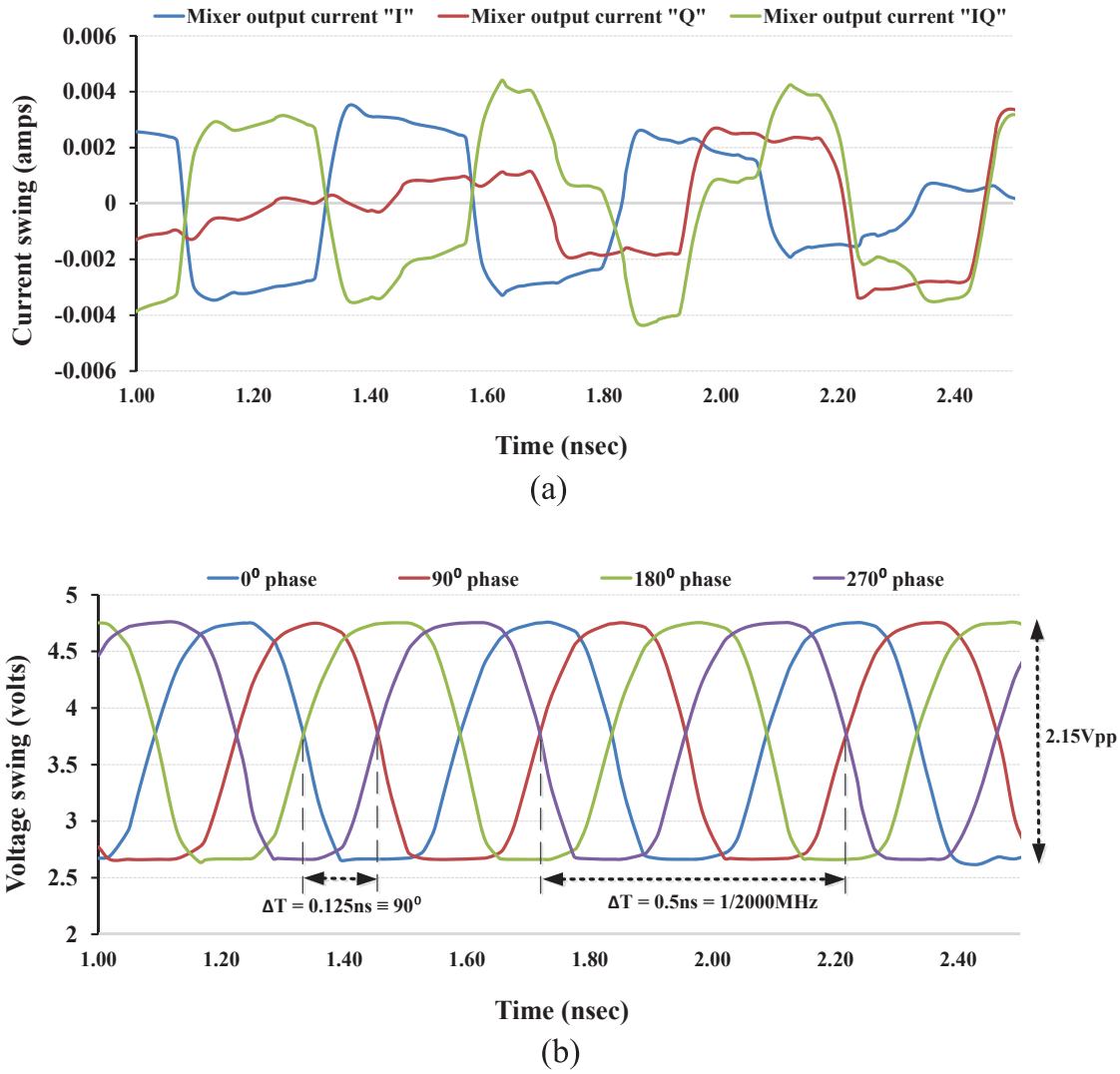

Figure 6.46: Mixer output current waveforms (a) and quadrature LO voltage signals (b)

the finite $1/g_{\mathrm{m}}$ and non-linear $1/g_{\mathrm{ds}}$ of the pMOS in the input feedback path. Any unwanted voltage fluctuations at the input node would be amplified by the non-ideal pMOS which are further amplified and distorted as the signal traverses the rest of the circuit. Increasing the current through this transistor in order to increase the g_{ds} could therefore improve linearity performance. This can be achieved without significantly increasing the current in the attenuator branch of the current-mirror stage, as that would influence the channel resistance of the Mixer and consequently the current gain of the input stage (see (6.44)). We also observe that while the Mixers are relatively linear ($\approx$ 40dBm, converted into power from the current

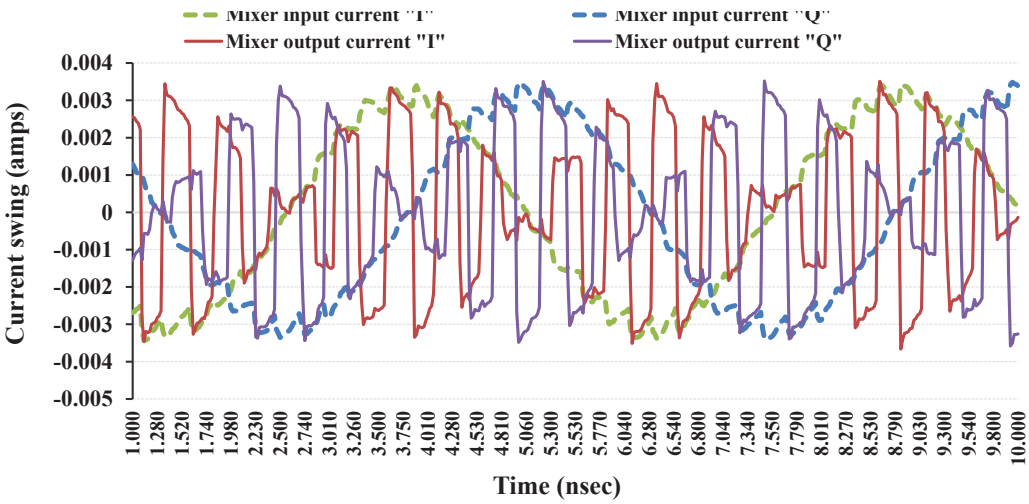

Figure 6.47: Mixer input and output current waveforms

domain), the CB stage introduces non-linearity which is comparable with the pMOS at the input stage.

All the gains are calculated from single-ended output (50Ω) to differential input (100Ω), across any one path, In-phase 'I' or Quadrature 'Q'. The gain accuracy for an input frequency of 200 MHz (second tone at 220 MHz) is better than ±0.5 dB, illustrated in Figure 6.55, although this has not been simulated against temperature variations.

The output noise spectral density (NSD) is approximately −158.5 dBm/Hz and varies with the control voltage, as illustrated in Figure 6.56 The dynamic range ia calculated with respect to the noise in bandwidth of 60 MHz, corresponding to the UMTS Band-I (2110 MHz - 2170 MHz). From the trend for the dynamic range shown in Figure 6.56 we determine that the SNR degrades by 0.722dB for every dB of attenuation. This can be compared with typical passive π and T attenuators whose SNR degrades approximately 1 dB for every dB of attenuation.

The Figure 6.57 shows the degradation of the output noise floor and the dynamic range. From the trend for the dynamic range shown, we determine that the SNR degrades by 0.033dB for every dB of attenuation, which indicates that the output noise may not depend on the amplitude of the input signal.

The Figures 6.58 and 6.59 indicate the dynamic range due to noise (only), measured in a bandwidth of 60 MHz.

The Figure 6.60 shows the noise voltage versus frequency, corresponding to a DAC output current of 20 mApp and input tones at 200 MHz and 220 MHz. Figures 6.61 and 6.62 show noise performance corresponding to an LO power of 0 dBm and also control voltages 0.0 V, 2.0 V and 4.5 V, respectively. The noise at 20 MHz carrier offset does not significantly change with LO power or input signal power, but varies 0.722dB for every dB of attenuation produced when the control voltage is changed.

All of the noise calculations are without the influence of the LO phase noise. Based on our

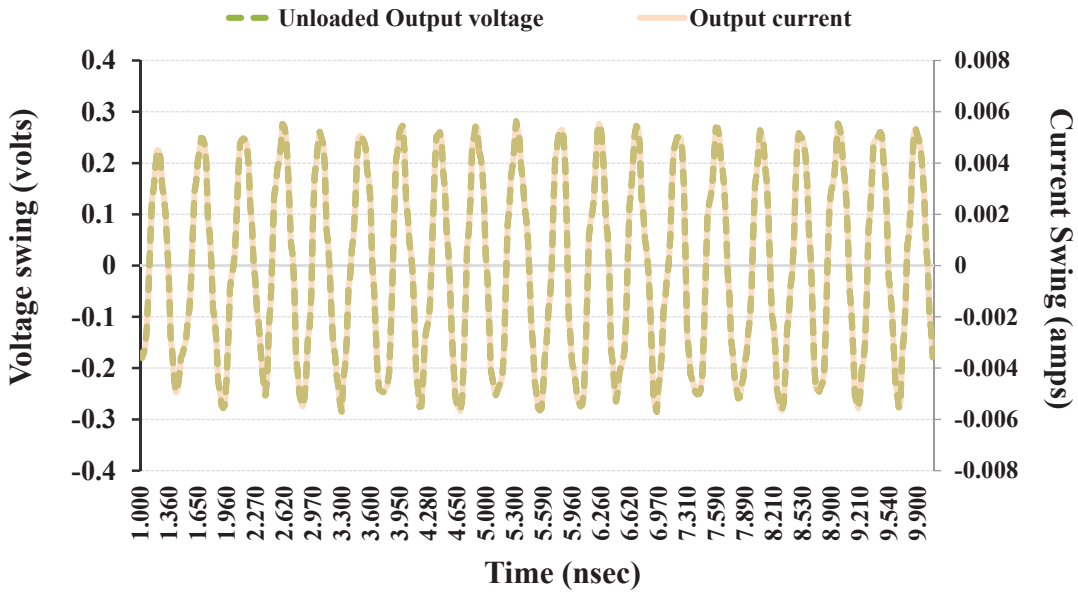

Figure 6.48: RF output voltage and current across the output (50Ω) impedance-matching resistor

calculation for phase noise requirements (see Section 4.5), the noise performance at the output of the AQM could increase to approximately $10\log[10^{\frac{-158.4\text{dBm/Hz}-30}{10}}+10^{\frac{-157\text{dBm/Hz}-30}{10}}]+30 = -154.7$ dBm/Hz, under the assumption that they are sufficiently uncorrelated. From these simulations, we notice that despite efforts taken minimise noise, a majority of the noise can be attributed to the IF biasing circuitry, that is then up-converted to RF. The noise at low frequencies is also pronounced indicating the significant contribution of the bias-networks, which is also up-converted to carrier frequency.

Simulations were also performed over temperature, where a drop in performance was observed over the low and high extremes. The graph 6.63 shows the various performance criteria simulated from $-40°$ Cel. to $+90°$ Cel.

From Figure 6.64 we notice a significant change in the slope of the linear-in-dB gain curve with respect to the control voltage, over a range of temperatures. This highlights an issue of temperature stability in the design, which will need to be addressed in future developments of this work.

6.10 Monte Carlo simulations

In order to observe the impact on performance of a randomised distribution of electrical parameters of the design, Monte Carlo simulations of 100 runs were also performed. The Figure 6.65 shows the distribution of OIP3, power gain, voltage gain, current gain, output

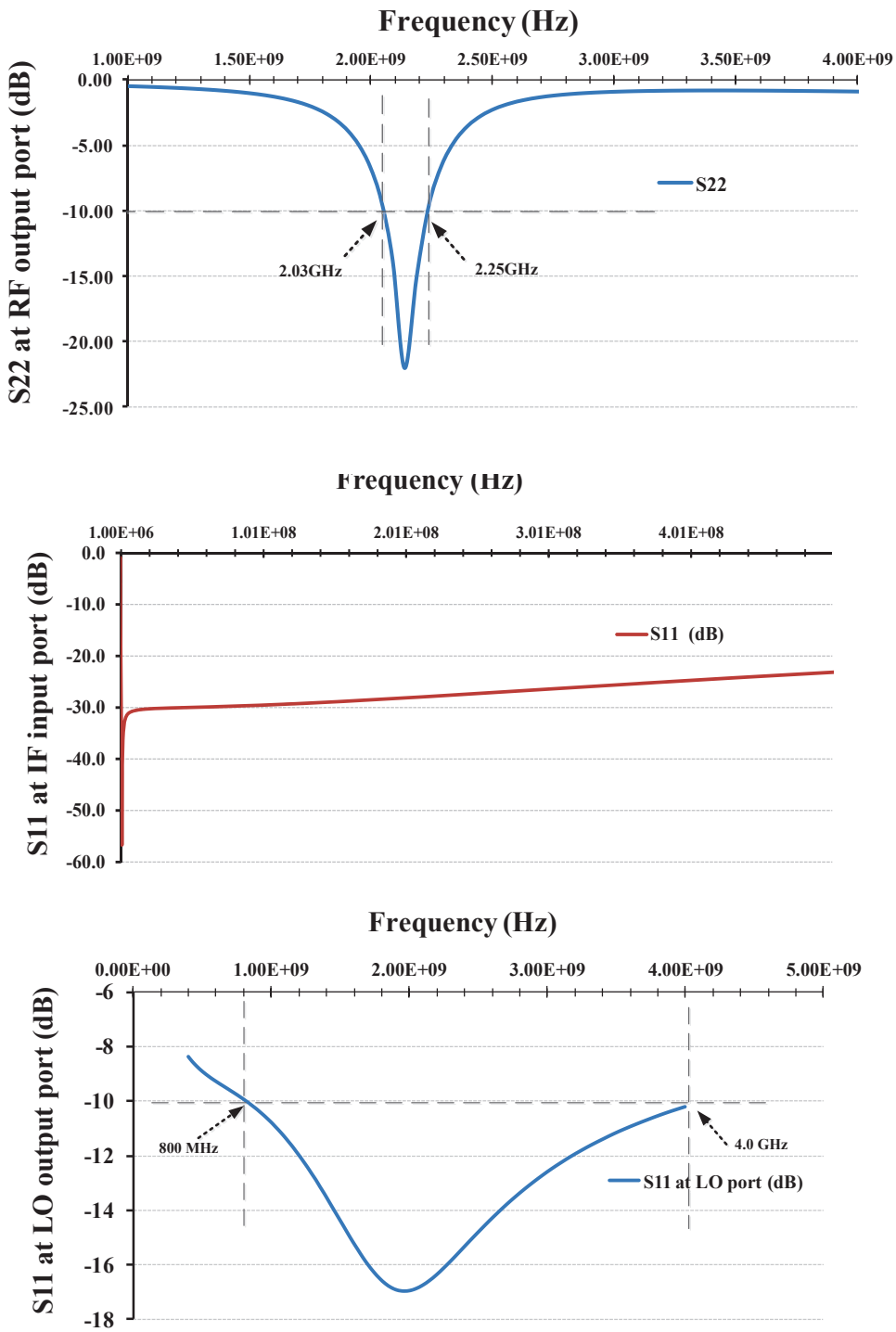

Figure 6.49: S11 at the IF input port and LO port of the AQM and S22 at the RF output port

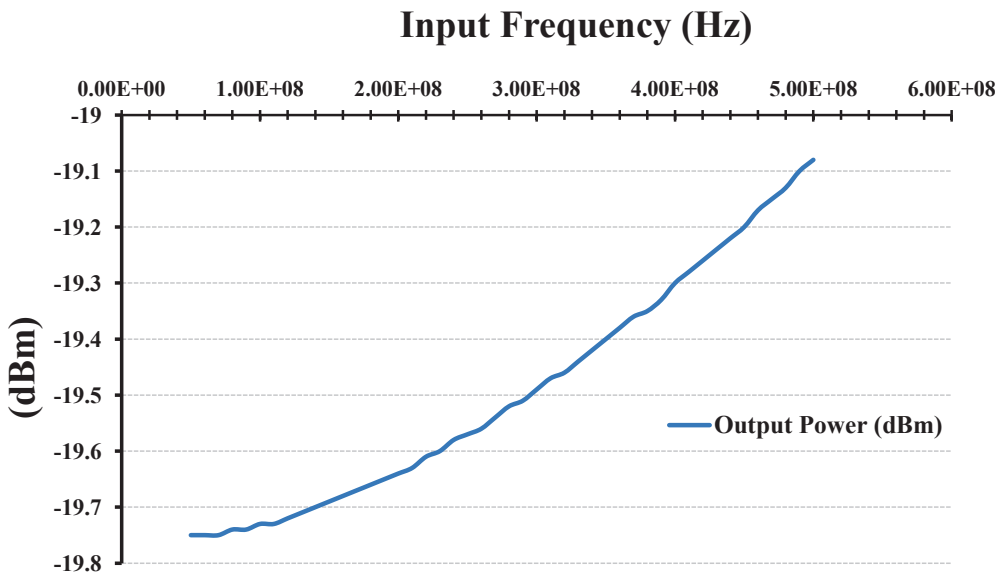

Figure 6.50: IF stage output power showing IF bandwidth

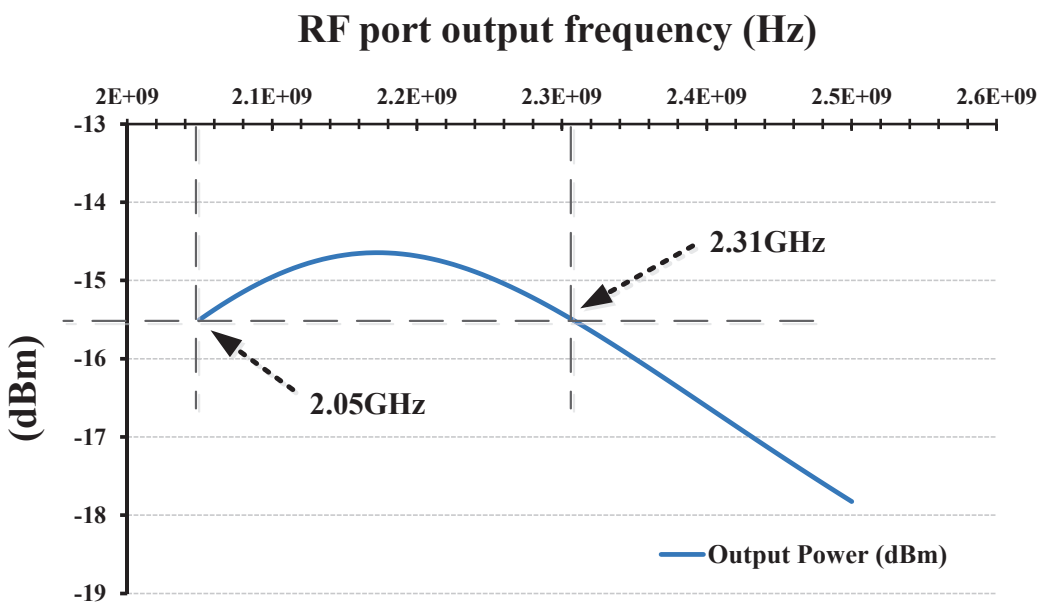

Figure 6.51: Output frequency sweep showing 1 dB RF bandwidth

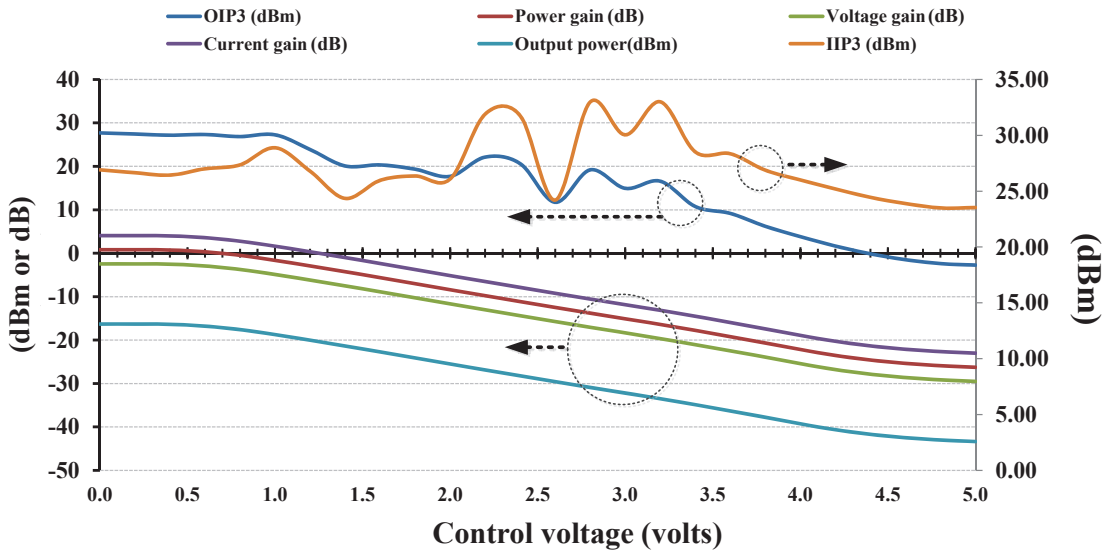

Figure 6.52: OIP3, power gain, voltage gain, current gain and IIP3 for 50 MHz and 70 MHz input-tone frequencies

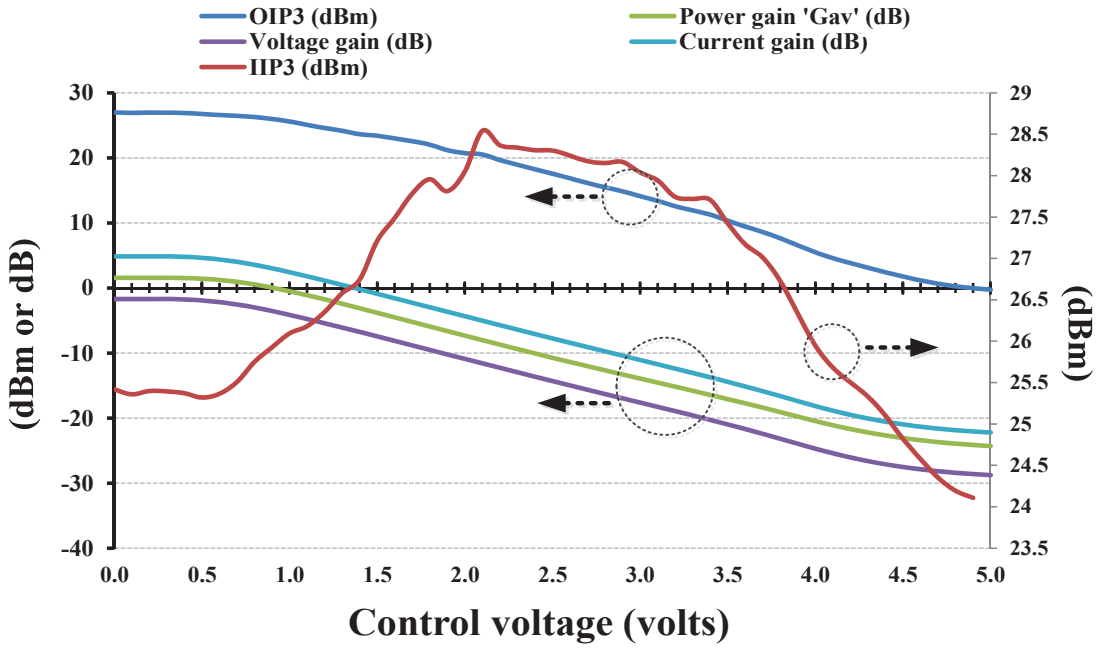

Figure 6.53: OIP3, power gain, voltage gain, current gain and IIP3 for 200 MHz and 220 MHz input-tone frequencies

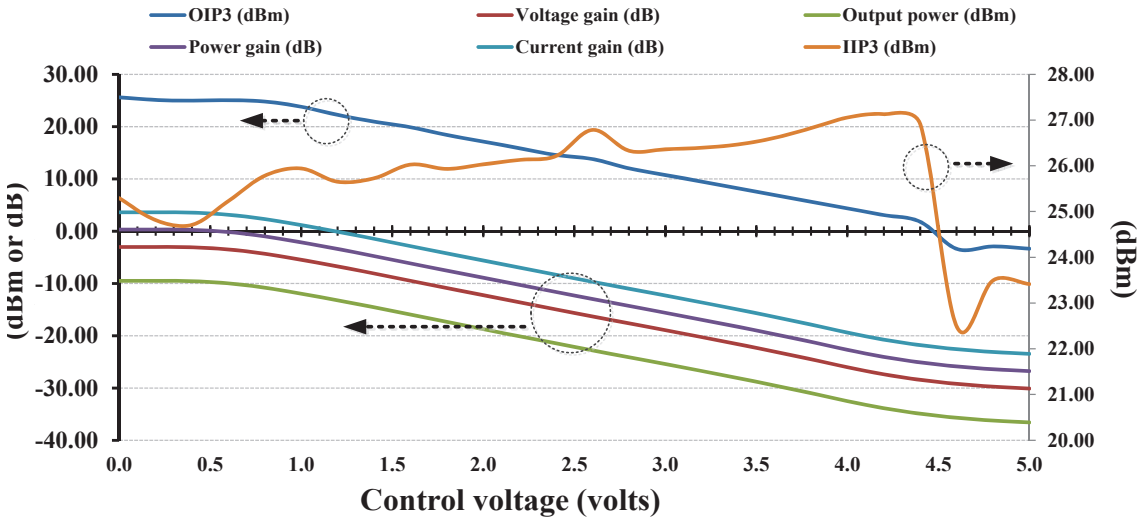

Figure 6.54: OIP3, power gain, voltage gain, current gain and IIP3 for 350 MHz and 370 MHz input-tone frequencies

noise spectral density (at 20 MHz offset), single tone output power (at 100 MHz), carrier feed-through and sideband suppression.

6.11 Summary

In this chapter we have presented the design of a variable-gain AQM which meets the performance requirements derived from our previous analyses (see Table 6.1). The AQM features three stages, starting with an active attenuation stage with a current-mirror under-stage and input network. The output of the attenuator drives a passive current-driven mixer whose output current signal is amplified by an inductively degenerated CB stage. The differential-to-single mode conversion is achieved by an on-chip transformer. Due to the fact that the design operates almost entirely in current-mode, the bandwidth of operation is relatively high, limited only by the bandwidth of the balun at the output. The current-mode operation also allows a second mixer stage to be added (at the input of the CB stage), thereby sharing the CB output stage for better power efficiency. This fits with the novel solution we proposed in Chapter 5, to mitigate the DAC issue of limited dynamic range. The modulator in its nominal performance achieves a high IIP3 of better than 24 dBm, with a gain control range of 24dB (variable from 1.5 dB to -23 dB) stable to within ± 0.5 dB accuracy. The simulated output noise floor is better than -158 dBm/Hz, at rated output power, across a matched load. Simulations indicate a total power consumption of approximately 260 mA from a 3.3 V supply. Of this, the bias network consumes 93.3 mA, the attenuator stage and the CB output stage together consume 84.8 mA and the LO buffers draw less than 80 mA. Designing to a 3.3 V supply gives this design an advantage because it allows to AQM to be closely integrated with the DAC which also draws the same from the same 3.3 V for its analog

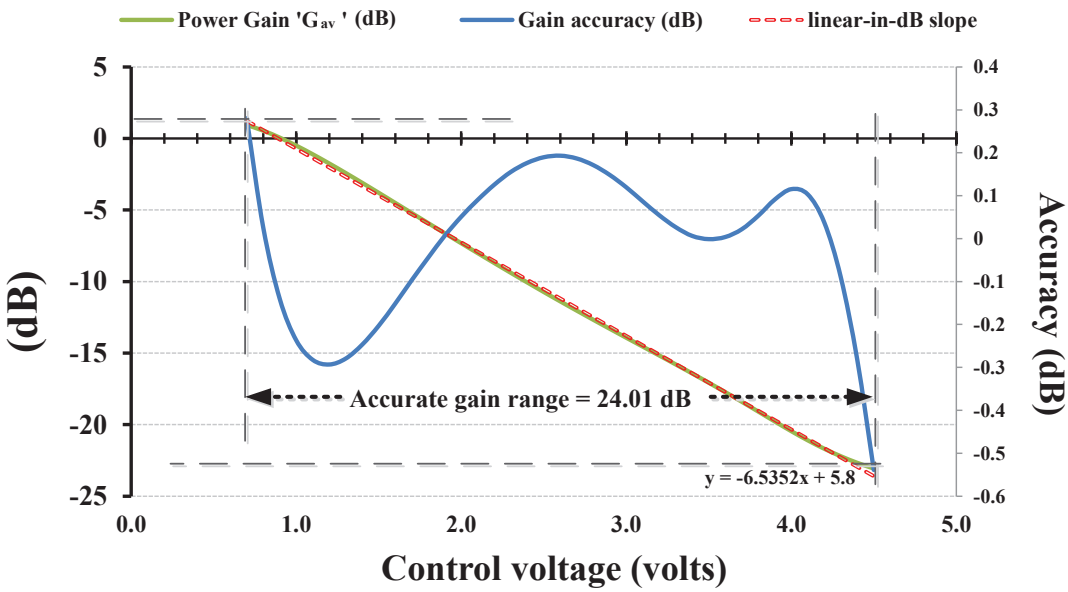

Figure 6.55: Accuracy and range of the power gain with respect to the control voltage ($F_{\mathrm{IF}} = 200$ MHz)

circuitry. The modulator has an IF (-1 dB) bandwidth better than 350 MHz and is capable of handling signals very close to DC at the IF port, supporting zero-IF up-conversion as well. The RF bandwidth however, is relatively smaller, limited by the Balun to < 350 MHz. This is because we tradeoff bandwidth for better noise and linearity performance. Flexibility in the DC operating point would be a useful feature given that the AQM can be interfaced to DACs which have a different common mode DC voltage. Consequently, any improvements in the performance of the AQM could be lost in the interfacing with the DAC. We observe that the AQM maintains the same nominal performance for common-mode voltages between 2.0V and 2.8V. While the LO Poly-Phase Filter operates over a wide range from 400 MHz to 3.4 GHz providing at least 40 dB of sideband suppression, the RF output bandwidth limits the number of bands that can be covered. With proper tuning of the double-tuned output transformer, however, there is a possibility to enhance the bandwidth. More broadband gain stages can be used at the output, but with non-linearity and noise penalties. While increased non-linearity can be partially compensated by increasing the current, particularly in the prominent contributor, the pMOS of the current-mirror input stage, the increased noise could become a limiting factor for the tradeoff. The power consumption is still relatively lower than some of the best-in-class (e.g. TRF37033) modulators available in the market today, making further improvements possible. Reliability has been partially addressed in the design, for example, by ensuring that breakdown voltages are not exceeded at any time, or by choosing the right dimensions to mitigate electro-migration. There are still other issues that remain, particularly the temperature stability of all the performance parameters, which

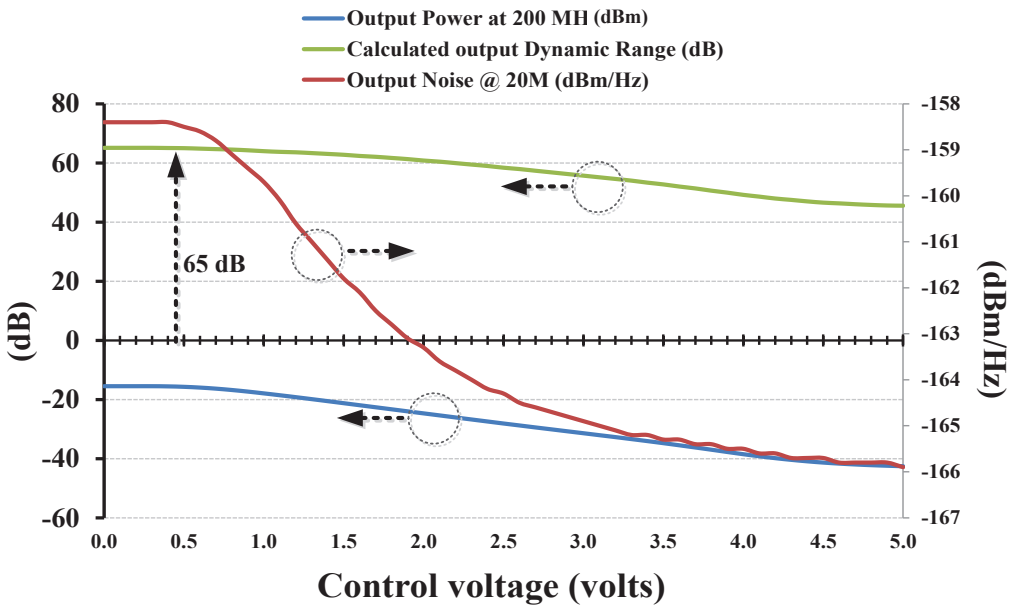

Figure 6.56: Output NSD, single-tone output power and calculated dynamic range, with respect to the control voltage ($F_{\mathrm{IF}} = 200$ MHz)

is suggested for completion of this work. Other open issues include ESD protection and a low-power or temporary shut-down facility, which are highlighted for improvement of the concept.

For all of the sub-stages, we have discussed the bandwidth, gain and noise performance in detail, deriving expressions for the same, where feasible. At several points in the design, we have also presented analyses of the tradeoffs in terms of non-linearity, frequency response, noise performance and the gain required. These discussions based on established works provides useful inputs for taking the design towards prototyping.

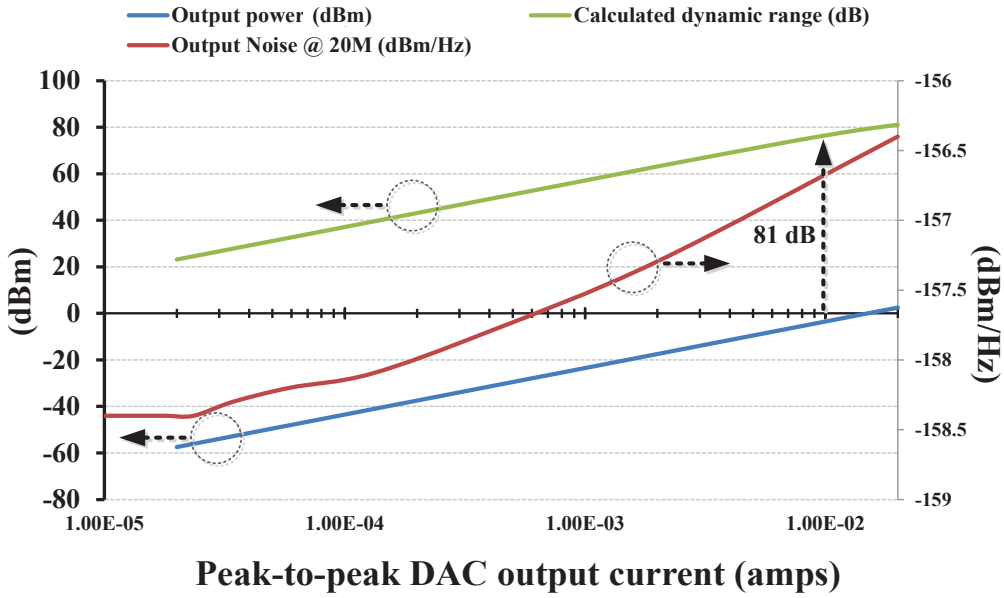

Figure 6.57: Output NSD, single-tone output power and calculated dynamic range, with respect to the DAC output current ($F_{\mathrm{IF}} = 200$ MHz)

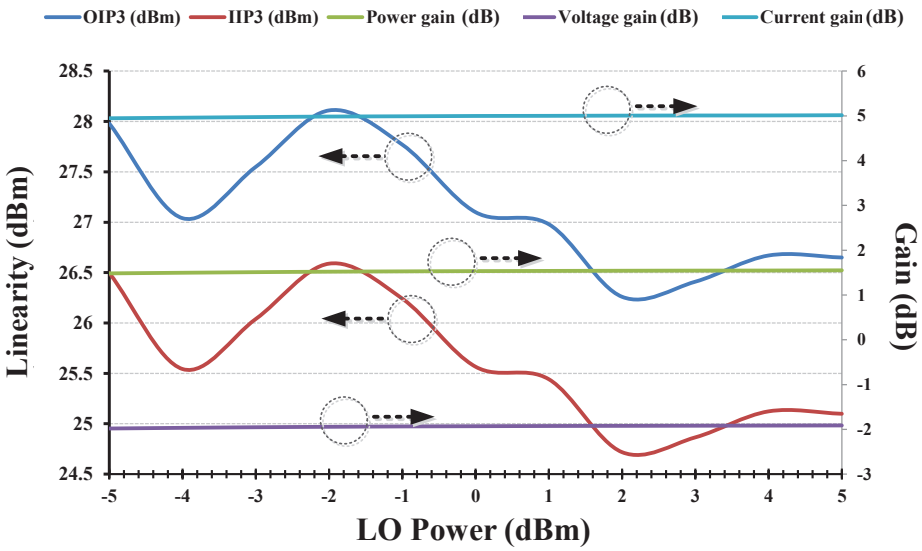

Figure 6.58: Output NSD, single-tone output power and calculated dynamic range, with respect to LO power sweep ($F_{\mathrm{IF}} = 200$ MHz)

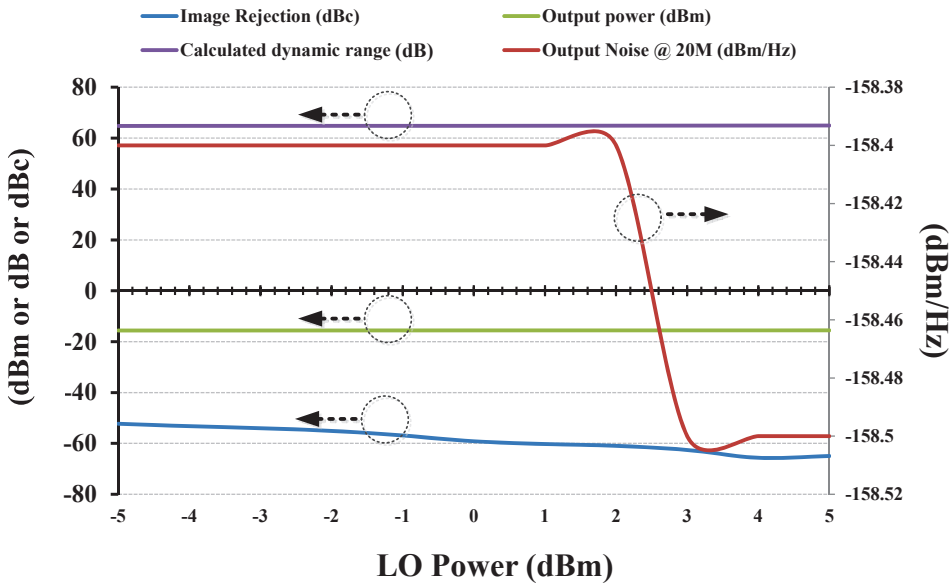

Figure 6.59: Output NSD, single-tone output power and calculated dynamic range, with respect to LO power sweep ($F_{\mathrm{IF}} = 100$ MHz)

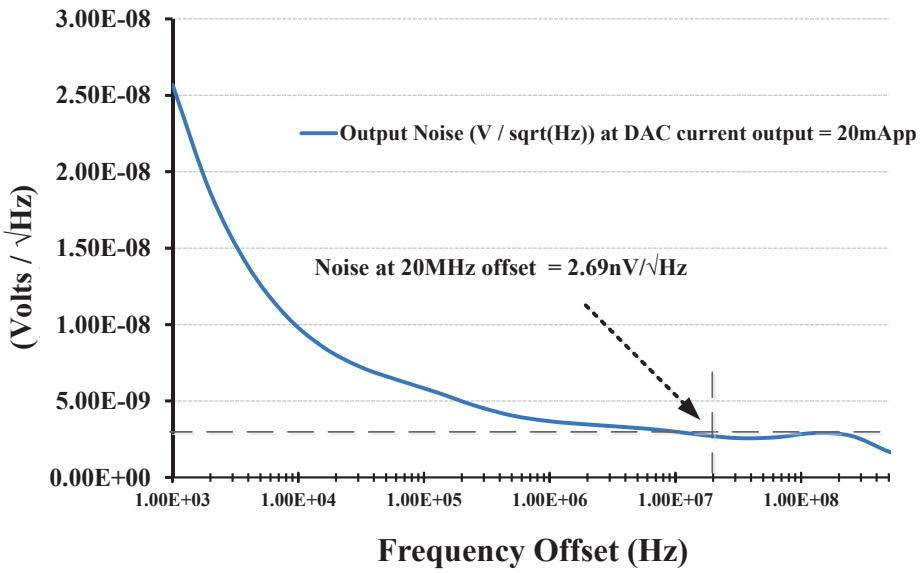

Figure 6.60: Output noise versus frequency for a DAC output current of 20 mApp, LO power = 0 dBm, $F_{\mathrm{IF}} = 200$ MHz

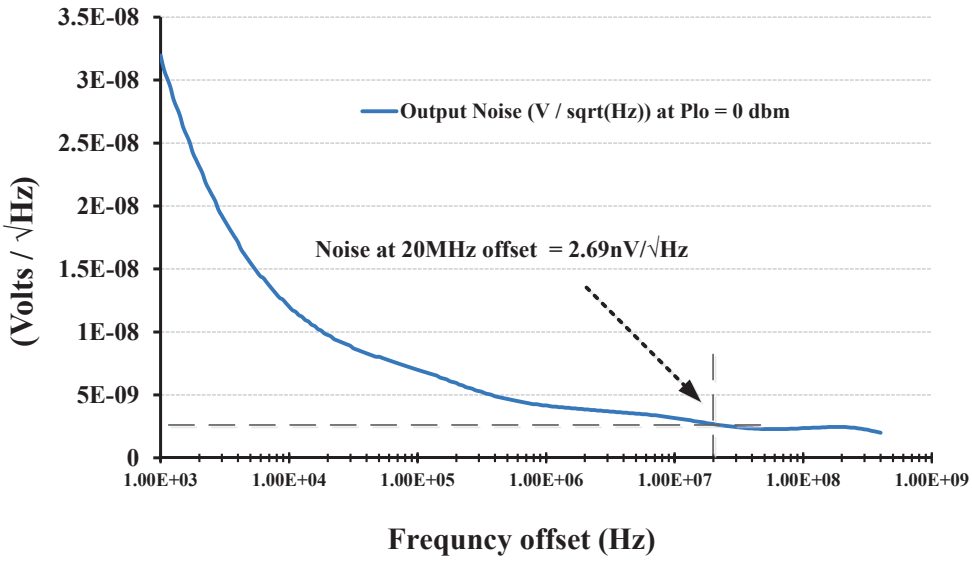

Figure 6.61: Output noise versus frequency for a DAC output current of 5 mApp, LO power = 0 dBm, $F_{\mathrm{IF}} = 200$ MHz

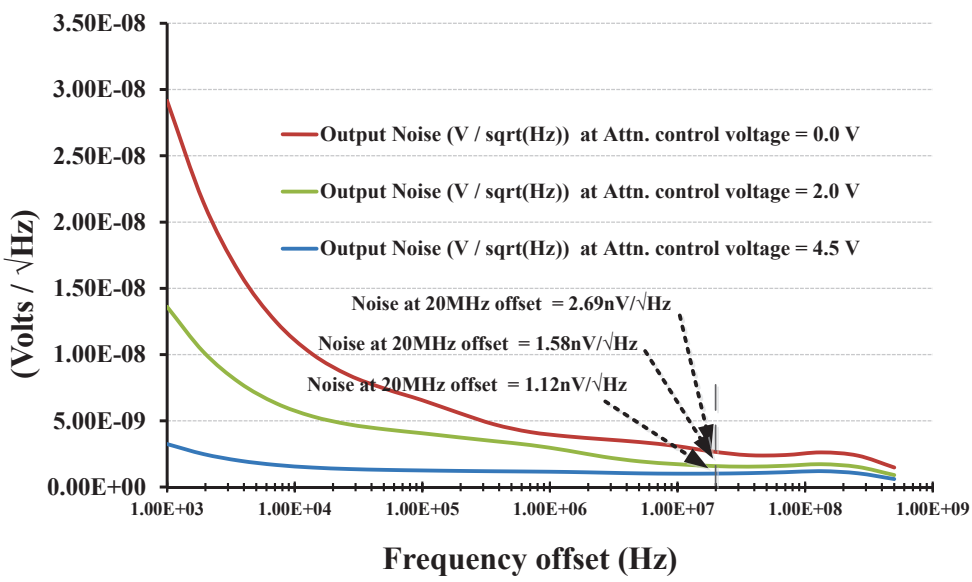

Figure 6.62: Output noise versus frequency for a DAC output current of 5 mApp, LO power = 0 dBm, $F_{\mathrm{IF}} = 200$ MHz and control voltage = 0.0V, 2.0V and 4.5V

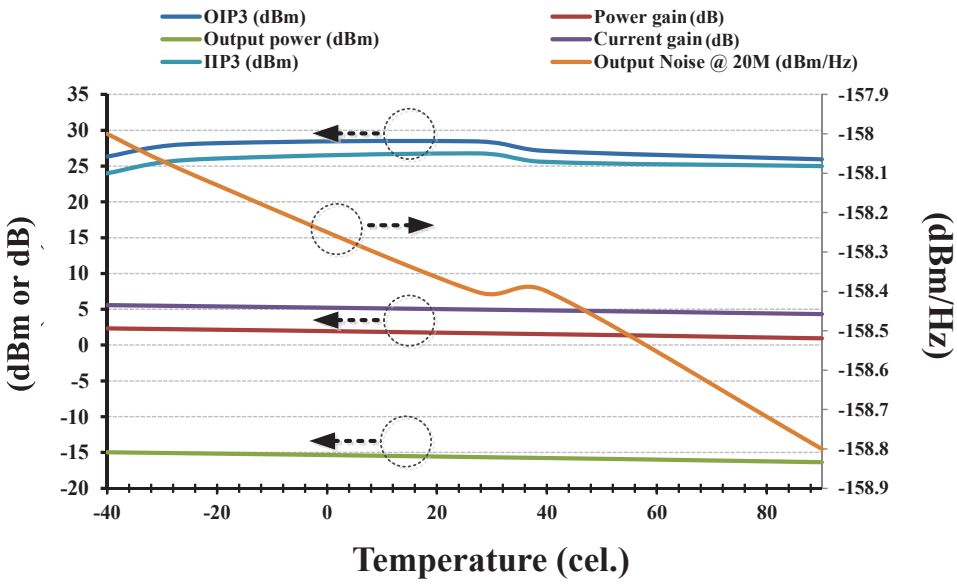

Figure 6.63: OIP3, power gain, voltage gain, current gain and IIP3 at 100 MHz, 120 MHz input tone frequencies, at control voltage = 0.0V, with respect to temperature

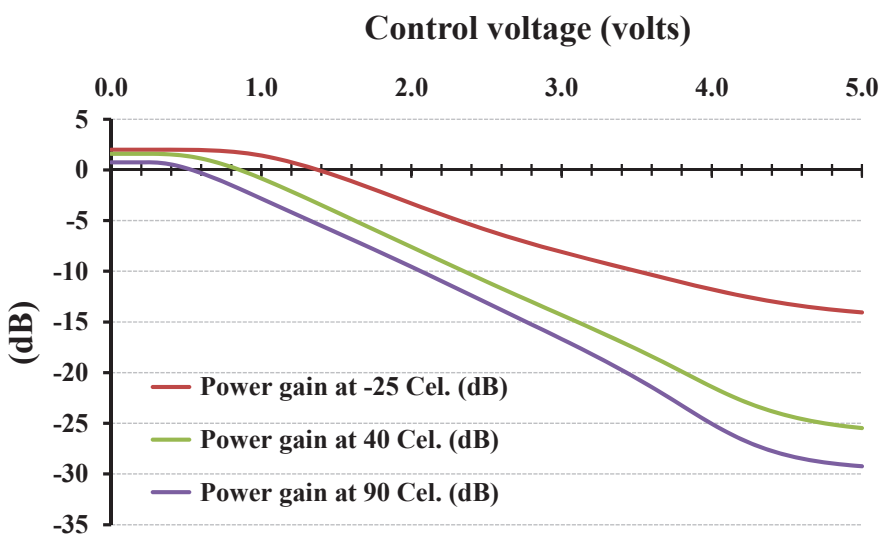

Figure 6.64: Power gain simulated at control voltage = 0.0V, with respect to temperature. The degradation in the slope of the linear-in-dB is readily observable

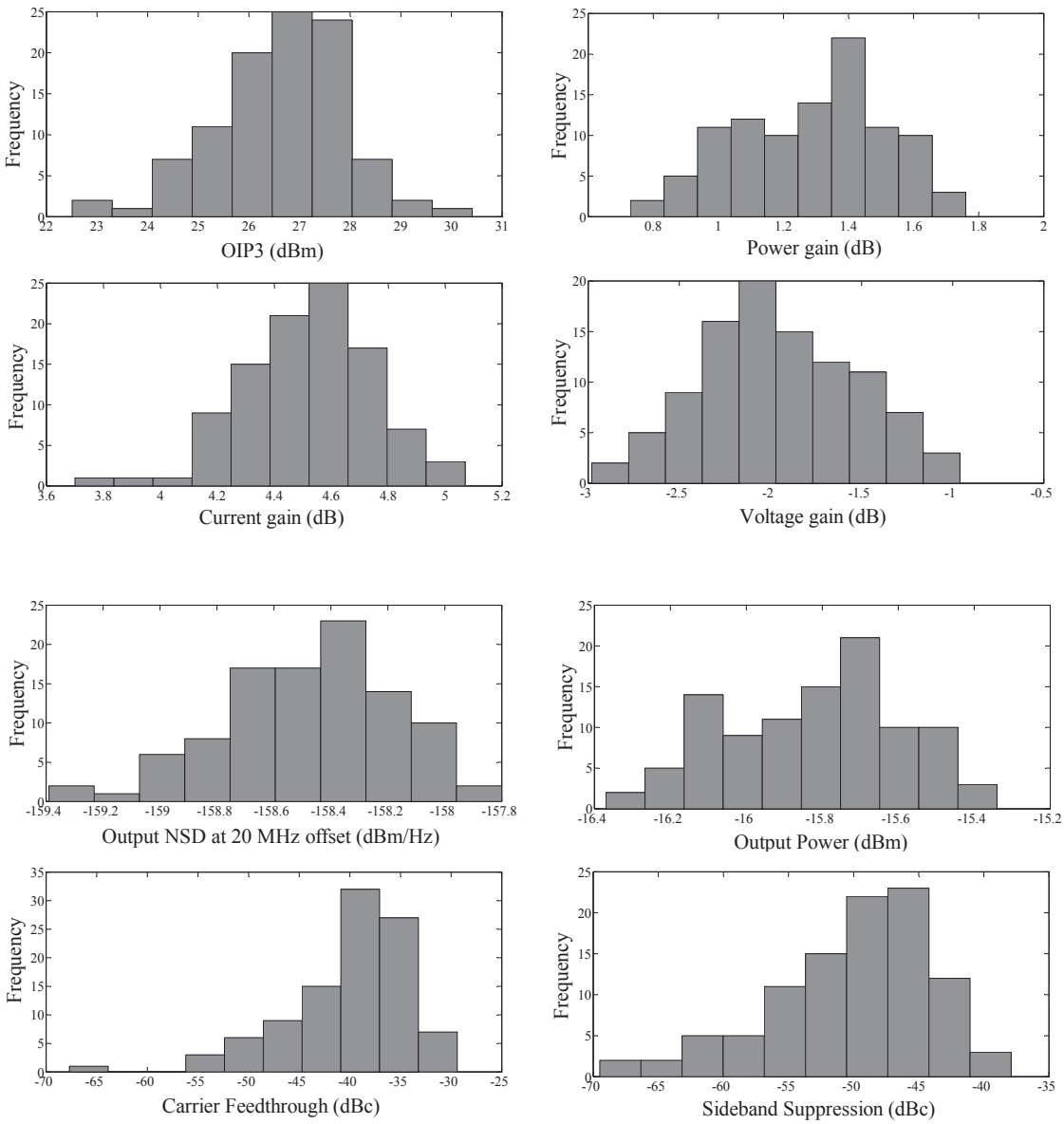

Figure 6.65: Distributions of performance parameters (a) OIP3, power gain, voltage gain, current gain and (b) output noise spectral density (at 20 MHz offset), single tone output power (at 100 MHz), carrier feed-through sideband suppression, over Monte Carlo simulations of 100 runs.

Conclusion

In this work, we have explored the need and feasibility of a multi-standard BStn radio Tx which can simultaneously support cellular carriers of GSM/EDGE, WCDMA and LTE. The benefits of moving from the existing single-carrier radio card to a more efficient multi-carrier radio have been shown to be multi-fold. This shift, however, entails demanding performance requirements for the transceiver. We began in Chapter 2 by considering some of the ecosystemic factors which define the operating conditions for such a Tx, including carrier configurations, transmission bandwidth etc. These factors are critical to specifying the dynamic range and bandwidth requirements of the transmitter which we consider in the rest of our analysis.

With the PA being the most power hungry block in the cartesian up-conversion chain, enhancing its performance is paramount to enhancing the overall performance of the Tx. In order to relax the native performance requirements of the PA, it is assisted or compensated by the DPD in the baseband domain. While we have not investigated DPD algorithms, it has been previously shown to become increasingly complex when combining multiple signals in time domain. Simultaneously, the Peak to Average Power Ratio of the aggregate signal also increases. In Chapter 4, we have evaluated the increasing PAPR for several multi-mode multi-carrier signal configurations, with the objective of identifying the worst case PAPR for multi-mode transmission. This was shown to be approximately 13 dB. The values obtained here are critical to the dimensioning of active blocks in the chain, particularly the Doherty PA, depending on the carrier aggregation. In the process of equalising the different time domain sample rates, we briefly touched upon the issue of fractional rate sampling and the demanding low-pass filtering requirements associated with it.

The expansion of the signal due to the DPD worsens the PAPR, making the Crest Factor Reduction methods critical to achieving acceptable levels of PAPR. Based on the known performance of best-in-class products, we have incorporated a compensated PAPR of roughly 9.6 dB for BC2 transmitters and 7 dB for those of BC1, when calculating the dynamic range of the DAC and the AQM. Previous works have shown multi-mode CFR as being difficult to design, as they are based on a tradeoff between in-channel distortion (EVM) and spectral leakage (ACLR and adherence to the Spectrum Emissions Mask), both of which are demanding requirements. In our analysis, the CFR is the single largest contributor to the EVM, adding noise and distortion in the digital domain.

EVM and spectral leakage are critical to system design and in Chapter 3 we discussed several aspects of these 3GPP metrics. EVM and spectral leakage are introduced and worsened by transmitter impairments. We have shown the impact of the primary impairments,

namely - IQ imbalance, phase noise, DC and frequency offset, LO leakage, in-channel non-linear distortion and broadband noise, which produce errors in the the analog domain. This analysis was based on previous works which helped us develop relationships between EVM and the distortion mechanisms. The objective was to demonstrate the synthesis of worst-case requirements for these contributors starting from 3GPP system-level EVM specifications.

Like EVM, the spectrum leakage specifications of 3GPP also result in demanding performance requirements. For worst-case performance budgeting, we have considered the specifications of the GSM/EDGE standard, which is most demanding in terms of non-linearity requirements, while LTE signals define the close-offset phase noise requirements. The equivalent two-tone OIP3 non-linearity specifications (> 79 dBm) were derived in Chapter 3, based on the relationship developed using multi-tone Intermodulation Distortion enhancement. A less stringent requirement (OIP3$>$ 68.45 dBm) was suggested for multi-mode transmitters which do not support GSM/EDGE carriers, (BC1). Similarly, the demanding[50] broadband noise floor (< -95 dBm/Hz), phase noise mask (≤ -45 dBc or $\leq 0.3°$ R.M.S.), IQ imbalance (-45 dBc) and LO leakage (-40 dBc) requirements were also synthesized from spectrum leakage and EVM specifications.

In Chapter 4, we considered the sensitivities of the various carriers when distributing the performance requirements among the various components of the Tx chain. A simple methodology of performance budgeting was also suggested, relating system specs to block performance requirements, which could help in improving the budget. We also explained the process of noise and linearity budgeting using the method highlighted. There are several goals towards which a transmitter can be optimised, including power consumption, size, cost of materials etc. We find that although developing a generalized model for each block of the transmitter would be very valuable for evaluation of the transmitter performance, it would be complicated because there can be numerous design solutions for the same block, each with their own tradeoffs for noise, bandwidth, linearity, gain, area, cost and power consumption. The suggested performance budget in Chapter 4 is based on the result of many iterations, using best-in-class products as references, where possible. This would need to be updated as performances and technologies improve.

With a requirement of less than 5% (as applicable to GSM/EDGE carriers), the EVM requirement becomes challenging to satisfy, especially at lower power levels, because of the difficulties in lowering the noise floor. The issue of reduced dynamic range due to the increasing PAPR and the multi-mode power control mechanisms were discussed in Chapter 3. In keeping with the high dynamic range requirements, the conceptual design of a variable-gain Analog Quadrature Modulator in the NXP SiGe BiCMOS QUBiC process, was presented in Chapter 5. The introduction of this block in the chain allows us to bypass the DAC dynamic range limitation highlighted in Chapter 3. In the process of discussing tradeoffs and choices at various critical points in the schematic, we also highlighted some of the issues in the design, particularly the RF output bandwidth and the temperature stability, which is suggested for further development of this work.

The analyses were based on first order assumptions of the distortion mechanisms in the transmitter and therefore present scope for further development of this work, both in terms of

[50]The broadband noise floor and filtering requirements will likely be significant factors in phased-array antenna systems, if adhering to similar 3GPP performance requirements.

the modeling of the impairments and also in incorporating other second order impairments. In this work, we did not cover the feedback receiver or the observation path receiver because the specifications of the feedback path are closely coupled with the best-in-class DPD algorithms. A closer investigation of DPD mechanisms and PA/Filter/Antenna technologies would improve the completeness of this work.

To conclude, we have presented the flow of the design of a unified multi-mode transmitter starting from an analysis of requirements based on the 3GPP specifications, synthesised circuit-level performance criteria and finally, presented the design of a critical block in the chain. The methodology of design suggested and validated in this work, also allows one to easily relate system-level specifications to circuit-level performance requirements. We have also highlighted tradeoffs, issues and scope for further development of this work.

Appendix A

The Simplified Concept of Pre-Distortion

A.1 Basics of Pre-Distortion

Although this is far from practice, if we were to assume only third order power-series[1] non-linearity for an amplifier, we have its time domain output to be,

$$V_{\text{out}} = a_1 V_x + a_3 V_x^3 \tag{A.1}$$

where, V_x is the amplifier input voltage and a_1, a_3 represent the power-series coefficients. If V_x is expressed as the non-linear output of the pre-distorter stage with V_{in} as the input, we have,

$$V_x = b_1 V_{in} + b_3 V_{in}^3 \tag{A.2}$$

where, b_1 and b_3 are the coefficients of the pre-distorter. The output of the PA can then be expressed as,

$$V_{\text{out}} = a_1(b_1 V_{in} + b_3 V_{in}^3) + a_3(b_1 V_{in} + b_3 V_{in}^3)^3 \tag{A.3a}$$

which expands to,

$$V_{\text{out}} = a_1 b_1 V_{in} + (a_1 b_3 + a_3 b_1^3) V_{in}^3 + 3a_3 b_1^2 b_3 V_{in}^5 + 3a_3 b_3^2 b_1 V_{in}^7 + a_3 b_3^3 V_{in}^9 \tag{A.3b}$$

As per [34], clearly, by setting $b_3 = -\frac{a_3 b_1^3}{a_1}$, we can cancel out the 3rd order non-linearity of the PA. However, this will also generate additional distortion terms of higher order. The effect of pre-distortion (PD) here is that in canceling out in-band or close-in distortion, more unwanted products at large carrier offsets are generated. Consequently, the PD will also have to generate higher terms in order to cancel out higher frequency terms. This is the

[1] This is mathematically the Taylor series centered at zero, also known as the MacLaurin series. By assuming a power-series non-linearity, we ignore the phase of the non-linearity coefficients when combining non-linear by-products.

expansion of the signal that compensates for the compression of the PA. Although the ACLR requirement of the carrier might be met, this becomes a challenge when addressing spectral purity masks at large carrier offsets. If were to replace V_{in} to have a single cosine component, we obtain V_{out} to be,

$$\begin{aligned} V_{\text{out}} = & \left(a_1b_1 + \frac{3a_1b_3}{4} + \frac{3a_3b_1^3}{4} + \frac{63a_3b_3^3}{128} + \frac{105a_3b_1b_3^2}{64} + \frac{15a_3b_1^2b_3}{8}\right)\cos(\omega t) \\ & + \left(\frac{a_1b_3}{4} + \frac{a_3b_1^3}{4} + \frac{21a_3b_3^3}{64} + \frac{63a_3b_1b_3^2}{64} + \frac{15a_3b_1^2b_3}{16}\right)\cos(3\omega t) \\ & + \left(\frac{9a_3b_3^3}{64} + \frac{21a_3b_1b_3^2}{64} + \frac{3a_3b_1^2b_3}{16}\right)\cos(5\omega t) \\ & + \left(\frac{9a_3b_3^3}{256} + \frac{3a_3b_1b_3^2}{64}\right)\cos(7\omega t) + \left(\frac{a_3b_3^3}{256}\right)\cos(9\omega t) \end{aligned} \tag{A.4}$$

With 2nd order non-linearity, this effect is worsened (see Equation A.5). Leakage and second-degree effects involving 2nd order non-linearity in low-power RF stages have been amply demonstrated earlier (e.g. [137]), implying that the input to the PA from a preceding stage having 2nd degree non-linearity, cannot be ignored, let alone the 2nd order non-linearity of the PA itself.

$$\begin{aligned} V_{\text{out}} = & (a_1b_1)V_{\text{in}} + (a_2b_1^2 + a_1b_2)V_{\text{in}}^2 + (a_3b_1^3 + 2a_2b_2b_1 + a_1b_3)V_{\text{in}}^3 \\ & + (a_2b_2^2 + 2a_2b_1b_3 + 3a_3b_1^2b_2)V_{\text{in}}^4 + (3a_3b_1b_2^2 + 3a_3b_1^2b_3 + 2a_2b_2b_3)V_{\text{in}}^5 \\ & + (a_2b_3^2 + a_3b_2^3 + 6a_3b_1b_2b_3)V_{\text{in}}^6 + (3a_3b_2^2b_3 + 3a_3b_1b_3^2)V_{\text{in}}^7 + (3a_3b_2b_3^2)V_{\text{in}}^8 + (a_3b_3^3)V_{\text{in}}^9 \end{aligned} \tag{A.5}$$

Evidently, in trying to achieve the goal of minimising the 3rd order non-linearity, additional higher frequency terms are generated in the process of compensation. Consequently, the bandwidth of PD'ed output signal increases, increasing requirements on the performance of the Digital-Signal-Processing (DSP) hardware that needs to manipulate it. State of the art DPD solutions address signal bandwidths of approximately 60MHz (e.g. 2170MHz-2110MHz) with up to 5th order non-linearity using typical high-performance DSP cores have speeds of approximately 350MHz. With DPD solutions covering multiple bands at once, this stresses the performance of the DSP and highlights one of the issues in DPDs today, which are limited to a large extent by the bandwidth and speed of the DSP available.

Appendix B

Basic Polynomial Non-linearity Mechanisms

B.1 Intermodulation Distortion

In keeping with our previous assumption that IM3 is the single largest contributor to the in-band spectral leakage, if we were to assume power-series non-linearity as given by A.1 and inputs comprising of two sinusoids given by B.1, then the resulting products are as given by Equation B.2. The various non0linear distortion products are indicated in the equation below.

$$V_{\text{in}} = V_1 \cos(\omega_1 t) + V_2 \cos(\omega_2 t) \tag{B.1}$$

$$\begin{aligned}
V_{\text{out}} &= a_1(V_{in}) + a_3(V_{in})^3 \\
&= a_1(V_1 \cos(\omega_1 t) + V_2 \cos(\omega_2 t)) + a_3(V_1 \cos(\omega_1 t) + V_2 \cos(\omega_2 t))^3 \\
&= \left.\begin{aligned}
&\left(\frac{3\,a_3\,{V_1}^3}{4} + \frac{3\,a_3\,V_1\,{V_2}^2}{2} + a_1\,V_1\right)\cos(\omega_1 t) \\
&+ \left(\frac{3\,a_3\,{V_1}^2\,V_2}{2} + \frac{3\,a_3\,{V_2}^3}{4} + a_1\,V_2\right)\cos(\omega_2 t)
\end{aligned}\right\}\text{fundamental frequencies} \\
&\quad \left.\begin{aligned}
&+ \frac{3\,{V_1}^2\,V_2\,a_3\,\cos(2\,\omega_1 t - \omega_2 t)}{4} \\
&+ \frac{3\,V_1\,{V_2}^2\,a_3\,\cos(\omega_1 t - 2\,\omega_2 t)}{4}
\end{aligned}\right\}\text{in-band IMD products} \\
&\quad \left.\begin{aligned}
&+ \frac{3\,V_1\,{V_2}^2\,a_3\,\cos(\omega_1 t + 2\,\omega_2 t)}{4} \\
&+ \frac{3\,{V_1}^2\,V_2\,a_3\,\cos(2\,\omega_1 t + \omega_2 t)}{4}
\end{aligned}\right\}\text{out-of-band IMD products} \\
&\quad \left.+ \frac{\left({V_2}^3\,a_3\right)}{4}\cos(3\,\omega_2 t) + \frac{\left({V_1}^3\,a_3\right)}{4}\cos(3\,\omega_1 t)\right\}\text{out-of-band harmonics}
\end{aligned} \tag{B.2}$$

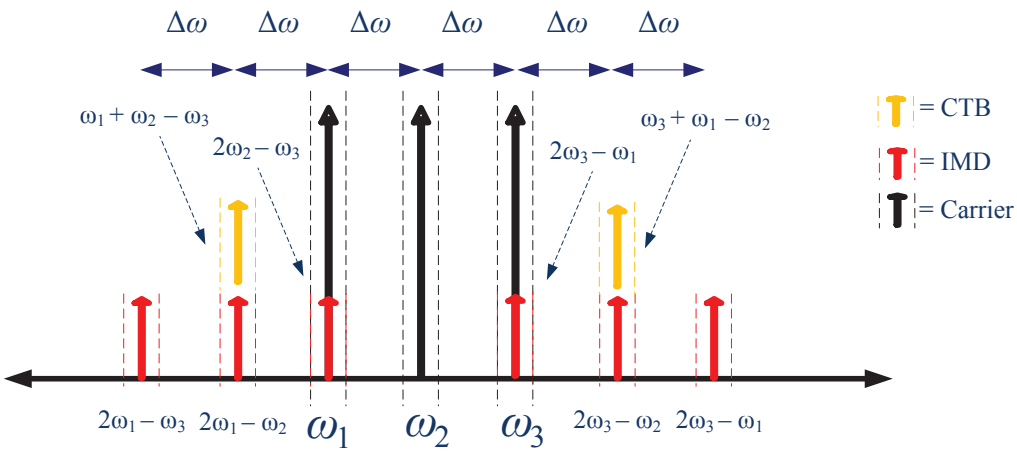

Figure B.1: IMD and CTB products from 3-tone input subject to 3rd order non-linearity

B.2 Composite Triple Beat

Increasing the number of tones in expression B.1 would show the presence of yet another effect of 3rd order non-linearity which we have not considered so far. This effect is common to multi-carrier transmission scenarios, particularly well-known in the broadcast of Television signals. We illustrate the case for 3 tones, where

$$V_{\text{in}} = V_1 \cos(\omega_1 t) + V_2 \cos(\omega_2 t) + V_3 \cos(\omega_3 t) \tag{B.3}$$

The corresponding output signal is given by

$$\begin{aligned} V_{\text{out}} &= a_1(V_{in}) + a_3(V_{in})^3 \\ &= a_1(V_1 \cos(\omega_1 t) + V_2 \cos(\omega_2 t) + V_3 \cos(\omega_2 t)) \\ &\quad + a_3(V_1 \cos(\omega_1 t) + V_2 \cos(\omega_2 t) + V_3 \cos(\omega_2 t))^3 \end{aligned}$$

By expanding and combining similar terms, we get

$$
\begin{aligned}
V_{\text{out}} = \; & \left.\begin{aligned}
& \left(\frac{3\,a_3\,{V_1}^3}{4} + \frac{3\,a_3\,V_1\,{V_2}^2}{2} + \frac{3\,a_3\,V_1\,{V_3}^2}{2} + a_1\,V_1\right)\cos(\omega_1 t) \\
& + \left(\frac{3\,a_3\,{V_1}^2\,V_2}{2} + \frac{3\,a_3\,{V_2}^3}{4} + \frac{3\,a_3\,V_2\,{V_3}^2}{2} + a_1\,V_2\right)\cos(\omega_2 t) \\
& + \left(\frac{3\,a_3\,{V_1}^2\,V_3}{2} + \frac{3\,a_3\,{V_2}^2\,V_3}{2} + \frac{3\,a_3\,{V_3}^3}{4} + a_1\,V_3\right)\cos(\omega_3 t)
\end{aligned}\right\} \text{fundamental frequencies} \\
& \left.\begin{aligned}
& + \frac{3\,{V_1}^2\,V_2\,a_3\,\cos(2\,\omega_1 t - \omega_2 t)}{4} + \frac{3\,{V_1}^2\,V_3\,a_3\,\cos(2\,\omega_1 t - \omega_3 t)}{4} \\
& + \frac{3\,{V_2}^2\,V_3\,a_3\,\cos(2\,\omega_2 t - \omega_3 t)}{4} + \frac{3\,V_1\,{V_2}^2\,a_3\,\cos(\omega_1 t - 2\,\omega_2 t)}{4} \\
& + \frac{3\,V_1\,{V_3}^2\,a_3\,\cos(\omega_1 t - 2\,\omega_3 t)}{4} + \frac{3\,V_2\,{V_3}^2\,a_3\,\cos(\omega_2 t - 2\,\omega_3 t)}{4}
\end{aligned}\right\} \text{in-band IMD products} \\
& \left.\begin{aligned}
& + \frac{3\,V_1\,{V_2}^2\,a_3\,\cos(\omega_1 t + 2\,\omega_2 t)}{4} + \frac{3\,{V_1}^2\,V_2\,a_3\,\cos(2\,\omega_1 t + \omega_2 t)}{4} \\
& + \frac{3\,V_1\,{V_3}^2\,a_3\,\cos(\omega_1 t + 2\,\omega_3 t)}{4} + \frac{3\,{V_1}^2\,V_3\,a_3\,\cos(2\,\omega_1 t + \omega_3 t)}{4} \\
& + \frac{3\,V_2\,{V_3}^2\,a_3\,\cos(\omega_2 t + 2\,\omega_3 t)}{4} + \frac{3\,{V_2}^2\,V_3\,a_3\,\cos(2\,\omega_2 t + \omega_3 t)}{4}
\end{aligned}\right\} \text{out-of-band IMD products} \\
& \left.\begin{aligned}
& + \frac{3\,V_1\,V_2\,V_3\,a_3\,\cos(\omega_1 t + \omega_2 t - \omega_3 t)}{2} \\
& + \frac{3\,V_1\,V_2\,V_3\,a_3\,\cos(\omega_1 t - \omega_2 t + \omega_3 t)}{2}
\end{aligned}\right\} \text{in-band CTB products} \\
& \left.\begin{aligned}
& + \frac{3\,V_1\,V_2\,V_3\,a_3\,\cos(\omega_1 t - \omega_2 t - \omega_3 t)}{2} \\
& + \frac{3\,V_1\,V_2\,V_3\,a_3\,\cos(\omega_1 t + \omega_2 t + \omega_3 t)}{2}
\end{aligned}\right\} \text{out-of-band CTB products} \\
& \left.+ \frac{\left({V_1}^3\,a_3\right)}{4}\cos(3\,\omega_1 t) + \frac{\left({V_2}^3\,a_3\right)}{4}\cos(3\,\omega_2 t) + \frac{\left({V_3}^3\,a_3\right)}{4}\cos(3\,\omega_3 t)\right\} \text{out-of-band harmonics}
\end{aligned}
\tag{B.4}
$$

where the CTB refers to the terms containing $\omega_1 \pm \omega_2 \pm \omega_2$. The gain or amplitudes associated with CTB products ($\frac{3}{2}$) is double that of the IMD ($\frac{3}{4}$).

With higher number of carriers, this effect is naturally worsened. This is evident from the case for 6 tones illustrated in Figure B.2. Consequently, the CTB products are very critical in defining the conformance of the non-linear device, to the spectral mask specifications as well as the purity of the signal itself. The distortion of signal at its frequency of operation depends on the modulated aggressor carriers that modulate the wanted signal, and is referred to as Cross-Modulation (CMD).

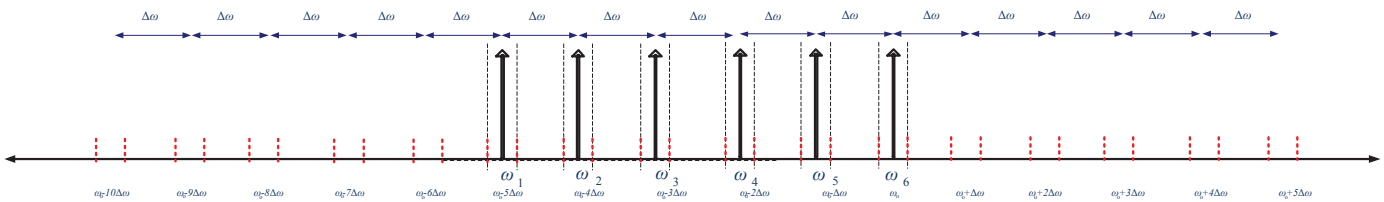

		2ω6-ω1	2ω6-ω2	2ω5-ω1	2ω5-ω2	2ω4-ω1	2ω4-ω2	2ω3-ω1	2ω3-ω2	2ω3-ω2	2ω3-ω1	2ω4-ω2	2ω4-ω1	2ω5-ω2	2ω5-ω1	2ω6-ω2	2ω6-ω1
			ω6+ω5-ω1	2ω6-ω3	2ω6-ω4	2ω5-ω3	2ω5-ω4	2ω4-ω3	2ω5-ω6	2ω5-ω6	2ω4-ω3	2ω5-ω4	2ω5-ω3	2ω6-ω4	2ω6-ω3	ω6+ω5-ω1	
				ω6+ω4-ω1	ω5+ω4-ω1	2ω6-ω5	ω1-ω1+ω6	ω1+ω6-ω2	ω1+ω5-ω2	ω1+ω5-ω2	ω1+ω6-ω2	ω1-ω1+ω6	2ω6-ω5	ω5+ω4-ω1	ω6+ω4-ω1		
				ω6+ω5-ω2	ω6+ω3-ω1	ω5-ω1+ω3	ω2-ω2+ω6	ω1-ω1+ω5	ω1+ω6-ω3	ω1+ω6-ω3	ω1-ω1+ω5	ω2-ω2+ω6	ω5-ω1+ω3	ω6+ω3-ω1	ω6+ω5-ω2		
					ω6+ω4-ω2	ω5-ω2+ω4	ω3-ω3+ω6	ω2+ω6-ω3	ω1-ω1+ω4	ω1-ω1+ω4	ω2+ω6-ω3	ω3-ω3+ω6	ω5-ω2+ω4	ω6+ω4-ω2			
					ω6+ω5-ω3	ω6+ω2-ω1	ω4+ω3-ω1	ω2-ω2+ω5	ω2+ω5-ω3	ω2+ω5-ω3	ω2-ω2+ω5	ω4+ω3-ω1	ω6+ω2-ω1	ω6+ω5-ω3			
						ω6+ω3-ω2	ω4-ω4+ω6	ω3+ω6-ω4	ω2+ω6-ω4	ω2+ω6-ω4	ω3+ω6-ω4	ω4-ω4+ω6	ω6+ω3-ω2				
						ω6+ω4-ω3	ω5+ω2-ω1	ω3-ω3+ω5	ω2-ω2+ω4	ω2-ω2+ω4	ω3-ω3+ω5	ω5+ω2-ω1	ω6+ω4-ω3				
						ω6+ω5-ω4	ω5+ω3-ω2	ω4+ω2-ω1	ω3+ω2-ω1	ω3+ω2-ω1	ω4+ω2-ω1	ω5+ω3-ω2	ω6+ω5-ω4				
							ω5+ω4-ω3	ω4+ω3-ω2	ω3+ω5-ω4	ω3+ω5-ω4	ω4+ω3-ω2	ω5+ω4-ω3					
							ω5-ω5+ω6	ω4+ω6-ω5	ω3+ω6-ω5	ω3+ω6-ω5	ω4+ω6-ω5	ω5-ω5+ω6					
							ω6-ω6+ω6	ω4-ω4+ω5	ω3-ω3+ω4	ω3-ω3+ω4	ω4-ω4+ω5	ω6-ω6+ω6					
							ω6-ω6+ω6	ω5-ω5+ω5	ω4-ω4+ω4	ω4-ω4+ω4	ω5-ω5+ω5	ω6-ω6+ω6					
								ω6-ω6+ω5	ω5-ω5+ω4	ω5-ω5+ω4	ω6-ω6+ω5						
									ω6-ω6+ω4	ω6-ω6+ω4							

Legend

IMD voltage multiplication = x1

CTB voltage multiplication = x2

η_3 14.31

TOTAL (dB)															
Correlated sum	**0.00**	**9.54**	**15.56**	**20.00**	**23.52**	**26.44**	**27.96**	**28.63**	**28.63**	**27.96**	**26.44**	**23.52**	**20.00**	**15.56**	**9.54**	**0.00**
Uncorrelated sum	**0.00**	**6.99**	**10.00**	**12.55**	**14.31**	**15.91**	**16.72**	**17.08**	**17.08**	**16.72**	**15.91**	**14.31**	**12.55**	**10.00**	**6.99**	**0.00**
Δ(correlated-uncorrelated)	*0.00*	*2.55*	*5.56*	*7.45*	*9.21*	*10.53*	*11.24*	*11.55*	*11.55*	*11.24*	*10.53*	*9.21*	*7.45*	*5.56*	*2.55*	*0.00*

Figure B.2: Non-linearity products from a six carrier input to 3rd order polynomial non-linearity

B.3 Cross Modulation

If, in the above equation, the sinusoids $V_1 \cos(\omega_1 t)$ and $V_2 \cos(\omega_2 t)$ were replaced by signals having amplitude modulation, as in $V_1(t)\cos(\omega_1 t) + V_2 \cos(\omega_2 t)$, the impact of amplitude CMD becomes evident. From Equation B.4, the resulting CMD terms at carrier frequencies ω_1, ω_2 and ω_3 are highlighted below.

As mentioned earlier, the CMD at carrier frequency depends on the relative strength of the modulation on the aggressor carriers. With RAN-sharing mechanisms incorporated into the BStn, this becomes particularly troublesome when dealing with carriers that have independent power control. The effect is pronounced and noticeable in modulated carriers. An example of an aggregate of 3 GSM/EDGE carriers and 2 WCDMA carriers through a device with simulated, polynomial series non-linearity is illustrated in Figure B.3. When non-linear blocks are cascaded as illustrated by Equation A.1 and A.2, spectral purity becomes a challenge and the the analysis even more tedious. For the sake of simplicity we ignore CMD and highlight it for further study.

$$\begin{aligned}
\text{CMD products} = &\left(\underbrace{\frac{3\,a_3\,V_1(t)^3}{4} + \frac{3\,a_3\,V_1(t)\,V_2(t)^2}{2} + \frac{3\,a_3\,V_1(t)\,V_3(t)^2}{2}}_{\text{CMD terms at } \omega_1} + a_1\,V_1(t)\right)\cos(\omega_1 t) \\
&+ \left(\underbrace{\frac{3\,a_3\,V_1(t)^2\,V_2(t)}{2} + \frac{3\,a_3\,V_2(t)^3}{4} + \frac{3\,a_3\,V_2(t)\,V_3(t)^2}{2}}_{\text{CMD terms at } \omega_2} + a_1\,V_2(t)\right)\cos(\omega_2 t) \\
&+ \left(\underbrace{\frac{3\,a_3\,V_1(t)^2\,V_3(t)}{2} + \frac{3\,a_3\,V_2(t)^2\,V_3(t)}{2} + \frac{3\,a_3\,V_3(t)^3}{4}}_{\text{CMD terms at } \omega_3} + a_1\,V_3(t)\right)\cos(\omega_3 t)
\end{aligned} \tag{B.5}$$

B.4 Intermodulation Enhancement

The case of non-linearity with 6 tones input was considered above. The equations are tedious, so we presented the tabulation of the different IMD products assuming 3rd order non-linearity is dominant. Figure B.2 demonstrates the accumulation of IMD terms at various frequency offsets from the carrier. As has been pointed out on on numerous occasions, the correlation or the phase relationship between the carriers is particularly important. Here, we assume phase correlation between all carriers, resulting in voltage addition, which is twice the value obtained by addition in power, for a two-tone with equal tone powers. Typically, the randomness in the modulated carriers ensures uncorrelation and subsequently less pessimistic spectral regrowth. Volterra series modeling [82] incorporates the phase of the non-linearity and the ensuing phase information of the non-linearity bi-products. This would allow for better prediction of cascade chain non-linearity and is therefore highlighted for future work.

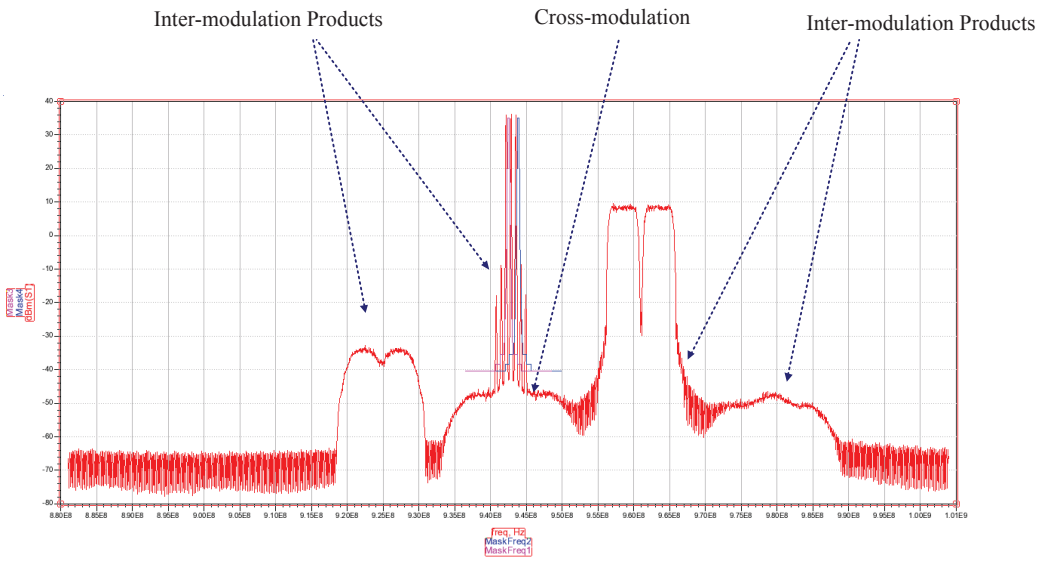

Figure B.3: Simulated Cross Modulation (CMD) between 3 GSM/EDGE and 2 WCDMA carriers under 3rd order polynomial non-linearity

To understand the influence of the phase relationship between the carriers, let us consider a signal $V_1 \cos(\omega_1 t + \phi_1)$ at frequency ω_1. If a signal $V_2 \cos(\omega_1 t + \phi_2)$ is added to this signal, then, depending on phase relationship between the two sinusoids, several output power combinations arise. If $\phi_1 = \phi_2 - \pi$ and $2V_1 = V_2 = 2A$, the R.M.S. power of $V_1 \cos(\omega_1 t + \phi_1) + V_2 \cos(\omega_1 t + \phi_2) = A \cos(\omega_1 t + \phi_2)$ across a 1Ω load is $(A/\sqrt{2})^2 = A^2/2$ in the linear domain. Therefore there is no increase in power relative the single tone. For $\phi_1 = \phi_2$, the R.M.S. power of the combination $V_1 \cos(\omega_1 t + \phi_1) + V_2 \cos(\omega_1 t + \phi_2) = 3A \cos(\omega_1 t + \phi_1)$ is, $(3A/\sqrt{2})^2 = 9A^2/2$. The corresponding increase in power is 9.54dB. This is the highest increase in power. If the phase relationship is such that $0 < |\phi_1 - \phi_2| < \pi$, the resulting power is somewhere between 0 and 9.5dB above the single tone power. If we consider the two signals to be independent and identically distributed (i.i.d., i.e., uncorrelated), the RMS or Expected power of the combination is give by $\mathbb{E}[|A \cos(\omega_1 t + \phi_1) + 2A \cos(\omega_1 t + \phi_2)|^2] = \mathbb{E}[|A \cos(\omega_1 t + \phi_1)|^2] + \mathbb{E}[|2A \cos(\omega_1 t + \phi_2)|^2] = (A/\sqrt{2})^2 + 4A/\sqrt{2})^2 = 5A^2/2$. This corresponds to an increase in R.M.S. power of 6.98dB. The peak power however remains at 9.54dB above and the minimum power, equal to the initial single tone. We observe the same result if we expand the result and apply it to the non-linearity polynomial expression of Equation B.4. The fluctuations in the relative phase between two carriers produces not only peaking but also cancellation of IMD products at the output. We also refer to this concept in the section on PAPR (see 4.3.9). Based on the original works of [76] and [74], useful expressions to determine the enhancement of the near carrier-edge frequency-band IMD, CTB and also CMD can be obtained. In 4.30, we represent the growth of this IM3 level at this location, by

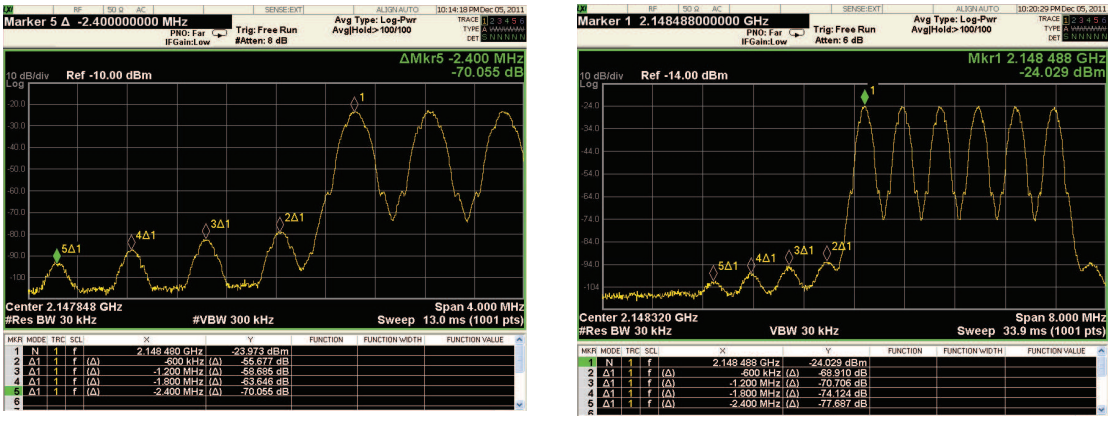

Uncorrelated signals **Correlated signals**

Figure B.4: Measurements at the output of a typical RF Base Station small-signal chain, showing non-linearity products from a six (EDGE) carrier input, indicating it is comparable to 3rd order polynomial non-linearity. *Courtesy: NXP Semiconductors, 2011*

the factor η_3 on the log-scale, based on one such special case. The case for both correlated and uncorrelated carriers is indicated in the bottom rows of Figure B.2. The figure below shows measurements[1] results from 6 GMSK carriers input to a device with $\approx$ 27dBm of OIP3.

[1]These specific measurements were carried out by the Applications Engineering team located in Caen, France.

Appendix C

Multi-mode DAC Dynamic Range Requirements

Table C.1: Multi-mode DAC dynamic range requirements

		Units	dBFS	cumulative dBFS	
Full scale DAC voltage (FS)	1.00	Vpk-pk	0.00	0.00	
Margin	1.00	dB	-1.00	-1.00	
Multimode signal PAPR	13.00	dB	-13.00	-14.00	
Crest Factor Reduction (CFR)	6.00	dB	6.00	-8.00	
Digital Pre-distortion (DPD)	2.00	dB	-2.00	-10.00	
DAC RMS output power developed (matched load)	-6.02	dBm	-10.00		
TX Gain required for49dBm (80W) @ARP RMS Tx power	55.05	dB			
Number of carriers	6.00		-7.78		
Resulting power per carrier OBW				**-17.78**	dBFS/OBW
Per Carrier Powers		**Units**	**dBFS**		**Units**
GSM per carrier Power (50Ohms)	-71.58	dBm/Hz	-	**-78.57**	dBFS/Hz

Continued on the next page . . .

Table C.1: (continued)

		Units	dBFS	cumulative dBFS	
WCDMA per carrier Power (50Ohms)	-84.42	dBm/Hz	-	-91.41	dBFS/Hz
LTE per carrier Power (50Ohms)	-80.79	dBm/Hz	-	-87.78	dBFS/Hz
Adjacent Channel Leakage Specifications		**Units**	**dBFS**		**Units**
Transmitter Gain (DAC to ARP) (see DAC output power)	55.05	dB			
Wideband noise floor requirement (in-band) GSM & WCDMA	-145.05	dBm/Hz	-152.04	-149.03	dBFS/Hz
Large Offset Spectral Mask GSM (offset¿1.8MHz)	-152.05	dBm/Hz	-159.04	-156.03	dBFS/Hz
ORFS GSM (offset ¡1.8MHz)	-133.34	dBm/Hz	-140.33	-140.33	dBFS/Hz
ACLR1 WCDMA (2.5MHz offset)	-129.42	dBm/Hz	-136.41	-136.41	dBFS/Hz
ACLR1 LTE (carrier/2 offset)	-125.79	dBm/Hz	-132.78	-132.78	dBFS/Hz
ACLR2 WCDMA/LTE calculated together for lack of space)	-134.42	dBm/Hz	-141.41	-141.41	dBFS/Hz
Exception: Absolute limit specified for the non-linearity (WCDMA)	-145.05	dBm/Hz	-152.04	-149.03	dBFS/Hz
Resulting ORFS or ACLR requirement (GSM_cls1, WCDMA)	-134.42	dBm/Hz	-141.41	-141.41	dBFS/Hz
Thermal noise floor	-174.00	dBm/Hz	-180.99	-177.98	dBFS/Hz
Resulting toughest Specification				**-156.03**	dBFS/Hz
Spurious Emissions Specifications		**Units**	**dBFS**		**Units**

Continued on the next page . . .

Table C.1: (continued)

		Units	dBFS	cumulative dBFS	
Uplink band desensitisation	-123.00	dBm/Hz		-126.98	dBFS/Hz
Spurious emissions limits for BC2, Category B	-149.77	dBm/Hz	-153.75	-153.75	dBFS/Hz
Resulting toughest Specification				**-153.75**	**dBFS/Hz**
Margins		**Units**	**dBFS**	**cumulative**	**Units**
Margin to accommodate TX chain contribution (Tx Margin)	9.00	dB	-9.00	-165.05	dBFS/Hz
Design Margin	2.00	dB	-2.00	-167.05	dBFS/Hz
Loss from matched load	-3.01	dB	-3.01	**-164.04**	dBFS/Hz
Dynamic Range Requirements		**Units**			**Units**
SNR	**-160.04**	dBm/Hz		-164.04	dBFS/Hz
SFDR	75.18	dBc		**75.18**	dBc
ENOB required				12.90	bits
Actual resolution required (+2 bits INL/DNL)				**14.90**	bits
Clock requirements		**Units**			
Signal Bandwidth (baseband)	60.00	MHz			
IF frequency	153.60	MHz			
DPD bandwidth	300.00	MHz			
Input sampling frequency	600.00	MSps			
DAC interpolation factor	2.00	x			
Interpolation of Signal (w/ DPD)	2.00	x			
DAC output Sampling Frequency	**1.21**	GSps	F_dac = 2 X (2 X ((5 X signal)+ IF))		

Appendix D

Derivations from Chapter 6

D.1 Derivation RF voltage visible at the IF node of the Mixers

This section expands equations 6.28 in greater detail, describing the voltage available across RF load (ignoring higher odd-order harmonics) that is visible at the IF node of the mixers. Assuming an ideal square-wave for the LO signal, the voltage across the RF port of the mixer, due to the IF signal current is given by,

$$V_{RF}(t) = \left(\frac{2}{\pi} i_{IF}(t) cos(\omega_{LO} t) * z_{RF}(t)\right) \tag{D.1}$$

The poor reverse isolation results in the RF node voltage being visible at the IF node due to the LO switching action as is demonstrated by the equations below.

$$V_{IF}(t) = i_{IF}(t).R_{ON} + \left(\frac{2}{\pi} i_{IF}(t) cos(\omega_{LO} t) * z_{RF}(t)\right) \frac{2}{\pi} cos(\omega_{LO} t) \tag{D.2}$$

Considering only the second term of the expression on the right,

$$\left(\frac{2}{\pi} i_{IF}(t) cos(\omega_{LO} t) * z_{RF}(t)\right) \frac{2}{\pi} cos(\omega_{LO} t) \tag{D.3}$$

Since the t is an independent variable, the we can move $cos(w_{LO} t)$ into the integral of the convolution above, as follows.

$$\begin{aligned} &\frac{4}{\pi^2} \int_{-\infty}^{\infty} cos(\omega_{LO} t) i_{IF}(\tau) cos(\omega_{LO} \tau) z_{RF}(t-\tau)\, d\tau \\ =&\frac{4}{\pi^2} \int_{-\infty}^{\infty} i_{IF}(\tau) cos(\omega_{LO} \tau) cos(\omega_{LO}(t-\tau+\tau)) z_{RF}(t-\tau)\, d\tau \\ =&\frac{4}{\pi^2} \int_{-\infty}^{\infty} i_{IF}(\tau) cos(\omega_{LO} \tau) z_{RF}(t-\tau) \left(cos(\omega_{LO}(t-\tau) + \omega_{LO}\tau)\right)\, d\tau \end{aligned} \tag{D.4}$$

$$
\begin{aligned}
=&\frac{4}{\pi^2}\int_{-\infty}^{\infty} i_{IF}(\tau)cos(\omega_{LO}\tau)z_{RF}(t-\tau)\big(cos(\omega_{LO}(t-\tau)cos(\omega_{LO}\tau)\\
&\quad - sin(\omega_{LO}(t-\tau)sin(\omega_{LO}\tau)\big)\,d\tau\\
=&\frac{4}{\pi^2}\int_{-\infty}^{\infty} i_{IF}(\tau)cos(\omega_{LO}\tau)z_{RF}(t-\tau)\frac{1+cos(2\omega_{LO}\tau)}{2}\,d\tau-\\
&\frac{4}{\pi^2}\int_{-\infty}^{\infty} i_{IF}(\tau)sin(\omega_{LO}(t-\tau))z_{RF}(t-\tau)\frac{sin(2\omega_{LO}\tau)}{2}\,d\tau
\end{aligned}
\tag{D.5}
$$

This can be re-written as,

$$
\begin{aligned}
=&\frac{2}{\pi^2}[i_{IF}(t)*z_{RF}(t)cos(\omega_{LO}t)+i_{IF}(t)cos(2\omega_{LO}t)*z_{RF}(t)cos(\omega_{LO}t)\\
&-i_{IF}(t)sin(2\omega_{LO}t)*z_{RF}(t)sin(w_{LO}t)]
\end{aligned}
\tag{D.6}
$$

Expressing cosine and sine terms using Euler's identity, we obtain,

$$
\begin{aligned}
=&\frac{1}{\pi^2}\Bigg[i_{IF}(t)*z_{RF}(t)(e^{j\omega_{LO}t}+e^{-j\omega_{LO}t})\\
&+i_{IF}(t)(e^{j2\omega_{LO}t}+e^{-j2\omega_{LO}t})*z_{RF}(t)\frac{(e^{j\omega_{LO}t}+e^{-j\omega_{LO}t})}{2}\\
&-i_{IF}(t)(e^{j2\omega_{LO}t}+e^{-j2\omega_{LO}t})*z_{RF}(t)\frac{(e^{j\omega_{LO}t}+e^{-j\omega_{LO}t})}{2}\Bigg]
\end{aligned}
\tag{D.7}
$$

Now, we return to the main expression of D.2. Taking Laplace transforms of both sides, yields

$$
\begin{aligned}
=&\frac{1}{\pi^2}\Bigg[I_{IF}(s)Z_{RF}(s-j\omega_{LO})+I_{IF}(s)Z_{RF}(s+j\omega_{LO})\\
&+(I_{IF}(s-j2\omega_{LO})+I_{IF}(s-j2\omega_{LO}))\frac{(Z_{RF}(s-j\omega_{LO}))+(Z_{RF}(s+j\omega_{LO}))}{2}\\
&+(I_{IF}(s-j2\omega_{LO})-I_{IF}(s-j2\omega_{LO}))\frac{(Z_{RF}(s-j\omega_{LO}))-(Z_{RF}(s+j\omega_{LO}))}{2}\Bigg]
\end{aligned}
\tag{D.8}
$$

This finally evaluates to,

$$
\begin{aligned}
=&\frac{1}{\pi^2}[I_{IF}(s)Z_{RF}(s-j\omega_{LO})+I_{IF}(s)Z_{RF}(s+j\omega_{LO})+I_{IF}(s-j2\omega_{LO})Z_{RF}(s-j\omega_{LO})\\
&+(I_{IF}(s-j2\omega_{LO})Z_{RF}(s+j\omega_{LO}))]
\end{aligned}
\tag{D.9}
$$

Having solved both the terms of Equation D.2, we can express the Laplace transform of the equation as,

$$
\begin{aligned}
V_{IF}(s)=I_{IF}(s).R_{ON}+&\frac{1}{\pi^2}[I_{IF}(s)Z_{RF}(s-j\omega_{LO})+I_{IF}(s)Z_{RF}(s+j\omega_{LO})\\
&+I_{IF}(s-j2\omega_{LO})Z_{RF}(s-j\omega_{LO})\\
&+(I_{IF}(s-j2\omega_{LO})Z_{RF}(s+j\omega_{LO}))]
\end{aligned}
\tag{D.10}
$$

It is readily noticeable from the above equation that at the frequencies of the IF signal current $i_{IF}(t)$, there is also a voltage across the RF impedance that has an IF component (second term of D.10). Setting $s = j\omega_{-IF}$ also reveals that presence of image frequency $I_{IF}(j\omega_{-IF})Z_{RF}(j\omega_{-IF} + j\omega_{LO})$ signal which causes fluctuations at the IF port. The reader is referred to [113] for a more thorough analysis, applicable to radio receivers.

D.2 Input Impedance of the Common-Emitter Stage with Series-Series/Shunt-Shunt Feedback

Analysing the influence of shunt-shunt (parallel) feedback on a network is done fairly easily by means of the Y-parameter network. If we assume the feedback network to comprise of a series combination of a resistor R_{fb} and a capacitor C_{fb}, we can calculate the resulting Y-parameters of the network with feedback as follows.

We begin by determining the Y-parameters of the Common-Emitter stage without the feedback network, at mid- and high-frequency.

$$Y_{11,ce} = \frac{\frac{\frac{gm}{\beta_f}+sC_\pi}{1+Z_E\left(gm+\frac{gm}{\beta_f}+sC_\pi\right)} + sC_{bc}}{1 + r_{bb}\left(\frac{\frac{gm}{\beta_f}+sC_\pi}{1+Z_E(gm+\frac{gm}{\beta_f}+sC_\pi)} + sC_{bc}\right)} \tag{D.11}$$

$$Y_{12,ce} = \frac{-sC_{bc}}{1 + r_{bb}\left(\frac{\frac{gm}{\beta_f}+sC_\pi}{1+Z_E(gm+\frac{gm}{\beta_f}+sC_\pi)} + sC_{bc}\right)} \tag{D.12}$$

$$Y_{21,ce} = \frac{\frac{gm}{1+Z_E\left(gm+\frac{gm}{\beta_f}+sC_\pi\right)} - sC_{bc}}{1 + r_{bb}\left(\frac{\frac{gm}{\beta_f}+sC_\pi}{1+Z_E(gm+\frac{gm}{\beta_f}+sC_\pi)} + sC_{bc}\right)} \tag{D.13}$$

$$Y_{22,ce} = \frac{sC_{bc}\left(1 + r_{bb}\left(\frac{\frac{gm}{\beta_f}+sC_\pi}{1+Z_E\left(gm+\frac{gm}{\beta_f}+sC_\pi\right)} + \frac{gm}{1+Z_E\left(gm+\frac{gm}{\beta_f}+sC_\pi\right)}\right)\right)}{1 + r_{bb}\left(\frac{\frac{gm}{\beta_f}+sC_\pi}{1+Z_E(gm+\frac{gm}{\beta_f}+sC_\pi)} + sC_{bc}\right)} \tag{D.14}$$

where r_{bb} is the resistance of the Base terminal, β_f is the forward current gain and Z_E is the degeneration impedance across the Emitter terminal.

The Y-parameters of the feedback network are as follows.

$$Y_{11,fb} = \frac{1}{R_{fb} + \frac{1}{sC_{fb}}} \tag{D.15}$$

$$Y_{12,fb} = \frac{1}{R_{fb} + \frac{1}{sC_{fb}}} \tag{D.16}$$

$$Y_{21,fb} = \frac{1}{R_{fb} + \frac{1}{sC_{fb}}} \tag{D.17}$$

$$Y_{22,fb} = \frac{1}{R_{fb} + \frac{1}{sC_{fb}}} \tag{D.18}$$

The Y-parameters of the resulting network can be determined by simply adding the Y-parameters of the primary network and the feedback network, giving,

$$\begin{aligned} Y_{11,cew/fb} &= Y_{11,ce} + Y_{fb} \\ Y_{12,cew/fb} &= Y_{12,ce} + Y_{fb} \\ Y_{21,cew/fb} &= Y_{21,ce} + Y_{fb} \\ Y_{22,cew/fb} &= Y_{22,ce} + Y_{fb} \end{aligned} \tag{D.19}$$

where, $Y_{11,fb}, Y_{12,fb}, Y_{21,fb}, Y_{22,fb} = Y_{fb} = \frac{1}{R_{fb}+\frac{1}{sC_{fb}}}$.

Assuming a load admittance of Y_L, we combine expressions D.11 - D.19, to determine the input impedance of the CE stage to be,

$$Zin, cewfb = \frac{1}{Y_{11,cew/fb} + \frac{Y_{12,cew/fb}Y_{21,cew/fb}}{Y_{22,cew/fb}+Y_L}} \tag{D.20}$$

Bibliography

[1] G. Fischer, "Future challenges in R&D with respect to mobile communication basestations," Bell Labs Research, Tech. Rep., January 2008.

[2] A. Conte. (2012, February) Power consumption of base stations. FP7 - TREND Workshop. Alcatel-Lucent Bell Labs France. Retrieved from http://www.fp7-trend.eu/.

[3] Altera. (2009, March) Simplifying Simultaneous Multimode RRH Design. http://www.altera.com/literature/wp/wp-01097-arria-ii-gx-multimode-rrh.pdf.

[4] O. Arnold, F. Richter, G. Fettweis, and O. Blume, "Power consumption modeling of different base station types in heterogeneous cellular networks," in *Proceedings of the 19th Future Network and Mobile Summit*, June 2010, pp. 1–8.

[5] G. Fischer, "Next-generation base station radio frequency architecture," *Bell Labs Technical Journal*, vol. 12(2), pp. 3–18, 2007.

[6] F. Richter, A. Fehske, and G. Fettweis, "Energy efficiency aspects of base station deployment strategies for cellular networks," in *Proceedings of the 70th Vehicular Technology Conference (VTC Fall)*, September 2009, pp. 1–5.

[7] "The impact of ICT on global emissions," Global eSustainability Initiative (GeSI), McKinsey & Company, Tech. Rep., November 2007.

[8] G. P. Fettweis and E. Zimmermann, "ICT energy consumption - trends and challenges," in *Proceedings of the 11th International Symposium on Wireless Personal Multimedia Communications*, vol. 2, no. 4, September 2008.

[9] B. Hagerman, D. Imbeni, J. Barta, A. Pollard, R. Wohlmuth, and P. Cosimini, "WCDMA 6-sector deployment - case study of a real installed UMTS-FDD network," in *Proceedings of the 63rd Vehicular Technology Conference (VTC Spring)*, vol. 2, May 2006, pp. 703–707.

[10] S. Kowlgi, "Multi-mode GSM/WCDMA/LTE Base Station Transmitter : System level requirements analysis," PANAMA Project, Tech. Rep., June 2010.

[11] S. Kowlgi and C. Berland, "Linearity considerations for multi-standard cellular base station transmitters," in *Proceedings of the 41st European Microwave Conference (EuMC)*, October 2011, pp. 226–229.

[12] S. Kowlgi, P. Mattheijssen, C. Berland, and T. Ridgers, "Evm considerations for convergent multi-standard cellular base-station transmitters," in *Personal Indoor and Mobile Radio Communications (PIMRC), 2011 IEEE 22nd International Symposium on*, sept. 2011, pp. 1865 –1869.

[13] ——, "System level considerations for convergent GSM/EDGE/WCDMA/LTE multi-standard Base-Station RF transmitters," *IEEE Circuits and Systems Magazine*, *In preparation*.

[14] S. Kowlgi, L. Gambus, T. Ridgers, and C. Berland, "Design of a DC-300MHz passive current-driven quadrature modulator with 24dB attenuation range with ±0.5db accuracy, 1.5dB power gain and > 24dBm iip3, in SiGe BiCMOS," *Electronic Letters*, *In preparation*.

[15] S. Kowlgi, "System level considerations for Multi-mode Base-Station transmitter design," Presentation, PAR4CR Project, Technical University of Eindhoven, July 2010, (and April 2011).

[16] *E-UTRA, UTRA and GSM/EDGE; Multi-Standard Radio (MSR) Base Station (BS) radio transmission and reception, 3GPP TS 37.104*, 3GPP TSG-RAN Std., September 2009.

[17] "WCDMA frequency refarming - overview," Nokia Siemens Networks, Tech. Rep., 2008.

[18] "Offering 3G services in the 900MHz band," Nokia Siemens Networks, Tech. Rep., 2009.

[19] *Evolved Universal Terrestrial Radio Access (E-UTRA); Base Station (BS) radio transmission and reception (Release 8), 3GPP TS 36.104 v8.5.0*, 3GPP TSG-RAN Std., Rev. 8.5.0, March 2009.

[20] S. Sesia, I. Toufik, and M. Baker, *LTE - The UMTS Long Term Evolution.* John Wiley & Sons Ltd., 2009.

[21] Internet, http://ec.europa.eu/information_society/policy/ecomm/radio_spectrum/topics/reorg/dividend/index_en.htm.

[22] Internet, http://www.intomobile.com/2009/12/11/up-to-19-lte-networks-to-go-live-in-2010-36-networks-to-be-operational-in-2012-list-of-who-and-where.html.

[23] T. Sowlati, D. Rozenblit, R. Pullela, M. Damgaard, E. McCarthy, D. Koh, D. Ripley, F. Balteanu, and I. Gheorghe, "Quad-band GSM/GPRS/EDGE polar loop transmitter," *IEEE Journal of Solid-State Circuits*, vol. 39, no. 12, pp. 2179–2189, December 2004.

[24] R. Staszewski, J. Wallberg, S. Rezeq, C.-M. Hung, O. Eliezer, S. Vemulapalli, C. Fernando, K. Maggio, R. Staszewski, N. Barton, M.-C. Lee, P. Cruise, M. Entezari, K. Muhammad, and D. Leipold, "All-digital PLL and GSM/EDGE transmitter in 90nm CMOS," in *Proceedings of the IEEE Solid-State Circuits Conference (ISSCC)*, vol. 1, February 2005, pp. 316–600.

[25] J. Groe, "Polar transmitters for wireless communications," *IEEE Communications Magazine*, vol. 45, no. 9, pp. 58–63, September 2007.

[26] A. Kavousian, D. Su, M. Hekmat, A. Shirvani, and B. Wooley, "A digitally modulated polar CMOS power amplifier with a 20-MHz channel bandwidth," *IEEE Journal of Solid-State Circuits*, vol. 43, no. 10, pp. 2251–2258, October 2008.

[27] J. Choi, D. Kim, D. Kang, and B. Kim, "A polar transmitter with CMOS programmable hysteretic-controlled hybrid switching supply modulator for multistandard applications," *IEEE Transactions on Microwave Theory and Techniques*, vol. 57, no. 7, pp. 1675–1686, July 2009.

[28] G. Strasser, B. Lindner, L. Maurer, G. Hueber, and A. Springer, "On the spectral regrowth in polar transmitters," in *IEEE MTT-S International Microwave Symposium Digest*, June 2006, pp. 781–784.

[29] J. Zhuang, K. Waheed, and R. Staszewski, "A technique to reduce phase/frequency modulation bandwidth in a polar RF transmitter," *IEEE Transactions on Circuits and Systems I: Regular Papers*, vol. 57, no. 8, pp. 2196–2207, August 2010.

[30] P.-I. Mak, S.-P. U, and R. Martins, "Transceiver architecture selection: Review, state-of-the-art survey and case study," *IEEE Circuits and Systems Magazine*, vol. 7, no. 2, pp. 6–25, Second Quarter 2007.

[31] *Dual, 16-Bit, 1230 MSPS, TxDAC+ Digital-to-Analog Converter*, Rev. b ed., Analog Devices. [Online]. Available: www.analog.com/static/imported-files/data_sheets/AD9122.pdf

[32] *Quad-Channel, 16-Bit, 1.25 GSPS Digital-to-Analog Converter, DAC3484*, Rev. a ed., Texas Instruments, http://www.ti.com/lit/ds/symlink/dac3484.pdf.

[33] *Dual 16-bit DAC, LVDS interface, up to 1.25 Gsps, x2, x4 and x8 interpolating*, NXP Semiconductors. [Online]. Available: www.nxp.com/documents/data_sheet/DAC1627D1G25.pdf

[34] S. C. Cripps, *RF Power Amplifiers for Wireless Communications*, 2nd ed. Artech House Inc., 2006.

[35] L. R. Kahn, "Single sideband transmission by envelope elimination and restoration," in *Proceedings of the Institute of Radio Engineers*, vol. 40, July 1952, pp. 803–806.

[36] H. Chireix, "High power outphasing modulation," *Proceedings of the Institute of Radio Engineers*, vol. 23, no. 11, pp. 1370–1392, November 1935.

[37] P. Eloranta, P. Seppinen, S. Kallioinen, T. Saarela, and A. Parssinen, "A multimode transmitter in 0.13μm CMOS using direct-digital RF modulator," *IEEE Journal of Solid-State Circuits*, vol. 42, no. 12, pp. 2774–2784, December 2007.

[38] R. Wesson, "Linearization techniques for RF PAs," NXP Semiconductors, Internal presentation, September 2011, internal communication.

[39] "Public consultation on the award of licenses in the 800 MHz and 2.6 GHz frequency bands for ultra high-speed mobile services," Autorité de Régulation des Communications Électroniques, Tech. Rep., June 2009.

[40] "The use of Mobile Bands in CEPT," European Communications Office, Tech. Rep., 2009.

[41] "Compatibility study for UMTS operating within the GSM900 and GSM1800 Bands; ECC Report 82," Electronics Communications Committee, Tech. Rep., May 2006.

[42] K. Johansson, "Cost effective deployment strategies for heterogeneous wireless networks," Ph.D. dissertation, KTH Royal Institute of Technology, 2007.

[43] L. Qianhao, "A milestone of GSM base stations," *ZTE Technologies*, vol. 10, no. 2, pp. 11–13, 2010.

[44] *14-Bit 400 MSPS 2x/4x Interpolating Digital-to-Analog Converter*, Rev. a ed., Texas Instruments. [Online]. Available: http://www.ti.com/lit/ds/symlink/dac5674.pdf

[45] G. Fettweis, M. Lohning, D. Petrovic, M. Windisch, P. Zillmann, and W. Rave, "Dirty RF: a new paradigm," in *Proceedings of the IEEE 16th International Symposium on Personal, Indoor and Mobile Radio Communications (PIMRC)*, vol. 4, September 2005, pp. 2347–2355.

[46] M. Valkama, A. Springer, and G. Hueber, "Digital signal processing for reducing the effects of RF imperfections in radio devices; An overview," in *Proceedings of 2010 IEEE International Symposium on Circuits and Systems (ISCAS)*, June 2010, pp. 813–816.

[47] Qualcomm Europe, "LTE BS EVM Requirement Methodology," 3GPP, Tech. Rep. R4-070228. [Online]. Available: http://www.3gpp.org/ftp/tsg_ran/WG4_Radio/TSGR4_42/Docs/R4-070228.zip

[48] *GSM/EDGE Radio Access Network; Radio Transmission and Reception (Release 9)*, 3GPP TSG-RAN Std., Rev. 9.5.0, 2011.

[49] S. Cavalcanti, Francisco Rodrigo Porto; Andersson, *Optimizing Wireless Communication Systems*. Springer, 2009.

[50] *UTRA Base Station (BS) radio transmission and reception (FDD) (Release 8)*, 3GPP TSG-RAN Std. 25.104, Rev. 8.6.0, 2009.

[51] A. Georgiadis, "Gain, phase imbalance, and phase noise effects on error vector magnitude," *IEEE Transactions on Vehicular Technology*, vol. 53, no. 2, pp. 443–449, March 2004.

[52] R. Liu, Y. Li, H. Chen, and Z. Wang, "EVM estimation by analyzing transmitter imperfections mathematically and graphically," *Analog Integrated Circuits and Signal Processing*, vol. 48, pp. 257–262, 2006.

[53] C. Zhao and R. Baxley, "Error vector magnitude analysis for OFDM systems," in *Proceedings of the Fortieth Asilomar Conference on Signals, Systems and Computers (ACSSC '06)*, November 2006, pp. 1830–1834.

[54] J. Tubbax, B. Come, L. Van der Perre, S. Donnay, M. Engels, H. D. Man, and M. Moonen, "Compensation of IQ imbalance and phase noise in OFDM systems," *IEEE Transactions on Wireless Communications*, vol. 4, no. 3, pp. 872–877, May 2005.

[55] *GSM/EDGE Radio Access Network; Modulation (Release 11)*, 3GPP TSG-RAN Std. 45.004, Rev. 11.0.0, September 2012.

[56] S. Freisleben, "Semi-analytical computation of error vector magnitude for UMTS SAW filters," in *Proceedings of the IEEE Ultrasonics Symposium*, vol. 1, October 2002, pp. 109–112.

[57] H. Arslan and H. Mahmoud, "Error vector magnitude to SNR conversion for nondata-aided receivers," *IEEE Transactions on Wireless Communications*, vol. 8, no. 5, pp. 2694–2704, May 2009.

[58] C.-H. Yih, "Analysis and compensation of DC offset in OFDM systems over frequency-selective rayleigh fading channels," *IEEE Transactions on Vehicular Technology*, vol. 58, no. 7, pp. 3436–3446, September 2009.

[59] C. J. Meyer, "AN-50: Measuring the peak-to-average power of digitally modulated signals," Boonton Electronics, Tech. Rep., April 1993.

[60] "IEEE standard definitions of physical quantities for fundamental frequency and time metrology—random instabilities," *IEEE STD 1139-2008*, no. 27, pp. c1–35, 2008.

[61] Agilent, Technologies, "Effects of physical impairments on OFDM signals," 3GPP TSG-RAN WG5, Tech. Rep., November 2006.

[62] A. Garcia Armada, "Understanding the effects of phase noise in orthogonal frequency division multiplexing (OFDM)," *IEEE Transactions on Broadcasting*, vol. 47, no. 2, pp. 153–159, June 2001.

[63] T. Schenk and P. Mattheijssen, "Analysis of the influence of phase noise in MIMO OFDM based WLAN systems," in *Proceedings of Symposium IEEE Benelux Chapter on Communications and Vehicular Technology (SCVT2003)*, 2003, pp. 1–8.

[64] Q. Zou, A. Tarighat, and A. Sayed, "Joint compensation of IQ imbalance and phase noise in OFDM wireless systems," *IEEE Transactions on Communications*, vol. 57, no. 2, pp. 404–414, February 2009.

[65] T. Pollet, M. Van Bladel, and M. Moeneclaey, "BER sensitivity of OFDM systems to carrier frequency offset and Wiener phase noise," *IEEE Transactions on Communications*, vol. 43, no. 234, pp. 191–193, 1995.

[66] P. Robertson and S. Kaiser, "Analysis of the effects of phase-noise in orthogonal frequency division multiplex (OFDM) systems," in *Proceedings of the IEEE International Conference on Communications*, vol. 3, June 1995, pp. 1652–1657.

[67] D. Petrovic, W. Rave, and G. Fettweis, "Effects of phase noise on OFDM systems with and without PLL: Characterization and compensation," *IEEE Transactions on Communications*, vol. 55, no. 8, pp. 1607–1616, August 2007.

[68] L. Piazzo and P. Mandarini, "Analysis of phase noise effects in OFDM modems," *IEEE Transactions on Communications*, vol. 50, no. 10, pp. 1696–1705, October 2002.

[69] R. Estanqueiro-Santos and N. Carvalho, "EVM estimation in RF/Wireless components," in *Proceedings of the IEEE 18th International Symposium on Personal, Indoor and Mobile Radio Communications (PIMRC)*, September 2007, pp. 1–5.

[70] P. Gilabert, G. Montoro, and E. Bertran, "On the wiener and hammerstein models for power amplifier predistortion," in *Microwave Conference Proceedings, 2005. APMC 2005. Asia-Pacific Conference Proceedings*, vol. 2, 2005, pp. 4 pp.–.

[71] L. Ding and G. Zhou, "Effects of even-order nonlinear terms on power amplifier modeling and predistortion linearization," *IEEE Transactions on Vehicular Technology*, vol. 53, no. 1, pp. 156–162, January 2004.

[72] D. Pimingsdorfer, A. Holm, B. Adler, G. Fischerauer, R. Thomas, A. Springer, and R. Weigel, "Impact of SAW RF and IF filter characteristics on UMTS transceiver system performance," in *Proceedings of the IEEE Ultrasonics Symposium*, vol. 1, 1999, pp. 365–368.

[73] Motorola, "UE Power Management for E-UTRA," 3GPP TSG RAN, Tech. Rep. R1-060144, January 2005.

[74] M. Leffel, "Intermodulation distortion in a multi-signal environment," *RF Design Magazine*, pp. 78–84, June 1995.

[75] J. Martins, N. Carvalho, and J. Pedro, "Intermodulation distortion of third-order nonlinear systems with memory under multisine excitations," *IEEE Transactions on Microwave Theory and Techniques*, vol. 55, no. 6, pp. 1264–1271, June 2007.

[76] R. Larkin, "Multiple-signal intermodulation and stability considerations in the use of linear repeaters," in *Proceedings of the 41st IEEE Vehicular Technology Conference (VTC)*, May 1991, pp. 747–752.

[77] *App. note AN10921 - BLF7G20LS-200 Doherty 1.805 to 1.88 GHz RF power amplifier*, NXP Semiconductors, July 2010. [Online]. Available: http://www.broadcom.com/products/Base-Station-and-Small-Cells/Digital-Front-End-Processors/OP6180

[78] H. Holma and A. Toskala, Eds., *WCDMA for UMTS: HSPA Evolution and LTE*, 5th ed. John Wiley & Sons Ltd., 2010.

[79] ——, *LTE for UMTS-OFDMA and SC-FDMA based radio access*, 1st ed. John Wiley & Sons Ltd., 2009.

[80] C. Liu, H. Xiao, Q. Wu, and F. Li, "Linear RF power amplifier design for wireless signals: a spectrum analysis approach," in *Proceedings of the IEEE International Conference on Acoustics, Speech, and Signal Processing (ICASSP)*, vol. 4, April 2003, pp. 568–571.

[81] H. Pretl, L. Maurer, W. Schelmbauer, R. Weigel, B. Adler, and J. Fenk, "Linearity considerations of W-CDMA front-ends for UMTS," in *IEEE MTT-S International Microwave Symposium Digest*, vol. 1, 2000, pp. 433–436.

[82] P. Wambacq, G. Gielen, P. Kinget, and W. Sansen, "High-frequency distortion analysis of analog integrated circuits," *IEEE Transactions on Circuits and Systems II: Analog and Digital Signal Processing*, vol. 46, no. 3, pp. 335–345, March 1999.

[83] W. Sansen, "Distortion in elementary transistor circuits," *IEEE Transactions on Circuits and Systems II: Analog and Digital Signal Processing*, vol. 46, no. 3, pp. 315–325, March 1999.

[84] J. Sevic and M. Steer, "On the significance of envelope peak-to-average ratio for estimating the spectral regrowth of an RF/microwave power amplifier," *IEEE Transactions on Microwave Theory and Techniques*, vol. 48, no. 6, pp. 1068–1071, June 2000.

[85] Agilent Technologies, "Characterizing Digitally Modulated Signals with CCDF Curves," 2000. [Online]. Available: cp.literature.agilent.com/litweb/pdf/5968-6875E.pdf

[86] Motorola, "Comparison of PAR and Cubic Metric for power de-rating," 3GPP TSG RAN, Tech. Rep. (R1-040642), May 2004.

[87] S. H. Han and J. H. Lee, "An overview of peak-to-average power ratio reduction techniques for multicarrier transmission," *IEEE Wireless Communications*, vol. 12, no. 2, pp. 56–65, April 2005.

[88] M. Deumal, A. Behravan, T. Eriksson, and J. L. Pijoan, "Evaluation of performance improvement capabilities of PAPR-reducing methods," *Wireless Personal Communications*, vol. 47, no. 1, pp. 137–147, October 2008. [Online]. Available: http://dx.doi.org/10.1007/s11277-007-9397-6

[89] H. Friis, "Noise figures of radio receivers," *Proceedings of the IRE*, vol. 32, no. 7, pp. 419–422, July 1944.

[90] A. Oguz, D. Morche, C. Dehollain, and E. Isa, "Adaptive power reconfigurability for preventing excessive power dissipation in wireless receivers," in *Proceedings of the 17th*

IEEE International Conference on Electronics, Circuits, and Systems (ICECS), December 2010, pp. 371–374.

[91] *Analysis of Phase Noise in Oscillators*, November, 1991.

[92] "Clock Jitter and Phase Noise Conversion," Maxim, Tech. Rep., December 2004, application Note.

[93] A. Netsell, "Interpret and apply EVM to RF system design," *Microwaves & RF*, vol. 40, pp. 83–94, 2001.

[94] Intel, Sprint, "Dynamic RAN Sharing Enhancements," 3GPP TSG-SA Work Group1 , Tech. Rep. S1-124483, November 2012.

[95] 3GPP TSG SA Plenary Meeting - 54, "Proposed WID on Study on RAN Sharing Enhancements," 3GPP TSG SA, Tech. Rep. SP-110820, December 2011.

[96] M. Gerogiokas, "System and method of operating a wireless base station with quantized use of transmitter power," U.S. Patent US6 795 716, September 21, 2004.

[97] R. H. Walden, "Analog-to-digital converter survey and analysis," *IEEE Journal on Selected Areas in Communications*, vol. 17, no. 4, pp. 539–550, April 1999. [Online]. Available: http://dx.doi.org/10.1109/49.761034

[98] G. Fischer, "Analogue-Digital Balance in the context of high efficiency amplifiers," in *Proceedings of the 41st European Microwave Conference (EuMC)*, October 2011.

[99] P. Deixler, A. Rodriguez, W. De Boer, H. Sun, R. Colclaser, D. Bower, N. Bell, A. Yao, R. Brock, Y. Bouttement, G. Hurkx, L. Tiemeijer, J. Paasschens, H. Huizing, D. Hartskeerl, P. Agrarwal, P. Magnee, E. Aksen, and J. Slotboom, "QUBiC4X: An ft/fmax = 130/140GHz SiGe:C-BiCMOS manufacturing technology with elite passives for emerging microwave applications," in *Proceedings of the 2004 Meeting on Bipolar/BiCMOS Circuits and Technology*, September 2004, pp. 233–236.

[100] www.nxp.com/documents/datasheet/dac1627d1g25.pdf.

[101] J. D. Cressler, Ed., *Silicon Heterostructure Handbook*. Taylor & Francis Group, LLC., 2005.

[102] P. Kinget, "Device mismatch and tradeoffs in the design of analog circuits," *IEEE Journal of Solid-State Circuits*, vol. 40, no. 6, pp. 1212–1224, June 2005.

[103] P. R. Gray, P. J. Hurst, S. H. Lewis, and R. G. Meyer, *Analysis and Design of Analog Integrated Circuits*, 5th ed. Wiley; New York, 2009.

[104] A. Bilotti and E. Mariani, "Noise characteristics of current mirror sinks/sources," *IEEE Journal of Solid-State Circuits*, vol. 10, no. 6, pp. 516–524, December 1975.

[105] J. Bergervoet, D. Leenaerts, G. de Jong, E. van der Heijden, J.-W. Lobeek, and A. Simin, "A 1.95GHz sub-1dB NF, +40dBm OIP3 WCDMA LNA with variable attenuation in SiGe:C BiCMOS," in *Proceedings of the ESSCIRC*, September 2011, pp. 227–230.

[106] H. Tanimoto, M. Koyama, and Y. Yoshida, "Realization of a 1-V active filter using a linearization technique employing plurality of emitter-coupled pairs," *IEEE Journal of Solid-State Circuits*, vol. 26, no. 7, pp. 937–945, July 1991.

[107] K. Kimura, "The ultra-multi-tanh technique for bipolar linear transconductance amplifiers," *IEEE Transactions on Circuits and Systems I: Fundamental Theory and Applications*, vol. 44, no. 4, pp. 288–302, April 1997.

[108] B. Gilbert, "The multi-tanh principle: a tutorial overview," *IEEE Journal of Solid-State Circuits*, vol. 33, no. 1, pp. 2–17, January 1998.

[109] M. Granger-Jones, B. Nelson, and E. Franzwa, "A broadband high dynamic range voltage controlled attenuator MMIC with IIP3 ¿ +47dBm over entire 30dB analog control range," in *IEEE MTT-S International Microwave Symposium Digest*, June 2011, pp. 1–4.

[110] H. Joba, Y. Takahashi, Y. Matsunami, K. Itoh, S. Shinjo, N. Suematsu, D. Malhi, D. Wang, K. Schelkle, and P. Bacon, "W-CDMA SiGe TX-IC with high dynamic range and high power control accuracy," in *Proceedings of the IEEE Radio Frequency Integrated Circuits (RFIC) Symposium*, 2002, pp. 27–30.

[111] H. Dogan and R. Meyer, "Intermodulation distortion in CMOS attenuators and switches," *IEEE Journal of Solid-State Circuits*, vol. 42, no. 3, pp. 529–539, March 2007.

[112] H. Dogan, R. Meyer, and A. Niknejad, "Analysis and design of RF CMOS attenuators," *IEEE Journal of Solid-State Circuits*, vol. 43, no. 10, pp. 2269–2283, October 2008.

[113] A. Mirzaei, H. Darabi, J. Leete, X. Chen, K. Juan, and A. Yazdi, "Analysis and optimization of current-driven passive mixers in narrowband direct-conversion receivers," *IEEE Journal of Solid-State Circuits*, vol. 44, no. 10, p. 2678/2688, October 2009.

[114] M. Terrovitis and R. Meyer, "Noise in current-commutating CMOS mixers," *IEEE Journal of Solid-State Circuits*, vol. 34, no. 6, pp. 772–783, June 1999.

[115] A. Shahani, D. Shaeffer, and T. Lee, "A 12 mW wide dynamic range CMOS front end for a portable GPS receiver," in *Proceedings of the 43rd IEEE International Solid-State Circuits Conference (ISSCC)*, February 1997, pp. 368 –369, 487.

[116] S. Kang, B. Choi, and B. Kim, "Linearity analysis of CMOS for RF application," *IEEE Transactions on Microwave Theory and Techniques*, vol. 51, no. 3, pp. 972–977, March 2003.

[117] Y. Tsividis and C. McAndrew, *Operation and Modeling of the MOS Transistor*. Oxford University Press, USA, 2003.

[118] T. Soorapanth, , and T. H. Lee, "RF linearity of short-channel MOSFETs," in *Proceedings of the First International Workshop on Design of Mixed-Mode Integrated Circuits and Applications*, 1997, pp. 81–84.

[119] H. Khatri, P. Gudem, and L. Larson, "Simulation of intermodulation distortion in passive CMOS FET mixers," in *IEEE MTT-S International Microwave Symposium Digest (MTT '09)*, June 2009, pp. 1593–1596.

[120] J. Gardiner, "The relationship between cross-modulation and intermodulation distortions in the double-balanced modulator," *Proceedings of the IEEE*, vol. 56, no. 11, pp. 2069–2071, November 1968.

[121] D. Surana and J. Gardiner, "Gain and distortion properties of FET mixers and modulators," *IEEE Transactions on Electromagnetic Compatibility*, vol. EMC-16, no. 1, pp. 29–38, February 1974.

[122] ——, "Calculation of intermodulation distortion levels in f.e.t. mixers and modulators," *Electronics Letters*, vol. 7, no. 8, pp. 167–169, 1971.

[123] B. Razavi, *Principles of Data Conversion System Design*. Wiley-IEEE Press, 1995.

[124] H. Darabi and A. Abidi, "Noise in RF-CMOS mixers: a simple physical model," *IEEE Journal of Solid-State Circuits*, vol. 35, no. 1, pp. 15–25, January 2000.

[125] I. Darwazeh and B. Wilson, "Hybrid pi; common base analysis," *IEEE Transactions on Circuits and Systems*, vol. 37, no. 5, pp. 655–656, May 1990.

[126] S. Chehrazi, A. Mirzaei, and A. Abidi, "Noise in current-commutating passive FET mixers," *IEEE Transactions on Circuits and Systems I: Regular Papers*, vol. 57, no. 2, pp. 332–344, February 2010.

[127] S. Chehrazi, R. Bagheri, and A. Abidi, "Noise in passive FET mixers: a simple physical model," in *Proceedings of the IEEE Custom Integrated Circuits Conference*, oct. 2004, pp. 375 – 378.

[128] M. J. Gingell, "A symmetrical polyphase network," U.S. Patent 3 559 042 & 3 618 133, January 26, 1971.

[129] J. Crols and M. Steyaert, "An analog integrated polyphase filter for a high performance low-IF receiver," in *Proceedings of the Symposium on VLSI Circuits*, jun 1995, pp. 87–88.

[130] S. Galal, H. Ragaie, and M. Tawfik, "RC sequence asymmetric polyphase networks for RF integrated transceivers," *IEEE Transactions on Circuits and Systems II: Analog and Digital Signal Processing*, vol. 47, no. 1, pp. 18–27, January 2000.

[131] F. Behbahani, Y. Kishigami, J. Leete, and A. Abidi, "CMOS mixers and polyphase filters for large image rejection," *IEEE Journal of Solid-State Circuits*, vol. 36, no. 6, pp. 873–887, June 2001.

[132] L. A. Goodman, "On the Exact Variance of Products," *Journal of the American Statistical Association*, vol. 55, no. 292, pp. 708–713, December 1960. [Online]. Available: http://dx.doi.org/10.2307/2281592

[133] J. Archer, J. Granlund, and R. Mauzy, "A broad-band VHF mixer exhibiting high image rejection over a multidecade baseband frequency range," *IEEE Journal of Solid-State Circuits*, vol. 16, no. 4, pp. 385–392, August 1981.

[134] Razavi and Behzad, *RF Microelectronics*, ser. Prentice Hall Communications Engineering and Emerging Technologies Series. Prentice Hall, 1997.

[135] M. McNutt, S. LeMarquis, and J. Dunkley, "Systematic capacitance matching errors and corrective layout procedures," *IEEE Journal of Solid-State Circuits*, vol. 29, no. 5, pp. 611–616, May 1994.

[136] V. Rideout, "A note on a parallel-tuned transformer design," Bell Systems Technical Journal, Tech. Rep., 1948.

[137] V. Aparin and L. Larson, "Modified derivative superposition method for linearizing FET low-noise amplifiers," *IEEE Transactions on Microwave Theory and Techniques*, vol. 53, no. 2, pp. 571–581, February 2005.